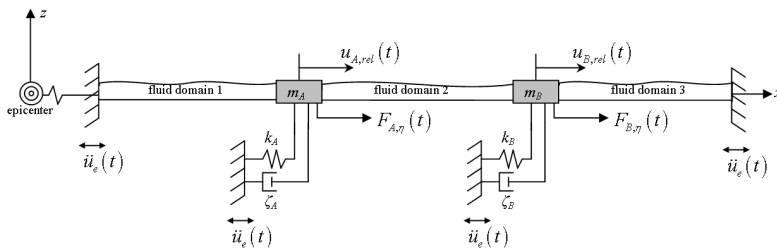
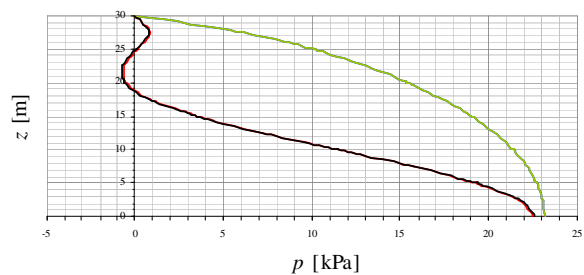


# Hydrodynamic pressures on large lock structures



Hydrodynamic pressure on a lock gate



Graduation committee:  
 prof. drs. ir. J.K. Vrijling  
 prof. dr. A.V. Metrikine  
 ir. W.F. Molenaar  
 ir. J. Manie  
 ir. P. Carree

Author : Marco Versluis  
 Student ID : 1213393

Date : April 2010



# Hydrodynamic pressures on large lock structures

Master of Science thesis

for acquisition of the degree  
Master of Science in Civil Engineering  
at Delft University of Technology

by  
Marco Versluis

April 2010

*Graduation committee:*

**prof. drs. ir. J.K. Vrijling (chairman)**

Section of Hydraulic Engineering, Faculty of Civil Engineering and Geosciences, Delft University of Technology

**prof. dr. A.V. Metrikine**

Section of Structural Mechanics, Faculty of Civil Engineering and Geosciences, Delft University of Technology

**ir. W.F. Molenaar**

Section of Hydraulic Engineering, Faculty of Civil Engineering and Geosciences, Delft University of Technology

**ir. J. Manie**

Software Development Engineer, TNO DIANA

**ir. P. Carree**

Senior Structural Engineer, Witteveen+Bos Consulting Engineers



## Preface

---

This thesis marks the end of my study Civil Engineering at Delft University of Technology at the department of Hydraulic Engineering, faculty of Civil Engineering and Geosciences. This research project has been performed in cooperation the engineering company Witteveen+Bos. Witteveen+Bos participated as subcontractor in the tender design of the Panama Canal Third Set of Locks Project. The Panama isthmus is an area prone to earthquakes and therefore seismic loading is an important aspect in the design of the new Post-Panamax locks. Based on this project I chose the subject of my thesis: hydrodynamic pressure on large lock structures as a result of earthquakes. The project also serves as a case study.

I would like to thank my supervisors: prof. drs. ir. J.K. Vrijling, prof. dr. A.V. Metrikine and ir. W.F. Molenaar from the faculty, ir. J. Manie from TNO DIANA and ir. P. Carree from Witteveen+Bos for their guidance and feedback.

Special thanks to my family who have always supported me.

Marco Versluis  
Rotterdam, April 2010



## Abstract

---

When a navigation lock, dam, or any other structure with water is subjected to an earthquake, one of the dynamic loads will be hydrodynamic pressure. This is the pressure exerted by the fluid on the structure as a result of the different behavior in motion of solid and fluid. To determine this pressure there are several methods available which focus mainly on large dams or fluid storage containers. The hydrodynamic behavior of these types of structures is different and these methods may or may not be applicable for navigation locks. Therefore an analysis is made to determine the factors that contribute to the hydrodynamic pressure distribution on large lock structures.

As a case study the Third Set of Locks Project of the Panama Canal is used. This expansion project ensures that the Panama Canal can process larger ships than the current *Panamax* class of ships, which dimensions are limited by the existing locks. Therefore larger locks are required which will operate next to the existing locks. The new locks are planned to be operational in 2014-2015. The Panama region is prone to earthquakes which could result in large hydrodynamic pressures on the locks.

For the evaluation of hydrodynamic pressures on the gates and walls of large lock structures, two analytical (1D and 2D) and one 2D finite-element model are made. These models are based on linear theory. Three main aspects that contribute to hydrodynamic pressure are treated in detail:

- Lock dimensions and water levels;
- The effect of surface waves on the hydrodynamic pressure distribution;
- The stiffness of the structure.

In terms of dimensions, one of the main differences between lock chambers and large dams is the length of the chamber or reservoir. The length of the chamber affects the hydrodynamic pressures in two ways: it limits the impulsive (added mass) pressures but causes additional convective pressures due to sloshing. In general, the effect of the chamber length on the magnitude of the hydrodynamic pressure is however limited. Only in the case of a length over water depth ratio of 4 or smaller, there is a reduction of the pressure. For length over depth ratio higher than 4, results are identical. This means only the water close to the gate or wall reacts and that for large length the two boundaries can be treated individually. This is in agreement with the concept of added mass, which assumes a body of water moving with a wall. A phase difference between two boundaries has therefore almost no effect. Note that this can change for higher excitation frequencies.

The second way the chamber length influences the hydrodynamic pressure is a result of sloshing, which cannot occur in a semi-infinite environment. Although for the large lock chambers many sloshing frequencies can be found, in reality it takes too long for surface waves to cross the chamber to start the sloshing phenomenon. By that time the earthquake is already over. In case of a very small length also little to no sloshing effects are to be expected. If linear surface waves are neglected in the evaluation, the sloshing phenomenon cannot be identified. Given the fact that neglecting surface waves greatly simplifies the analysis and has almost no outcome on the solution; it can be concluded that this assumption of neglecting surface waves is also valid for navigation locks. This conclusion is based on the results obtained by the two analytical models. In the finite element results, no sloshing frequencies could be identified.

Another difference in dimensions between navigation locks and large, high-head dams is the water depth. If compressibility of water is taken into account, the impounded water has eigenfrequencies for hydrodynamic pressure. These eigenfrequencies are inversely proportional to the water depth, meaning that the fundamental eigenfrequency is lower for larger water depth. The water depth inside a navigation lock is directly related to the draught of the design vessel and is therefore much smaller than in the case of a high-head dam. For the maximum water depth of the Post-Panamax locks, around 30 m, the fundamental eigenfrequency related to compressibility is larger than the frequencies at which the most energy of an earthquake is distributed. For excitation frequencies below this fundamental eigenfrequency, the amplitude of hydrodynamic pressure is almost independent of the excitation frequency. Also, the assumption of incompressible water gives in this situation similar results. Therefore, the limited water depth in navigation locks means that in practice the hydrodynamic pressure is constant for the considered frequencies and the assumption of incompressible water is valid. The pressure distribution along the face of a gate/wall remains parabolic in this frequency range. For higher excitation frequencies, above the fundamental eigenfrequency related to compressibility, the pressure distribution is no longer parabolic, but sinusoidal and the assumptions are not valid anymore.

The above conclusions are based on the assumption of rigid gates and/or walls. With the aid of the 2D finite element model rigid gates were replaced with gates with a certain bending stiffness. The bending stiffness of the used gates and the position of the supports are estimated, but the result in amplitude is significantly different. The maximum pressure along the face is no longer at the bottom of the gate, but higher up. Although this applies to a single case, it shows that the assumption of rigid gates/walls has to be applied with care.

Based on the findings of this thesis the following recommendations can be made:

- The performed analyses are performed in a 2D environment, with direction of earthquake loading perpendicular to a lock gate. Other source-to-site directions and the effects of the side walls are not incorporated. The reduced amount of water that can react in both cases should lead to a reduction of the hydrodynamic pressure compared to the case in a 2D environment. This is shown by effect of the length of the chamber. The presence of a ship inside the lock chamber during an earthquake might also reduce the hydrodynamic pressure on the structure as the amount of water inside the chamber is less due to the displacement of the vessel. With a 3D analysis these effects can be investigated.
- Surface waves and effects like sloshing have little to no influence on the total pressure distribution. Therefore the assumption that the pressure at the water surface is equal to zero is also valid for navigation locks and recommended for practical design.
- The stiffness of the structure is not incorporated in the solution of the 2D analytical model or the Westergaard and Housner solution. An adaption of the 2D finite element model showed that the stiffness and support system of a lock gate do change the loading on the lock gate. Therefore it is recommended that a preliminary analysis is made to investigate if a closed or (semi-)opened gate, or the chamber itself can be treated as rigid. If not, the stiffness of the structure should be incorporated in the evaluation, as it can result in a significant in- or decrease of the hydrodynamic loading.
- Not only the horizontal component of an earthquake, but also the vertical component causes hydrodynamic pressures on walls. This aspect is not treated in this thesis, but would be an interesting element to include in future studies. The vertical component is in general smaller than the horizontal component.
- Analyses made in this thesis are done in the frequency domain; a time domain analysis is not performed but gives more insight in the hydrodynamic pressures during the event of an earthquake.
- The existing analytical methods by Westergaard or Housner give adequate accuracy and can be used in early design stages. The loads can be evaluated by means of pressure or the concept of added mass. An estimate for the accuracy can be obtained by comparing a spectrum with the fundamental eigenfrequency for the maximum design water level. For later design stages the use of advanced methods should be used to determine the hydrodynamic pressures and consequently the response of the structure. As stated before, the analytical Westergaard and Housner approaches do not incorporate the frequency-dependent motion of the structure, but assume a rigid behavior. A finite element analysis using fluid-structure interaction can incorporate these effects and will therefore give in general a more accurate result. That this is not always the case followed from the finite element model used in this thesis, which failed to identify possible sloshing frequencies.

# Table of contents

<b>PREFACE</b> .....	<b>V</b>
<b>ABSTRACT</b> .....	<b>VII</b>
<b>TABLE OF CONTENTS</b> .....	<b>IX</b>
<b>LIST OF FIGURES</b> .....	<b>XI</b>
<b>LIST OF TABLES</b> .....	<b>XII</b>
<b>LIST OF SYMBOLS</b> .....	<b>XIII</b>
<b>1. INTRODUCTION</b> .....	<b>1</b>
1.1. OBJECTIVES OF THESIS .....	1
1.2. LAYOUT OF THESIS .....	1
<b>2. PROJECT BACKGROUND</b> .....	<b>3</b>
2.1. HISTORY OF THE PANAMA CANAL .....	3
2.2. CURRENT LAYOUT OF THE PANAMA CANAL .....	3
2.3. THIRD SET OF LOCKS EXPANSION PROJECT .....	4
2.4. PROPOSED DESIGN .....	5
2.4.1. General and chamber dimensions .....	5
2.4.2. Lock heads.....	6
2.4.3. Lock gates .....	8
<b>3. EARTHQUAKES</b> .....	<b>9</b>
3.1. INTRODUCTION .....	9
3.2. TYPES OF EARTHQUAKES .....	9
3.3. SEISMIC WAVES .....	10
3.3.1. P-waves .....	10
3.3.2. S-waves .....	11
3.3.3. Rayleigh waves.....	11
3.3.4. Love-waves .....	11
<b>4. COMMONLY USED PROCEDURES FOR (HYDRO)DYNAMIC ANALYSES</b> .....	<b>13</b>
4.1. INTRODUCTION .....	13
4.2. QUASI-STATIC (SEISMIC COEFFICIENT METHOD) .....	13
4.3. RESPONSE SPECTRUM ANALYSIS .....	14
4.4. TIME-HISTORY ANALYSIS.....	14
4.5. HYBRID FREQUENCY TIME DOMAIN ANALYSIS .....	15
4.6. A BRIEF INTRODUCTION TO THE FINITE ELEMENT METHOD .....	15
4.7. HYDRODYNAMIC PRESSURES .....	16
4.7.1. Hydrodynamic pressure according to Westergaard .....	16
4.7.2. Hydrodynamic pressure according to Housner .....	18
4.7.3. Transformation to added mass .....	21
<b>5. SITE CONDITIONS AND PRELIMINARY ASSESSMENT</b> .....	<b>23</b>
5.1. BOUNDARY CONDITIONS .....	23
5.1.1. Seismic conditions.....	23
5.1.2. Soil and rock properties .....	23
5.2. PRELIMINARY ASSESSMENT: THE WESTERGAARD AND HOUSNER FORMULAS APPLIED .....	23
5.3. HOUSNER'S MATHEMATICAL MODEL .....	25
5.3.1. Introduction to Housner's model .....	25
5.3.2. Response spectrum approach.....	25
5.3.3. SDOF approach .....	26
5.3.4. Conclusions Housner's model.....	27
<b>6. ONE-DIMENSION MODEL FOR WAVE INTERACTION</b> .....	<b>29</b>
6.1. INTRODUCTION 1D MODEL.....	29
6.2. STRATEGY .....	29
6.3. THE 1D MODEL OF A LOCK HEAD .....	30
6.4. EQUATIONS OF MOTION .....	34
6.5. STEADY-STATE SOLUTIONS .....	34
6.6. BOUNDARY CONDITIONS .....	35
6.7. APPLYING BOUNDARY AND INTERFACE CONDITIONS .....	36
6.8. SOLUTIONS IN THE FREQUENCY DOMAIN .....	36
6.8.1. Solution to the wave equation only.....	36
6.8.2. Response to inertia force.....	37
6.9. NUMERIC VALUES.....	37
6.10. CONCLUSIONS 1D MODEL FOR WAVE INTERACTION .....	39

<b>7.</b>	<b>TWO-DIMENSIONAL MODEL FOR HYDRODYNAMIC PRESSURE</b> .....	<b>43</b>
7.1.	INTRODUCTION 2D MODEL.....	43
7.2.	STRATEGY.....	43
7.3.	2D MODEL AND BOUNDARY CONDITIONS.....	44
7.4.	EIGENFREQUENCIES OF THE SYSTEM.....	45
7.5.	STEADY-STATE SOLUTION.....	46
7.6.	SOLUTION IN THE FREQUENCY DOMAIN.....	46
7.7.	NUMERIC VALUES.....	47
7.8.	FREQUENCY DOMAIN RESULTS OF THE 2D MODEL.....	47
7.8.1.	Eigenfrequencies.....	47
7.8.2.	Hydrodynamic pressure at bottom of gate (situation long lock chamber).....	48
7.8.3.	Hydrodynamic pressure at top of gate (situation long lock chamber).....	48
7.8.4.	Hydrodynamic pressure at bottom of gate (situation shorter intermediate chamber).....	50
7.8.5.	Hydrodynamic pressure at top of gate (situation shorter intermediate chamber).....	50
7.8.6.	Hydrodynamic pressure along the face of the gate (situation long lock chamber).....	51
7.8.7.	Hydrodynamic pressure along the face of the gate (situation shorter intermediate chamber).....	53
7.8.8.	The effect of surface waves.....	55
7.8.9.	Length and depth of lock chamber.....	55
7.9.	COMPARISON WITH WESTERGAARD'S RESULTS.....	56
7.10.	CONCLUSIONS 2D MODEL FOR HYDRODYNAMIC PRESSURE.....	57
7.10.1.	Solution.....	57
7.10.2.	Resonance effects.....	57
7.10.3.	Effect of surface waves.....	58
7.10.4.	Phase difference and chamber length.....	58
7.10.5.	Compressibility effects.....	58
<b>8.</b>	<b>TWO-DIMENSIONAL MODEL FOR FLUID-STRUCTURE INTERACTION</b> .....	<b>59</b>
8.1.	INTRODUCTION.....	59
8.2.	STRATEGY.....	60
8.3.	PREPROCESSING: ELEMENT TYPES AND NUMERICAL VALUES.....	60
8.3.1.	Introduction.....	60
8.3.2.	Element types.....	61
8.3.3.	Numerical values.....	62
8.4.	RESULTS IN THE FREQUENCY DOMAIN.....	63
8.4.1.	Introduction.....	63
8.4.2.	Hydrodynamic pressure at bottom of gate (situation long lock chamber).....	63
8.4.3.	Hydrodynamic pressure at bottom of gate (situation shorter intermediate chamber).....	67
8.4.4.	Hydrodynamic pressure along the face of the gate (situation long lock chamber).....	69
8.4.5.	Hydrodynamic pressure along the face of the gate (situation shorter intermediate chamber).....	74
8.4.6.	Effect of the stiffness of the gates.....	78
8.4.7.	Semi-infinite chamber.....	81
8.5.	CONCLUSIONS 2D MODEL FOR FLUID-STRUCTURE INTERACTION.....	84
8.5.1.	Solution.....	84
8.5.2.	Comparison of results with the 2D analytical model.....	84
8.5.3.	Compressibility effects.....	84
8.5.4.	Special models.....	84
<b>9.</b>	<b>CONCLUSIONS AND RECOMMENDATIONS</b> .....	<b>87</b>
9.1.	CONCLUSIONS.....	87
9.2.	RECOMMENDATIONS.....	87
	<b>REFERENCES</b> .....	<b>89</b>
	<b>APPENDIX A: GEOLOGICAL MAP OF THE ISTHMUS OF PANAMA</b> .....	<b>A.1</b>
A.1	EXPLANATION.....	A.1
	<b>APPENDIX B: DERIVATIONS AND DETAILED CALCULATIONS</b> .....	<b>B.1</b>
B.1	THE WESTERGAARD AND CHOPRA SOLUTIONS IN DETAIL.....	B.1
B.2	SOLVING HOUSNER'S SDOF MODEL.....	B.2
B.3	DERIVATION OF THE 1D SHALLOW WATER EQUATIONS.....	B.3
B.3.1	Introduction.....	B.3
B.3.2	Continuity equation.....	B.3
B.3.3	Momentum balance equation.....	B.4
B.4	DERIVATION OF THE 1D WAVE EQUATION.....	B.7
B.5	SOLVING THE 1D MODEL UNDER WAVE LOADING.....	B.7
B.5.1	Fluid boundaries.....	B.7
B.5.2	Gates A & B.....	B.8
B.6	DERIVATION OF THE 2D WAVE EQUATION.....	B.8
B.7	SOLVING THE 2D MODEL FOR HYDRODYNAMIC PRESSURE.....	B.9
B.7.1	Homogenous solution.....	B.9
B.7.2	Steady-state solution.....	B.10
	<b>APPENDIX C: THE FINITE ELEMENT PROGRAM DIANA</b> .....	<b>C.1</b>
C.1	WORKFLOW IN DIANA.....	C.1
C.2	DIANA BROCHURE AND BACKGROUND THEORY FSI.....	C.1

## List of figures

FIGURE 2.1 CROSS-SECTION OF THE PANAMA CANAL	3
FIGURE 2.2 LAYOUT OF THE PANAMA CANAL	4
FIGURE 2.3 CONCEPTUAL ISOMETRIC VIEW OF THE NEW LOCKS COMPLEX (ADAPTED FROM [PANAMA CANAL AUTHORITY, 2006])	4
FIGURE 2.4 AERIAL VIEW OF THE CONSTRUCTION SITES OF THE NEW LOCKS, INDICATED BY RED ARROW (ADAPTED FROM [PANAMA CANAL AUTHORITY, 2006])	4
FIGURE 2.5 COMPARISON BETWEEN VESSEL AND LOCK DIMENSIONS OF THE NEW AND EXISTING LOCKS (ADAPTED FROM [PAYER, 2005])	5
FIGURE 2.6 ARTIST IMPRESSION OF THE POST-PANAMAX LOCKS, PACIFIC SIDE	6
FIGURE 2.7 CROSS-SECTION WITH MAIN DIMENSIONS OF THE L-WALL TYPE LOCK CHAMBER	6
FIGURE 2.8 ARTIST IMPRESSION OF A LOCK HEAD UNDER CONSTRUCTION	6
FIGURE 2.9.A TOP VIEW WITH STRUCTURAL COMPONENTS LOCK HEADS (SOURCE: WITTEVEEN+BOS)	7
FIGURE 2.9.B LONGITUDINAL CROSS-SECTION WITH STRUCTURAL COMPONENTS LOCK HEADS	7
FIGURE 2.9.C CROSS-SECTION OF A LOCK HEAD WITH THE STRUCTURAL COMPONENTS	7
FIGURE 2.10 SKETCH CROSS-SECTION OF LOCK GATE	8
FIGURE 3.1 TECTONIC PLATES IN THE REGION	9
FIGURE 3.2 SUBDUCTION ZONE AT BOUNDARY OF OCEANIC AND CONTINENTAL PLATE (SOURCE: ROBERT SIMMON, NASA GSFC)	9
FIGURE 3.3 TYPES OF FAULTS	10
FIGURE 3.4 MAJOR FAULT LINES IN THE CANAL ZONE (ADAPTED FROM U.S. (SOURCE: U.S. GEOLOGICAL SURVEY) GEOLOGICAL SURVEY, 1998])	10
FIGURE 3.5 TYPES OF SEISMIC WAVES	10
FIGURE 4.1 ACCELERATION TIME HISTORY OR ACCELEROGRAM	13
FIGURE 4.2 PROCEDURE FOR MAKING	14
FIGURE 4.3 HORIZONTAL RESPONSE SPECTRA FOR A DAMPING RATIO OF 5%	14
FIGURE 4.4 DISCRETIZATION OF A DOMAIN BY MEANS OF ELEMENTS	15
FIGURE 4.5 INTERPOLATION BY SHAPE FUNCTIONS	16
FIGURE 4.6 HYDRODYNAMIC PRESSURE DISTRIBUTION FOR THE ORIGINAL (LEFT) AND SIMPLIFIED PARABOLA (RIGHT) WESTERGAARD SOLUTIONS (ADAPTED FROM [WESTERGAARD, 1933])	17
FIGURE 4.7 CORRECTION FACTOR ON THE WESTERGAARD FORMULA IN CASE OF SHORT RESERVOIR	18
FIGURE 4.8 HYPERBOLIC FUNCTIONS	19
FIGURE 4.9 HOUSNER'S MATHEMATICAL MODEL FOR IMPULSIVE AND CONVECTIVE HYDRODYNAMIC FORCES (ADAPTED FROM [USACE, EM 1110-2-6051])	19
FIGURE 4.10 HYDRODYNAMIC PRESSURE DISTRIBUTION IN THE CASE OF $d/L > 1.6$ ACCORDING TO HOUSNER	20
FIGURE 5.1 COMPARISON OF HYDRODYNAMIC PRESSURE ACCORDING TO THE WESTERGAARD AND HOUSNER FORMULAS	24
FIGURE 5.2 SDOF MASS-SPRING SYSTEM FOR CALCULATING SLOSHING FORCE	26
FIGURE 5.3 DIMENSIONLESS AMPLITUDE-FREQUENCY RESPONSE FUNCTION FOR HOUSNER'S SDOF MODEL	27
FIGURE 6.1 SKETCH CROSS-SECTION OF AN ARBITRARY LOCK HEAD	30
FIGURE 6.2 1D MODEL OF A LOCK HEAD	30
FIGURE 6.3 HYDROSTATIC PRESSURES AND REFERENCE LEVEL	31
FIGURE 6.4 SDOF MASS-SPRING SYSTEM	32
FIGURE 6.5 PROCEDURE FOR FINDING SOLUTION IN THE FREQUENCY AND TIME DOMAIN (ADAPTED FROM [KRAMER, 1996])	33
FIGURE 6.6 SITUATION AT INTERFACE GATE-WATER WHEN GATE MOVES IN POSITIVE X-DIRECTION	34
FIGURE 6.7 MODES SHAPE FOR THE FIRST THREE EIGENFREQUENCIES	36
FIGURE 6.8 THE FREQUENCY RESPONSE OF LOCK GATE A UNDER DIFFERENT COMPONENTS OF LOADING, INCLUDING DETAIL	40
FIGURE 6.9 THE FREQUENCY RESPONSE OF LOCK GATE B UNDER DIFFERENT COMPONENTS OF LOADING, INCLUDING DETAIL	41
FIGURE 7.1 2D MODEL FOR HYDRODYNAMIC PRESSURES, WITH BOUNDARY CONDITIONS	45
FIGURE 7.2 HYDRODYNAMIC PRESSURES; WITH (TOP) AND WITHOUT (BOTTOM) PHASE DIFFERENCE BETWEEN THE GATES	48
FIGURE 7.3 HYDRODYNAMIC PRESSURES; WITH (TOP), WITHOUT (CENTER) PHASE DIFFERENCE BETWEEN THE GATES AND DETAIL (BOTTOM)	49
FIGURE 7.4 HYDRODYNAMIC PRESSURES, WITH (TOP) AND WITHOUT (BOTTOM) A PHASE DIFFERENCE BETWEEN THE GATES	50
FIGURE 7.5 HYDRODYNAMIC PRESSURES, WITH (TOP) AND WITHOUT (BOTTOM) A PHASE DIFFERENCE BETWEEN THE GATES	51
FIGURE 7.6 HYDRODYNAMIC PRESSURE DISTRIBUTION AT $\omega_e \approx 0.63$ RAD/S (0.1 HZ)	52
FIGURE 7.7 HYDRODYNAMIC PRESSURE DISTRIBUTION AT $\omega_e \approx 2.51$ RAD/S (0.4 HZ)	52
FIGURE 7.8 HYDRODYNAMIC PRESSURE DISTRIBUTION AT $\omega_e \approx 6.28$ RAD/S (1 HZ)	52
FIGURE 7.9 HYDRODYNAMIC PRESSURE DISTRIBUTION AT $\omega_e \approx 37.70$ RAD/S (6 HZ)	53
FIGURE 7.10 HYDRODYNAMIC PRESSURE DISTRIBUTION AT $\omega_e \approx 0.63$ RAD/S (0.1 HZ)	53
FIGURE 7.11 HYDRODYNAMIC PRESSURE DISTRIBUTION AT $\omega_e \approx 2.51$ RAD/S (0.4 HZ)	54
FIGURE 7.12 HYDRODYNAMIC PRESSURE DISTRIBUTION AT $\omega_e \approx 6.28$ RAD/S (1 HZ)	54
FIGURE 7.13 HYDRODYNAMIC PRESSURE DISTRIBUTION AT $\omega_e \approx 37.70$ RAD/S (6 HZ)	54
FIGURE 7.14 HYDRODYNAMIC PRESSURES IN CASE OF A ZERO PRESSURE BOUNDARY CONDITION	55
FIGURE 7.15 MAXIMUM HYDRODYNAMIC PRESSURE AT THE BOTTOM OF A GATE FOR DIFFERENT CHAMBER LENGTHS AT 1 HZ	56
FIGURE 7.16 THE WESTERGAARD SOLUTION IN COMPARISON WITH EQUATION (7.18), WITH DETAIL FOR LOW FREQUENCIES	57
FIGURE 8.1 2D MODEL FOR FEM ANALYSIS WITH RIGID GATES	59
FIGURE 8.2 2D MODEL FOR FEM ANALYSIS WITH FLEXIBLE GATES	60
FIGURE 8.3 2D MODEL FOR SEMI-INFINITE FEM ANALYSIS WITH RIGID GATE	60
FIGURE 8.4 FEM MESH FOR MODEL 2D	61
FIGURE 8.5 THE BCL635 FLUID-STRUCTURE ELEMENT, LINE, 3+3 NODES (ADAPTED FROM [TNO DIANA, 2008])	62
FIGURE 8.6 NODAL CONNECTIVITY FOR 2D FLUID-STRUCTURE INTERACTION (ADAPTED FROM [TNO DIANA, 2008])	62
FIGURE 8.7A HYDRODYNAMIC PRESSURES FOR CASE 1A	64
FIGURE 8.7B HYDRODYNAMIC PRESSURES FOR CASE 1B	64
FIGURE 8.7C HYDRODYNAMIC PRESSURES FOR CASE 1C (BOTTOM AND TOP LEVEL OF GATE)	65
FIGURE 8.7D HYDRODYNAMIC PRESSURES FOR CASE 1D (BOTTOM AND TOP LEVEL OF GATE)	66
FIGURE 8.8A HYDRODYNAMIC PRESSURES FOR CASE 2A	67
FIGURE 8.8B HYDRODYNAMIC PRESSURES FOR CASE 2B	67
FIGURE 8.8C HYDRODYNAMIC PRESSURES FOR CASE 2C (BOTTOM AND TOP LEVEL OF GATE)	68
FIGURE 8.8D HYDRODYNAMIC PRESSURES FOR CASE 2D (BOTTOM AND TOP LEVEL OF GATE)	69
FIGURE 8.9 HYDRODYNAMIC PRESSURE DISTRIBUTION AT $\omega_e = 2\pi$ RAD/S (1.00 HZ)	70
FIGURE 8.10 HYDRODYNAMIC PRESSURE DISTRIBUTION AT $\omega_e = \omega_1/2 \approx 37.70$ RAD/S (6.00 HZ)	71
FIGURE 8.11 HYDRODYNAMIC PRESSURE DISTRIBUTION AT $\omega_e < \omega_1 \approx 75.40$ RAD/S (12.00 HZ)	71
FIGURE 8.12 HYDRODYNAMIC PRESSURE DISTRIBUTION AT $\omega_e > \omega_1 \approx 76.97$ RAD/S (12.25 HZ)	72
FIGURE 8.13 HYDRODYNAMIC PRESSURE DISTRIBUTION AT $\omega_e = (\omega_1 + \omega_2)/2 \approx 152.37$ RAD/S (24.25 HZ)	72
FIGURE 8.14 HYDRODYNAMIC PRESSURE DISTRIBUTION AT $\omega_e < \omega_2 \approx 227.77$ RAD/S (36.25 HZ)	73
FIGURE 8.15 HYDRODYNAMIC PRESSURE DISTRIBUTION AT $\omega_e > \omega_2 \approx 229.34$ RAD/S (36.50 HZ)	73
FIGURE 8.16 HYDRODYNAMIC PRESSURE DISTRIBUTION AT $\omega_e = 2\pi \approx 6.28$ RAD/S (1.00 HZ)	74
FIGURE 8.17 HYDRODYNAMIC PRESSURE DISTRIBUTION AT $\omega_e = \omega_1/2 \approx 37.70$ RAD/S (6.00 HZ)	75
FIGURE 8.18 HYDRODYNAMIC PRESSURE DISTRIBUTION AT $\omega_e < \omega_1 \approx 75.40$ RAD/S (12.00 HZ)	75
FIGURE 8.19 HYDRODYNAMIC PRESSURE DISTRIBUTION AT $\omega_e > \omega_1 \approx 76.97$ RAD/S (12.25 HZ)	76
FIGURE 8.20 HYDRODYNAMIC PRESSURE DISTRIBUTION AT $\omega_e = (\omega_1 + \omega_2)/2 \approx 152.37$ RAD/S (24.25 HZ)	76
FIGURE 8.21 HYDRODYNAMIC PRESSURE DISTRIBUTION AT $\omega_e < \omega_2 \approx 227.77$ RAD/S (36.25 HZ)	77
FIGURE 8.22 HYDRODYNAMIC PRESSURE DISTRIBUTION AT $\omega_e > \omega_2 \approx 229.34$ RAD/S (36.50 HZ)	77
FIGURE 8.23 HYDRODYNAMIC PRESSURES (CASE FLEXIBLE GATES, LONG LOCK CHAMBER): BOTTOM OF GATE (TOP), COMPARISON WITH CASE 1D (CENTER) AND TOP OF GATE (BOTTOM)	79
FIGURE 8.24 HYDRODYNAMIC PRESSURES (CASE FLEXIBLE GATES, SHORTER INTERMEDIATE CHAMBER): BOTTOM OF GATE (TOP), COMPARISON WITH CASE 2D (CENTER) AND TOP OF GATE (BOTTOM)	80
FIGURE 8.25 HYDRODYNAMIC PRESSURE DISTRIBUTION IN CASE OF FLEXIBLE GATES: SITUATION LONG LOCK CHAMBER (TOP) AND SITUATION SHORTER INTERMEDIATE CHAMBER (BOTTOM)	81
FIGURE 8.26 HYDRODYNAMIC PRESSURES (CASE SEMI-INFINITE CHAMBER): BOTTOM OF GATE INCLUDING COMPARISON WITH CASE 1D (TOP) AND TOP OF GATE (BOTTOM)	83
FIGURE 8.27 HYDRODYNAMIC PRESSURE DISTRIBUTION IN CASE OF SEMI-INFINITE CHAMBER: REAL (TOP) AND IMAGINARY PARTS (BOTTOM)	83
FIGURE B.1 HYDRODYNAMIC PRESSURES ACCORDING TO CHOPRA	B.2
FIGURE B.2 CONTROL AREA FOR DERIVATION OF THE CONTINUITY EQUATION	B.4
FIGURE B.3 CONTROL VOLUME FOR DERIVATION OF THE MOMENTUM BALANCE EQUATION	B.4
FIGURE B.4 CONTROL AREA FOR DERIVATION OF THE MOMENTUM BALANCE EQUATION	B.6

## List of tables

---

TABLE 5.1 DIFFERENCES BETWEEN A LEVEL 1 AND LEVEL 2 EARTHQUAKE AS DEFINED IN THE PROGRAM OF REQUIREMENTS .....	23
TABLE 5.2 ROCK MASS PROPERTIES OF BEDROCK PRESENT AT THE PACIFIC AND ATLANTIC SITES.....	23
TABLE 5.3 ADDED MASS COMPARISON FOR LONG RESERVOIRS OR LOCK CHAMBERS .....	25
TABLE 5.4 RESULTS FOR HOUSNER'S SDOF MODEL (1 <sup>ST</sup> MODE ONLY).....	27
TABLE 7.1.A FIRST 25 EIGENFREQUENCIES FOR THE LONG LOCK CHAMBER .....	47
TABLE 7.1.B FIRST 25 EIGENFREQUENCIES FOR THE SHORTER INTERMEDIATE CHAMBER.....	47
TABLE 7.2 SELECTED EXCITATION FREQUENCIES WITH CORRESPONDING FIGURES (SITUATION LONG LOCK CHAMBER) .....	51
TABLE 7.3 SELECTED EXCITATION FREQUENCIES WITH CORRESPONDING FIGURES (SITUATION SHORTER INTERMEDIATE CHAMBER).....	53
TABLE 8.1 SELECTED EXCITATION FREQUENCIES WITH CORRESPONDING FIGURES (SITUATION LONG LOCK CHAMBER) .....	70
TABLE 8.2 SELECTED EXCITATION FREQUENCIES WITH CORRESPONDING FIGURES (SITUATION LONG LOCK CHAMBER) .....	74

## List of symbols

Not all symbols have been listed as some have only local meaning. A few symbols have more than one meaning.

### English

Symbol	Description	SI unit
$a$	acceleration	[m/s <sup>2</sup> ]
$c$	damping coefficient	[kg/s]
$c_p$	celerity of pressure waves	[m/s]
$c_P$	celerity of P-waves	[m/s]
$c_R$	celerity of Rayleigh waves	[m/s]
$c_S$	celerity of S-waves	[m/s]
$c_w$	celerity of surface waves	[m/s]
$C_n$	constant taking in account compressibility of water in the Westergaard formula	[-]
$d$	constant water depth	[m]
$E$	Young's modulus	[Pa]
$f_e$	harmonic excitation frequency	[Hz]
$F_1$	force related to convective pressure (1 <sup>st</sup> mode)	[N/m]
$F_d$	hydrostatic force	[N/m]
$F_e$	earthquake force	[N/m]
$F_\eta$	wave force	[N/m]
$g$	acceleration of gravity	[m/s <sup>2</sup> ]
$G$	shear modulus	[Pa]
$h$	height on which hydrodynamic forces acts in Housner's model	[m]
$h$	total water depth	[m]
$\hat{H}$	complex frequency response function for $\eta$	[m]
$I$	momentum	[N·s]
$k$	spring stiffness	[N/m]
$k$	wavenumber	[m <sup>-1</sup> ]
$k_h$	horizontal seismic coefficient	[-]
$K_1$	spring stiffness related to convective pressure (1 <sup>st</sup> mode) in Housner's model	[N/m]
$K$	bulk modulus	[Pa]
$L$	distance, (half) lock chamber length	[m]
$m$	mass	[kg/m]
$m_{am}$	added mass	[kg/m]
$M$	P-wave modulus	[Pa]

$M$	total water mass in chamber in Housner's model	[kg/m]
$M_0$	mass related to impulsive pressure in Housner's model	[kg/m]
$M_1$	mass related to convective pressure (1 <sup>st</sup> mode) in Housner's model	[kg/m]
$M_w$	moment magnitude	[-]
$p$	(hydrodynamic) pressure	[Pa]
$\hat{p}$	complex frequency response function for $p$	[Pa]
PGA	peak ground acceleration	[m/s <sup>2</sup> ]
$R_a$	acceleration response spectrum	[m/s <sup>2</sup> ]
$t$	time variable	[s]
$T$	period	[s]
$T_1$	fundamental eigenperiod	[s]
$T_e$	harmonic excitation period	[s]
$T_n$	eigenperiod	[s]
$T_r$	return period	[s]
$u$	displacement	[m]
$\ddot{u}_e$	earthquake excitation acceleration	[m/s <sup>2</sup> ]
$x$	horizontal coordinate	[m]
$y$	vertical coordinate	[m]
$z$	vertical coordinate	[m]

*Greek*

Symbol	Description	SI unit
$\beta$	correction factor on Westergaard's formula	[-]
$\gamma$	specific weight	[N/m <sup>3</sup> ]
$\varepsilon$	volumetric strain	[-]
$\zeta$	damping ratio	[-]
$\eta$	surface wave amplitude	[m]
$\lambda$	wavelength	[m]
$\nu$	Poisson's ratio	[-]
$\rho$	density	[kg/m <sup>3</sup> ]
$\sigma$	stress	[Pa]
$v$	flow velocity	[m/s]
$\varphi$	phase	[-]
$\omega_e$	(angular) harmonic excitation frequency	[rad/s]
$\omega_n$	(angular) natural frequency	[rad/s]

---

# 1. Introduction

---

## 1.1. Objectives of thesis

The objective of this thesis is to research the earthquake induced hydrodynamic pressure on a lock structure. When a navigation lock is subjected to an earthquake, the structure itself and the water inside the chamber will react differently. The different behavior causes a reaction load by the water on the lock structure. Besides an always present hydrostatic pressure, an earthquake will exert an extra hydrodynamic pressure on the lock. The magnitude of this hydrodynamic pressure depends on many aspects. The effect of each of these aspects on the hydrodynamic pressure will be investigated by a series of models. The following aspects will be treated in detail:

- Lock dimensions and water levels  
The amount of water has a large influence on the pressure distribution. In general the principle of "the more water, the more pressure", holds. But the way the water reacts inside a lock chamber is different than e.g. behind a dam. Seismic waves, originating from the source of earthquake, travel towards the structure with a certain velocity. This means that for large structure the acceleration at a certain point of time is not constant for the whole structure. For navigation locks this means that one side vibrates different from the other side because of this phase lag. The dimensions of a lock chamber (chamber length, width and water depth) are different than dams or fluid storage container, which results in a possible different behavior.
- The effect of surface waves on the hydrodynamic pressure distribution  
When a contained body of water – with a free surface – is set in motion, waves at the surface will be generated. These waves influence the hydrodynamic pressure below and at the water surface. If the wave pressure is small enough compared with the total pressure, the effect can be neglected which simplifies a computation, which is done with most methods to calculate hydrodynamic pressures. The conditions under which such an assumption is valid, or not, will be investigated.
- Stiffness of the structure  
The hydrodynamic pressure on a structure depends on the stiffness of that structure. A rigid wall behaves different than a flexible wall. Because the hydrodynamic pressure is a reaction load, it is influenced by the stiffness.

There are many methods available for the calculation of hydrodynamic pressure: from relative simple analytical formulas to full computer-based analyses. The analytical formula's are based on large dams or fluid storage containers, which each have a different scale than navigation locks and are affected differently by the above mentioned aspects. The available analytical methods will be reviewed for the application to navigation locks.

Besides the previously mentioned aspects, other factors contribute to the hydrodynamic loading on a lock structure. These include the e.g. the presence of ship inside a lock, the opening and closing of gates and the direction of the source of the earthquake. Models in this thesis are based upon a closed lock gates or walls which are loaded perpendicular and have no ships inside the lock chambers. The models focus on large lock structures, the Third Set of Locks project of the Panama Canal is used as a case example for dimensions. A total of three models will be discussed:

1. An analytical 1D model of a lock head to investigate the effect of surface waves;
2. An analytical 2D model of a single lock chamber which includes all of the above mentioned aspects, except the stiffness of the lock (gates);
3. A computer-based model based on the analytical 2D model, but with the ability to include e.g. the stiffness of the lock gates.

With these three models the hydrodynamic pressure on a lock structure will be investigated. The response of the structure is not treated in detail.

## 1.2. Layout of thesis

More information about the history and the expansion project of the Panama Canal, which is used as a case study, can be found in the next chapter. Background theory about earthquakes and (hydro)dynamic analyses is treated in chapters 3 and 4. In chapter 5 the site conditions specific for the Panama Canal are listed and a preliminary assessment of the magnitude of hydrodynamic pressure is made. Further chapters (6, 7 and 8) treat the above-mentioned three models.



## 2. Project background

### 2.1. History of the Panama Canal

Plans for the construction of a canal between the Atlantic and Pacific Oceans date back to the late 16<sup>th</sup> century. The strategic situation of the Panama Isthmus led to the construction of the Panama Railway from 1850 to 1855, which was the first fast and less risky alternative for the trading routes used prior to the 19<sup>th</sup> century to transport goods between the two oceans.

After the success of Suez Canal in 1869 the French started to work on the Panama Canal in 1880, but construction was abandoned in 1893 due to several problems. The French plan was to build a canal on sea level, which proved to be very difficult. Combined with deceases, landslides and insufficient knowledge about the geology and hydrology of the country, the attempt cost the lives of about 21,900 workers. After the failed attempt by the French, the Americans continued the work in 1904. Because Panama was under Colombian control, the United States had to negotiate with Colombia for the construction and exploitation of the canal. The ratification of the treaty failed and the United States both politically and military supported the independence of Panama in 1903, for which in return they gained control of the Canal Zone. The American plan was to build the canal with locks and artificial lakes. By the use of heavy machinery and attempts to eliminate decease, the canal was finished within ten years of construction; the Panama Canal opened on August 15, 1914. Although the working conditions and hygiene were improved, still 5,609 workers died completing the Canal. The size of the ships that could pass trough the canal was limited to the size of the locks, which measure a length of 304.8 m and a width of 33.5 m. The canal has a total length of 80 km and a maximum elevation of 25.9 m above sea level at Gatún Lake. The concept of expansion of the canal is not new. In 1940 the construction of a new set of locks started to allow the passage of larger battleships. In 1942 the project was postponed due to the outbreak of the 2<sup>nd</sup> World War. Although the plan was initially rushed, after the attack on Pearl Harbor in late 1941 it became clear that even larger and larger battleships had become obsolete and therefore the construction of the new set of locks did no longer have a high priority.

After the war the Canal Zone was gradually passed over to the Panamanian government. This progress was completed with the start of the new millennium, after this date the Panamanians are in full control of the Canal Zone. The growth of commercial (container) ships after the war lead to the *Panamax* class of ships. These ships are the largest ships that can pass through the locks and have a displacement of over 70,000 t and a capacity of 5000 TEU<sup>1</sup>. With the continuing increase of container vessel dimensions, there is a renewed interest in expanding the Panama Canal.

### 2.2. Current layout of the Panama Canal

The locks of the Panama carry vessels from both oceans to the Gatún Lake and vice versa. The layout of the Panama Canal is shown in figures 2.1 and 2.2; a passage from the Atlantic Ocean to the Pacific Ocean is as follows:

- Vessels from the Atlantic side enter Limón Bay (Bahía Límón), passing breakwaters. The bay also serves as anchorage for waiting ships;
- After 3.2 km the three-stage Gatún locks (total length of 1.9 km) carry vessels to the artificial Gatún Lake;
- Vessel will sail 24.2 km over the lake to the Chagres River (Rio Chagres) and another 8.5 km through the river before they reach the Gaillard Cut. The Gatún Lake is created by several dams in the region and also feeds water to the locks by means of gravity;
- The Gaillard or Culebra Cut has a total length 12.6 km. This artificial waterway proved to be one of the most difficult aspects in the construction of the canal due to the many landslides;
- At the end of Gaillard Cut ships enter the single-stage Pedro Miguel lock, which has a total length of 1.4 km;
- The next stage is the 1.7 km long Miraflores lake;
- Ships enter the two-stage, 1.7 km long Miraflores lock complex;

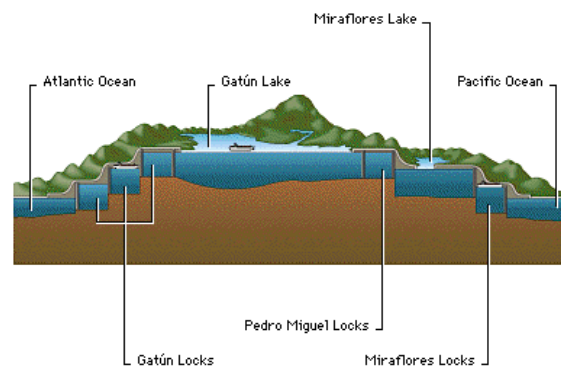


**Figure 2.1 Cross-section of the Panama Canal (source: Microsoft Encarta, Microsoft Corporation)**

<sup>1</sup> Twenty-foot Equivalent Unit, a standard container size with a length of 20 ft (6.1 m)

- Finally, a 13.2 km long entrance channel connects the Miraflores locks to the Gulf of Panama and the Pacific Ocean. During the crossing of the channel vessels will pass under the Bridge of the Americas, which has a clearance of 61.3 m at high tide. While the locks determine the maximum allowed draught and beam of Panamax vessels, the air draft would be limited by the clearance under the Bridge of the Americas.

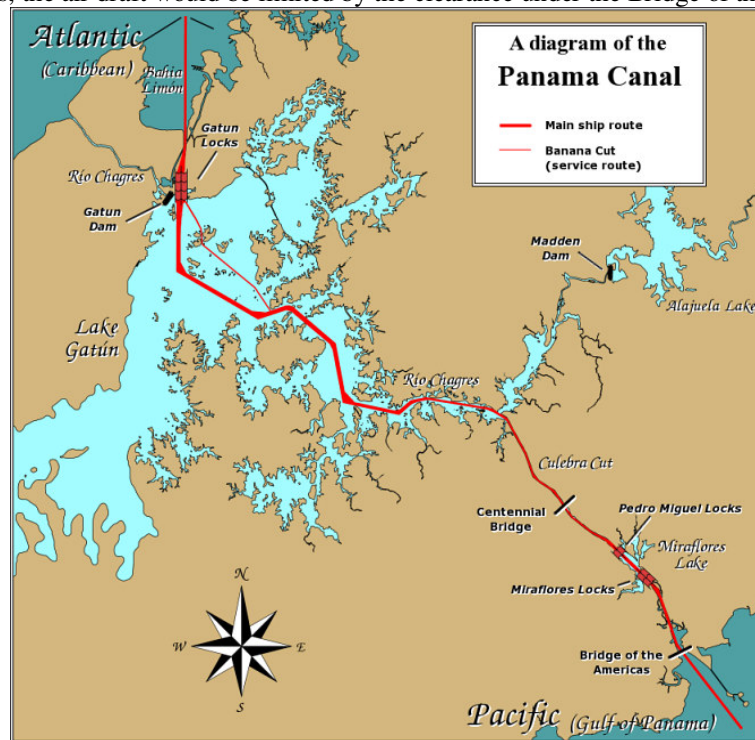


Figure 2.2 Layout of the Panama Canal

### 2.3. Third Set of Locks Expansion Project

The Panama Canal Authority, or ACP<sup>2</sup>, made a master plan from which it concludes that the option of a new set of locks next to the existing ones is the best way to increase the capacity of the canal. The plan was approved by a national referendum on October 22, 2006 and the project began on September 3, 2007. The total costs of the project are estimated to be \$5.25 billion. The plan [PANAMA CANAL AUTHORITY, 2006] consist out three phases: the construction of new navigation locks on each side of the canal; deepening and widening existing channels and connect them to the new locks and lastly, to raise the water level of Gatún Lake to increase the usable water reserve capacity. A layout of the new locks can be found in figures 2.3 and 2.4.

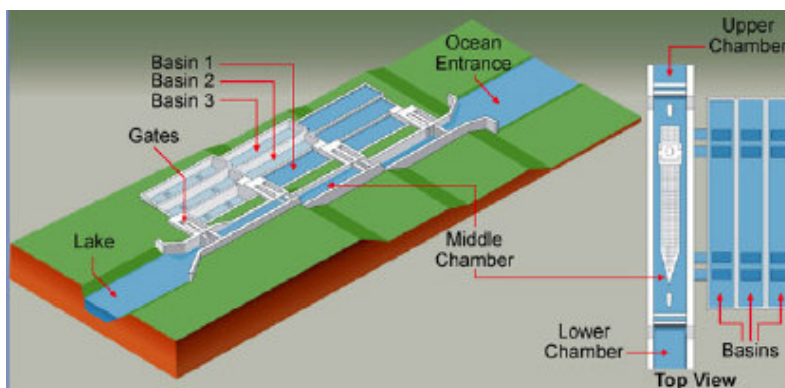


Figure 2.3 Conceptual isometric view of the new locks complex (adapted from [PANAMA CANAL AUTHORITY, 2006])



Figure 2.4 Aerial view of the construction sites of the new locks, indicated by red arrow (adapted from [PANAMA CANAL AUTHORITY, 2006])

<sup>2</sup> Spanish abbreviation for *Autoridad del Canal de Panamá*

The locks will have a three-stage flight with adjacent water saving basins. Rolling gates are used, while the existing locks have miter gates. Similar to the existing locks, each lock head has dual gates for redundancy reasons. The new locks will be built next to the existing locks, in the old excavations of 1940-1942. The chambers will have a length of 427 m and a width of 55 m. A comparison between the new and existing locks can be found in figure 2.5. The ships will be assisted through the lock chambers by tugboats, unlike the existing locks where this is done with small locomotives. The smaller dimensions relative to the lock chamber reduces the hydrodynamic friction when a vessel is maneuvering through the lock. It is considered to be uneconomically to design the locks larger than the 12,000 TEU capacity currently planned [PAYER, 2005]. In mid-July 2009 the contract was awarded to the consortium *Grupo Unidos por el Canal* to which the graduation company Witteveen+Bos was part of under lead designer MWH (Montgomery Watson Harza, United States), Tetra Tech (United States) and Iv-Groep (The Netherlands) during the tender stage. The consortium consists out of many more parties from around the world. The new locks are planned to be operational in 2014-2015, one hundred years after the opening of the existing locks.

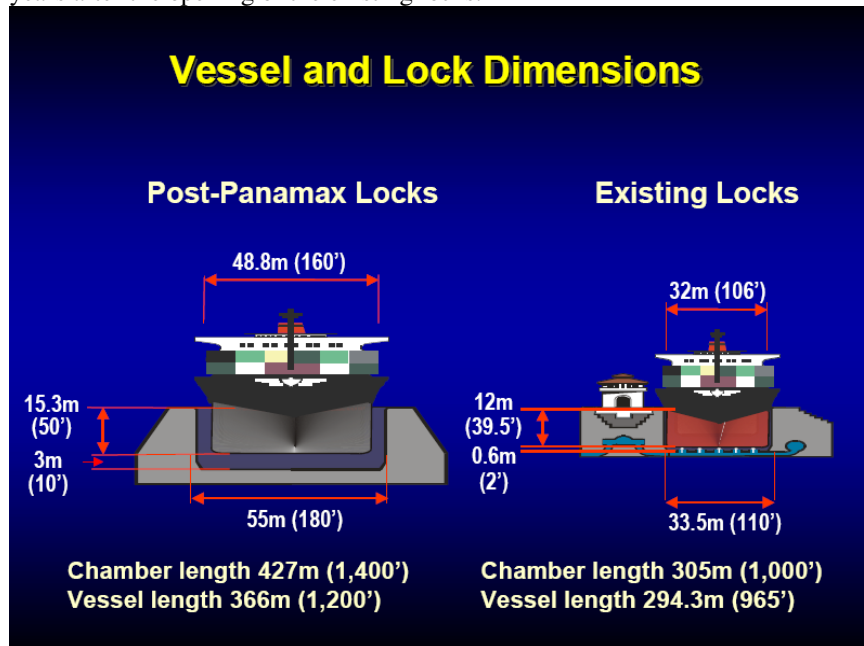


Figure 2.5 Comparison between vessel and lock dimensions of the new and existing locks (adapted from [PAYER, 2005])

## 2.4. Proposed design

Figures and numbers in the following sections are based on a conceptual and/or tender design. They are given for illustrative purposes only and are subjective to changes.

### 2.4.1. General and chamber dimensions

The new Atlantic and Pacific lock complexes are in principle identical to each other, as are the lock heads and gates. Both locks have a three-stage flight with single chambers and rolling gates. The existing locks have unidirectional miter gates and double lock chambers. Water saving basins will be applied to limit water losses from the Gatún Lake during lock cycles. Figure 2.6 shows an artist impression of the new locks. The inner dimensions of the lock chamber have been discussed in paragraph 2.3: a chamber length of 427 m and a width of 55 m.

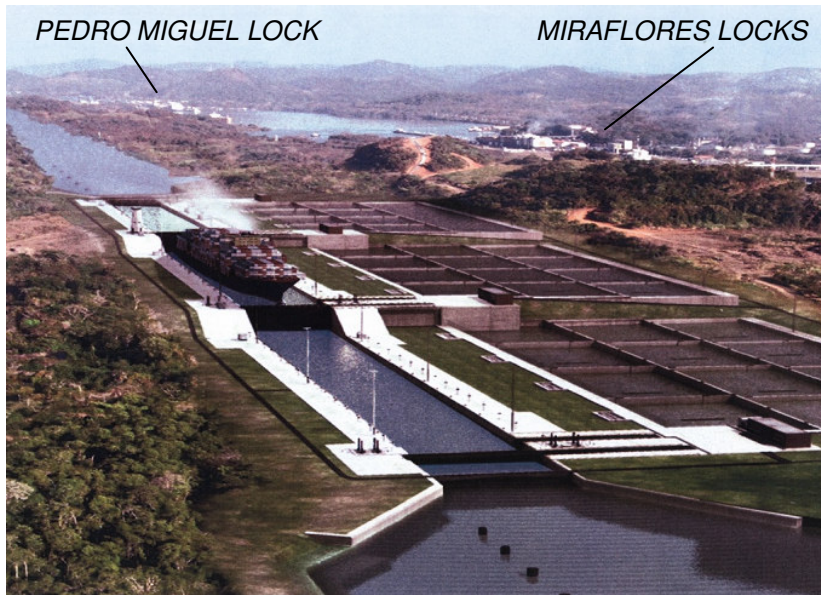


**Figure 2.6** Artist impression of the Post-Panamax locks, Pacific side

The chambers are designed as gravity type L-wall with a bottom slab of about 1 m as bottom protection. The main dimensions are given in the sketch of figure 2.7. The dimensions of the L-wall vary for each chamber, but differences are minor. As most solid gravity structures the inner area of the L-wall consists out of a fill material. In this case mass concrete will be used while for the outer walls and bottom structural concrete will be used.

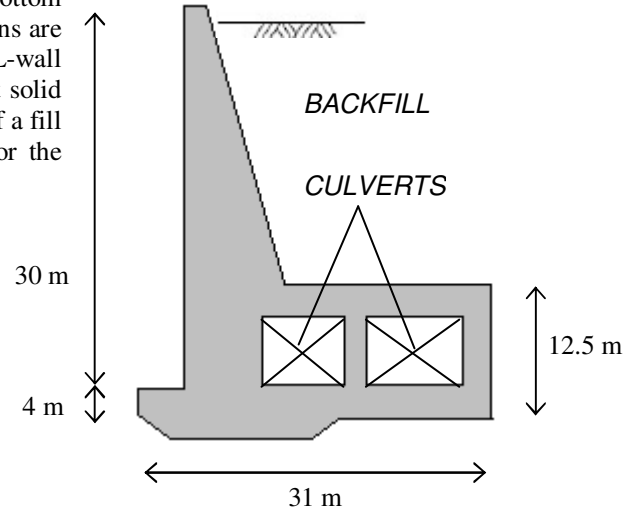


**Figure 2.7** Cross-section with main dimensions of the L-wall type lock chamber

#### 2.4.2. Lock heads

Figure 2.8 shows an artist impression of one of the lock heads under construction. Sketches of the top view and cross-sections of the lock heads with main dimensions can be found in figure 2.9. As with the L-walls, some differences exist between the lock heads. These dimensions change for different locations and cross-sections. No roof is applied on the recesses; a requirement of the client is the ability to remove the lock gates directly from their recesses. Without a roof, the 14 m wide center wall behaves like a cantilever wall. As the center wall is mainly loaded with reaction forces from the lock gates, the dimensions of this wall are for the most part determined by seismic loading.

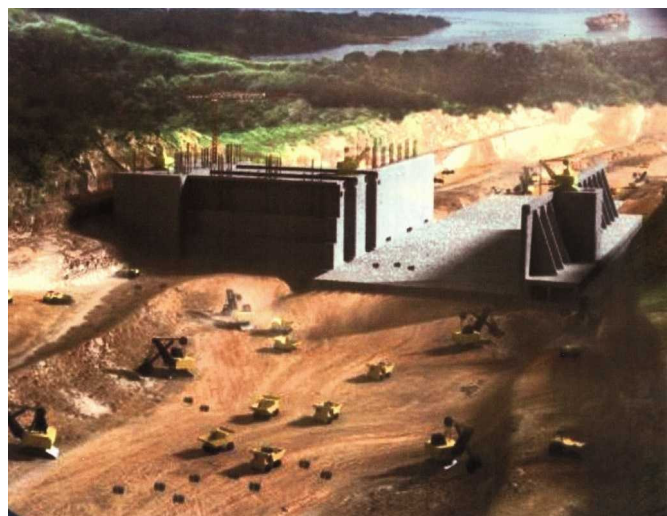


**Figure 2.8** Artist impression of a lock head under construction

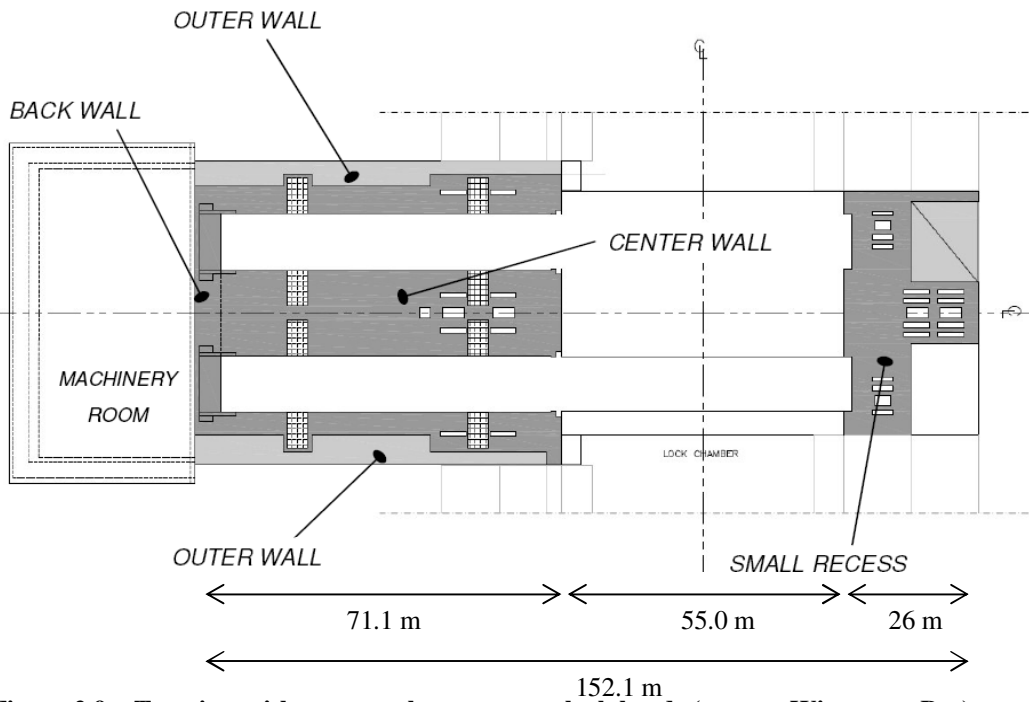


Figure 2.9.a Top view with structural components lock heads (source: Witteveen+Bos)

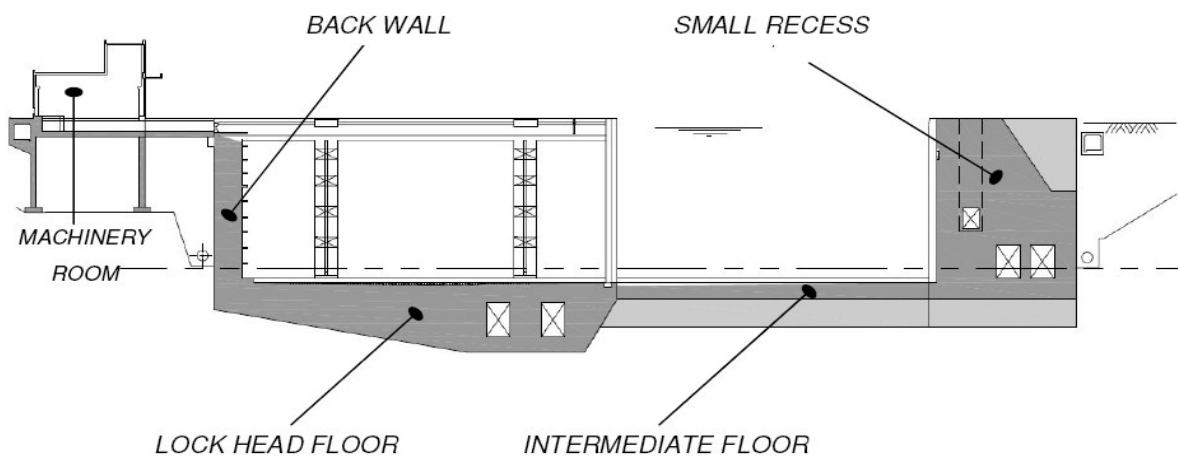


Figure 2.9.b Longitudinal cross-section with structural components lock heads (source: Witteveen+Bos)

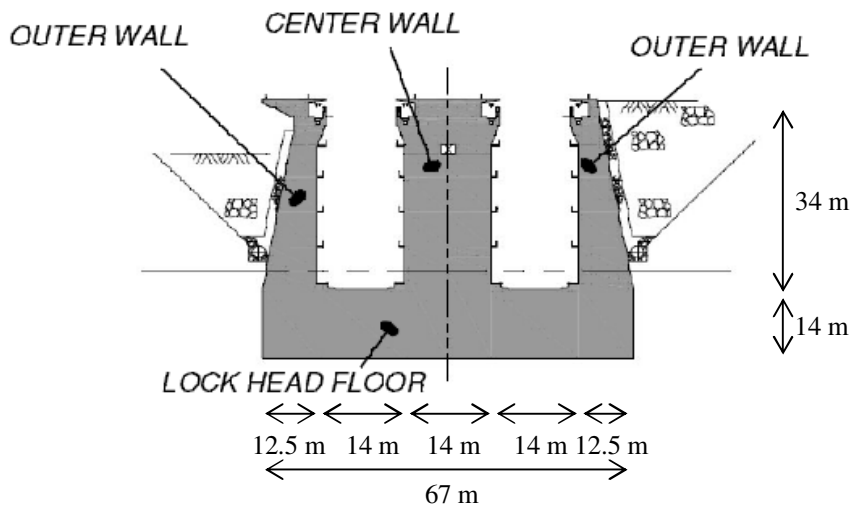


Figure 2.9.c Cross-section of a lock head with the structural components (source: Witteveen+Bos)

### 2.4.3. Lock gates

With a total of eight lock heads, a number of sixteen lock gates are required. The lock gates of one lock head are interchangeable. The governing lock gate has the following dimensions:

- Length: 57.6 m;
- Width: 10.0 m;
- Height: 31.9 m.

The governing lock gate is located at upstream side of the lowest chamber on the Pacific side.

The interior of the gates consists out of truss elements and ballast tanks at the center of the gate. Figure 2.10 shows a typical cross-section of a lock gate.

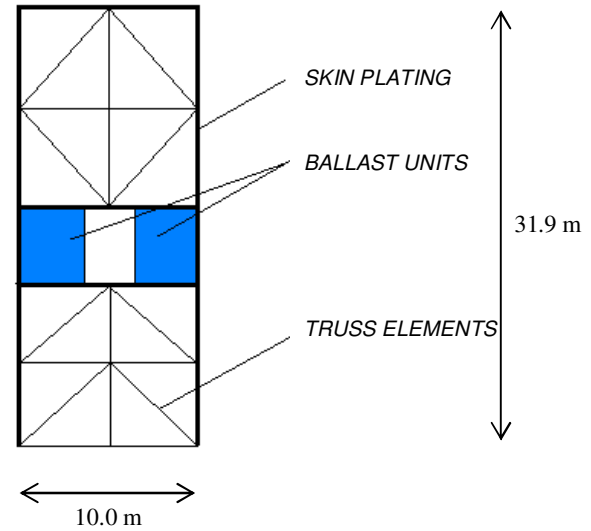


Figure 2.10 Sketch cross-section of lock gate

## 3. Earthquakes

### 3.1. Introduction

This thesis will focus on the dynamic, earthquake induced loading of the new Post-Panamax locks, specifically on the hydrodynamic pressures. The geological situation at Panama is a major source for earthquakes. The presence of four major tectonic plates and several minor plates makes the Panama isthmus prone to earthquakes, as can be seen in figure 3.1. The economic value of the Panama Canal makes earthquakes one of the most important design aspects for the new set of locks.

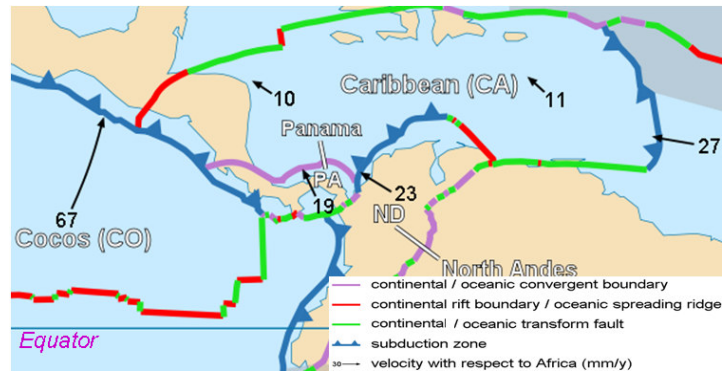


Figure 3.1 Tectonic plates in the region

### 3.2. Types of earthquakes

Two major sources of earthquakes can be distinguished: earthquakes originating from edges of tectonic plate boundaries and earthquakes that are caused by local fault lines. Earthquakes of the latter category are called crustal or shallow earthquakes. The different types of movement of the tectonic plates cause different types of earthquakes. They depend on the type of plate, oceanic or continental, and the direction in which they are moving. These directions can be convergent, divergent or of the transform fault type where plates move past each other. For the Panama region the convergent type is present where oceanic and continental plates move towards each other. The denser oceanic plate is moving underneath a less dense continental plate. This process is called subduction and occurs at both the North and South of the Panama plate. These locations are called the North, respectively the South Panama Deformed Belt. Subduction earthquakes are caused when the boundary between oceanic and continental plates ruptures. This boundary has the form of a trench and is located out of the coast. When the oceanic plates melt inside the earth's mantle, the magma rises and causes volcanic mountain ranges. An example of a subduction zone is given in figure 3.2. Subduction earthquakes have a low rate of occurrence, but high magnitudes in the order of 8+.

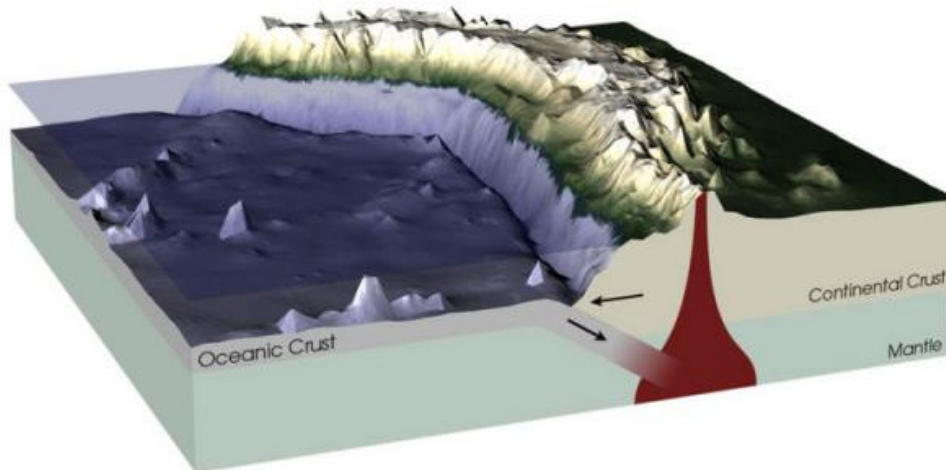
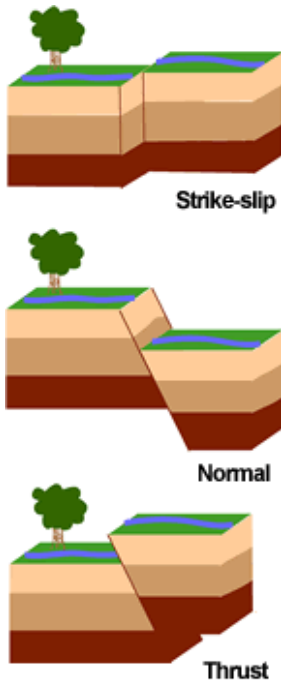
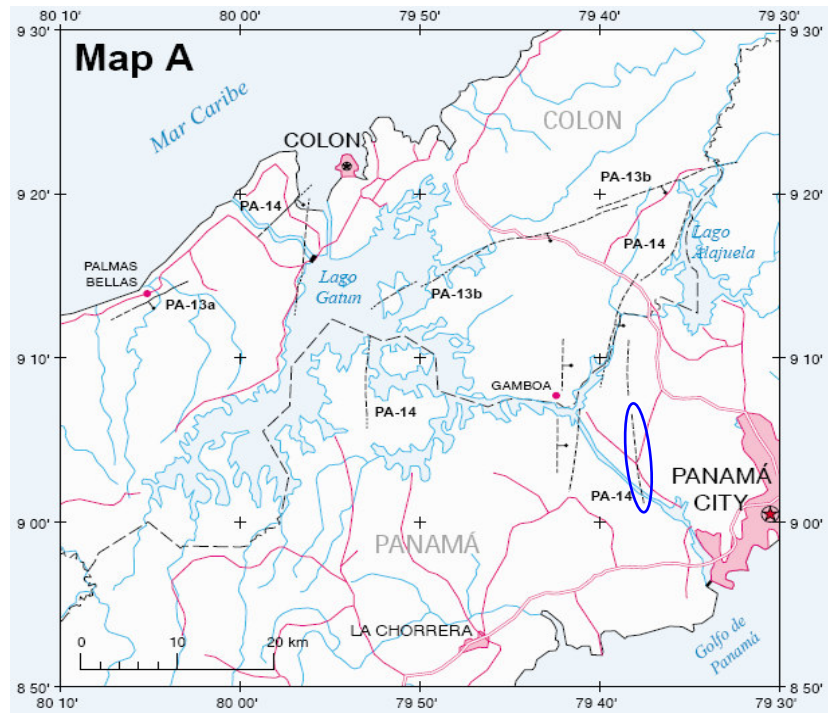


Figure 3.2 Subduction zone at boundary of oceanic and continental plate (source: Robert Simmon, NASA GSFC)

Crustal earthquakes occur away from plates boundaries and are caused by sudden stress relief in fault lines. These fault lines are planar fractures in rock where both sides move in different directions. Crustal earthquakes are random and unpredictably, but their magnitude is usually low. The most common types are given in figure 3.3.



**Figure 3.3** Types of faults (source: U.S. Geological Survey)



**Figure 3.4** Major fault lines in the Canal Zone (adapted from U.S. GEOLOGICAL SURVEY, 1998)

For the Atlantic side the dominant source of seismic activity is the Rio Gatún fault (PA-13b), for the Pacific side this is the Pedro Miguel-Limon fault (part of PA-14). The location [U.S. GEOLOGICAL SURVEY, 1998] of these two faults can be found in appendix A and figure 3.4, where the Pedro Miguel-Limón fault line has been indicated with an oval. The presence of the North Panama Deformed Belt could cause a subduction earthquake at the Atlantic lock site.

### 3.3. Seismic waves

The waves that are caused by the earthquake propagate in two ways through the earth, in two types: body and surface waves. The propagation can be by means of compression and shear, as seen in figure 3.5. For body waves they are called P- and S-waves, for surface waves they are called Rayleigh and Love waves. Each type of seismic wave can be identified by means of a seismograph, provided that they are located close enough to the source of the earthquake. The hypo- and epicenter of an earthquake can be calculated from this difference in propagation speed. Surface waves have the behavior of a combination of longitudinal and transverse waves. Contrary to body waves, surface wave that travel trough the earth's crust are dispersive. For inhomogenous solids, e.g. where the density varies with depth, the wave velocity depends on the wavelength. For an ideal, homogenous flat elastic surface waves are not dispersive. In the next sections each of these types of waves are explained. The given expressions are linear elastic relations for homogenous isotropic materials.

#### 3.3.1. P-waves

P-waves (primary or pressure waves) are longitudinal waves that are the fastest type of seismic waves, with velocities in excess of 5 km/s for hard types of rock like granite.

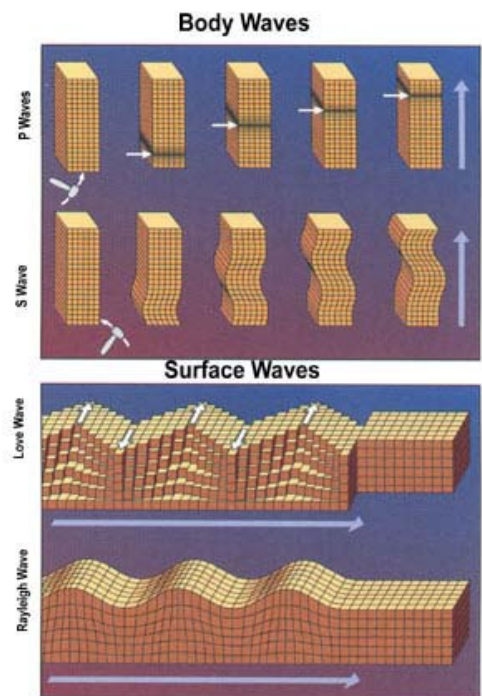


**Figure 3.5** Types of seismic waves (source: U.S. Geological Survey)

The velocity can be calculated by means of equation (3.1).

$$c_p = \sqrt{\frac{M}{\rho}} \quad (3.1)$$

in which:

$c_p$	=	celerity of the P-wave	[m/s]
$M$	=	P-wave modulus	[Pa]
$\rho$	=	density of the considered medium	[kg/m <sup>3</sup> ]

The P-wave modulus is one of the moduli of elasticity and can be expressed in terms of the Young's modulus and coefficient of lateral contraction by means of equation (3.2).

$$M = E \frac{1-\nu}{(1+\nu)(1-2\nu)} \quad (3.2)$$

in which:

$E$	=	Young's modulus	[Pa]
$\nu$	=	Poisson's ratio	[-]

### 3.3.2. S-waves

S-waves (secondary or shear wave) are transverse waves. The wave speed is in the order of about 60% of P-waves, but the amplitude is larger and therefore more destructive. The velocity of an S-wave follows from equation (3.3). Unlike P-waves, S-waves do not propagate through liquids, as liquids do not support shear stresses. For this reason S-waves only travel through the earth's crust and mantle, and not through the core. Body waves do not travel in a straight line, because the stiffness and density increases with depth. Instead, they refract towards the earth's surface.

$$c_s = \sqrt{\frac{G}{\rho}} \quad (3.3)$$

in which:

$c_s$	=	celerity of the S-wave	[m/s]
$G$	=	shear modulus	[Pa]

The shear modulus can be expressed in terms of the Young's modulus and Poisson's ratio by means of:

$$G = \frac{E}{2(1+\nu)} \quad (3.4)$$

### 3.3.3. Rayleigh waves

Rayleigh waves travel as ripples on the Earth's surface. Soil particles, represented by cubes in figure 3.5, move in an elliptical path when the Rayleigh waves pass by. Rayleigh waves have therefore the same characteristics as ocean surface waves. The wave speed is equal to the one of S-waves or slightly less, usually 90%.

### 3.3.4. Love-waves

Love waves are surface waves that cause horizontal shearing of the ground. They travel slightly faster than Rayleigh waves.



## 4. Commonly used procedures for (hydro)dynamic analyses

### 4.1. Introduction

There are many methods available for the dynamic analyses of structures. A selected number of them will be treated in this chapter. The most simplistic is the quasi-static method, where dynamic forces are modeled as static loads based on the maximum acceleration of the earthquake, the PGA<sup>3</sup>.

Another method is the use of response spectra, which represent the relation between the maximum acceleration of a structure and the maximum acceleration of an earthquake. These are not the same and depend on the eigenfrequencies of the structure.

Time history analyses use the accelerograms recorded from an earthquake as input. An example can be found in figure 4.1:

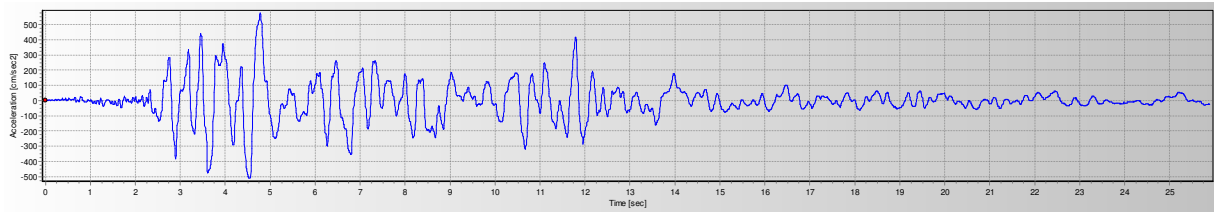


**Figure 4.1** Acceleration time history or accelerogram

By means of integration, time histories of velocity and displacement are obtained. The calculation can be done in the time or frequency domain, the latter approach is preferred from mathematical point of view. The solution in the time domain can then be obtained by integrating over the earthquake's spectrum. With this method the response to the whole earthquake can be examined and not only the response to the extreme values.

An advanced method is HFTD<sup>4</sup>, which is an iterative procedure where the non-linear effects in the frequency domain are accounted in the time domain. In a linear case the solution in the frequency domain is achieved by superposition. If the response is non-linear this principle of superposition is not valid.

The above-mentioned methods for dynamic analysis will be discussed further in the following paragraphs:

- Quasi-static (seismic coefficient method): paragraph 4.2;
- Response spectrum analysis : paragraph 4.3;
- Time-history analysis : paragraph 4.4;
- Hybrid Frequency Time Domain analysis: paragraph 4.5.

In paragraph 4.6 the general solving procedure of the Finite Element Method or FEM is explained. This numerical approach will be applied in chapter 8.

For the hydrodynamic pressures on a structure exerted by an earthquake two methods are widely used: the methods by Westergaard and Housner. Both these methods have a different background and applicability. These two methods are usually applied in a quasi-static form, but are also applicable for variable accelerations. The two methods are treated in detail in paragraph 4.7.

### 4.2. Quasi-static (seismic coefficient method)

The seismic coefficient method (SCM) has traditionally been used to evaluate seismic loading on structures. According to the USACE<sup>5</sup> this method may still be used for preliminary and stability analyses [USACE, EM 1110-2-6053]. In the SCM earthquake forces are simply treated as static forces and are combined with other static loads like hydrostatic and soil pressures and dead weights. The analysis is mainly concerned with sliding and rotational stability where the structure is treated as a rigid body. The inertia forces of the structure are calculated by multiplying the structural mass, added masses of water body and effects due to dynamic soil pressures, times a seismic coefficient. This coefficient is expressed as a fraction of the gravitational acceleration  $g$ . For the horizontal seismic coefficient  $k_h$ , usually a reduction factor is applied in relation to the PGA. The USACE uses a reduction factor of 2/3 for the evaluation of the potential of sliding [USACE, EM 1110-2-6053] and other analyses for gravity structures. In [NOZU *et al.*, 2004] an average relation of 0.6 PGA for  $k_h$  is derived for gravity-type quay walls.

<sup>3</sup> Peak Ground Acceleration

<sup>4</sup> Hybrid Frequency Time Domain

<sup>5</sup> United States Army Corps of Engineers

### 4.3. Response spectrum analysis

With this method the peak responses of a linear elastic structure can be determined by response spectra representing the ground motions. The response spectra can be general, taken from sources as the USACE [USACE, EM 1110-2-6051] or the Eurocodes, or site specific. Response spectra represent the acceleration of multiple SDOF<sup>6</sup> systems, when exposed to an earthquake loading. For small periods ( $T < 0.05$  s) the accelerations are equal to the PGA, meaning that for short periods the structure will have the same acceleration as the ground. For long periods the acceleration of the structure is minimal and the structure will have the same maximum displacements as the ground. For excitation periods in the order of the eigenperiods of the structure will have a higher acceleration than the earthquake due to resonance effects. The procedure for making response spectra is visualized in figure 4.2: the input signal is applied to multiple SDOF systems, each with a different eigenperiod. The output is the maximum response at the eigenperiods.

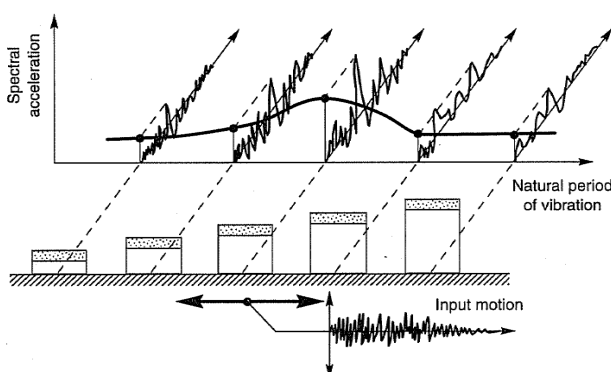


Figure 4.2 Procedure for making response spectra (adapted from [KRAMER, 1996])

The response spectra for the new Atlantic and Pacific locks are given in figure 4.3. They are provided by the APC and are based on a damping ratio of 5% and for periods between 0.01 and 2.5 seconds. The peak period for all four spectra is 0.2 s. The spectrum depends largely on the amount of damping, which is determined by earthquake's magnitude, source-to-site distance and local site conditions.

In practice the damping characteristics are expressed in equivalent viscous damping ratios. An advantage is that this leads to convenient equations of motion. A disadvantage is that the viscous damping is dependent of the excitation frequency. A solution to this is to use hysteretic damping, which is defined as a damping force proportional to the strain, but in phase with the velocity. For linear-elastic analyses, normally a viscous damping ratio of 5% is used. For non-linear analyses a higher value of damping can be used, because of the energy dissipation caused by non-linear effects like joint-opening or cracking.

The maximum response of the structure due to earthquake loading is evaluated by combining modal superposition and multicomponent input. The accuracy of this method depends on the number of considered modes and the combination used for multicomponent modal earthquake responses.

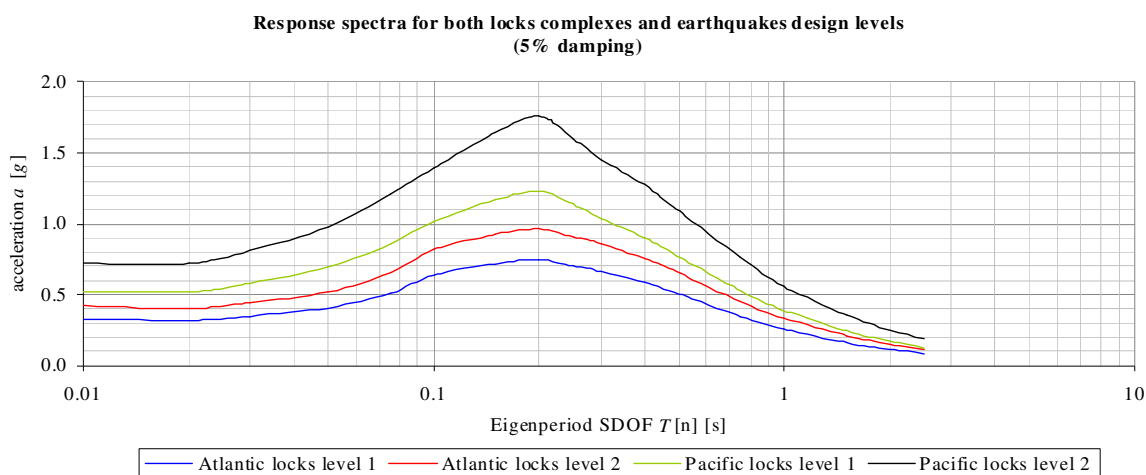


Figure 4.3 Horizontal response spectra for a damping ratio of 5%

### 4.4. Time-history analysis

With a time-history analysis the complete response history of structures to earthquake loading can be computed, instead of only the extreme values. This method gives therefore a good insight of the behavior of the structure as valuable time-dependent information is provided, this make time-history analyses suitable for study of non-linear effects. The analysis can be done either in the time or frequency domain.

<sup>6</sup> Single degree of freedom, in contrast to MDOF's: multi degrees of freedom

In the time domain the analysis is carried out most of the time by step-by-step procedures. The loading and response history are divided into time intervals or steps. Numerical integration is used to satisfy the equations of motion. The response during each step is computed from the initial conditions, which follow from the previous step. Besides this explicit method, the response can also be computed from data from the same step. With this implicit method iteration procedures are required. For the analysis in the time domain modal superposition can be used to uncouple the equations of motion.

An alternative approach to analyze in the time domain is an analysis in the frequency domain. Especially when the equations of motion contain frequency-dependent terms like damping, this approach is superior to an analysis in the time domain. The response of the structure is computed by means of harmonic components of the ground motion, obtained by Fourier transformation. The total solution is obtained by modal superposition if applicable, or else per frequency step. The first method is however superior in terms of calculation time, but cannot be applied in all cases.

#### 4.5. Hybrid Frequency Time Domain analysis

In the case that the dynamic response of a structure is non-linear and frequency-dependent, modal superposition is not applicable. A method to cope with this is HFTD [TNO DIANA, 2008], where the non-linear aspects are accounted for in the time domain. In the frequency domain the linearized problem is computed where the non-linear effects are taken into account by a pseudo-force. The general approach to this iterative process is as follows:

1. Computing the pseudo-force in the time domain;
2. Transformation of the pseudo-force to the frequency domain;
3. Solving the linearized equations of motion;
4. The solution in the frequency domain is transformed to the time domain;
5. Check for convergence criteria. If convergence is not achieved, the output is used to calculate a new pseudo-force in step 1.

#### 4.6. A brief introduction to the Finite Element Method

The Finite Element Method or FEM is numerical procedure for finding solution to partial differential and integral equations. This is achieved by discretization of the problem into numerical model consisting out of elements and nodes; together they form a mesh. For each of the elements the equations are solved for the boundary conditions on that specific element from adjacent elements or external loading. The partial differential equations are approximated by ordinary differential equations related to the degrees of freedom of the nodes of the element. The solution is obtained by linear algebra and interpolation methods. The nodes ensure that different elements act as one part of the model as they form the connection in a model. In general it applies that more elements mean more accuracy, but also more required calculation time. Elements can have different dimension (from 0D up to 3D) and orders: linear, quadratic or higher. For higher order elements the same applies as to more elements: more accuracy, but with more calculation time. The FEM is widely applied in different branches of engineering.

The general FEM procedure is as follows<sup>7</sup>:

1. Identify governing equation, e.g. a partial differential equation;
2. Define the FEM model by approximate the governing equation, e.g. by a direct approach or shape functions;
3. Discretization of the domain by elements, as explained in figure 4.4;

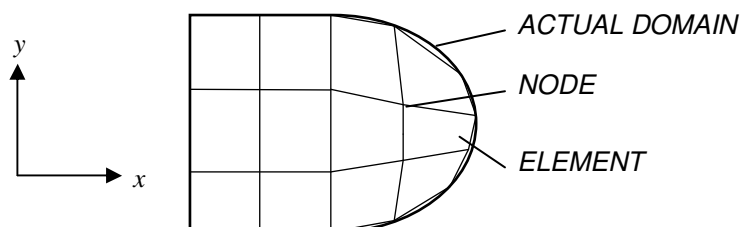


**Figure 4.4 Discretization of a domain by means of elements**

4. Apply the approximation of the variable over the element, as shown in figure 4.5;

<sup>7</sup> Based upon [KWON, 2005]

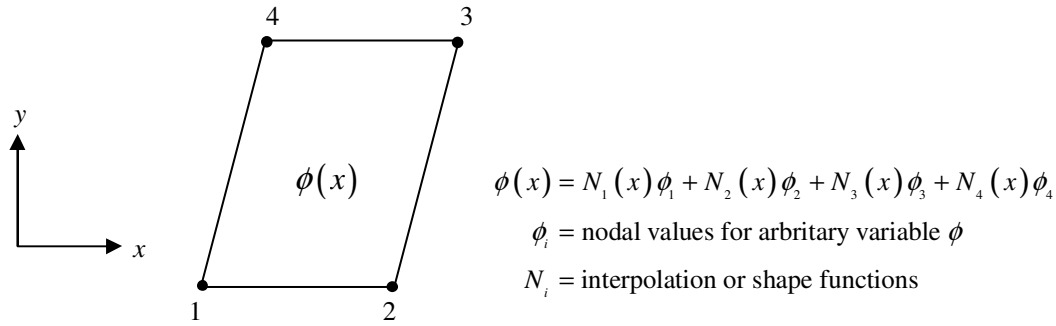


**Figure 4.5 Interpolation by shape functions**

5. Determine the element stiffness matrix;

$$[K]^e \{\phi\}^e = \{f\}^e \quad (4.1)$$

with:

$$\begin{aligned} [K]^e &= \text{element stiffness matrix} \\ \{\phi\}^e &= \text{element vector of unknown variables, e.g. displacements} \\ \{f\}^e &= \text{element load vector} \end{aligned}$$

6. Assemble the global stiffness matrix;

$$[K]\{\phi\} = \{F\} \quad (4.2)$$

with:

$$\begin{aligned} [K] &= \text{global stiffness matrix} \\ \{\phi\} &= \text{global element vector of unknown variables} \\ \{F\} &= \text{global element load vector} \end{aligned}$$

7. Solve the matrix equation to find the unknowns;

$$\{\phi\} = [K]^{-1} \{F\} \quad (4.3)$$

8. Calculate other values of interest from the obtained solution (postprocessing) e.g.:

$$\frac{d\phi}{dx}, \text{ etc.}$$

## 4.7. Hydrodynamic pressures

### 4.7.1. Hydrodynamic pressure according to Westergaard

Westergaard was the first to find a solution for hydrodynamic pressures on dams during earthquakes. His solution [WESTERGAARD, 1933] is based on the 2D wave equation for compressible fluids, which has the shape of an infinite summation of sines, see equation (4.4). Westergaard himself developed a simple approximation formula, which has the shape of a parabola, see equation (4.5). A graphical representation of both formulas can be found in figure 4.6.

$$p(z) = \frac{8\rho k_h g d}{\pi^2} \sum_{n=1,3,5,\dots,\infty} \frac{1}{n^2 C_n} \sin\left(\frac{n\pi z}{2d}\right) \quad (4.4)$$

$$p(z) = \frac{7}{8} \rho k_h g \sqrt{dz} \quad (4.5)$$

with:

$$C_n = \sqrt{1 - \frac{16\rho d^2}{n^2 K T_e^2}} \quad (4.6)$$

in which:

$p$	=	hydrodynamic pressure at coordinate $z$	[Pa]
$\rho$	=	density of water	[kg/m <sup>3</sup> ]
$k_h$	=	horizontal seismic coefficient	[-]
$g$	=	acceleration of gravity	[m/s <sup>2</sup> ]
$d$	=	water depth	[m]
$z$	=	vertical coordinate ( $z = 0$ at surface level, $z = d$ at bottom level)	[m]
$C_n$	=	constant taking into account the compressibility of water	[-]
$K$	=	bulk modulus of water	[Pa]
$T_e$	=	harmonic excitation period	[s]

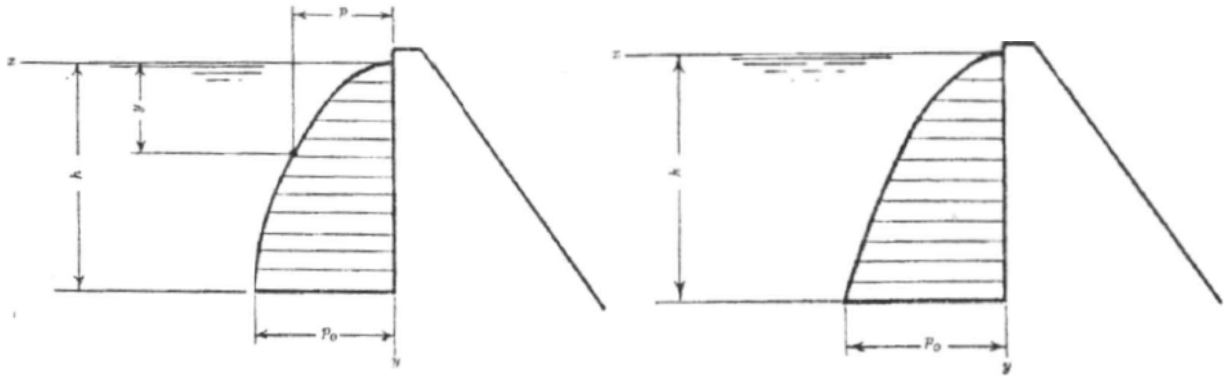


**Figure 4.6 Hydrodynamic pressure distribution for the original (left) and simplified parabola (right) Westergaard solutions (adapted from [WESTERGAARD, 1933])**

To derive his solution, Westergaard made the following assumptions:

- Pressure at water level is equal to zero, no vertical movement of water particles and no waves at the water surface;
- The dam is infinitely long and has a vertical face;
- The reservoir extends to infinity;
- The dam itself is rigid.

The hydrodynamic pressure is out of phase with the earthquake acceleration and therefore acts as an inertia force. This "added mass" depends on the harmonic excitation frequency. As an earthquake consists out of many frequencies, the concept of this added mass is in theory not applicable for quasi-static earthquake loading as it is not solely related to the amplitude of acceleration. With the assumption of incompressible fluid, the added mass becomes independent of the excitation frequency. This assumption is justified if the ratio of the water depth over the period of the harmonic ground motion is small enough, as shown by Bustamante *et al.* [CHOPRA, 1966]. With period close the resonance periods, errors become extremely large. Therefore Westergaard's simplified solution is only valid when the period of excitation is larger than the fundamental resonance period for water pressure (equation (4.7)), as shown by Chopra [CHOPRA, 1966].

$$T_1 = \frac{4d}{c_p} \quad (4.7)$$

with:

$$c_p = \sqrt{\frac{K}{\rho}} \quad (4.8)$$

in which:

$T_1$	=	fundamental eigenperiod	[s]
$c_p$	=	celerity of pressure waves in water (equal to the speed of sound)	[m/s]

The fundamental resonance period in equation (4.7) can be derived by setting equation (4.6) equal to zero for  $n = 1$ . With  $d \approx 30$  m and  $c_p \approx 1500$  m/s, this leads to a fundamental eigenperiod of 0.08 s or 12.5 Hz. Most the energy of an earthquake is distributed over frequencies much smaller than 12.5 Hz. Based on this criterion, the Westergaard formula is applicable for large lock structures. For values of  $n$  higher than 1, other eigenperiods can

be found. Even though these higher order eigenperiods can be derived from Westergaard's solution, the original solution itself does not produce real values for periods lower than the fundamental eigenperiod. This is shown in in paragraph 7.9. In [CHOPRA, 1966] a solution is presented which covers the whole frequency domain. Details about this solution can be found in appendix B.1.

Bustamante *et al.* [CHOPRA, 1966] have done research in the error introduced when ignoring surface wave for harmonic excitations; when including the compressibility of water. Their results are listed in equation (4.9).

$$\left\{ \begin{array}{ll} \text{error} < 0.05 & \text{if } d/T_e > 4.2\sqrt{d} \\ 0.05 < \text{error} < 0.20 & \text{if } 2.6\sqrt{d} < d/T_e < 4.2\sqrt{d} \\ \text{error} > 0.20 & \text{if } d/T_e < 2.6\sqrt{d} \end{array} \right. \quad (4.9)$$

From these results it can be concluded that low head dams are more prone to be affected by surface waves than high head dams. For  $d \approx 30$  m and  $T_e \approx 1$  s, no large errors are to be expected by ignoring surface waves in the longitudinal direction of the locks.

The major disadvantage of the Westergaard formula is absence of the effect of the reservoir length. In a discussion on Westergaard's paper [BRAHTZ AND HEILBRON, 1933]; a correction factor has been introduced on Westergaard's formula to take into account this effect. The correction factor  $\beta$  is a function of the reservoir length (normal to the dam)  $2L$  and the water depth, the correction factor is given in figure 4.7.

**Correction factor  $\beta$  for the Westergaard formula by Brahtz and Heilbron**

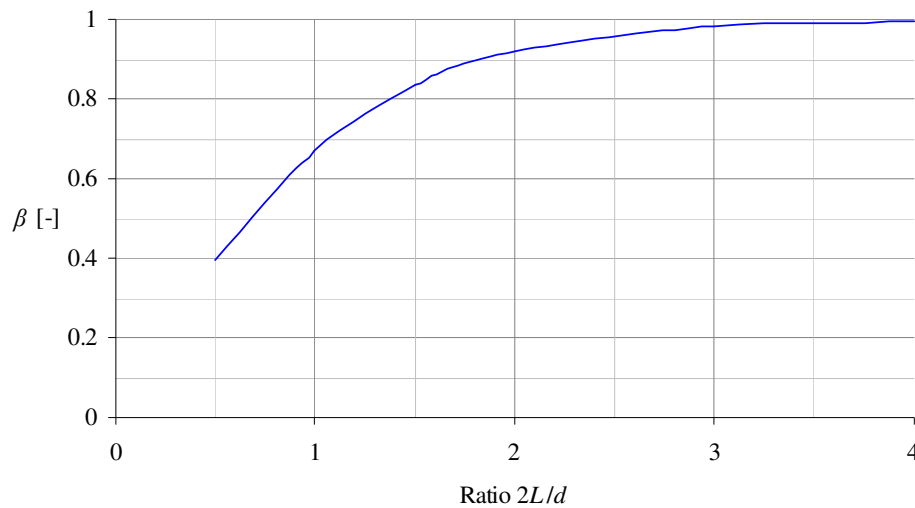


**Figure 4.7 Correction factor on the Westergaard formula in case of short reservoir**

#### 4.7.2. Hydrodynamic pressure according to Housner

Another widely used formula to calculate the hydrodynamic pressures is the one by Housner [HOUSNER, 1954]. This formula is derived for fluid containers under earthquake loading. Housner made a distinction between impulsive and convective pressures. The impulsive component relates to the portion of the fluid that moves in coherence with the structure (the added mass), while the convective component relates to effects like sloshing.

The main difference with the Westergaard formula is the effect of the length coordinate, which is taken equal to infinity by Westergaard. Housner uses a coordinate system with the origin in the center of the lock: the gates are located at  $x = \pm L$ . From equation (4.10) it can be seen that the length is taken into account by a hyperbolic tangent; details about hyperbolic functions can be found in figure 4.9. Therefore, for large longitudinal dimensions ( $2L > 4d$ ), the Housner formula gives more or less the same results as Westergaard's solution.

$$p(z) = \rho k_h g d \left( \frac{z}{d} - \frac{1}{2} \left( \frac{z}{d} \right)^2 \right) \sqrt{3} \tanh \left( \frac{\sqrt{3}L}{d} \right) \quad (4.10)$$

in which:

$$L = \text{half the length of the lock chamber} \quad [\text{m}]$$

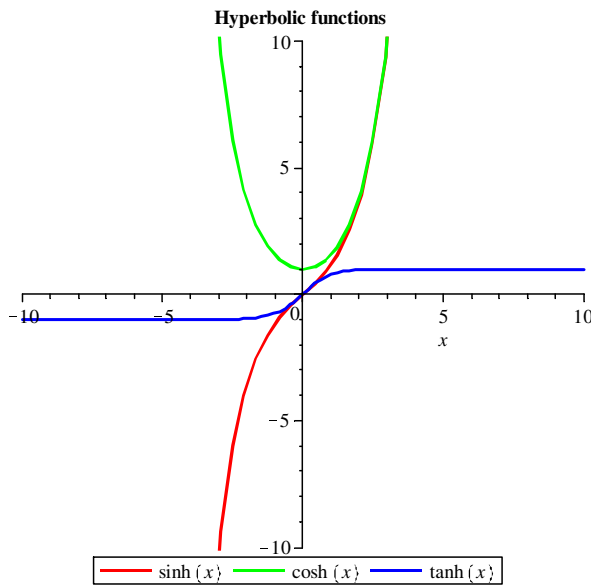


**Figure 4.8 Hyperbolic functions**

The excitation period in the Westergaard formula has almost no influence on the total pressure unless it is close to the eigenperiod. The period is therefore no parameter in the approximate Westergaard or Housner formula.

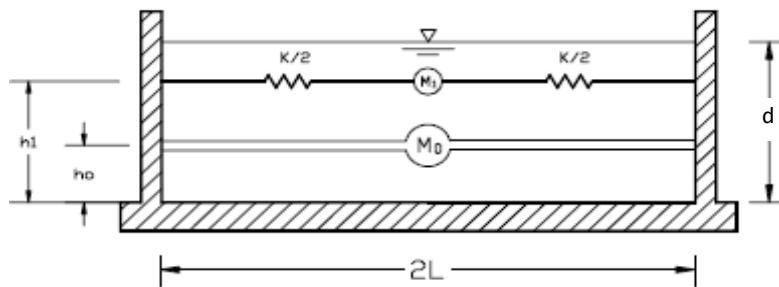


**Figure 4.9 Housner's mathematical model for impulsive and convective hydrodynamic forces (adapted from [USACE, EM 1110-2-6051])**

Besides an expression for the hydrodynamic pressures, Housner also made a model to calculate the force exerted on the structure due to sloshing effects. This model is shown in figure 4.9. The impulsive force is represented by a lumped mass  $M_0$ , acting on a height  $h_0$  (equation (4.11)).

$$M_0 = \left( \frac{d}{\sqrt{3}L} \tanh \left( \frac{\sqrt{3}L}{d} \right) \right) M$$

$$M = 2\rho dL \quad (4.11)$$

$$h_0 = \frac{3}{8}d$$

in which:

$$M_0 = \text{lumped impulsive mass per unit width} \quad [\text{kg/m}]$$

$$M = \text{total mass of water per unit width} \quad [\text{kg/m}]$$

$$h_0 = \text{height on which the impulsive force acts} \quad [\text{m}]$$

The sloshing force exerted on the lock is modeled by an equivalent mass  $M_1$  attached to the lock by a spring with a spring constant  $K_1$ , acting on a height  $h_1$ . The index 1 corresponds to the fundamental natural period for sloshing. This sloshing period is not equal to the resonance period for hydrodynamic water pressure as discussed in section 4.7.1. Formulas for these parameters, initially derived by Housner and later presented by Epstein [USACE, EM 1110-2-6051] are given in equations (4.12). Expressions for higher natural periods ( $n = 3, 5$ , etc.) can be found by substituting  $(Ln)$  for  $L$ .

$$\begin{aligned}
 M_1 &= \left( \sqrt{\frac{5}{18}} \frac{L}{d} \tanh \left( \sqrt{\frac{5}{2}} \frac{d}{L} \right) \right) M \\
 h_1 &= \left( 1 - \frac{\cosh \left( \sqrt{\frac{5}{2}} \frac{d}{L} \right) - 1}{\sqrt{\frac{5}{2}} \frac{d}{L} \sinh \left( \sqrt{\frac{5}{2}} \frac{d}{L} \right)} \right) d \\
 T_1 &= 2\pi \sqrt{\frac{L}{\sqrt{\frac{5}{2}} g \tanh \left( \sqrt{\frac{5}{2}} \frac{d}{L} \right)}} \\
 K_1 &= \frac{4\pi^2 M_1}{(T_1)^2} = \left( \frac{\frac{5}{6} g \tanh^2 \left( \sqrt{\frac{5}{2}} \frac{d}{L} \right)}{d} \right) M
 \end{aligned} \tag{4.12}$$

These equations are derived by Housner for fluid containers with  $d/L \leq 1.6$  and are therefore also applicable for navigation locks. For ratios of  $d/L > 1.6$ , equation (4.10) should only be used for the top part of the fluid ( $1.6L$ ). The lower part of the fluid should be treated as a rigid body exerting a pressure on the walls of:

$$p = \rho k_h g L \tag{4.13}$$

This is visualized in figure 4.10.

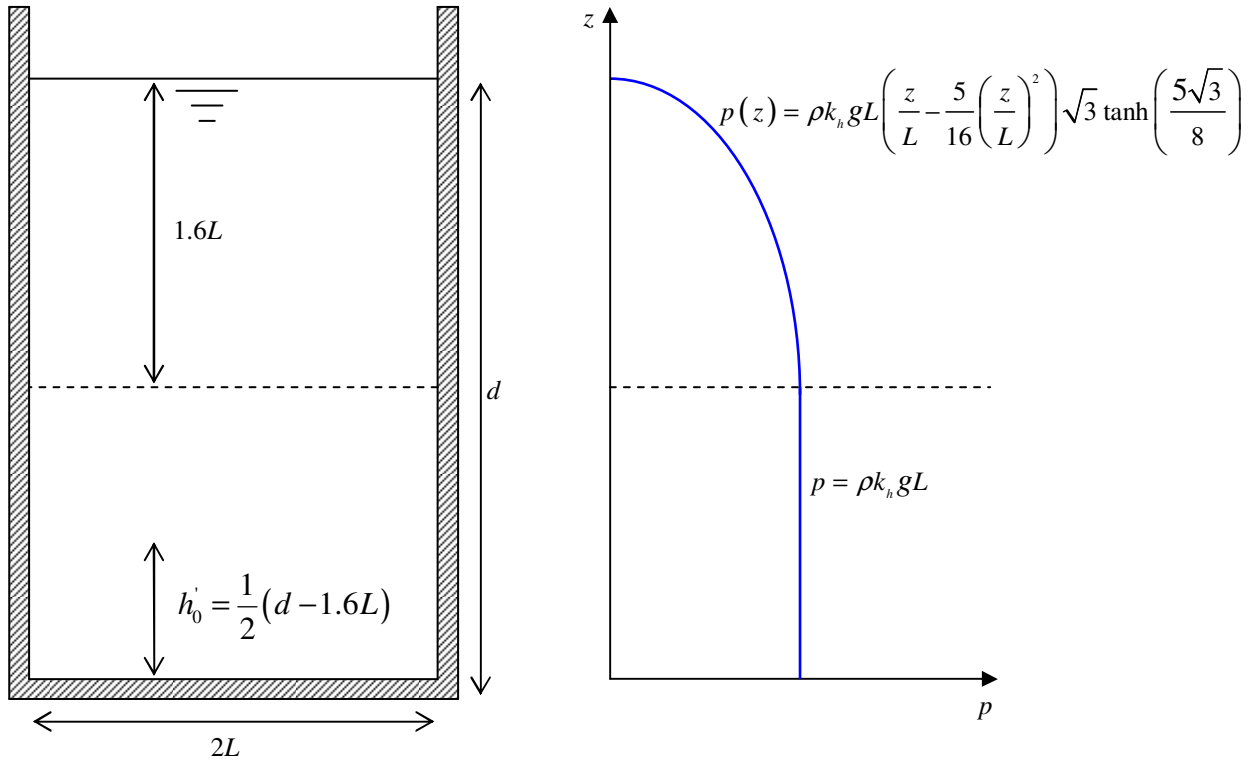


**Figure 4.10 Hydrodynamic pressure distribution in the case of  $d/L > 1.6$  according to Housner**

Expressed mathematically this gives:

$$p(z) = \begin{cases} \rho k_h g L \left( \frac{z}{L} - \frac{5}{16} \left( \frac{z}{L} \right)^2 \right) \sqrt{3} \tanh \left( \frac{5\sqrt{3}}{8} \right) \approx 1.375 \rho k_h g z \left( 1 - \frac{5}{16} \frac{z}{L} \right), & z \leq 1.6L \\ \rho k_h g L & , z > 1.6L \end{cases} \quad (4.14)$$

The rigid body force acts on a height of:

$$h_0' = \frac{1}{2} \left( 1 - 1.6 \frac{L}{d} \right) \quad (4.15)$$

The force exerted by sloshing at the fundamental period follows from equation (4.16).

$$F_1 = M_1 R_a \sin \left( \frac{2\pi}{T_1} t \right) \quad (4.16)$$

in which:

$F_1$	=	force related to convective pressure at the fundamental period	[N/m]
$R_a$	=	spectral acceleration at fundamental natural period obtained from the response spectrum of the earthquake ground motion	[m/s <sup>2</sup> ]
$t$	=	time variable	[s]

Besides the response spectrum method, the mass-spring system can also be solved analytically with the parameters of equation (4.12). Both approaches will be discussed in paragraph 5.3.

#### 4.7.3. Transformation to added mass

The hydrodynamic pressures can be transformed into equivalent added mass by dividing by the acceleration, leading to a mass per unit of surface area. Integration over the water depth yields:

$$m_{am} = \frac{1}{k_h g} \int_{z=0}^{z=H} p(z) dz \quad (4.17)$$

in which:

$m_{am}$	added water mass per unit width	[kg/m]
----------	---------------------------------	--------

The added mass has therefore the same distribution as the hydrodynamic pressure. In case of a FEM calculation the mass can be lumped into nodes if required.

Please note that this added mass approach corresponds to the pressure distribution of a single wall. The Housner method treats the added mass for the whole system, meaning that the value  $M_0$  calculated from equation (4.11) applies to two walls. Using equation (4.17) to calculate the added mass yields:

$$m_{am} = \frac{\rho d^2}{\sqrt{3}} \tanh \left( \frac{\sqrt{3}L}{d} \right) \quad (4.18)$$

while Housner's method in equation (4.11) results in:

$$m_{am} = \frac{2\rho d^2}{\sqrt{3}} \tanh \left( \frac{\sqrt{3}L}{d} \right) \quad (4.19)$$

The difference is exactly a factor 2, resulting from the model that the Housner approach uses. Per wall the net result is the same.



## 5. Site conditions and preliminary assessment

### 5.1. Boundary conditions

#### 5.1.1. Seismic conditions

For the project two types of earthquake levels are defined in the program of requirements. Also the PGA is different for the two sites. The differences between the two levels are explained in table 5.1.

Level 1 earthquake	Level 2 earthquake
Return period $T_r = 475$ years	Return period $T_r = 1000$ years
PGA Atlantic site = $0.330g = 3.237 \text{ m/s}^2$ PGA Pacific site = $0.522g = 5.121 \text{ m/s}^2$	PGA Atlantic site = $0.420g = 4.120 \text{ m/s}^2$ PGA Pacific site = $0.718g = 7.044 \text{ m/s}^2$
Response of structure: <ul style="list-style-type: none"> <li>• Linear-elastic behavior;</li> <li>• No damage is allowed that interferes with operations; the gates and corresponding mechanical equipment must operate immediately after the event without any loss of serviceability;</li> <li>• Displacements of the gates and lock heads shall be limited so that there is no leakage through any seal, joint, or opened crack.</li> </ul>	Response of structure: <ul style="list-style-type: none"> <li>• Inelastic behavior is allowed, but within limits;</li> <li>• Some damage is allowed, which may require temporary closure for repairs: e.g. the gates can fully retract in their recesses; permanent residual offsets may occur, but within limits;</li> <li>• These limits are: a horizontal displacement of the lock walls of <math>2.5\%</math> (displacement/wall height) and/or a rotation of <math>0.5^\circ</math>.</li> </ul>

**Table 5.1 Differences between a level 1 and level 2 earthquake as defined in the program of requirements**

#### 5.1.2. Soil and rock properties

Three main types of rock formations are present and are all of volcanic origin:

- Basalt at the Pacific site: basalt is medium hard to very hard and strong type of rock, it consist of dense, fine grained material; the structure of the basalt varies from massive to columnar jointed;
- La Boca at the Pacific site: the La Boca formation varies from very soft to medium-hard rock and is a sedimentary formation;
- Gatún at the Atlantic site: this formation was formed in a shallow marine basin and consists of a series of fine to very fine sandstone and siltstone.

In table 5.2 the rock mass properties of the three types of bedrock are given. Please note that these data are for rock mass and not for individual samples.

Type of rock	$\gamma$ [kN/m <sup>3</sup> ]	$E_{dyn}$ [GPa]	$\nu_{dyn}$ [-]	$G_{dyn}$ [GPa]	$c_p$ [m/s]	$c_s$ [m/s]
Basalt	22	8.0	0.35	3.0	2400	1150
La Boca	22	2.0	0.35	0.7	1200	570
Gatún	18	4.0	0.35	1.4	1870	900

**Table 5.2 Rock mass properties of bedrock present at the Pacific and Atlantic sites**

### 5.2. Preliminary assessment: the Westergaard and Housner formulas applied

For a preliminary assessment of the hydrodynamic pressures expected for the Third Set of Locks project the Westergaard and Housner solutions from sections 4.7.1 and 4.7.2 are used. With these methods the hydrodynamic pressure for earthquake levels 1 and 2 is calculated for the dimension of the new locks. A distinction is made between the lock chambers and the intermediate space between the two gates of a lock head. For the main lock chambers the distance between gates is slightly larger than the chamber length itself. Therefore the correct distance of 436 m is used and not the chamber length of 427 m, as described in section 2.4.1. The chambers are assumed to be fully filled with 30 m of water. The acceleration used for both levels is two-third of the PGA, as discussed in paragraph 4.2. Combined with the PGA's from table 5.1, this leads to accelerations of  $0.280g$  or  $2.75 \text{ m/s}^2$  and  $0.479g$  or  $4.70 \text{ m/s}^2$  for the Pacific site. Because the accelerations at the Pacific site are larger than those of the Atlantic site, only the Pacific site is considered. The calculated pressure can be found in figure 5.1. As a reference the hydrostatic pressure is added.

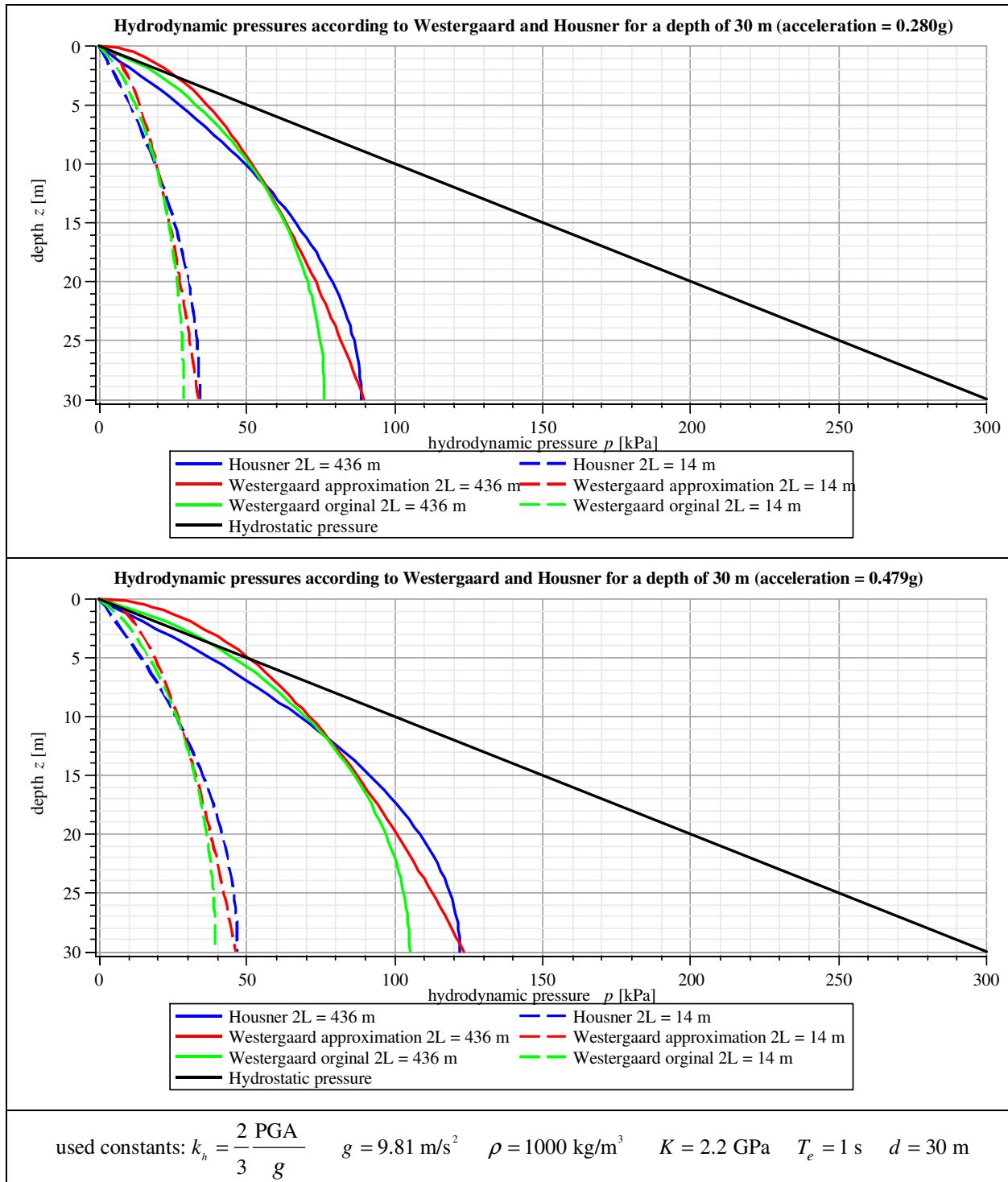


**Figure 5.1 Comparison of hydrodynamic pressure according to the Westergaard and Housner formulas**

Both the hydrodynamic pressures at sill level and the total pressure on the gate are consistent with each other. For the pressure against the inner sides of the gates, where 2L is equal to 14 m, the Housner or reduced Westergaard formula has to be applied. Westergaard's solutions, without the correction factor, give in this case wrong results.

Based on the background theory in paragraph 4.7 and the results of figure 5.1 the following can be concluded:

- Both approaches are applicable to lock chambers and give similar results. The hydrodynamic pressure distribution has a parabolic shape. Housner's method automatically incorporates the length of the lock chamber, for Westergaard's formula's a correction factor needs to be applied.
- Both the approximation formula by Westergaard and Housner's formula are applicable for periods above the fundamental eigenperiod in equation (4.7). For lock structures this is almost the case as the excitation periods

are well above it. This is a result of the limited water depth compared to e.g. dams. Because the compressibility of the fluid also no influence for the frequency range, there is no reason the use Westergaard's original formula. His own approximation gives more than accurate results for an early design. In table 5.3 a comparison in added mass between the three discussed methods is given in the case of a long reservoir or lock chambers; the results are identical to figure 5.1.

Method	Total added mass in case of long reservoir (times $\rho H^2$ )
Housner	$\frac{1}{\sqrt{3}} \approx 0.577$
Westergaard original	$\frac{16}{\pi^3} \sum_{n=1,3,5,\dots}^{\infty} \left( \frac{1}{n^3} \right) \approx 0.543$
Westergaard approximation	$\frac{7}{12} \approx 0.583$

**Table 5.3 Added mass comparison for long reservoirs or lock chambers**

### 5.3. Housner's mathematical model

#### 5.3.1. Introduction to Housner's model

In section 4.7.2 the theory behind Housner's mass-spring model for sloshing forces has been discussed. Two ways were discussed to evaluate the model; a response spectrum approach and solving the equation of motion of a SDOF mass-spring system. The equation for determining the convective forces in equation (4.12) are repeated here:

$$\begin{aligned}
 M_1 &= \left( \sqrt{\frac{5}{18}} \frac{L}{d} \tanh \left( \sqrt{\frac{5}{2}} \frac{d}{L} \right) \right) M \\
 h_1 &= \left( 1 - \frac{\cosh \left( \sqrt{\frac{5}{2}} \frac{d}{L} \right) - 1}{\sqrt{\frac{5}{2}} \frac{d}{L} \sinh \left( \sqrt{\frac{5}{2}} \frac{d}{L} \right)} \right) d \\
 T_1 &= 2\pi \sqrt{\frac{L}{\sqrt{\frac{5}{2}} g \tanh \left( \sqrt{\frac{5}{2}} \frac{d}{L} \right)}} \\
 K_1 &= \frac{4\pi^2 M_1}{(T_1)^2} = \left( \frac{\frac{5}{6} g \tanh^2 \left( \sqrt{\frac{5}{2}} \frac{d}{L} \right)}{d} \right) M
 \end{aligned} \tag{5.1}$$

In which  $M$  is the total mass of water inside the lock chamber per unit width.

#### 5.3.2. Response spectrum approach

The maximum sloshing force at the fundamental sloshing period now follows from:

$$F_{1,\max} = M_1 R_a = \left( \frac{\sqrt{10}}{3} \rho L^2 \tanh \left( \sqrt{\frac{5}{2}} \frac{d}{L} \right) \right) R_a \tag{5.2}$$

Where  $R_a$  corresponds to the acceleration obtained from the response spectrum at the fundamental sloshing period.

For the situation of  $H = 30$  m and  $L = 218$  m this leads to a fundamental sloshing period of 50.9 s. For the impounded water between two closed gates of a lock head the above formulas are not applicable as this situation exceeds the limit  $d/L$  ratio of 1.6 as described in section 4.7.2. However, the argument of hyperbolic tangent is now much larger than 1, meaning that it has reached its limit value of 1. This can be seen in figure 4.8. Therefore the expression for the fundamental resonance period effectively reduces to:

$$T_1 = 2\pi \sqrt{\frac{L}{\sqrt{\frac{5}{2}}g}} \approx 5.0 \sqrt{\frac{L}{g}} \quad (5.3)$$

which gives for  $L = 7$  m a fundamental sloshing period of 4.2 s.

For both these periods, accelerations from the response spectrum in figure 4.3 can be obtained. For the large chambers the acceleration would be almost zero, for the water between two gates of a lock head the response would be maximal 0.1g or 1 m/s. According to equation (5.2) this results in a sloshing force of 5.4 kN/m at a height of 25.6 m (0.85d). Modifications on Housner's formula for  $d/L > 1.6$  by Epstein [LIVAOGU, 2008] give even lower forces and acting height. A calculation of the impulsive force by means of equation (4.14) gives a result of 17.5 MN/m for the same acceleration of 0.1g. As the real accelerations of the gate will be higher, it can be concluded that sloshing effects are negligible compared with the impulsive effects according to the Housner method using a response spectrum.

### 5.3.3. SDOF approach

The hydrodynamic forces can also be evaluated using Housner's mathematical model with a SDOF system. This model is shown in figure 5.2. The earthquake is modeled as a harmonic excitation with a constant amplitude  $a_{\max}$ . The impulsive force is rigid; hence the force follows directly from the acceleration with Housner's formulas. The convective force follows from a SDOF mass-spring system. From the response spectrum approach follows that this effect is limited, therefore only one eigenfrequency is treated. The result is listed in equation (5.4) and the amplitude-frequency response function in figure 5.3. The amplitude-frequency response function is derived in appendix B.2.

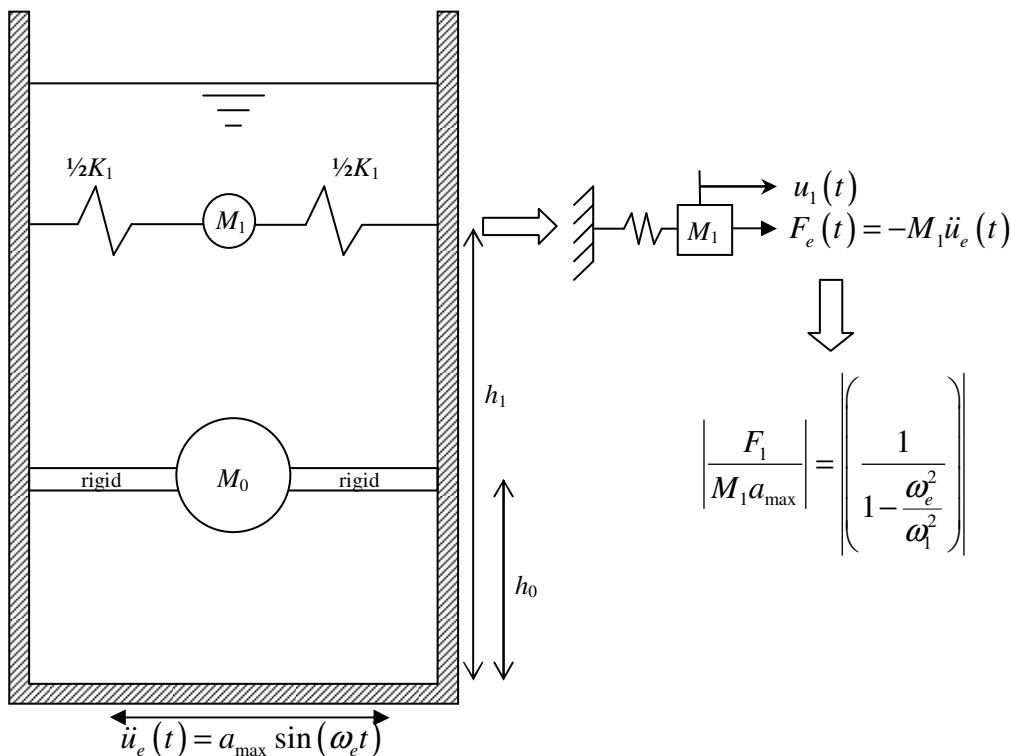


Figure 5.2 SDOF mass-spring system for calculating sloshing force

$$F_1 = -\frac{M_1 a_{\max}}{1 - \frac{\omega_e^2}{\omega_n^2}} \sin(\omega_e t) \quad (5.4)$$

Substituting the numeric values,  $d = 30$  m,  $L = 218$  m and  $\rho = 1040$  kg/m<sup>3</sup>, into equations (4.12) results in:

$$\begin{aligned} M_1 &= 11,160 \text{ t} \\ K_1 &= 170 \text{ kN/m} \\ \omega_1 &= 0.123 \text{ rad/s} \\ T_1 &= 50.9 \text{ s} \end{aligned} \quad (B.5)$$

In section 4.7.2 is discussed that in the case of  $d/L > 1.6$  the lower part of the fluid acts as a rigid body and therefore does not exert convective pressures on the walls. For  $L = 7$  m, this corresponds to 11.2 m on a total of 30 m. Substituting numeric the values,  $d = 1.6L = 11.2$  m,  $L = 7$  m and  $\rho = 1040$  kg/m<sup>3</sup>, into equation (4.12) results in:

$$\begin{aligned} M_1 &= 53 \text{ t} \\ K_1 &= 116 \text{ kN/m} \\ \omega_1 &= 1.479 \text{ rad/s} \\ T_1 &= 4.2 \text{ s} \end{aligned} \quad (5.6)$$

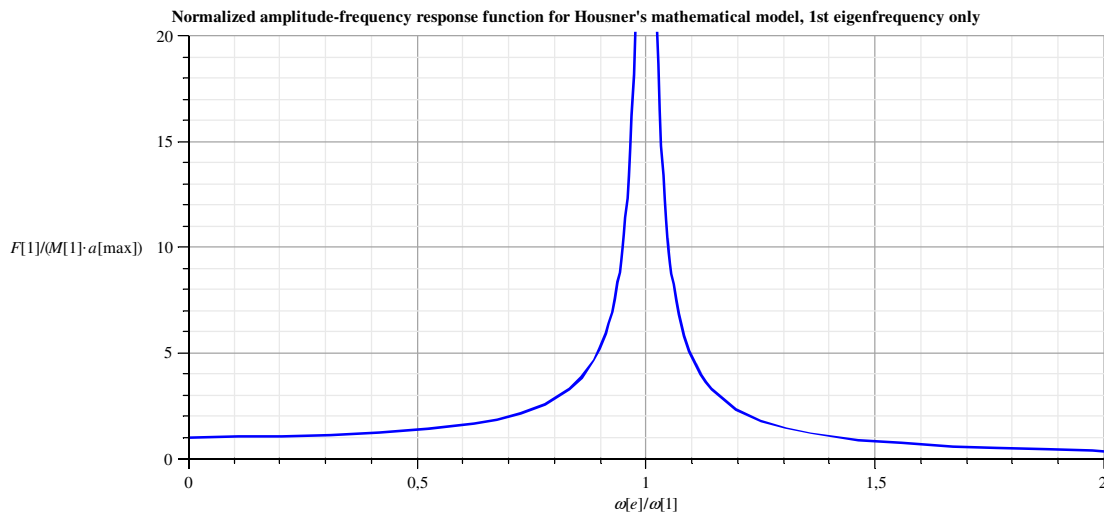


**Figure 5.3 Dimensionless amplitude-frequency response function for Housner's SDOF model**

With the aid of equation (5.4) and figure 5.3 the following results can be obtained for an excitation frequency of 1 s or 6.28 rad/s; the maximum acceleration is again defined as 2/3 of the PGA:

Situation [m]	$a_{\max}$ level 1 [m/s <sup>2</sup> ]	$a_{\max}$ level 2 [m/s <sup>2</sup> ]	$F_{1,\max}$ level 1 [kN/m]	$F_{1,\max}$ level 2 [kN/m]
$2L = 436$	0.280 $g = 2.75$	0.479 $g = 4.70$	12	20
$2L = 14$	0.280 $g = 2.75$	0.479 $g = 4.70$	9	15

**Table 5.4 Results for Housner's SDOF model (1<sup>st</sup> mode only)**

The SDOF approach shows similar results as the response spectrum approach: the convective effects are negligible compared to the impulsive effects. The sloshing force has the same order, the small difference results from the different earthquake input.

#### 5.3.4. Conclusions Housner's model

Two approaches are used to evaluate Housner's mathematical model. The convective or sloshing forces negligible compared the impulsive or "added mass" forces. This conclusion is based the dimensions of the Post-Panamax locks.



## 6. One-dimension model for wave interaction

### 6.1. Introduction 1D model

Both the Westergaard and Housner methods for the calculation of hydrodynamic pressures disregard the effect of surface waves. These waves are assumed to be negligible. In section 4.7.1 it is shown that low head dams are more prone to be effected by surface waves than high head dams. Contrary to dams, lock structures are not semi-infinite and reflective boundaries are present in close vicinity to each other. Generated surface wave will therefore reflect off the vertical gates or walls instead of moving away from e.g. a dam. Therefore, a 1D model will be used to investigate the generation of surface waves and the effect on lock gates. This analytical model is based on the 1D shallow water equations for the water inside the lock chambers. A characteristic of these equations is that the horizontal flow velocity is depth averaged and no vertical accelerations of fluid particles are taken into account, which is the case for shallow water. The lock chambers are far from shallow, but due limited vertical accelerations the shallow water equations are assumed to be applicable. A 2D model, where the vertical fluid accelerations are taken into account, will be discussed in chapter 7. For the 1D model the focus is made on the interaction between surface waves and motion of the gates. The situation is modeled with closed gates surrounded by bodies of water. For the gates SDOF mass-spring systems are used where the mass consists out of the dead weight of the gates – including enclosed water inside the gates – and the added mass as a result of impulsive hydrodynamic pressure. The surface waves are modeled with the wave equation, which can be derived from the shallow water equation. The wave equation is a linear, 2<sup>nd</sup> order partial differential equation. As the solution is sought in the form of the steady-state solution, two boundary conditions are necessary to solve the wave equation: one at each side of the lock chamber. The earthquake will be represented as a harmonic excitation, including a phase shift. In this way a solution in the frequency domain can be found. Integration of this solution in the frequency domain over an earthquake spectrum gives the solution in the time domain. This case-specific procedure is not treated in this thesis. One lock head with closed gates is considered, with no vessels in the chambers. The total force on the gates consists out of three parts in this model:

- The hydrostatic pressure; as this is of no influence on the dynamic behavior of the gates, the hydrostatic force will be disregarded. The hydrostatic force will have to be added to the hydrodynamic force to obtain the total solution;
- The impulsive part of the hydrodynamic pressure: for this loading the methods of Westergaard or Housner can be used. As the hydrodynamic pressures are directly related to the acceleration of the gates they will be incorporated in the equation of motion of the gates as an added mass;
- The pressures due to surface waves: for the wave pressure a hydrostatic approach is used, meaning that a rise of the water level causes an additional pressure or vice versa. Pressures will be integrated over the water depth to obtain forces.
- Lastly, the earthquake exerts an inertia force on the gates. This force will be directly applied on the mass-spring system as an external loading.

The result of this approach is two load cases: the inertia force and the force due to surface waves. Because the model is linear, the total response can be found by superposition of the responses of the individual load cases.

### 6.2. Strategy

The following steps will be followed:

1. Derivation of the governing equation that describe the motion of the water and gates. A derivation of the shallow water equations and the wave equation is given in appendices B.3 and B.4. The derivation is based on [BATTJES, 2002a&b] and [HOLTHUIJSEN, 2007], the results (equations (B.43) and (B.46)) are repeated here as equations (6.1) and (6.2):

*Shallow water equations:*

$$\frac{\partial h}{\partial t} + \frac{\partial(hv)}{\partial x} = 0$$

$$\frac{\partial(hv)}{\partial t} + \frac{\partial(hv^2)}{\partial x} + gh \frac{\partial h}{\partial x} = 0$$
(6.1)

Wave equation:

$$\frac{\partial^2 h}{\partial t^2} - c_w^2 \frac{\partial^2 h}{\partial x^2} = 0 \tag{6.2}$$

in which:

$h$	=	total water level	[m]
$v$	=	horizontal flow velocity	[m/s]
$c_w$	=	wave speed defined as defined in equation (B.47) and (6.8)	[m/s]

2. Making the model: determining the coordinate system, domain and the required boundary and interface conditions (paragraph 6.3);
3. Identify forces and writing down equations of motion (paragraph 6.4);
4. Find the steady-state solution to the equations of motions (paragraph 6.5);
5. Derive the boundary and interface conditions (paragraph 6.6);
6. Apply the boundary and interface conditions to the equations of motion to find the unique solution to the problem. As the problem is defined linear, the solutions to the different loading can be evaluated separately. (paragraph 6.7 and appendix B.5);
7. With the solution known, plots and a conclusion can be made on the effect of surface waves (paragraphs 6.8 through 6.10).

### 6.3. The 1D model of a lock head

For the model an arbitrary lock head like the one in figure 6.1 is used as a basis for the model. Over one gate there is a hydraulic head; the water level between the two gates of a lock head is equal to the water level of the chamber upstream. The 1D model based on the situation of figure 6.1 is given in figure 6.2; it will be explained further on in this paragraph.

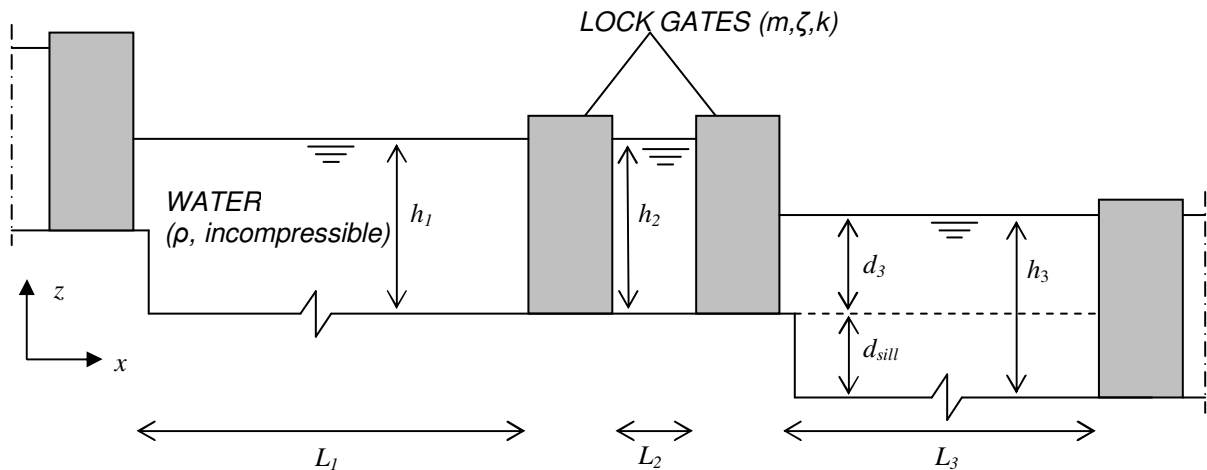


Figure 6.1 Sketch cross-section of an arbitrary lock head

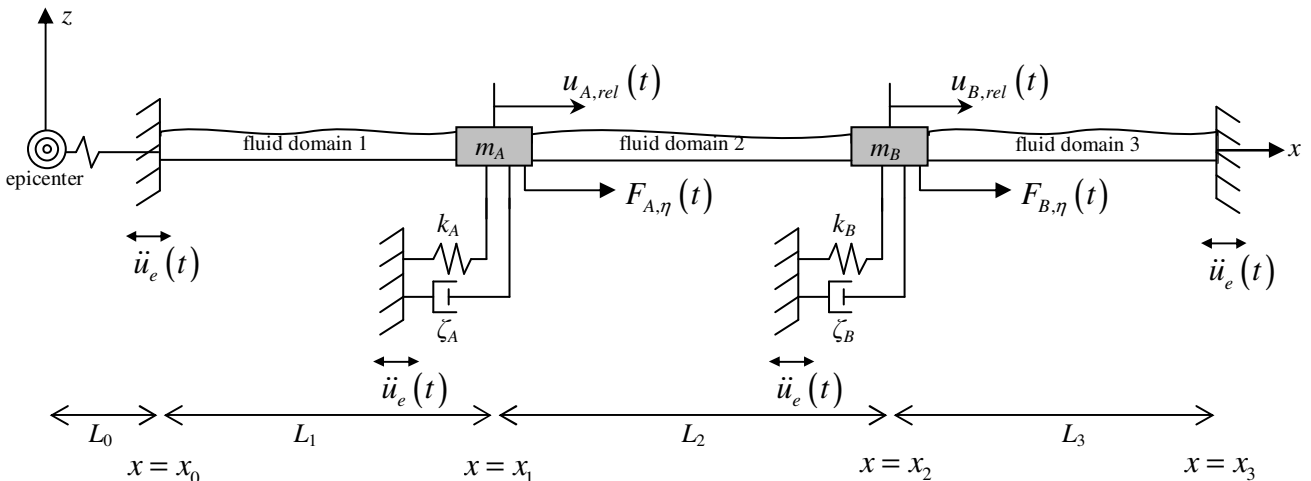


Figure 6.2 1D model of a lock head

Symbols used in figure 6.2:

$x, z$	=	coordinate system; the epicenter of the earthquake is taken as origin	[m]
$t$	=	time variable	[s]
$L$	=	distance	[m]
$u_{rel}$	=	displacement of gate A or B to the ground motion	[m]
$\ddot{u}_e$	=	earthquake ground acceleration	[m/s <sup>2</sup> ]
$F_\eta$	=	wave force on the gates A or B	[N]
$k$	=	spring stiffness of gate A or B	[N/m]
$\zeta$	=	damping ratio of gate A or B	[-]

The model will use two gates and three fluid domains:

1. Water in-between the two gates of a single lock head;
2. Water to the left side of the gates;
3. Water to the right side of the gates.

The latter two domains have a boundary at the gates at the other side of the lock chamber. These gates itself are not considered in the model. The two considered gates (named A and B) will be modeled with as a SDOF mass-spring system, with parameters mass  $m$ , damping ratio  $\zeta$  and spring constant  $k$ . The water in the three domains is modeled with the wave equation (6.2) and has a constant density  $\rho$ . The water level is split up into two parts: the still water level and the contribution due to surface waves:

$$h(x, t) = d + \eta(x, t) \quad (6.3)$$

in which:

$d$	=	still water level	[m]
$\eta$	=	amplitude of the surface elevation	[m]

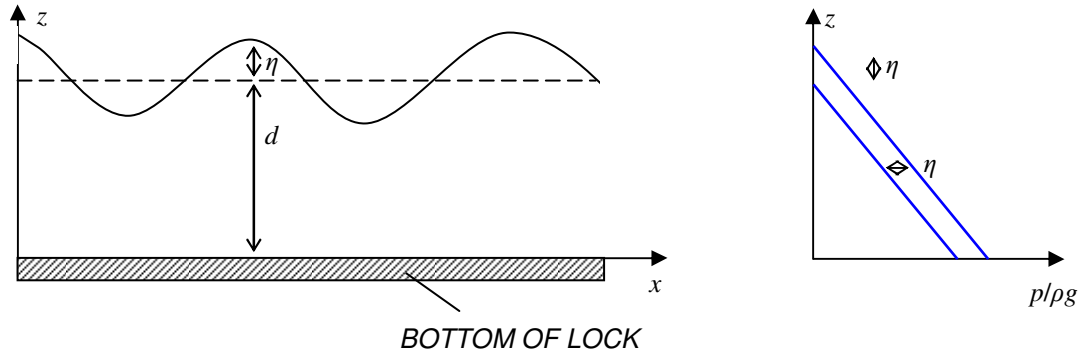


**Figure 6.3** Hydrostatic pressures and reference level

This leads to a constant hydrostatic pressure and an alternating wave pressure. The pressure distribution for the waves is also assumed to be hydrostatic, as shown in figure 6.3. According to the Coastal Engineering Manual [USACE, EM 1110-2-1100] this quasi-static assumption is valid for small wave heights. There are more advanced methods available for determining the quasi-static wave force on a vertical wall, e.g. Sainflou [MOLENAAR *et al.*, 2008; USACE, EM 1110-2-1100]. However, the quasi-hydrostatic approach follows directly from the definition used in equation (6.3) and gives an upper boundary value of the wave loading [MOLENAAR *et al.*, 2008]

The general formula for hydrostatic pressure follows from equation (B.32):

$$p = p_0 + \rho g (h - z) \quad (6.4)$$

$p_0$  (the atmospheric pressure) is taken equal to zero, the pressure on the gates therefore becomes:

$$p(x, z, t) = \rho g (h - z) = \rho g ((d + \eta) - z) \quad (6.5)$$

Integration of the pressure over the water depth leads to:

$$F_h(x, t) = \int_{z=0}^{z=d+\eta} p dz = \left[ \rho g (d + \eta) z - \frac{1}{2} \rho g z^2 \right]_0^{d+\eta} = \frac{1}{2} \rho g (d^2 + 2d\eta + \eta^2) \quad (6.6)$$

Linearization of equation (6.6) gives the hydrostatic and wave forces:

$$F_d = \frac{1}{2} \rho g d^2 \quad (6.7)$$

$$F_\eta(x, t) = \rho g d \eta(x, t)$$

in which:

$$\begin{aligned} F_d &= \text{the force due to hydrostatic pressure} \\ F_\eta &= \text{the linearized force due to surface waves} \end{aligned}$$

From figure 6.1 it shows that only the right gate has a static head difference. This means that on the left gates the resulting force due hydrostatic pressure is equal to zero. The wave speed for the three domains is based on the still water level. Note that for the third domain only the water above the sill level can react with the gate, but that for the wave speed the total water depth needs to be taken into account. The exact wave speed is a function of the total water level, but for small wave amplitudes the approximation in equation (6.8) can be used. This makes the wave speed a constant parameter:

$$c_w = \sqrt{gh} \approx \sqrt{gd} \quad (6.8)$$

Besides the earthquake induced wave forces also an inertia force is present. Therefore two dynamic forces are acting on the gates:

$$F_{tot}(t) = F_\eta(t) + F_e(t) \quad (6.9)$$

in which:

$$F_e(t) = \text{the inertia force on the gates}$$

In equation (6.9) the force due to the head difference has been omitted as it does not contribute to the dynamic behavior of gate B. The total displacement can therefore be found by adding the static displacement due to the head difference and the dynamic displacement together.

The total displacement of the gates consists out of two parts: the ground motion  $u_e$  and the motion of the gates relative the ground  $u_{rel}$ :

$$u_{rel} = u_{tot} - u_e \quad (6.10)$$

This is visualized in figure 6.4. The equation of motion for the based is based on the relative displacement to the ground; this way the displacement of the gates is corrected for the ground motion.

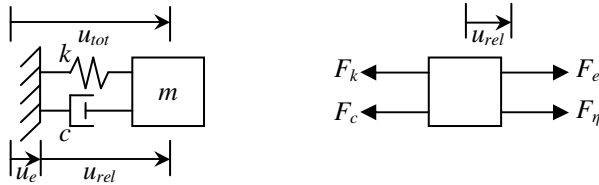


**Figure 6.4 SDOF mass-spring system**

Applying Newton's 2nd law on the SDOF mass-spring system for a displacement  $u_{rel}$  in the positive  $x$ -direction yields:

$$m\ddot{u}_{rel} = F_e + F_\eta - F_k - F_c \Rightarrow m\ddot{u}_{rel} + c\dot{u}_{rel} + ku_{rel} = F_e + F_\eta \quad (6.11)$$

The inertia force acts opposite to the gate motion and is therefore equal to:

$$F_e(t) = -m\ddot{u}_e(t) \quad (6.12)$$

At the boundaries the earthquake acceleration is directly applied.

Dividing equation (6.11) by the mass  $m$  leads to the following equation of motion:

$$\ddot{u}_{rel} + 2\zeta\omega_n\dot{u}_{rel} + \omega_n^2 u_{rel} = -\ddot{u}_e + f_\eta \quad (6.13)$$

in which:

$$\begin{aligned}
\omega_n &= \sqrt{\frac{k}{m}} \\
\zeta &= \frac{c}{c_{crit}} = \frac{c}{2\sqrt{km}} \\
\frac{c}{m} &= 2\zeta \frac{\sqrt{km}}{m} = 2\zeta\omega_n \\
f_\eta &= \frac{F_\eta}{m}
\end{aligned} \tag{6.14}$$

The value of  $\omega_n$  corresponds to the eigenfrequency of a gate;  $c_{crit}$  is called the critical damping and determines the damping behavior. The earthquake excitation is represented by a harmonic loading which can have the shape of a sine or a cosine:

$$\ddot{u}_e(t) = a \sin\left(\omega_e\left(t - \frac{x}{c_R}\right)\right) \quad \text{or} \quad \ddot{u}_e(t) = a \cos\left(\omega_e\left(t - \frac{x}{c_R}\right)\right) \tag{6.15}$$

in which:

$a$	=	(unit) acceleration	[m/s <sup>2</sup> ]
$\omega_e$	=	harmonic excitation frequency	[rad/s]
$c_R$	=	the celerity of Rayleigh waves	[m/s]

Because of the large dimensions of the new set of locks, it cannot be assumed that the earthquake excitation is equal for all parts of the lock structure. Therefore a phase-shift has been introduced, which takes into account the distance of the lock structure to the epicenter of the earthquake. Because the solution is sought in the frequency domain, the acceleration is set equal to 1 m/s for all frequencies. Equation (6.15) represents a harmonic loading, while an earthquake signal consists out of many harmonics. In figure 6.5 the procedure for finding the response by means of harmonics is explained:

- (a) Earthquake signal as input;
- (b) By means of a Fourier analysis the signal is transformed into a summation of harmonics or a spectrum;
- (c) A solution is obtained for a single harmonic or in the frequency domain;
- (d) A summation of these harmonics or an integration of the solution in the frequency domain over the spectrum gives a solution in the time domain;
- (e) This solution in the time domain is the response to the earthquake signal in (a).

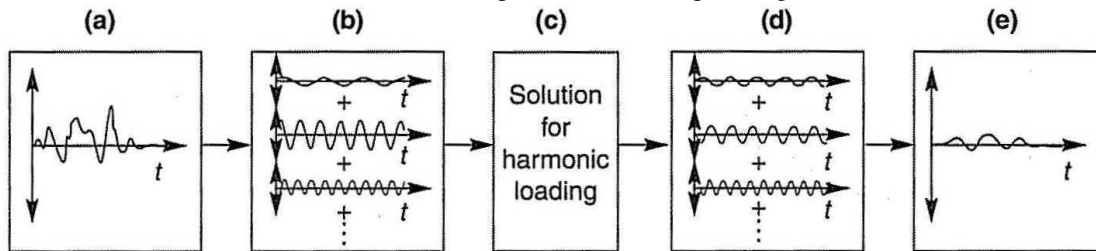


**Figure 6.5 Procedure for finding solution in the frequency and time domain (adapted from [KRAMER, 1996])**

By means of a spectral analysis the solution in the frequency domain can be transformed to the time domain. This procedure is not performed in this thesis.

For a frequency domain analysis it is convenient to work with complex<sup>8</sup> harmonics. For equation (6.15) this results in:

$$\ddot{u}_e(t) = ae^{i\omega_e\left(t - \frac{x}{c_R}\right)} = ae^{i\omega_e t} e^{-i\frac{\omega_e x}{c_R}} \tag{6.16}$$

<sup>8</sup> A (co)sine can be written in complex form with Euler's formula:  $e^{i\theta} = \cos \theta + i \sin \theta$ , where the real part corresponds to a cosine and the imaginary part to a sine

### 6.4. Equations of motion

The wave equation can be written in terms of the surface elevation by substituting equation (6.3) into equation (6.2). With all the equations of motion known, they can be specified for each fluid domain. As the hydrostatic forces are omitted, the equations of motions of both gates have the same shape and follow from equation (6.13). This figure also shows that a positive gate displacement causes wave forces in the negative  $x$ -direction. This leads to the following system of equations of motion:

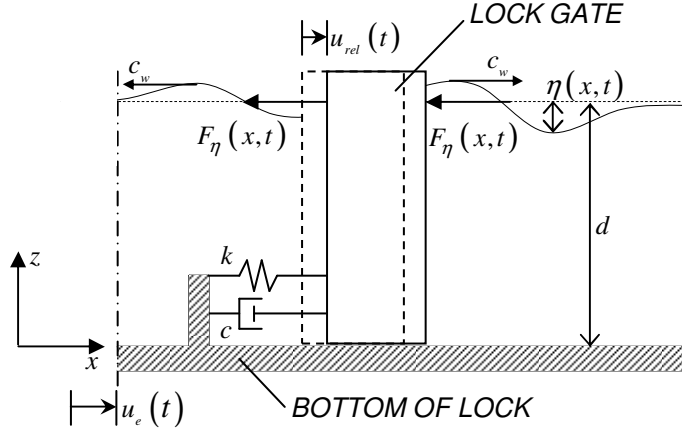


Figure 6.6 Situation at interface gate-water when gate moves in positive  $x$ -direction

Fluid domains:

$$\begin{aligned} \frac{\partial^2 \eta_1}{\partial t^2} - c_{w,1}^2 \frac{\partial^2 \eta_1}{\partial x^2} &= 0, & x_0 < x < x_1 \\ \frac{\partial^2 \eta_2}{\partial t^2} - c_{w,2}^2 \frac{\partial^2 \eta_2}{\partial x^2} &= 0, & x_1 < x < x_2 \\ \frac{\partial^2 \eta_3}{\partial t^2} - c_{w,3}^2 \frac{\partial^2 \eta_3}{\partial x^2} &= 0, & x_2 < x < x_3 \end{aligned} \quad (6.17)$$

Lock gates:

$$\begin{aligned} \ddot{u}_{A,rel} + 2\zeta\omega_{A,n}\dot{u}_{A,rel} + \omega_{A,n}^2 u_{A,rel} &= -\frac{\rho g}{m_A} \{d_1 \eta_1(x_1, t) + d_2 \eta_2(x_1, t)\} - a e^{i\omega_e t} e^{-i\frac{\omega_e x_1}{c_R}} \\ \ddot{u}_{B,rel} + 2\zeta\omega_{B,n}\dot{u}_{B,rel} + \omega_{B,n}^2 u_{B,rel} &= -\frac{\rho g}{m_B} \{d_2 \eta_2(x_2, t) + d_3 \eta_3(x_2, t)\} - a e^{i\omega_e t} e^{-i\frac{\omega_e x_2}{c_R}} \end{aligned} \quad (6.18)$$

in which the following data has been used:

- The damping ratios of both gates are equal;
- The epicenter of the earthquake is assumed to be at the upstream side at a distance  $L_0$ .

In order to find the steady-state solution to the system of equations (6.18), two boundary and four interface conditions will have to be applied to the steady-state solutions of the wave equations. Substituting of the results in the equations of motion of the gates yields the displacement of the gates. As the steady-state (particular) solutions are considered, the free vibrations of the gates (homogenous solutions) are disregarded. The free vibrations of the gates will disappear in time because of damping.

### 6.5. Steady-state solutions

For the steady-state solution to the wave equations in (6.17) the method of separation of variables is used. The steady-state solution will have the same complex form as the earthquake loading:

$$\eta_j(x, t) = \hat{H}_j(\omega_e, x) e^{i\omega_e t} \quad j = 1, 2, 3 \quad (6.19)$$

in which  $\hat{H}_j$  is the complex frequency response function for  $\eta$ . Substituting of equation (6.19) into the equations of motion leads to:

$$\hat{H}_j'' + \frac{\omega_e^2}{c_{w,j}^2} \hat{H}_j = 0 \quad (6.20)$$

Solving this 2<sup>nd</sup> order differential equation (6.20) gives:

$$\hat{H}_j(\omega_e, x) = A_j \cos\left(\frac{\omega_e x}{c_{w,j}}\right) + B_j \sin\left(\frac{\omega_e x}{c_{w,j}}\right) \quad (6.21)$$

in which  $A_j$  and  $B_j$  are (complex) constants.

Substituting this result back into equation (6.19) yields:

$$\eta_j(x, t) = \left( A_j \cos\left(\frac{\omega_e x}{c_{w,j}}\right) + B_j \sin\left(\frac{\omega_e x}{c_{w,j}}\right) \right) e^{i\omega_e t} \quad j = 1, 2, 3 \quad (6.22)$$

For the gates the same type of steady-state solution is used:

$$\begin{aligned} u_{A,rel}(t) &= \hat{U}_A e^{i\omega_e t} \\ u_{B,rel}(t) &= \hat{U}_B e^{i\omega_e t} \end{aligned} \quad (6.23)$$

where  $\hat{U}_A$  and  $\hat{U}_B$  are complex frequency response function for  $u_{A,rel}$  and  $u_{B,rel}$ .

## 6.6. Boundary conditions

At both boundaries, a boundary condition will have to be found. Analogously, at both sides of the gates a boundary condition will have to be found. They are all the same in these six positions in the sense that a movement of a gate causes a surface wave.

This relation can be found by a derivation from the momentum balance equation or directly from equation (B.23). The first approach will be used here; the linearized momentum balance equation (B.42) reads:

$$\frac{\partial(hv)}{\partial t} + gh \frac{\partial h}{\partial x} = 0 \quad (6.24)$$

With the substitution of equation (6.3), the momentum balance can be written in terms of  $\eta$ :

$$\frac{\partial}{\partial t}((d+\eta)v) + g(d+\eta) \frac{\partial}{\partial x}(d+\eta) = 0 \quad (6.25)$$

Elaboration gives:

$$d \frac{\partial v}{\partial t} + \eta \frac{\partial v}{\partial t} + v \frac{\partial \eta}{\partial t} + gd \frac{\partial \eta}{\partial x} + g\eta \frac{\partial \eta}{\partial x} = 0 \quad (6.26)$$

Again, neglecting the non-linear terms yields:

$$d \frac{\partial v}{\partial t} + gd \frac{\partial \eta}{\partial x} = 0 \quad \text{or} \quad \frac{\partial \eta}{\partial x} = -\frac{1}{g} \frac{\partial v}{\partial t} \quad (6.27)$$

At the position of the gates the compatibility conditions holds that the horizontal displacement of the fluid particles is equal to the horizontal displacement of the gate. This therefore also holds for the acceleration:

$$\frac{\partial \eta}{\partial x} = -\frac{1}{g} \frac{d^2 u_{tot}}{dt^2} = -\frac{1}{g} \ddot{u}_{tot} \quad (6.28)$$

Equation (6.28) is the required relation between gate movement and surface waves.

## 6.7. Applying boundary and interface conditions

As the model is defined linear, the responses to individual loading can be considered separately. The response to the wave forces only will be discussed in the next paragraph. The response to the inertia force only follows directly from the equation of motion. The combined solution is however large because of the dependence between gate motion and wave forces. For this reason the result is only visualized instead of listed. The procedure for finding the solution is treated in appendix B.5.

## 6.8. Solutions in the frequency domain

### 6.8.1. Solution to the wave equation only

The interaction between the two gates and three fluid domains leads to large and inconvenient solution, in which the effect of surface waves is difficult to recognize. For this purpose the case of a single chamber with rigid walls is considered. The equation of motion is the wave equation; the two boundary conditions are for this case:

$$\left. \frac{\partial \eta(x,t)}{\partial x} \right|_{x=0} = \left. \frac{\partial \eta(x,t)}{\partial x} \right|_{x=L} = -\frac{ae^{i\omega_e t}}{g} \quad (6.29)$$

Applied to equation (6.22) this leads to the following solution:

$$\eta(x,t) = -\frac{ac_w}{g\omega_e} \left\{ \frac{\left( \cos\left(\frac{\omega_e L}{c_w}\right) - 1 \right) \cos\left(\frac{\omega_e x}{c_w}\right) + \sin\left(\frac{\omega_e L}{c_w}\right) \sin\left(\frac{\omega_e x}{c_w}\right)}{\sin\left(\frac{\omega_e L}{c_w}\right)} \right\} e^{i\omega_e t} \quad (6.30)$$

This expression describes the state of the fluid under unit acceleration. The eigenfrequencies of the system follow from sine in the denominator:

$$\sin\left(\frac{\omega_e L}{c_w}\right) = 0 \Rightarrow \omega_n = k_n c_w = \frac{n\pi}{L} \sqrt{gd}, \quad n = 1, 2, \dots, \infty \quad (6.31)$$

with:

$$k_n = \frac{n\pi}{L}$$

in which:

$$k_n = \text{wavenumber} \quad [\text{m}^{-1}]$$

The eigenfrequencies are thus inversely proportional to the length and proportional to the water depth by square root. The modes shapes of the standing wave pattern can be found in figure 6.7. Only the odd eigenfrequencies cause sloshing: the even ones do not cause a pressure change at the location of the gates. The wavelengths follow from equation (6.32).

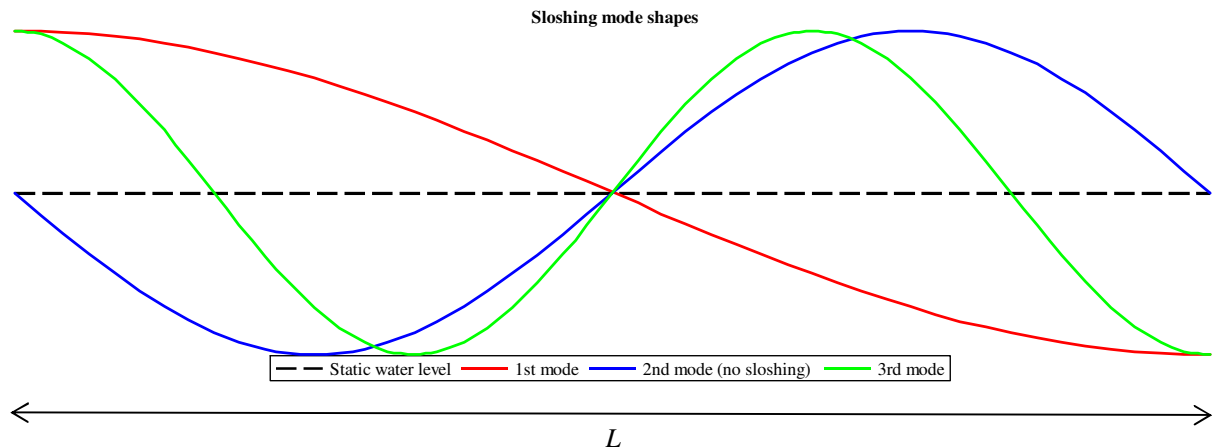


Figure 6.7 Modes shape for the first three eigenfrequencies

$$\lambda_n = \frac{2\pi}{k_n} = \frac{2L}{n} \quad (6.32)$$

in which:

$$\lambda_n = \text{wavelength} \quad [\text{m}]$$

From equation (6.32) follows the ratio between the wavelength and chamber length, this ratio is also visible in figure 6.7.

### 6.8.2. Response to inertia force

Disregarding the wave force in the equations of motion (6.18) results in:

$$\begin{aligned} \ddot{u}_{A,rel} + 2\zeta\omega_{A,n}\dot{u}_{A,rel} + \omega_{A,n}^2 u_{A,rel} &= -ae^{i\omega_e t} e^{-i\frac{\omega_e x_1}{c_R}} \\ \ddot{u}_{B,rel} + 2\zeta\omega_{B,n}\dot{u}_{B,rel} + \omega_{B,n}^2 u_{B,rel} &= -ae^{i\omega_e t} e^{-i\frac{\omega_e x_2}{c_R}} \end{aligned} \quad (6.33)$$

Substitution of the equation (6.23) into (6.33) leads to the following solution:

$$\begin{aligned} \hat{U}_A &= \frac{ae^{-i\frac{\omega_e x_1}{c_R}}}{\omega_e^2 - 2i\zeta\omega_{A,n}\omega_e - \omega_{A,n}^2} \\ \hat{U}_B &= \frac{ae^{-i\frac{\omega_e x_2}{c_R}}}{\omega_e^2 - 2i\zeta\omega_{B,n}\omega_e - \omega_{B,n}^2} \end{aligned} \quad (6.34)$$

The amplitude of the steady state vibrations follows from the modulus<sup>9</sup> of the complex amplitude.

## 6.9. Numeric values

Not all data is known, therefore some assumptions have been made for dimensions and masses.

### Fluid properties:

The water is assumed to be saline with a density of 1040 kg/m<sup>3</sup>.

### Lock dimensions

The lock dimensions given here are based on the distance between two gates and are therefore slightly larger than the real dimension of the lock chambers:

$$L_1 = 436 \text{ m}$$

$$L_2 = 14 \text{ m}$$

$$L_3 = 436 \text{ m}$$

The height of the sill is equal to 9 m.

### Water levels

The governing water levels for the lock head are:

$$d_1 = 30.87 \text{ m}$$

$$d_2 = 30.87 \text{ m}$$

$$d_3 = 15.24 \text{ m}$$

These water levels are relative to the bottom of the lock head, as depicted in figure 6.1.

<sup>9</sup> The modulus or absolute value of a complex number e.g.  $z$  follows from  $|z| = \sqrt{\text{Re}(z)^2 + \text{Im}(z)^2}$

Gate properties

The total mass of the gates consist out of:

- Dead weight of the steel structure (denoted as  $dw$ );
- Mass of water enclosed inside the gate or in buoyancy chambers ( $ew$ );
- Added water mass on the left, or upstream side of the gate ( $am, left$ );
- Added water mass on the right, or downstream side of the gate ( $am, right$ ).

Or, in formula:

$$m_j = m_{j,dw} + m_{j,ew} + m_{j,am,left} + m_{j,am,right} \quad j = A, B \quad (6.35)$$

The dead weight of a single gate is estimated to be in the order of 3000 t, which corresponds to 52 t per unit meter length of the gates. For the enclosed water it is assumed that the water level is 75% of the total gate height, this mass includes any mass inside the buoyancy chamber. This 75% results in a water mass of 248 t/m inside the lock gates. The sum of the dead load and enclosed water mass therefore is assumed to be 300 t/m.

The added water masses are calculated with the Housner method described in sections 4.7.2 and 4.7.3. From equation (4.19) follows the added mass for gates A and B:

$$m_{A,am,left} = 572.2 \text{ t/m}$$

$$m_{A,am,right} = 213.8 \text{ t/m}$$

$$m_{B,am,left} = 213.8 \text{ t/m}$$

$$m_{B,am,right} = 139.5 \text{ t/m}$$

It is known that the 1<sup>st</sup> eigenfrequency of gate B is equal to 10.2 rad/s. The 1<sup>st</sup> eigenmode results in the largest displacements normal to the face of the gates. The value is based on a total mass of the gate, including the added water mass component on both sides. With the assumed estimated total mass of gate B known a value of the spring stiffness  $k$  can be estimated as 68 MN/m. With this value the wet eigenfrequency of gate A is estimated to be 7.9 rad/s.

The damping ratio  $\zeta$  is taken equal to 2% for both gates to incorporate the effect of structural and hydrodynamic damping at the location of the gates.

In paragraph 3.3 it is mentioned that the wave speed of Rayleigh surface waves is about 90% of the S-wave speed. For the properties of the basalt bedrock this means a Rayleigh wave speed of about 1 km/s. The distance of the epicenter to the lock is incorporated in the model, but has minor influence as the phase different between the gate does remains the same. Because fault lines are located close the Pacific site, distance of 2.5 km is taken.

Summarized

$$\begin{aligned}
a &= 1 \text{ m/s}^2 \\
g &= 9.81 \text{ m/s}^2 \\
\rho &= 1040 \text{ kg/m}^3 \\
d_1 &= 30.87 \text{ m} \\
d_2 &= 30.87 \text{ m} \\
d_3 &= 15.24 \text{ m} \\
d_{sill} &= 9 \text{ m} \\
L_0 &= 2500 \text{ m} \\
L_1 &= 436 \text{ m} \\
L_2 &= 14 \text{ m} \\
L_3 &= 436 \text{ m} \\
m_A &= 1086 \text{ t/m} \\
m_B &= 653.3 \text{ t/m} \\
\omega_{A,n} &= 7.9 \text{ rad/s} \\
\omega_{B,n} &= 10.2 \text{ rad/s} \\
\zeta &= 2\% \\
c_R &= 1000 \text{ m/s}
\end{aligned} \tag{6.36}$$

**6.10. Conclusions 1D model for wave interaction**

In figures 6.8 and 6.9 the results of the 1D model are given: a wide frequency range from 0 to 15 rad/s and a detailed frequency range around the eigenfrequency of the gates.

From section 6.8.1 it is known that the interval between the different eigenfrequencies related to the wave forces are inversely proportional to the lock chamber length. This means that for chambers over 400 m long, the eigenfrequencies are very close to each other. This is clearly visible in the shape of the many spikes. Although the influence of the surface waves seems insignificant compared to the inertia force in terms of amplitude, the many eigenfrequencies may suggest otherwise.

The 1D model is a linear system with no damping in the fluid domains of the model. The motion of the fluid domains is described by the 1D wave equation, which is derived for small displacements. The large displacements at the eigenfrequencies are therefore in contradiction with the governing equation from which they are obtained. In reality such large water displacements do not occur for several reasons that are not incorporated in the model.

Therefore it must be concluded that the used 1D model is not well applicable for the problem. A non-linear model will most likely give more accurate results. With respect to obtained results, any amplitude larger than a certain value must be disregarded. Applied to the results, this would mean the response of the gates to wave loading is negligible. Higher amplitudes towards a frequency of 0 are the result of numerical errors.

The 1D model gives no conclusive to the state of the fluid under an earthquake, this as a result of the shortcomings of the model itself. The amplitude of the fluid and the wave corresponding forces are however very small compared to added mass component of hydrodynamic loading. The assumption of no surface waves is therefore valid for large lock structures.

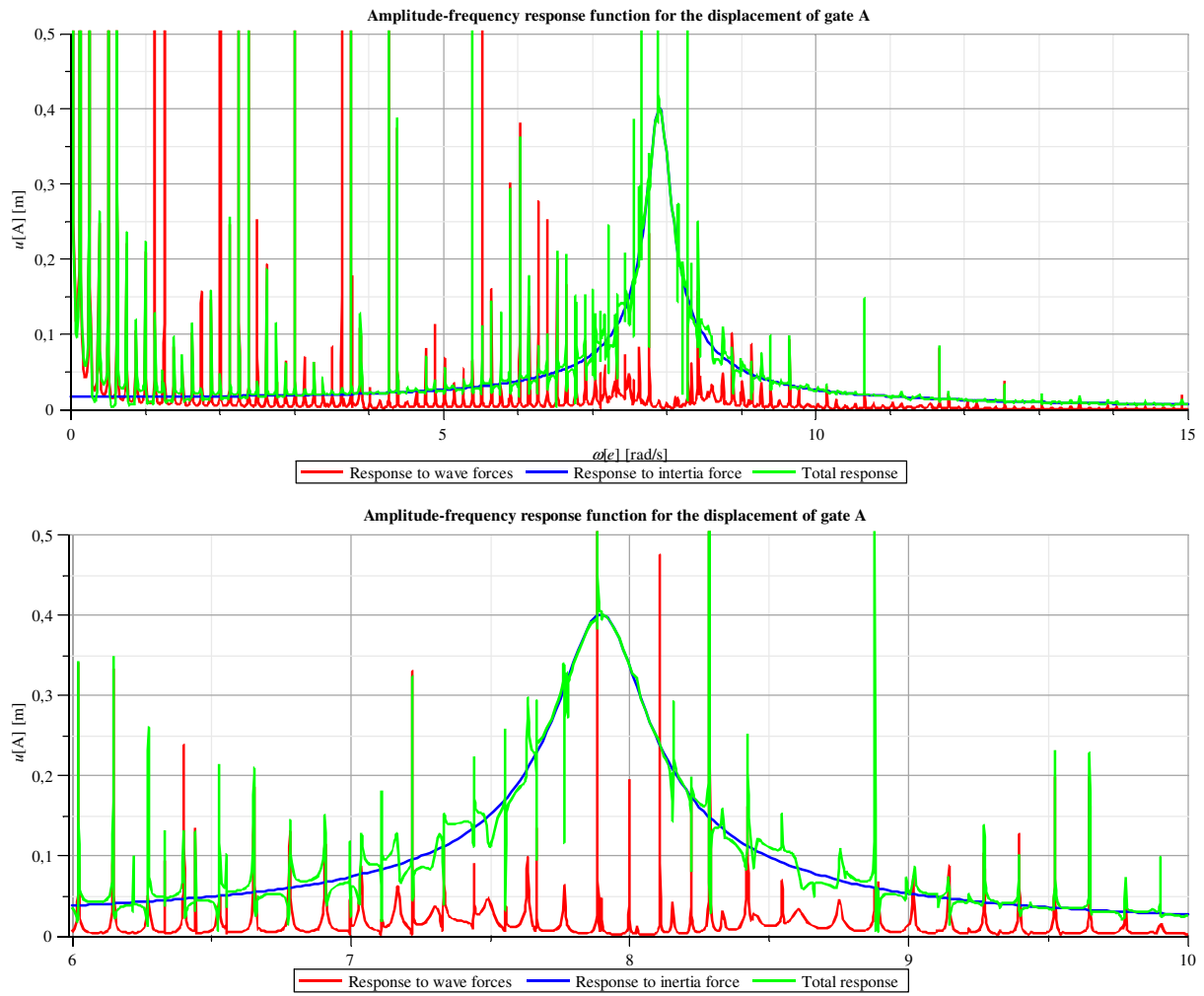
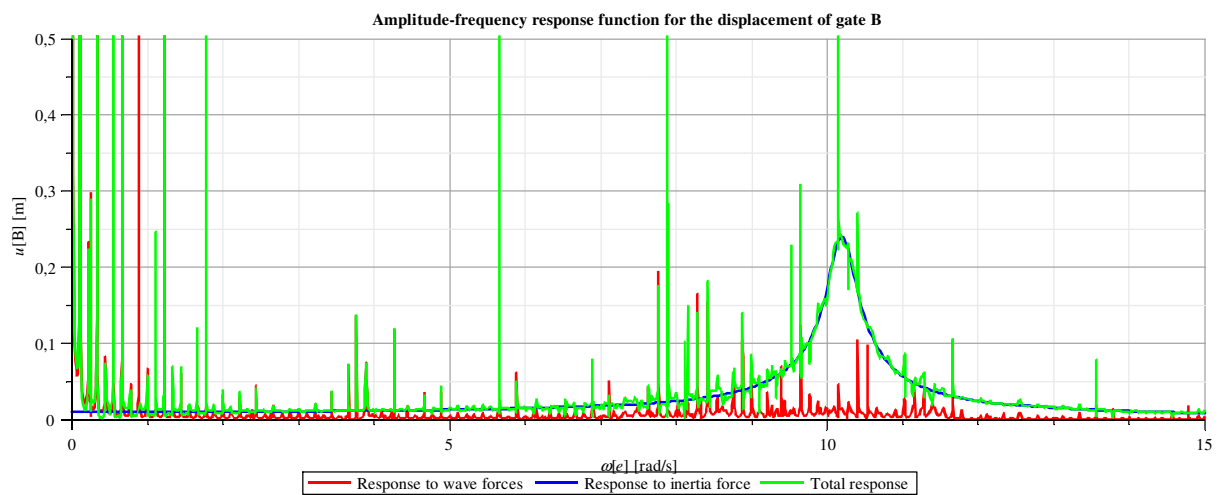
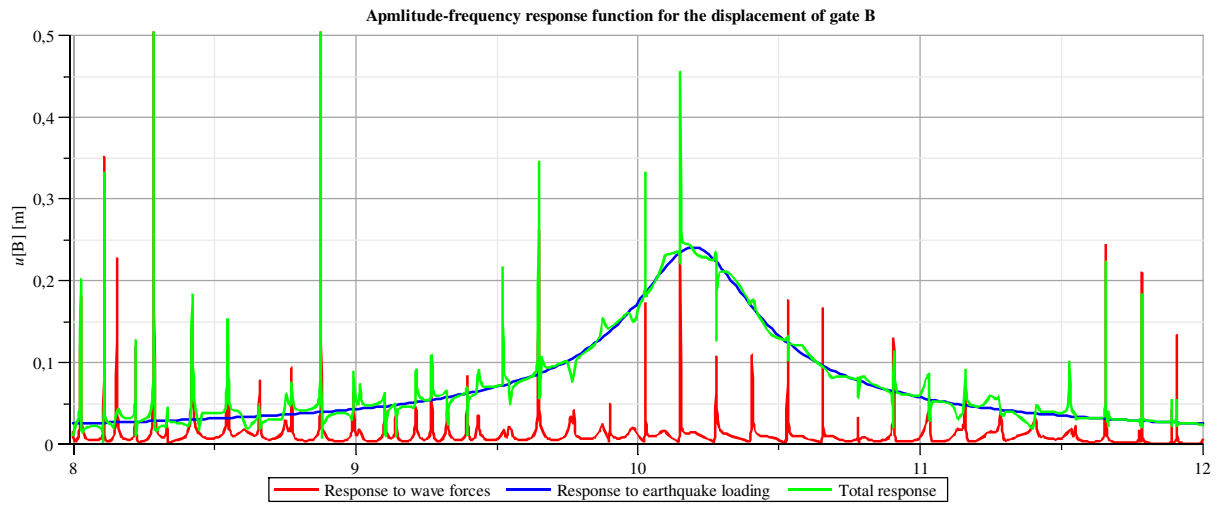


Figure 6.8 The frequency response of lock gate A under different components of loading, including detail





**Figure 6.9** The frequency response of lock gate B under different components of loading, including detail



## 7. Two-dimensional model for hydrodynamic pressure

### 7.1. Introduction 2D model

In the 1D model Housner's method is used to determine the hydrodynamic pressures as added mass. The effect of surface waves is considered separately. As stated before, both the Westergaard and Housner method are case specific and are originally not intended for usage with navigation locks but for large dams or fluid containers. Therefore a general derivation of hydrodynamic pressures is given, based on Westergaard's approach. He used two assumptions that are valid for large dams, these are:

- Situation is semi-infinite, the boundary at the other side of reservoir has no influence of the hydrodynamic pressure of the face of the dam;
- The effect of surface wave can be neglected.

In order to incorporate these effects, these two boundary conditions are altered so that they are more applicable to navigation locks:

- There is a moving gate/dam at the other side of the reservoir which moves which moves at the same frequency but with a phase shift relative to the other gate;
- The pressure at the still water surface is not zero, but equal to the wave induced pressure.

In order to simplify the analysis the water is assumed to be incompressible.

The other assumptions and boundary conditions will be the same:

- The gates have a vertical face;
- The gates are rigid, no stiffness is taken in account and therefore the acceleration along the face is constant;
- Only the horizontal component of the ground motion is considered.

The effect of surface waves is therefore included in the hydrodynamic pressure distribution. The results of a moving boundary at the other end of the reservoir leads to the reduced Westergaard formula as suggested by Brahtz and Heilbron. They assumed an identical earthquake motion and did not consider differences in amplitude, frequency or phase.

The governing equation is the 2D wave equation in terms of a velocity potential function or directly in terms of hydrodynamic pressure. The latter approach will be followed here. Both approaches use a single variable which is a function of  $x, z, t$ ; the horizontal and vertical displacements of fluid particles is incorporated in these variables.

### 7.2. Strategy

The following steps will be followed:

1. The hydrodynamic pressures on the gates will be calculated from the 2D wave equation, which is derived directly in terms of pressure. A derivation of the 2D wave equation is given in appendix B.6, the result is listed in equation (7.1):

*2D wave equation:*

$$\frac{\partial^2 p}{\partial x^2} + \frac{\partial^2 p}{\partial z^2} = \frac{1}{c_p^2} \frac{\partial^2 p}{\partial t^2} \quad (7.1)$$

2. In paragraph 7.3 the model is defined with the coordinate system, domain and required boundary conditions. The four boundary conditions required to solve equation (7.1) are derived here;
3. Find the steady-state solution to the governing equation (paragraph 7.5);
4. Apply the four boundary to the governing solution to find the specific steady-state solution for this case (paragraph 7.6 and appendix B.7);
5. With the substitution of the numerical values for the new canal locks (paragraph 7.7), the following aspects are treated in paragraph 7.8:
  - Hydrodynamic pressures on the bottom and top of the gates, for two chamber dimensions;
  - Hydrodynamic pressure for any lock chamber dimensions and the effect of phase delay;
  - Hydrodynamic pressure distributions along the face of a gate;
6. With the results known, a comparison between Westergaard's analytical result is made in paragraph 7.9;
7. Conclusions regarding the 2D analytical model are listed in paragraph 7.10.

### 7.3. 2D model and boundary conditions

For this model a single lock chamber is considered, no coupling between chambers, or gate dynamics. In order to solve the 2D wave equation four boundary conditions are necessary, two for the  $x$ -direction and two for the  $z$ -direction. Rigid boundaries are assumed, meaning that the  $x$ -coordinate of the boundaries along the face is constant in time. With a FEM discretization it is easier to incorporate the stiffness of the gates at the boundaries, than with an analytical approach. Therefore rigid gates will be used with the analytical approach, while the DIANA calculation will include both rigid and flexible gates. This way a direct comparison can be made between the analytical and FEM approach and the effect of flexible gates can be examined in DIANA. The DIANA calculation can be found in the next chapter.

If the compressibility of the fluid is taken into account the governing equation is the 2D wave equation. Without compressibility effects the governing equation reduces to the 2D Laplace equation:

$$\text{Compressible fluid: } \frac{\partial^2 p}{\partial x^2} + \frac{\partial^2 p}{\partial z^2} = \frac{1}{c_p^2} \frac{\partial^2 p}{\partial t^2} \quad (7.2)$$

$$\text{Incompressible fluid: } \frac{\partial^2 p}{\partial x^2} + \frac{\partial^2 p}{\partial z^2} = 0 \quad (7.3)$$

From equation (7.2) it can be seen that compressibility only has an effect for high frequencies, therefore it is disregarded for now.

The boundary conditions at  $x = 0$  and  $x = L$  have the same form as for the 1D model, but are now expressed in terms of the hydrodynamic pressure. Only the horizontal component of the earthquake will be considered. From equation (B.49) follows:

$$\frac{\partial p}{\partial x} = -\rho \frac{\partial v_x}{\partial t} \quad (7.4)$$

With the use of the compatibility condition at the positions of the gates, equation (7.4) can be written as:

$$\frac{\partial p}{\partial x} = -\rho \frac{\partial v_x}{\partial t} = -\rho \ddot{u}_{gate} \quad (7.5)$$

In the 1D model vertical fluid accelerations were disregarded. For the 2D situation they need to be specified by boundary conditions at the bottom the lock and at the surface water level. A rigid bottom of concrete or bedrock means that the vertical velocity is equal to zero, from equation (B.50) therefore follows:

$$\left. \frac{\partial p}{\partial z} \right|_{z=0} = 0$$

The boundary conditions at the surface level would be that the hydrodynamic pressure is zero if surface waves are neglected. Although the 1D model shows that this assumption is justified for the considered dimensions, the effect will be taken into account here. From figure 6.3 and equation (6.4) it shows that the pressure at the surface ( $z = d$ ) is equal to:

$$p = \rho g \eta \quad (7.6)$$

The vertical acceleration at  $z = d$  is therefore equal to:

$$\frac{\partial^2 \eta}{\partial t^2} = \frac{\partial v_z}{\partial t} = \frac{1}{\rho g} \frac{\partial^2 p}{\partial t^2} \quad (7.7)$$

Combining equation (7.7) with equation (B.50) yields:

$$\frac{\partial p}{\partial z} = -\frac{1}{g} \frac{\partial^2 p}{\partial t^2} \quad (7.8)$$

which is the free surface condition according to the linear wave theory.

The four boundary conditions are summarized in equation (7.9) and figure 7.1.

$$\begin{aligned}
\left. \frac{\partial p}{\partial x} \right|_{x=0} &= -\rho \ddot{u}_A \\
\left. \frac{\partial p}{\partial x} \right|_{x=L} &= -\rho \ddot{u}_B \\
\left. \frac{\partial p}{\partial z} \right|_{z=0} &= 0 \\
\left. \frac{\partial p}{\partial z} \right|_{z=d} &= -\frac{1}{g} \frac{\partial^2 p}{\partial t^2} \Big|_{z=d}
\end{aligned} \tag{7.9}$$

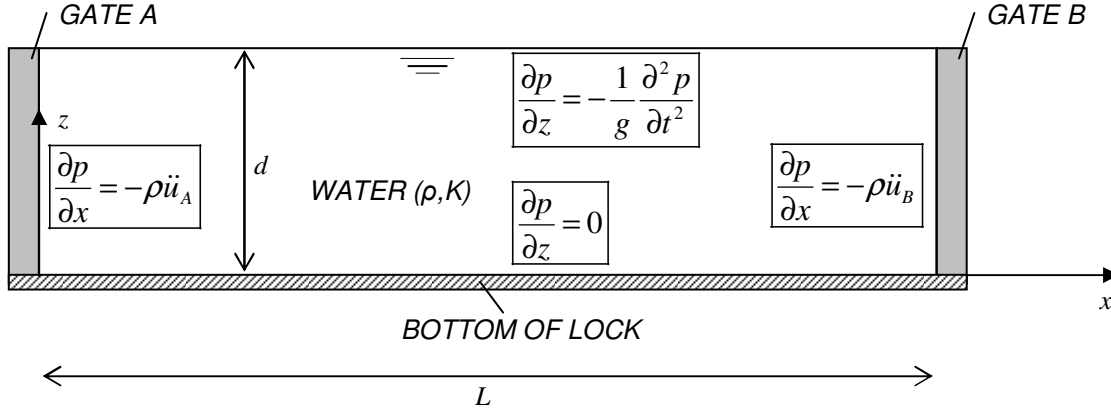


Figure 7.1 2D model for hydrodynamic pressures, with boundary conditions

#### 7.4. Eigenfrequencies of the system

In order to find the eigenfrequencies of the system, in the case of an incompressible fluid, a homogeneous solution is to be found. To do so, the forcing terms in the boundary condition are removed. The first two boundary conditions in equation (7.9) now read:

$$\left. \frac{\partial p}{\partial x} \right|_{x=0} = \left. \frac{\partial p}{\partial x} \right|_{x=L} = 0 \tag{7.10}$$

By means of the method of separation of variables the eigenfrequencies of the system are derived. The procedure is treated in appendix B7.1. The result from equation (B.66) is repeated in equation (7.11)

$$\omega_n^2 = k_n g \tanh(k_n d) = \frac{n\pi}{L} g \tanh\left(\frac{n\pi}{L} d\right), \quad n = 1, 2, \dots, \infty \tag{7.11}$$

In the case of shallow water,  $d \ll L$ , this expression reduces to:

$$\omega_n^2 = \frac{n\pi}{L} g \tanh\left(\frac{n\pi}{L} d\right) \stackrel{d \ll L}{\approx} \frac{n^2 \pi^2}{L^2} g d \tag{7.12}$$

The eigenfrequencies are in this case equal to:

$$\omega_n = \frac{n\pi}{L} \sqrt{gd} \tag{7.13}$$

which is the same result as found with the 1D model, equation (6.31).

Rewriting the sloshing frequencies according to Housner<sup>10</sup> in equation (4.12) in terms of angular frequency results in:

<sup>10</sup> Note that Housner uses  $2L$  to describe the length of the chamber; in equation (7.14) this is adapted to  $L$  to match the definition used in this chapter.

$$\omega_n^2 = \sqrt{10} \frac{n}{L} g \tanh\left(\sqrt{10} \frac{n}{L} d\right) \quad (7.14)$$

With  $\sqrt{10} \approx 3.16$  and  $\pi \approx 3.14$ , the results from the 2D model and Housner give approximately the same result.

### 7.5. Steady-state solution

Because of the rectangular fluid domain and constant boundary conditions along the edges, the problem can be solved by using the method of separation of variables. For the solution the same approach will be followed as with the 1D model: a steady-state solution in the complex frequency domain, where the real part of the solution corresponds to a cosine shaped loading and the imaginary part to a sine shaped loading. As it concerns a solution in the frequency domain, a unit acceleration  $a$  of  $1 \text{ m/s}^2$  for all frequencies is used. The horizontal earthquake excitations at gates A and B are therefore written as:

$$\begin{aligned} \ddot{u}_A(t) &= a e^{i\omega_e t} \\ \ddot{u}_B(t) &= a e^{i\omega_e t} e^{-i\varphi} \end{aligned} \quad (7.15)$$

in which  $\varphi$  is the phase-delay between the two gates, originating from the source in the negative  $x$ -domain, defined as:

$$\varphi = \frac{\omega_e L}{c_R} \quad (7.16)$$

The solution to equation (7.3) is sought in the form of:

$$p(x, z, t) = \hat{P}(x, z, \omega_e) e^{i\omega_e t} \quad (7.17)$$

in which  $\hat{P}$  is the complex frequency response function for the hydrodynamic pressure  $p$ .

The procedure to find the steady-state solution to equation (7.3) by means to the boundary conditions in equation (7.9) is described in appendix B7.2.

### 7.6. Solution in the frequency domain

In appendix B7.2 the steady-state solution is found for the Laplace equation (7.3) with respect to the boundary conditions in equation (7.9). The result of equation (B.79) is repeated here as equation (7.18):

$$\begin{aligned} p(x, z, t) &= \left\{ \sum_{n=0}^{\infty} B_n \cos(k_n x) \cosh(k_n z) + c_1 x + c_2 (x^2 - z^2) \right\} e^{i\omega_e t} \\ B_0 &= -c_1 \frac{L}{2} - c_2 \left( \frac{2gd}{\omega_e^2} + \frac{L^2}{3} - d^2 \right) \\ B_n &= \frac{2L}{n^2 \pi^2} \frac{c_1 (1 + (-1)^{n-1}) - 2c_2 L (-1)^n}{\cosh(k_n d) - k_n \sinh(k_n d) \frac{g}{\omega_e^2}}, \quad n = 1, 2, \dots, \infty \\ k_n &= \frac{n\pi}{L} \\ c_1 &= -\rho a \\ c_2 &= \frac{\rho a}{2L} (1 - e^{-i\varphi}) \\ \varphi &= \frac{\omega_e L}{c_R} \end{aligned} \quad (7.18)$$

This solution is without compressibility, hence the only eigenfrequencies present result from resonance due to the chamber length. To look more closely to this resonance effect, two specifics about this solution cases are treated

in detail: the influence of the phase-shift between the two boundaries and the effect of the surface waves. These last two effects are not treated in the Housner and Westergaard/Brahtz/Heilbron solutions. First numeric values are introduced to visualize the solution.

### 7.7. Numeric values

The same numerical values will be used as in chapters 5 and the 1D model. For the reader's convenience they are repeated here:

$$\begin{aligned}
 a &= 1 \text{ m/s}^2 \\
 \rho &= 1040 \text{ kg/m}^3 \\
 g &= 9.81 \text{ m/s}^2 \\
 d &= 30 \text{ m} \\
 L_{\text{chamber, long}} &= 436 \text{ m} \\
 L_{\text{chamber, short}} &= 14 \text{ m} \\
 c_R &= 1000 \text{ m/s}
 \end{aligned}
 \tag{7.19}$$

### 7.8. Frequency domain results of the 2D model

The following results are obtained from the solution in equation (7.18):

- Amplitude-frequency response function for the hydrodynamic pressure at the bottom of the gate;
- Amplitude-frequency response function for the hydrodynamic pressure at the top of the gate, case with surface waves only;
- Pressure distributions along the face of the gate for certain frequencies.

The following special cases that may or may not have an influence on the hydrodynamic pressure distribution are treated in detail:

- The effect of surface waves;
- The effect of a phase difference between the two boundaries;
- The effect of compressibility.

The above results are presented for two treated lock chamber dimensions: the large lock chamber of 436 m and short chamber of 14 m. When possible, results are also given for arbitrary dimensions.

#### 7.8.1. Eigenfrequencies

In table 5.1 the first 25 eigenfrequencies  $\omega_n$  are calculated by means of equation (7.11) for a depth of 30 m and the two length dimensions, 436 m and 14 m.

First 25 eigenfrequencies (situation long lock chamber) [rad/s]				
0.123	0.240	0.348	0.444	0.530
0.604	0.670	0.729	0.781	0.830
0.874	0.916	0.955	0.992	1.028
1.062	1.095	1.128	1.159	1.189
1.218	1.247	1.275	1.302	1.329

**Table 7.1.a First 25 eigenfrequencies for the long lock chamber**

First 25 eigenfrequencies (situation shorter intermediate chamber) [rad/s]				
1.484	2.098	2.570	2.967	3.318
3.634	3.925	4.197	4.451	4.692
4.921	5.140	5.350	5.551	5.746
5.935	6.117	6.295	6.467	6.635
6.799	6.959	7.116	7.269	7.418

**Table 7.1.b First 25 eigenfrequencies for the shorter intermediate chamber**

### 7.8.2. Hydrodynamic pressure at bottom of gate (situation long lock chamber)

This section treats the hydrodynamic pressure at coordinate (0;0) for excitation frequencies from 0 to 2.5 rad/s. This corresponds only to the lower end of the spectrum, but the result does not change for higher frequencies. This can be seen in figure 7.2. There are indeed eigenfrequencies, but the width of the peak is negligible. The results are given with and without the phase shift. The same values are obtained; the only difference is that in the case of a phase shift there are more peaks. Without a phase shift, only the odd eigenfrequencies are visible. This is a result of the odd constants  $B_n$  in equation (7.18) being zero. A similar result is obtained for the 1D model, where it is visualized in figure 6.7.

The given values are magnitudes, calculated as the absolute values of the pressure, unless stated otherwise.

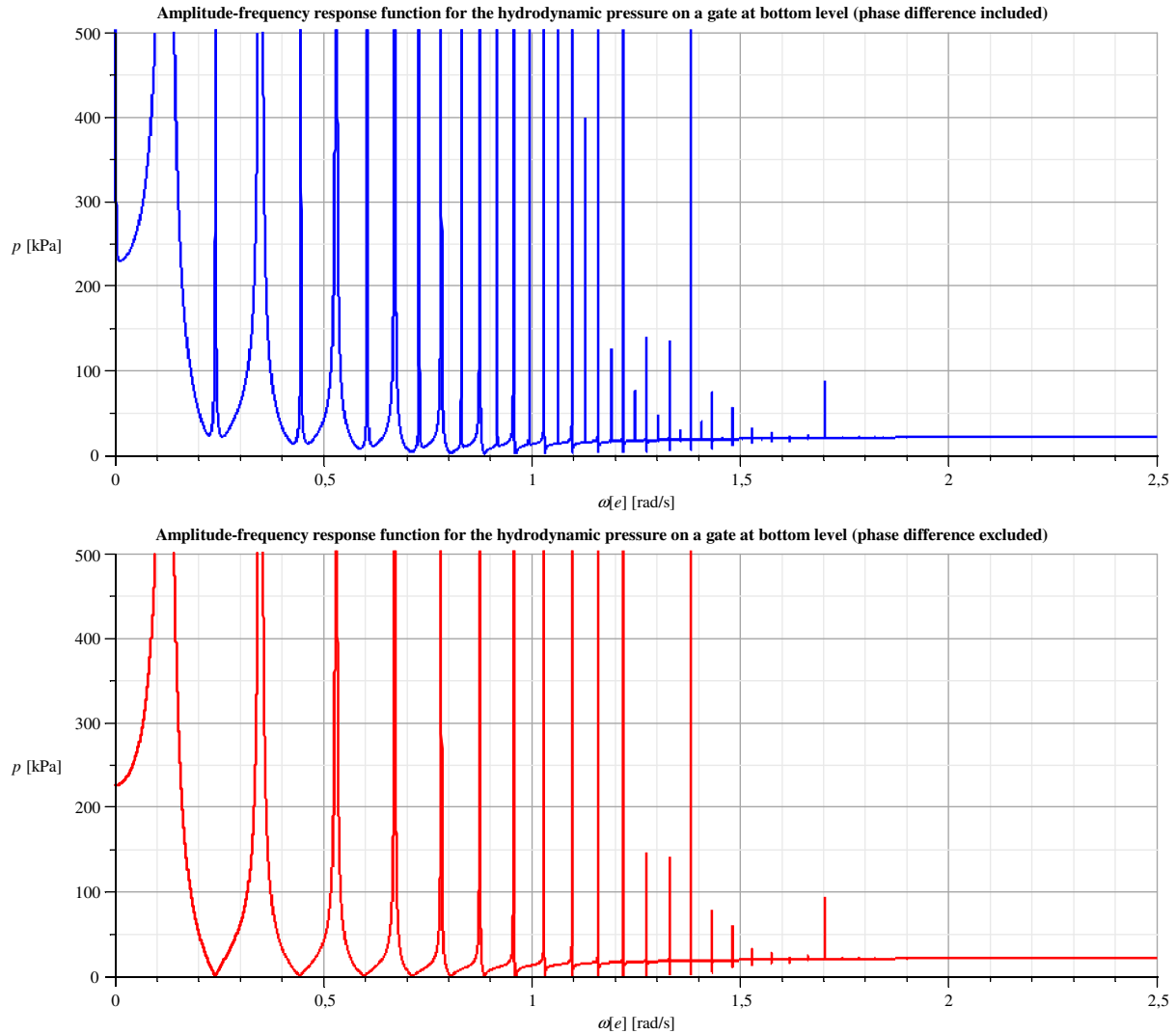
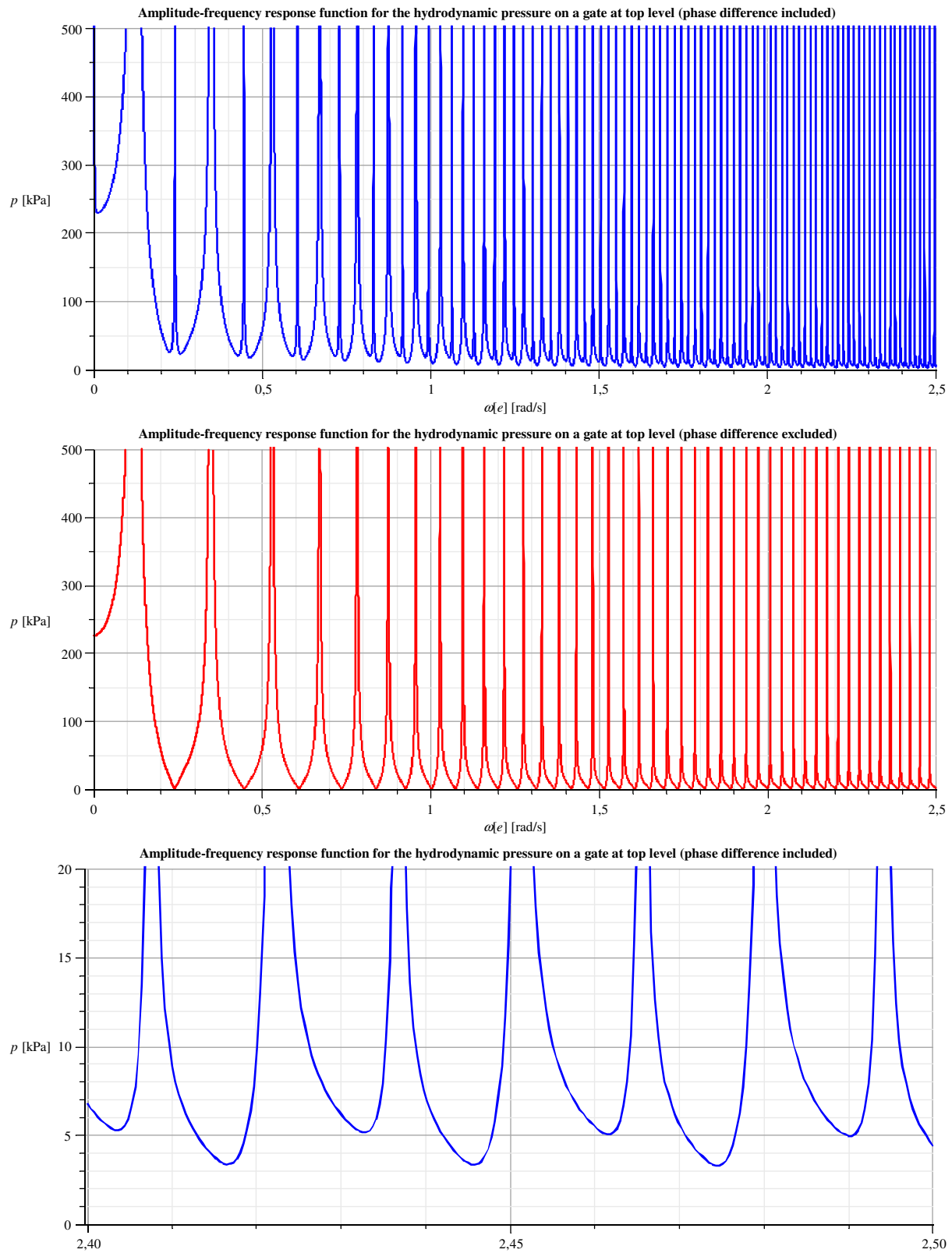


Figure 7.2 Hydrodynamic pressures: with (top) and without (bottom) phase difference between the gates

### 7.8.3. Hydrodynamic pressure at top of gate (situation long lock chamber)

At the top of the gates, at coordinate (0;d), a similar result can be observed. As a result of the used boundary condition, the pressure is not zero like in Westergaard's approach. Instead, there is a pressure with the same eigenfrequencies as at the bottom. These pressures are quite high and are a result of the used governing equation and boundary conditions. A pressure of 10 kPa would correspond to a wave amplitude of 1 m. The reliability of this result is discussed in the conclusion in section 7.10.



**Figure 7.3 Hydrodynamic pressures: with (top), without (center) phase difference between the gates and detail (bottom)**

#### 7.8.4. Hydrodynamic pressure at bottom of gate (situation shorter intermediate chamber)

Unlike with the large lock chamber, only the fundamental eigenfrequency is visible for the first 10 rad/s. This frequency-independent results from the low  $L/d$  ratio and indicates impulsive behavior. Because of the short distance between the gates, the phase difference causes an increase in pressure for higher frequencies.

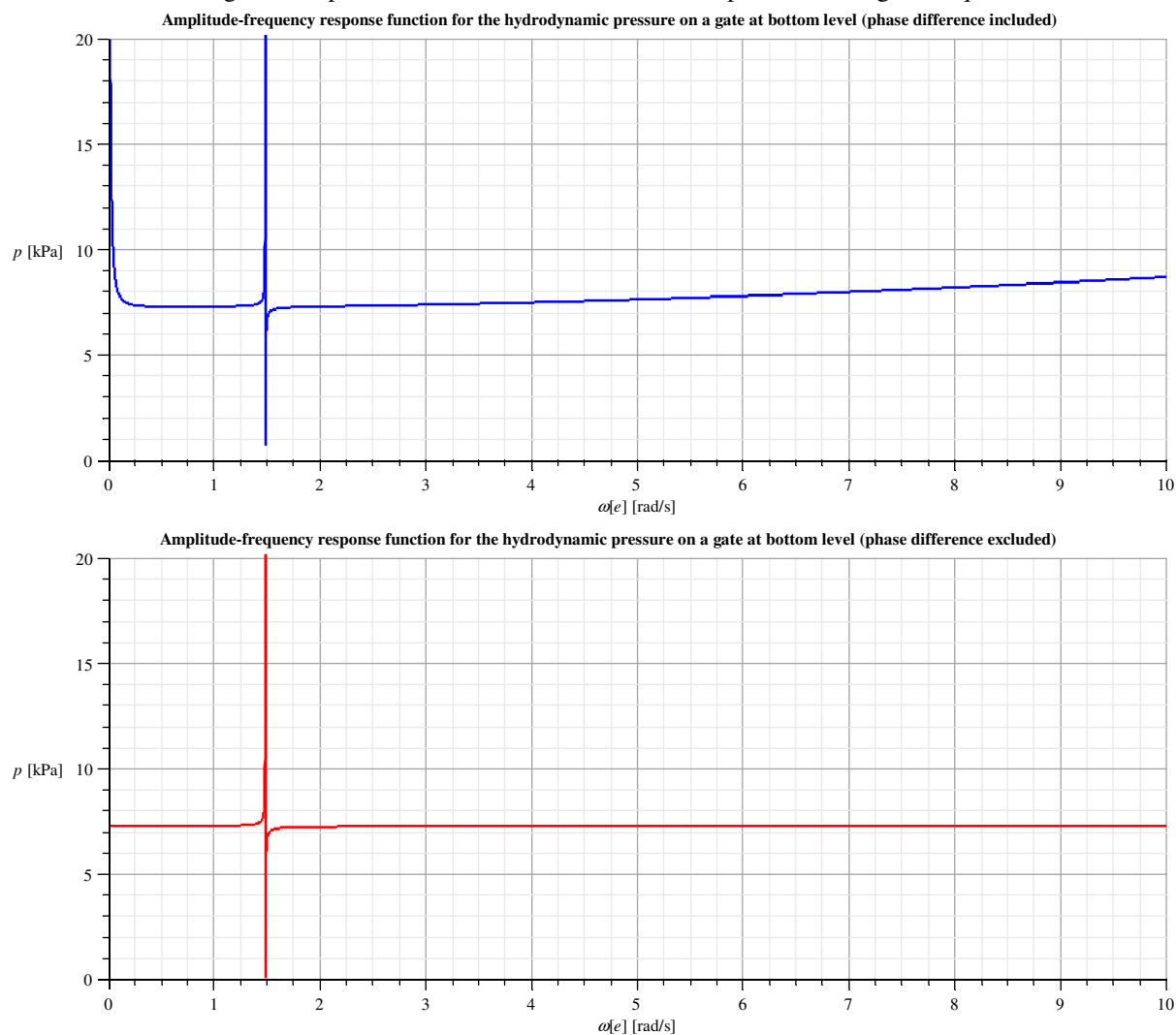


Figure 7.4 Hydrodynamic pressures, with (top) and without (bottom) a phase difference between the gates

#### 7.8.5. Hydrodynamic pressure at top of gate (situation shorter intermediate chamber)

At the top of the gate the same frequency behavior can be observed as with the large lock chamber. The amplitudes are however much smaller.

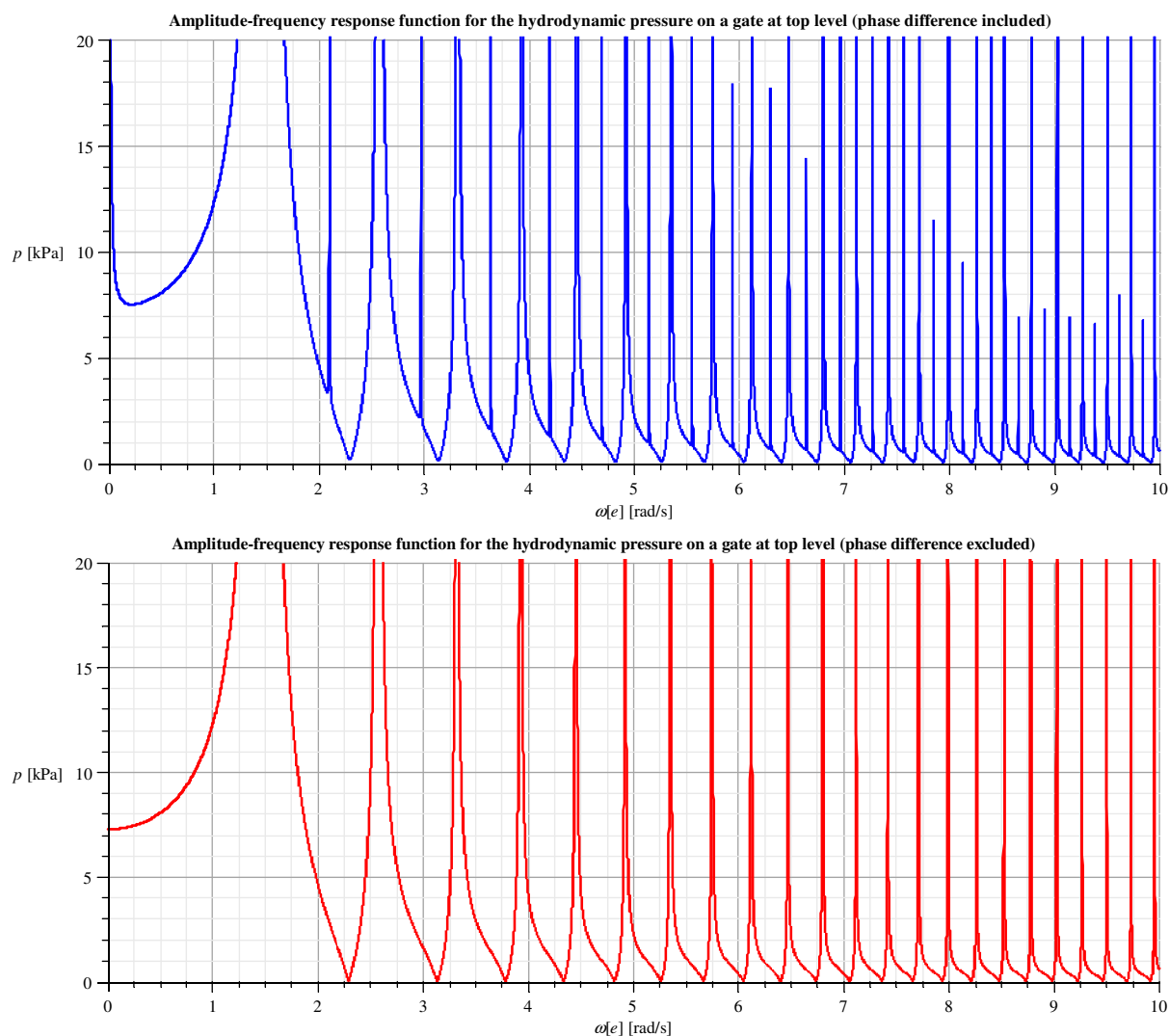


Figure 7.5 Hydrodynamic pressures, with (top) and without (bottom) a phase difference between the gates

### 7.8.6. Hydrodynamic pressure along the face of the gate (situation long lock chamber)

In the previous sections the maximum pressures at the top and bottom of the gate in the frequency domain has been discussed. This section treats the pressure distribution along the face of the gate at certain frequencies which can be found in table 7.2. The frequencies are mainly for the lower part of the spectrum; figure 7.2 shows no change for higher frequencies. Figure 7.9 shows the hydrodynamic pressure distribution at about half the value of the fundamental eigenfrequency related to compressibility from equation (4.7). The graphs are drawn up for  $x = 0$ . The pressure distributions show both the real and the imaginary part of equation (7.18).

Figure	Excitation frequency $\omega_e$ [rad/s]	Excitation frequency $f_e$ [Hz/s]	Excitation period $T_e$ [s]
Figure 7.6	0.63	0.1	10
Figure 7.7	2.51	0.4	2.5
Figure 7.8	6.28	1	1
Figure 7.9	37.70	6	0.67

Table 7.2 Selected excitation frequencies with corresponding figures (situation long lock chamber)

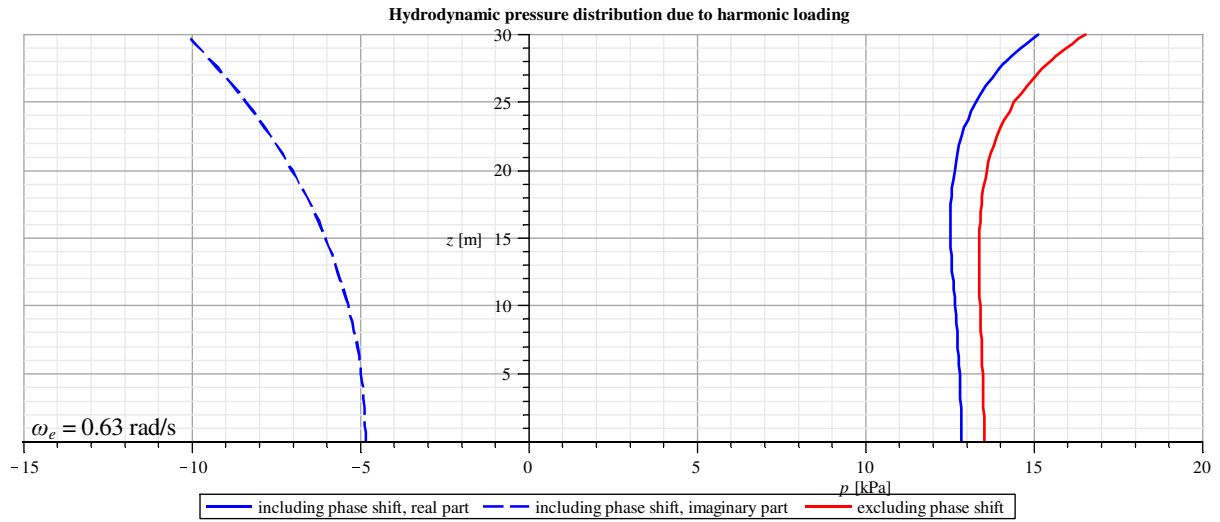


Figure 7.6 Hydrodynamic pressure distribution at  $\omega_e \approx 0.63$  rad/s (0.1 Hz)

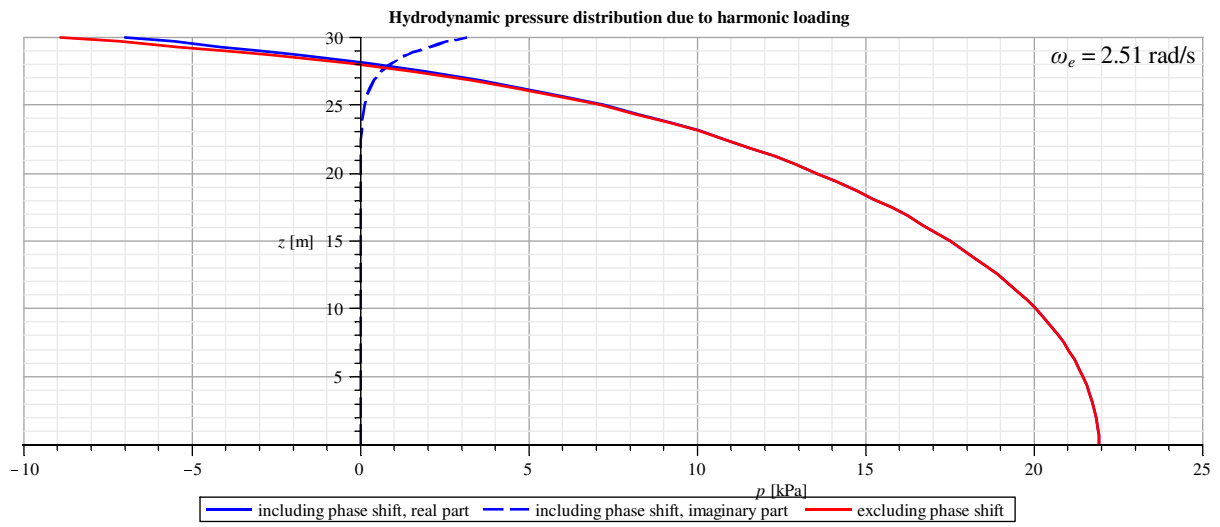


Figure 7.7 Hydrodynamic pressure distribution at  $\omega_e \approx 2.51$  rad/s (0.4 Hz)

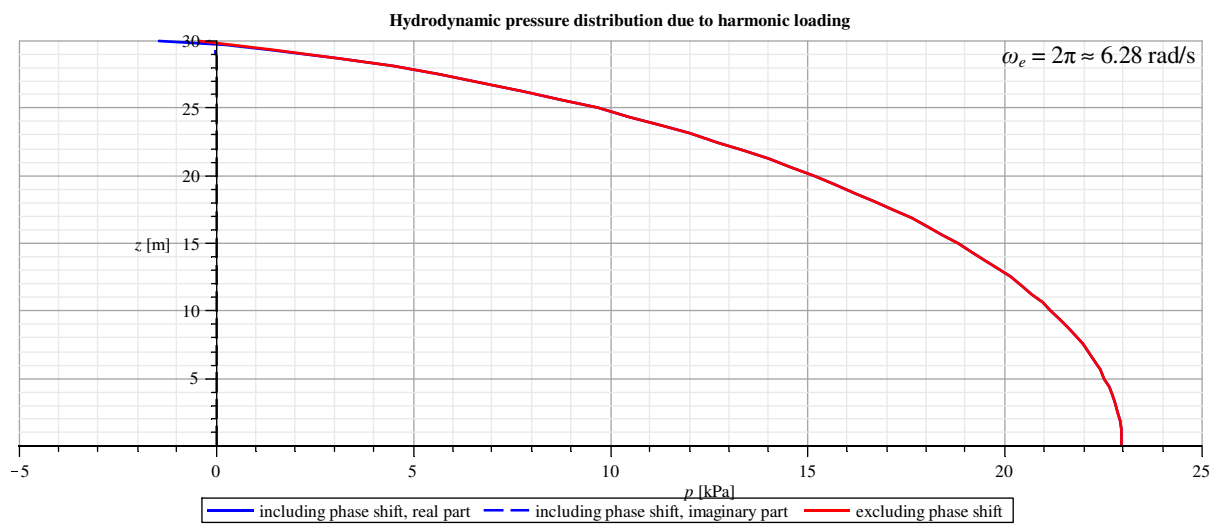


Figure 7.8 Hydrodynamic pressure distribution at  $\omega_e \approx 6.28$  rad/s (1 Hz)

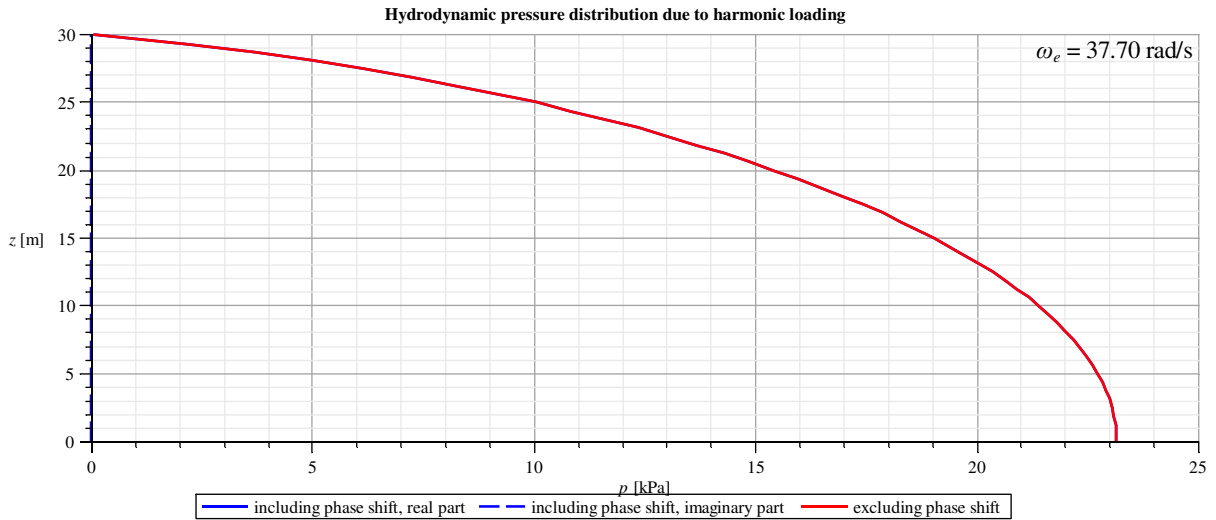


Figure 7.9 Hydrodynamic pressure distribution at  $\omega_e \approx 37.70$  rad/s (6 Hz)

As a result of the high wave pressures at the top of the gate for low frequencies, the pressure distribution for  $\omega_e \approx 0.63$  rad/s is not parabolic anymore: the pressure at the top is even larger than at the bottom of the gate. For higher frequencies the pressure distribution is parabolic with a small wave pressure at the top. At these frequencies a phase difference does not influence the pressure distribution on the gates.

**7.8.7. Hydrodynamic pressure along the face of the gate (situation shorter intermediate chamber)**

For the shorter intermediate chamber of a lock head the same procedure has been followed as the last section, the only difference being the length coordinate. The same frequencies have been used, corresponding figures can be found in table 7.3.

Figure	Excitation frequency $\omega_e$ [rad/s]	Excitation frequency $f_e$ [Hz/s]	Excitation period $T_e$ [s]
Figure 7.10	0.63	0.1	10
Figure 7.11	2.51	0.4	2.5
Figure 7.12	6.28	1	1
Figure 7.13	37.70	6	0.67

Table 7.3 Selected excitation frequencies with corresponding figures (situation shorter intermediate chamber)

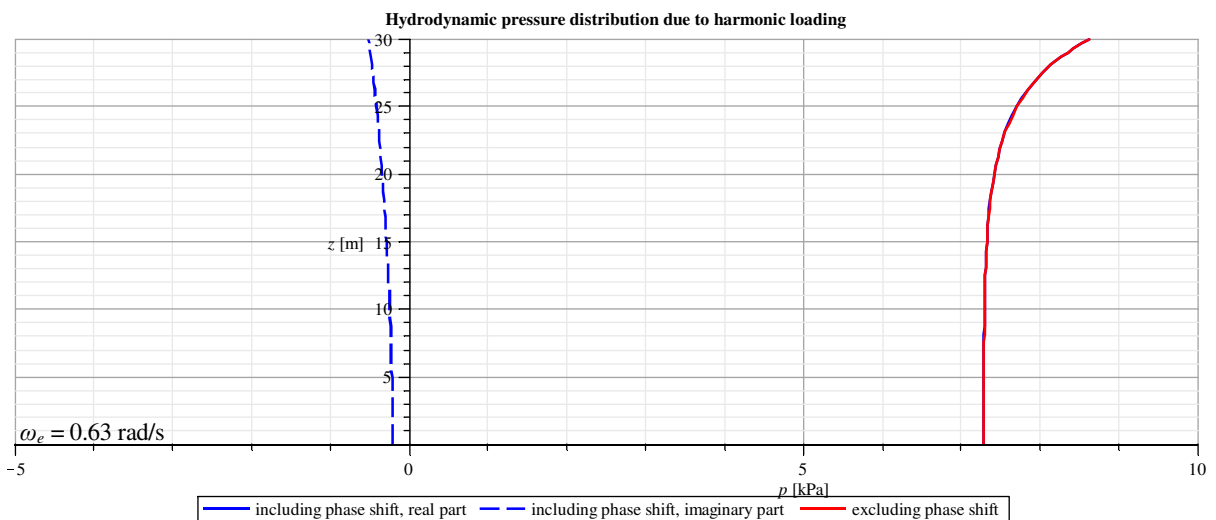


Figure 7.10 Hydrodynamic pressure distribution at  $\omega_e \approx 0.63$  rad/s (0.1 Hz)

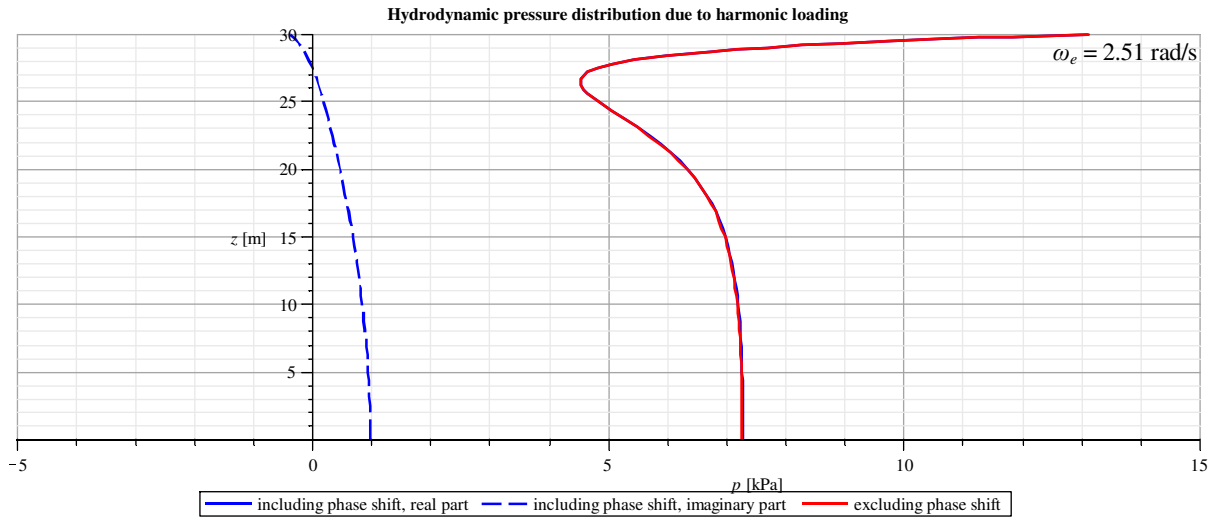


Figure 7.11 Hydrodynamic pressure distribution at  $\omega_e \approx 2.51$  rad/s (0.4 Hz)

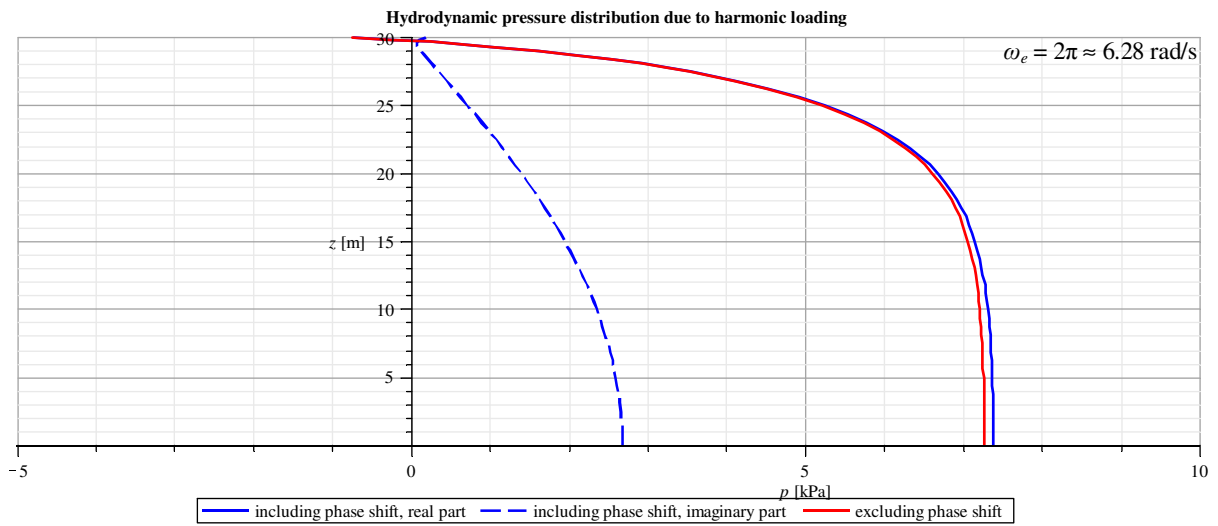


Figure 7.12 Hydrodynamic pressure distribution at  $\omega_e \approx 6.28$  rad/s (1 Hz)

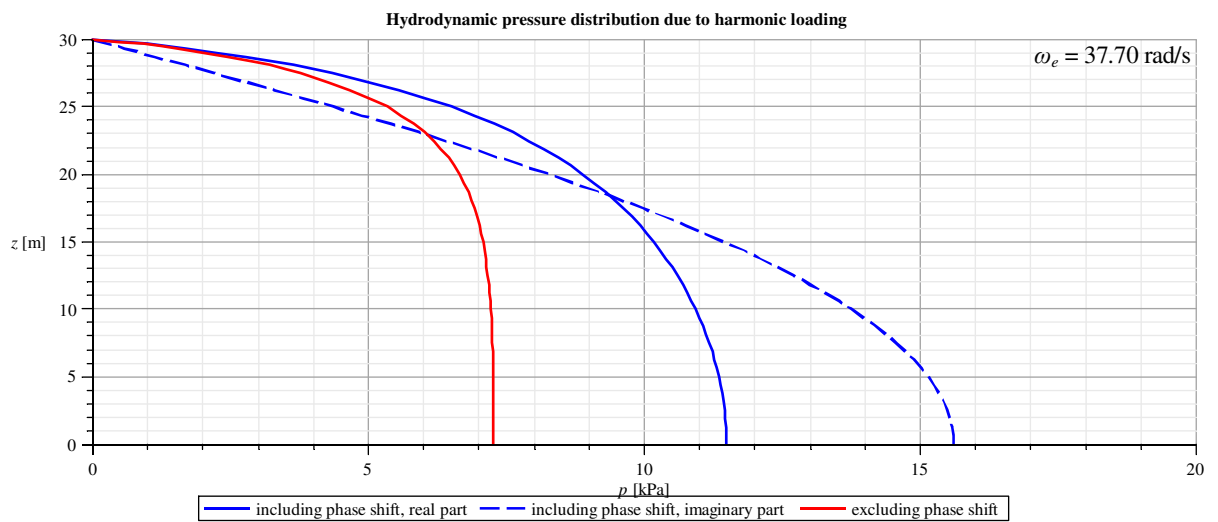


Figure 7.13 Hydrodynamic pressure distribution at  $\omega_e \approx 37.70$  rad/s (6 Hz)

The same remarks can be made as with the long chamber. Specific for this case is the utilization of more water for higher frequencies. For the lower frequencies it can be seen the pressure increase stagnates due to the small  $L/D$  ratio. This effect disappears for higher frequencies and unequal movement of the walls.

### 7.8.8. The effect of surface waves

The solution of equation (7.18) is derived for a free surface boundary condition. When this boundary condition is replaced by a zero pressure condition, the constants  $B_n$  change into:

$$B_n = \begin{cases} -\frac{1}{2}c_1L - c_2\left(\frac{L^2}{3} - d^2\right), & n = 0 \\ \frac{2L}{n^2\pi^2} \frac{c_1(1+(-1)^{n-1}) - 2c_2L(-1)^n}{\cosh(k_n d)}, & n = 1, 2, \dots, \infty \end{cases} \quad (7.20)$$

The other expressions in equation (7.18) remain the same. For details, refer to appendix B7.2. It shows that the frequency dependence disappears for this boundary condition. This clearly follows from figure 7.14, where no eigenfrequencies are present.

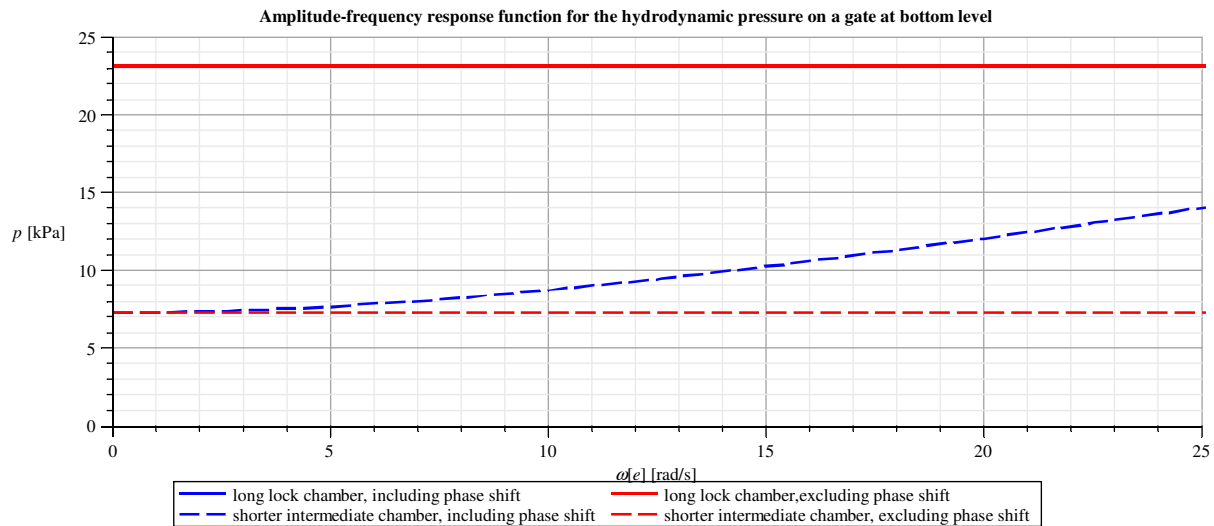


Figure 7.14 Hydrodynamic pressures in case of a zero pressure boundary condition

In the case that both gates move identical, the boundary condition at the surface is equal to  $p = 0$ , and the fluid is assumed to be incompressible; the fluid inside the chamber can only move as rigid body. No eigenfrequencies related to the chamber length are present. If the length between the gates is small there is an increase of pressure as a result of the phase difference. This results from the fact that in the case of a phase shift the volume of water is not constant anymore. This has no little to no influence for the lock chamber, but causes an increase at the lock heads for increasing excitation frequency. Given the fact the governing equation is derived for an incompressible, constant volume of water, this increase is not to be expected. An equal increase can be observed with the surface wave boundary condition in figure 7.4.

### 7.8.9. Length and depth of lock chamber

The effect of the length of the lock chamber on the maximum hydrodynamic pressure has been discussed in sections 4.7.1 and 4.7.2 with the reduced Westergaard and Housner models. From the solution in equation (7.18) it can be seen that the effect of the length of the chamber is introduced in the hyperbolic functions, similarly as in the formula by Housner (equation (4.10)). In figure 7.15 the influence of the parameter  $L$  is visualized, using the parameters in equation (7.19) and an excitation frequency of 1 Hz. As a reference the results of Housner<sup>11</sup>, Brahtz and Heilbron are also shown:

<sup>11</sup> Housner's notation of  $2L$  for the chamber length has been adapted to  $L$  for usage in figure 7.15

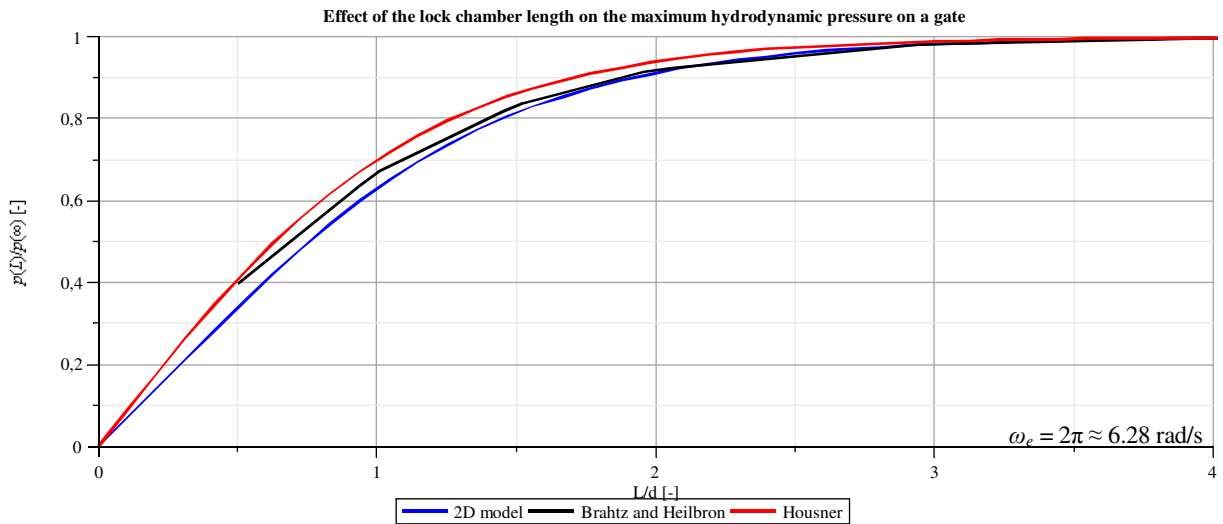
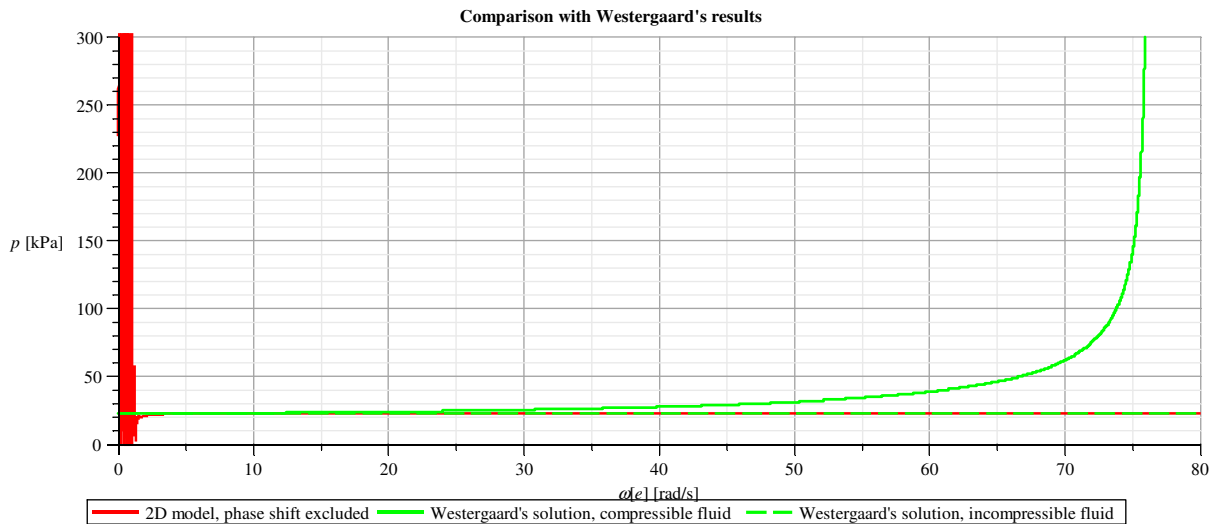


**Figure 7.15** Maximum hydrodynamic pressure at the bottom of a gate for different chamber lengths at 1 Hz

The results of equation (7.18) are in line with the results obtained by Housner, Brahtz and Heilbron. For all three models it shows that the length of the lock chamber has no influence on the hydrodynamic pressure if  $L > 4d$ . For lower  $L$  over  $d$  ratios the limited amount of water has a positive effect on the magnitude of the hydrodynamic pressure.

### 7.9. Comparison with Westergaard's results

The 2D model is based on Westergaard's approach, but with different boundary conditions and with absence of the compressibility of water. Therefore results should be comparable and differences due to the changed boundary conditions can be identified. Housner's solution is omitted from the comparison because Housner used a different approach to derive his solution. In figure 7.16 the maximum hydrodynamic pressures on a gate according to Westergaard (equation (4.4) for  $k_{hg} = 1 \text{ m/s}^2$ ) and the 2D model are shown for the lock chamber.



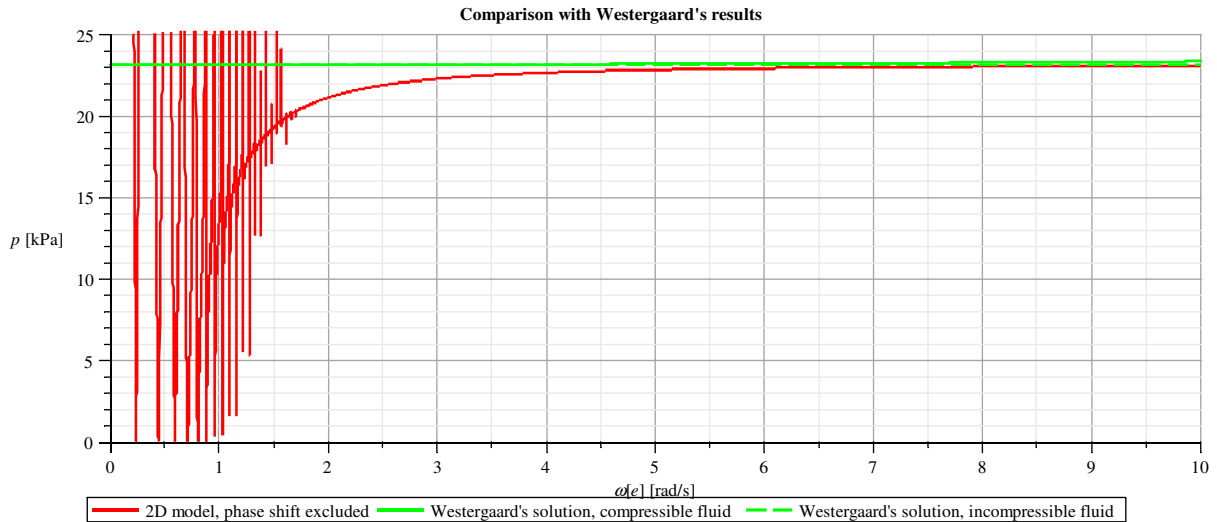


**Figure 7.16** The Westergaard solution in comparison with equation (7.18), with detail for low frequencies

The above results show that the 2D model gives similar results to the Westergaard solution. Apart from very low frequencies, the value of the hydrodynamic pressure is about the same: equation (7.18) converges to Westergaard's solution for incompressible fluid.

For very high frequencies, the compressibility of water causes additional eigenfrequencies related the water depth. As discussed in section 4.7.1 this is out the range of a typical earthquake spectrum and therefore not important for the evaluation of navigation locks, which have a limited water depth. For high-head structures, like hydroelectric dams, compressibility effects are in the frequency range of the earthquake and should be taken into account.

## 7.10. Conclusions 2D model for hydrodynamic pressure

### 7.10.1. Solution

The solution in equation (7.18) has been derived from the 2D wave equation which has one variable, the hydrodynamic pressure, as a function of  $x, z, t$ . In order to solve the wave equation four boundary conditions are required: two at the rigid gates (or walls), one at the bottom of the lock and one at the water surface. The fluid is taken as incompressible, because the compressibility only influences the solution at very frequencies. The gate are assumed rigid, this means that along the face the acceleration is constant. The solution is infinite summation of harmonic functions.

Two chamber dimensions are considered: the main lock chamber of the new locks and the intermediate space between the double gates at the lock heads. The results are presented in the frequency domain, for a unit acceleration of  $1 \text{ m/s}^2$ . Also pressure distributions over the height are given for certain harmonic frequencies.

The amplitude of the hydrodynamic pressure is linear related to the acceleration of the gates, this follows directly from the solution and also from solution obtained by Housner and Westergaard. The effect of the density of water is also linear, but this parameter is more or less constant for water.

### 7.10.2. Resonance effects

On basis of figure 7.2 and further, high pressures as a result from resonance might be expected. In reality this is not the case because of several reasons:

- As with the 1D model, the governing equation are derived for small displacements and linear surface waves. This means that for these high pressures at the eigenfrequencies, the conditions on which the governing equation is based, are not satisfied. In order to do so, a non-linear approach will have to be followed;
- The steady-state solution is a result of the input loading. The vibrations caused by earthquakes have a limited time span, in the order of 30 seconds. This is not long enough for resonance to take place. This can easily be seen from the following numerical example.

From table 7.1.a follows that the fundamental eigenfrequency for the lock chamber is  $0.123 \text{ rad/s}$ . The harmonic wave  $c_w$  speed follows from equation (7.21) [HOLTHUIJSEN, 2007]:

$$c_{w,n} = \frac{\omega_n}{k_n} = \sqrt{\frac{Lg}{n\pi} \tanh\left(\frac{n\pi d}{L}\right)} \quad (7.21)$$

For the fundamental eigenfrequency this would result in a celerity of 17.0 m/s. For a chamber length of 436 m this would mean that it takes 25.6 s for this wave to cross the lock chamber. This is too long compared the duration length of an earthquake to cause resonance. The travel time increases for higher frequencies and lower water depths. Also the group velocity of multiple waves is less than the velocity of a harmonic wave because of dispersion;

- And even if high water levels would occur, the water will simply flow over the sides of the lock. The pressures distributions in sections 7.8.6 and 7.8.7 are therefore in reality parabolic, as expected. The eigenfrequencies are present along the whole frequency domain, but the width of the peaks converges to zero for higher frequencies. The pressure is constant at these frequencies and therefore frequency-independent. For the pressures in the low frequency domain of figures 7.2 and 7.16 it is therefore valid to take for instance Westergaard's solution as upper limit. The pressures at the peaks do not occur as explained above and because of the limited duration of an earthquake the extreme low frequencies are not present in an earthquake spectrum. Neglecting surface waves gives the same result.

### 7.10.3. Effect of surface waves

The effect of surface waves has been treated in the 1D model, which specifically targeted this effect. For the 2D analytical model the effect of surface has also been incorporated in one of the boundary conditions. As a result of this boundary condition the eigenfrequencies related the length of the lock chamber can occur. If surface waves are not taken into account, these eigenfrequencies cannot be identified and only the impulsive part of the hydrodynamic pressure is found. As stated before, in practice the effect of surface waves is limited and neglecting them in the evaluation will not cause significant errors.

### 7.10.4. Phase difference and chamber length

In the solution the effect of the phase difference between the two boundaries has been taken into account. The unequal motion has little to no effect for the large lock chamber, other than it increases the number of eigenfrequencies. If the gates are close to each other, the phase shift can cause an increase of pressure at higher frequencies, but this is mainly the result of an error in the used model. In reality, where the volume of water is constant, phase effects are negligible.

The length of the lock chamber, or more specific the ratio length over water depth, is important for narrow chambers or fluid containers. The limited amount of water reduces the hydrodynamic pressure. The water inside can only behave as a rigid body. For chamber lengths greater than 4 times the water depth this effect disappears.

### 7.10.5. Compressibility effects

As stated before, the solution derived is for incompressible water. The high velocity of pressure waves in water results only for high frequencies in a change of the hydrodynamic pressure. This can be clearly seen in figure 7.16. The eigenfrequencies related to the compressibility decreases with increasing water depth. For navigation locks, with limited water depths, the fundamental eigenfrequencies is above the range of a typical earthquake spectrum. The eigenfrequencies found in the lower frequency domain result from convective effects, which are not influenced by the compressibility. Based on that, one can conclude that the compressibility of water can be neglected in the evaluation of navigation locks. However, for structures with large water depths, this assumption is in general not valid anymore.

In the absence of compressibility, the solution is almost identical to the Housner and (reduced) Westergaard results. One would find the same magnitude of hydrodynamic pressure.

## 8. Two-dimensional model for fluid-structure interaction

### 8.1. Introduction

The 2D analytical model is used as basis for the 2D FEM model. This way a comparison or validation can be made between the two. After that the FEM model can be modified to research various aspects that are not possible with the analytical model. The compressibility of water, which is not taken into account in the analytical approach, will be applied in the FEM model.

In appendix C.1 the procedure of working with DIANA is explained. In the analytical approach the assumption of rigid gates is used, because this leads to a constant acceleration over the height of the gates. In order to perform a FSI<sup>12</sup> analysis, data of the gates like mass and stiffness are required, and lead to eigenfrequencies and normal modes. As the 2D analytical model solely focuses on the loading on the gates, and not the response, some changes to the model will have to be applied. To make the gates rigid, and eliminate the normal modes of the gate, tyings are applied which ensure an infinite stiffness of the gates. In order to calculate hydrodynamic pressures there needs to be a differential motion between the gates and fluid. With rigid gates this is not the case; hence a solution of a SDOF mass-spring system is opted. This way the gates can move as a rigid body with a constant acceleration and hydrodynamic pressures can be calculated. Because of the SDOF mass-spring system the gates will not have a unit acceleration, therefore the output of the pressures is scaled to this value to obtain the correct results. This is achieved by dividing the hydrodynamic pressures by the acceleration of the gate. The effect of the eigenfrequency of the gate is thereby eliminated. Although the mass of gate and spring stiffness are estimated on basis on the real dimensions of the structure, the scaling procedure makes the results independent of the gate parameters. With the above mentioned changes, the hydrodynamic pressures as a result of rigid wall moving with an acceleration of  $1 \text{ m/s}^2$  can be computed. The absence of normal modes makes the solution by modal superposition impossible; hence a direct frequency response approach is used to find the solution. This method is however slower as for every frequency the solution needs to be calculated. The model with the springs and rigid gates is shown in figure 8.1. The model will be used to evaluate the following cases:

- 1a. long lock chamber, pressure at water surface is equal to zero, incompressible water;
- 1b. long lock chamber, pressure at water surface is equal to zero, compressible water;
- 1c. long lock chamber, linear surface waves, incompressible water;
- 1d. long lock chamber, linear surface waves, compressible water.

The same case will be evaluated for the water between two gates at the lock heads (cases 2a to 2d).

Besides these cases, three more will be evaluated with DIANA. In one case, for both chamber dimensions, the infinite rigidity of the gates is removed. The result is a certain bending stiffness for the gates which influences the hydrodynamic pressure distribution. This is achieved by the tyings are removed and two supports are added to the bases of the gates. This results in a non-rigid behavior of the gates. Details of this model can be found in figure 8.2. The non-rigid cases are based on cases 1d and 2d; linear surface waves and the compressibility of water are included.

The last case to be evaluated is a semi-infinite environment. Based on case 1d, the gates on one side are removed and replaced with a radiation boundary. This boundary ensures that (pressure) waves do not reflect off, but instead their energy leaves the model. Details of this model can be found in figure 8.3.

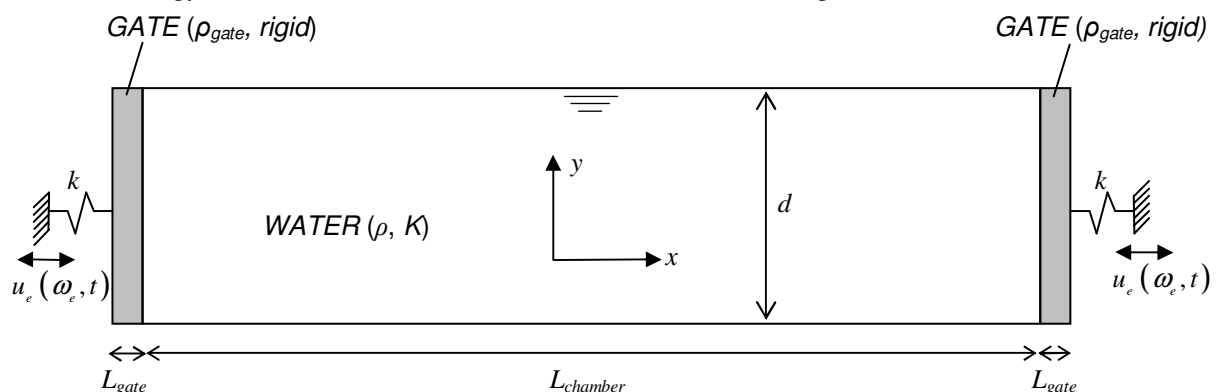


Figure 8.1 2D model for FEM analysis with rigid gates

<sup>12</sup> Fluid-Structure Interaction; for background theory about the procedure refer to appendix C.2

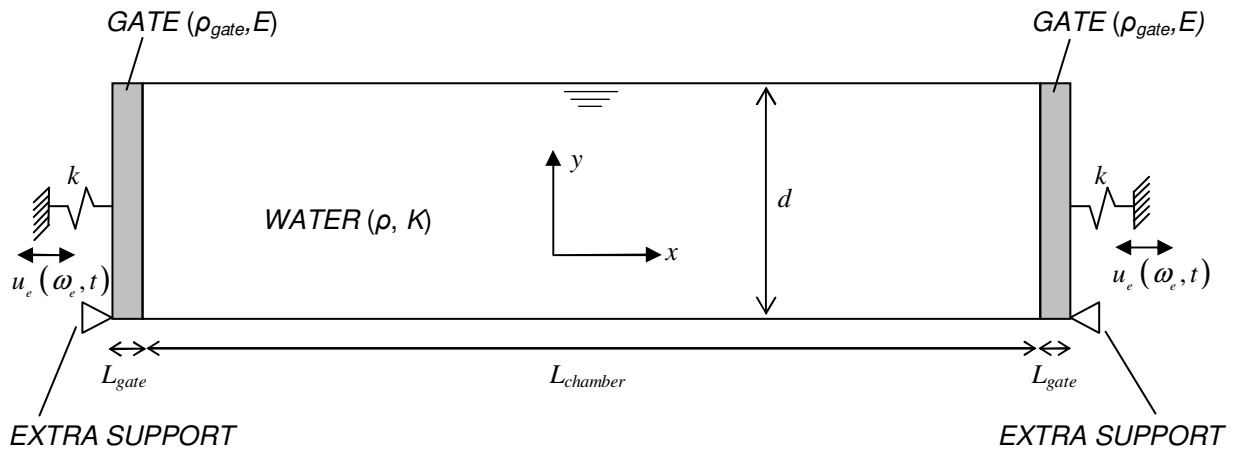


Figure 8.2 2D model for FEM analysis with flexible gates

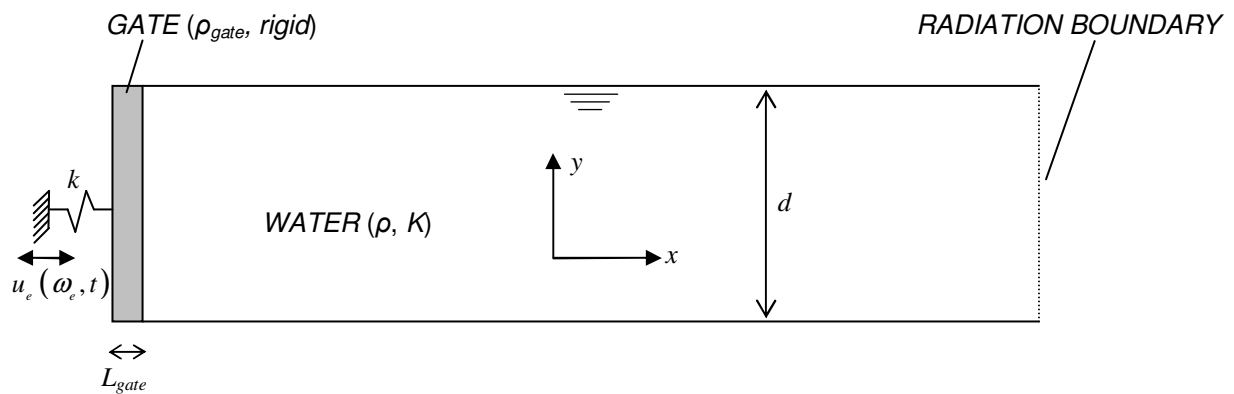


Figure 8.3 2D model for semi-infinite FEM analysis with rigid gate

The earthquake loading is modeled as a base acceleration of  $1 \text{ m/s}^2$  in order to find a solution in the frequency domain. The base acceleration is applied at the supports and does not contain a phase delay. A phase delay is not possible in DIANA when using frequency domain solutions.

## 8.2. Strategy

The following strategy will be followed for the FEM analysis. Details of the preprocessing process are listed in the next paragraph.

1. Make the geometry for the models (for each lock dimension one), set units and coordinate system;
2. Make a list with the materials and add material properties;
3. Make a list of the different properties in the model, like gates and fluid domain;
4. Mesh the geometry with the properties and add tyings;
5. Add supports and loading: the earthquake is applied as a base acceleration on the supports;
6. Add extra material data in DIANA before computing (optional);
7. Select computing procedure and output;
8. Postprocess the data and repeat the process for each case.

## 8.3. Preprocessing: element types and numerical values

### 8.3.1. Introduction

The dimensions of the geometry are identical to the analytical model. Refer to figures 8.1 to 8.3 for details. An example of the FEM mesh for model 2d is shown in figure 8.4. The meshes of the other models are almost identical, the main differences being the distance between the two gates and the boundary at the water surface level. Details of the different types of elements used in the DIANA analysis will be treated first.

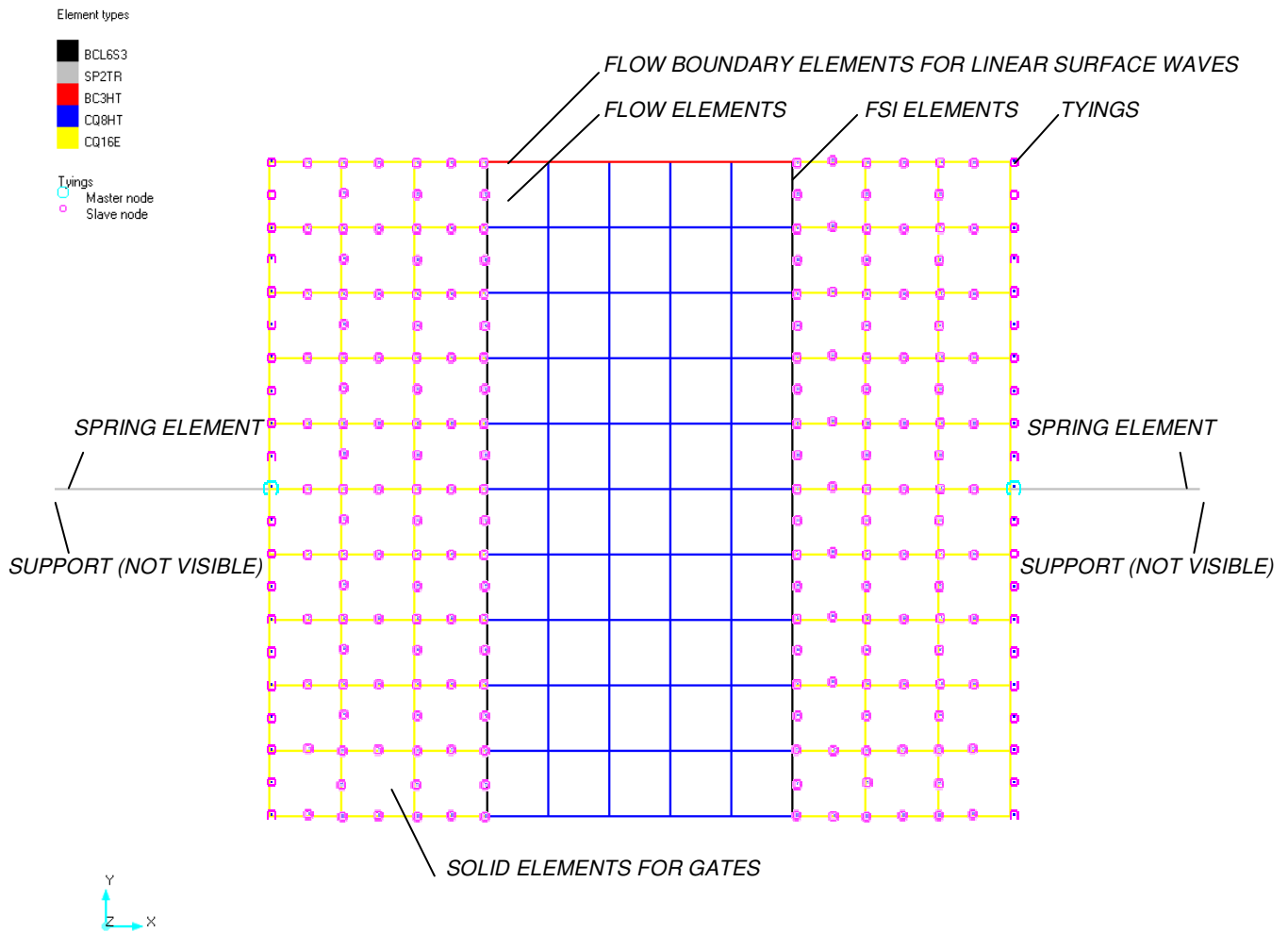


Figure 8.4 FEM mesh for model 2d

### 8.3.2. Element types

#### Solid elements

The lock gates are modeled with 2D plain strain elements with the following material properties:

- Young's modulus  $E$ ;
- Density  $\rho$ ;

If tyings are applied all over the gate, the specified Young's modulus no longer has any effect. The use of tyings leads to an infinite stiffness.

#### Flow elements

The flow elements are essentially dummy elements. They are modeled with 2D potential flow elements. Only a dummy value for the conductivity is applied. In the case of compressibility pressure wave speed  $c_p$  has to be added.

#### FSI elements

The 1D FSI elements relate the movement of the gate with the presence of water. The quadratic element type "BCL6S3" is used in DIANA. In figures 8.5 and 8.6 the functioning of the element is explained. At the fluid-structure boundary in figure 8.4 there are two nodes along the boundary, one on the fluid side and one at the structure side. The FSI elements contain the density information of the fluid  $\rho$ .

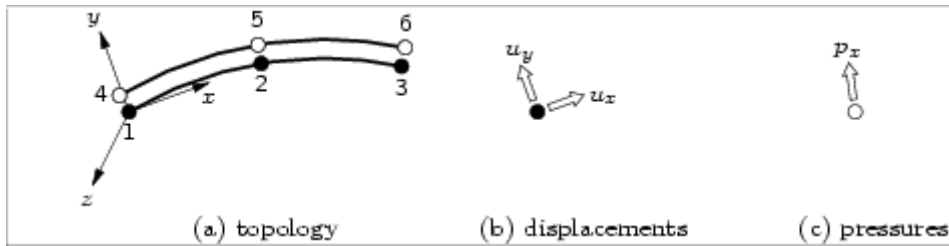


Figure 8.5 The BCL63S fluid-structure element, line, 3+3 nodes (adapted from [TNO DIANA, 2008])

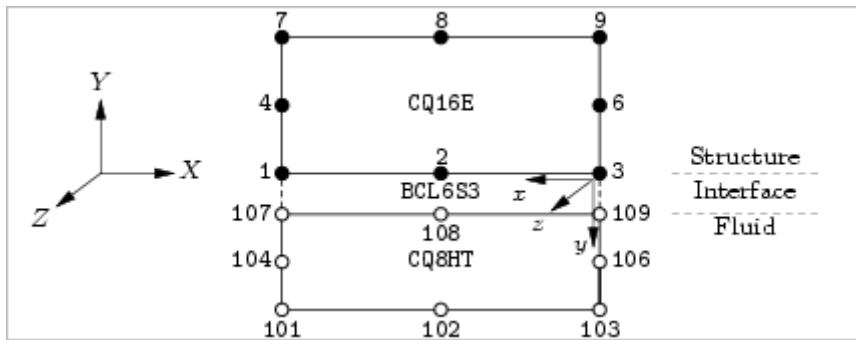


Figure 8.6 Nodal connectivity for 2D fluid-structure interaction (adapted from [TNO DIANA, 2008])

#### Flow boundary elements for linear surface waves

In paragraph 8.1 two boundary conditions for the water surface has been discussed: free surface waves or a zero pressure boundary. In the first case, the top edge of the fluid domain is meshed with quadratic 1D flow boundary elements. These elements ensure free surface waves if an acceleration of gravity  $g$  is defined. In the latter case the zero pressure boundary is achieved by an external loading of  $p = 0$ .

#### Flow boundary elements for radiation boundary

These elements are of the same types as used for the surface waves, but with different properties. In order to act as a radiation boundary the following properties have to be defined: the acceleration of gravity  $g$  and the water depth  $d$ . This combination of elements and properties is only used for the semi-infinite case.

#### Spring elements

As stated before the spring elements eliminate the effect of mode shapes on the pressure distribution along the face of the gates. The magnitude of order of the spring stiffness is discussed in paragraph 6.9. Besides the spring stiffness parameter  $k$  also a value for the damping coefficient  $c$  can be defined.

#### Tyings

The tyings work with a master node and slave nodes. The slave nodes will have the same displacement as the master nodes. This leads to a rigid gate, see figure 8.4 for details.

### 8.3.3. Numerical values

Most of the dimensions and material properties are identical to previous models. Because the gates are now actually modeled, instead of being represented by a rigid boundary, there are some specific FEM properties related to the gates itself. As the gates are modeled with plain strain elements, an average density is applied. In paragraph 6.9 it is discussed that the gates have a mass of 300 t/m, which corresponds to an average density of  $1000 \text{ kg/m}^3$ . For the spring stiffness the same 68 MN/m as discussed is used, this leads to a "dry" eigenfrequency of 15.06 rad/s. The eigenfrequency will be lower with the added mass of the fluid. The Young's modulus is that will be used is 100 GPa, this values is a rough estimate based on the bending stiffness of the gates in reality. The solid gates in the FEM model with an average density and Young's modulus now have the same order of bending stiffness as the actual gates, consisting of a steel truss and skin plating.

General:

$$\begin{aligned}
 \rho &= 1040 \text{ kg/m}^3 \\
 g &= 9.81 \text{ m/s}^2 \\
 L_{\text{chamber,lock}} &= 436 \text{ m} \\
 L_{\text{chamber,intermediate}} &= 14 \text{ m} \\
 K &= 2.2 \text{ GPa} \\
 d &= 30 \text{ m}
 \end{aligned} \tag{8.1}$$

Specific gate properties for FEM model:

$$\begin{aligned}
 E &= 100 \text{ GPa} \\
 \rho_{\text{gate}} &= 1000 \text{ kg/m}^3 \\
 k &= 68 \text{ MN/m}
 \end{aligned}$$

Solver settings:

$$\begin{aligned}
 \text{Frequency domain} &= 0 \text{ to } 40 \text{ Hz (0 to } 251.3 \text{ rad/s)} \\
 \text{Step size} &= 0.25 \text{ Hz } (\pi/2 \approx 1.57 \text{ rad/s)} \\
 \text{Number of steps} &= 161
 \end{aligned}$$

## 8.4. Results in the frequency domain

### 8.4.1. Introduction

For the cases 1a to 2d and the extra cases discussed in paragraph 8.1 the solution in the frequency domain has been computed for the bottom nodes. For the cases with linear surface waves also the hydrodynamic pressure at the top nodes of a gate has been computed. Because of the absence of a phase difference the amplitudes of the pressure are equal for both gates. Given pressure are absolute values unless stated otherwise. In the derivation of the momentum balance equation in appendix B.3.2 and subsequently boundary conditions, a compressive pressure is denoted as positive. This sign convention is common in fluid and soil mechanics. In DIANA the conventions from solid mechanics are adopted, which states a tensile stress as positive and compressive stress as negative. In order to have the same sign convention between the analytical and FEM results, the results from DIANA are transformed to the sign convention used in the analytical approach.

### 8.4.2. Hydrodynamic pressure at bottom of gate (situation long lock chamber)

In figure 8.7 the hydrodynamic pressures for cases 1a to 1d are given. A frequency range of 0 to 250 rad/s used. This relatively large range is selected to include compressibility effects, which occur at high frequencies. With this range the 1<sup>st</sup> two eigenfrequencies related to compressibility are included; they can be found from equation (4.7) and appendix B.1, but are also listed below:

$$\omega_n = \frac{\pi(2n-1)c_p}{2d}, \quad n = 1, 2, \dots, \infty \tag{8.2}$$

For the numerical values in equation (8.1) this leads to  $\omega_1 \approx 76.15$  rad/s and  $\omega_2 \approx 228.46$  rad/s. The fundamental eigenfrequency is clearly visible in figure 8.7; the second one almost not visible due to the chosen step size. Above the first eigenfrequency related to the water depth, more eigenfrequencies are visible. Below, the solution is identical to Westergaard's.

The two cases without compressibility show a constant pressure of the same magnitude as obtained by Westergaard and the 2D analytical model.

On basis of the 2 analytical models, one would expect to see also eigenfrequencies related to the chamber length at the cases which take into account surface waves. Although cases 1c and 1d show larger pressures at the top of the gates at low frequencies, the pattern and magnitudes differ from the 2D analytical model. Without this effect, the cases with and without surface waves give almost the same result.

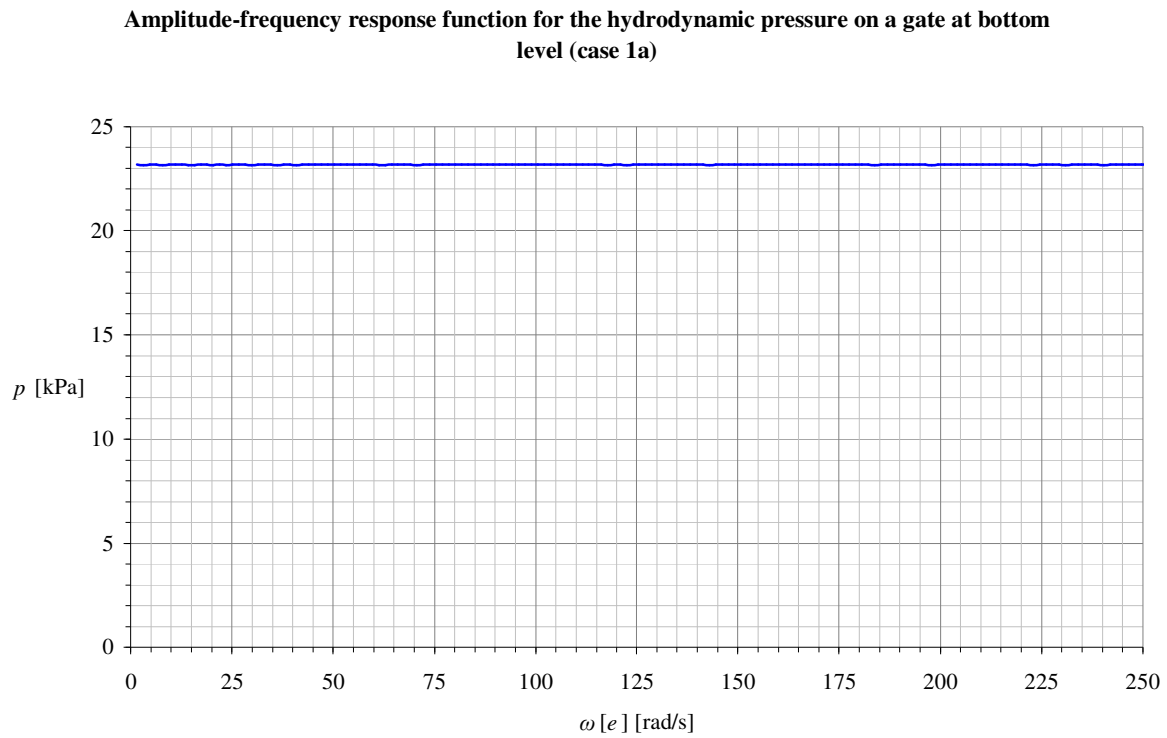


**Figure 8.7a** Hydrodynamic pressures for case 1a

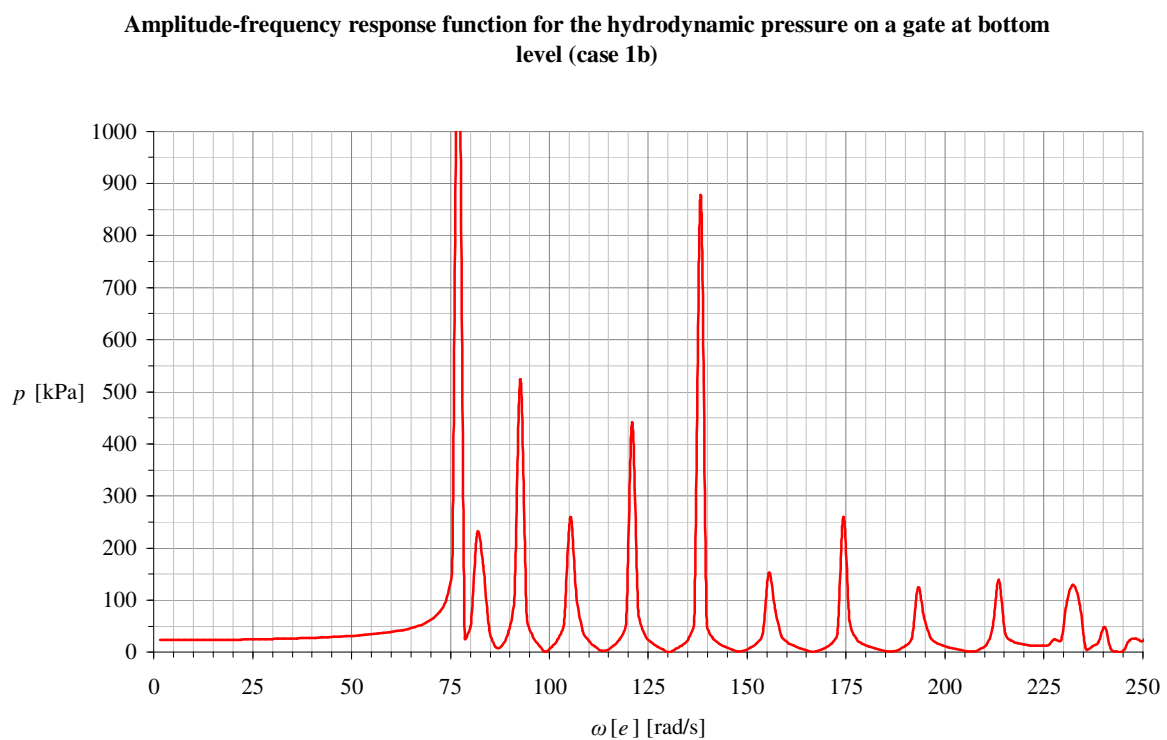


**Figure 8.7b** Hydrodynamic pressures for case 1b

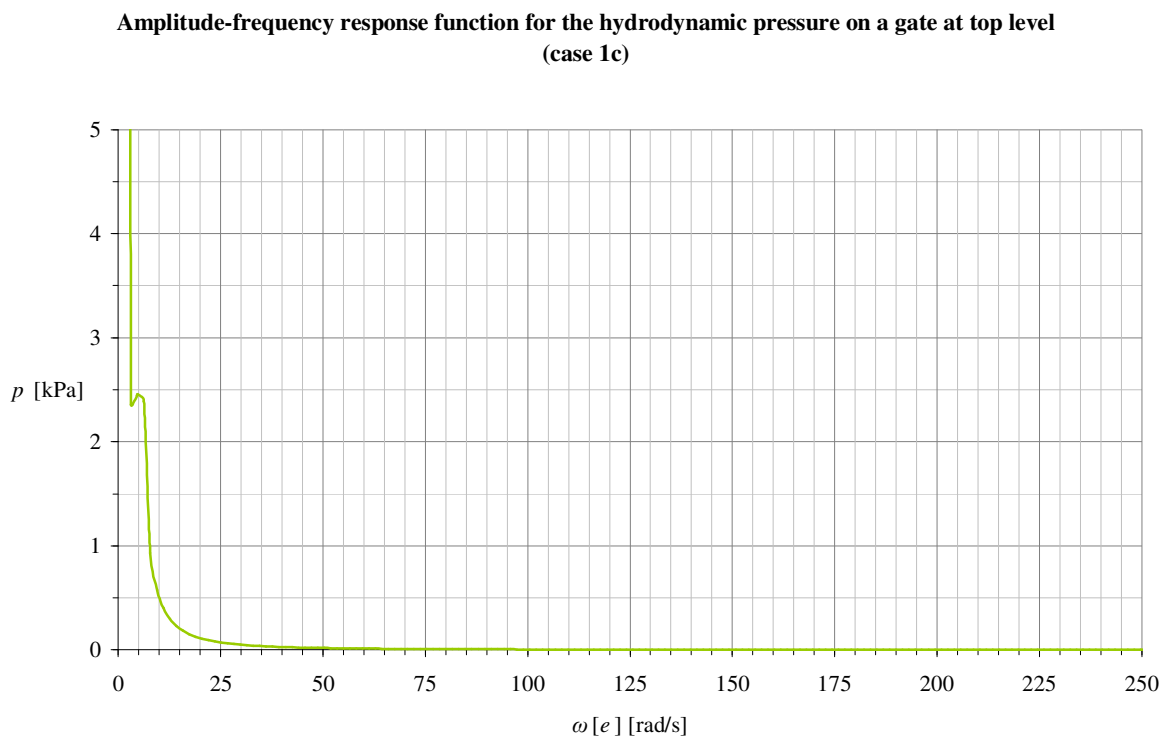
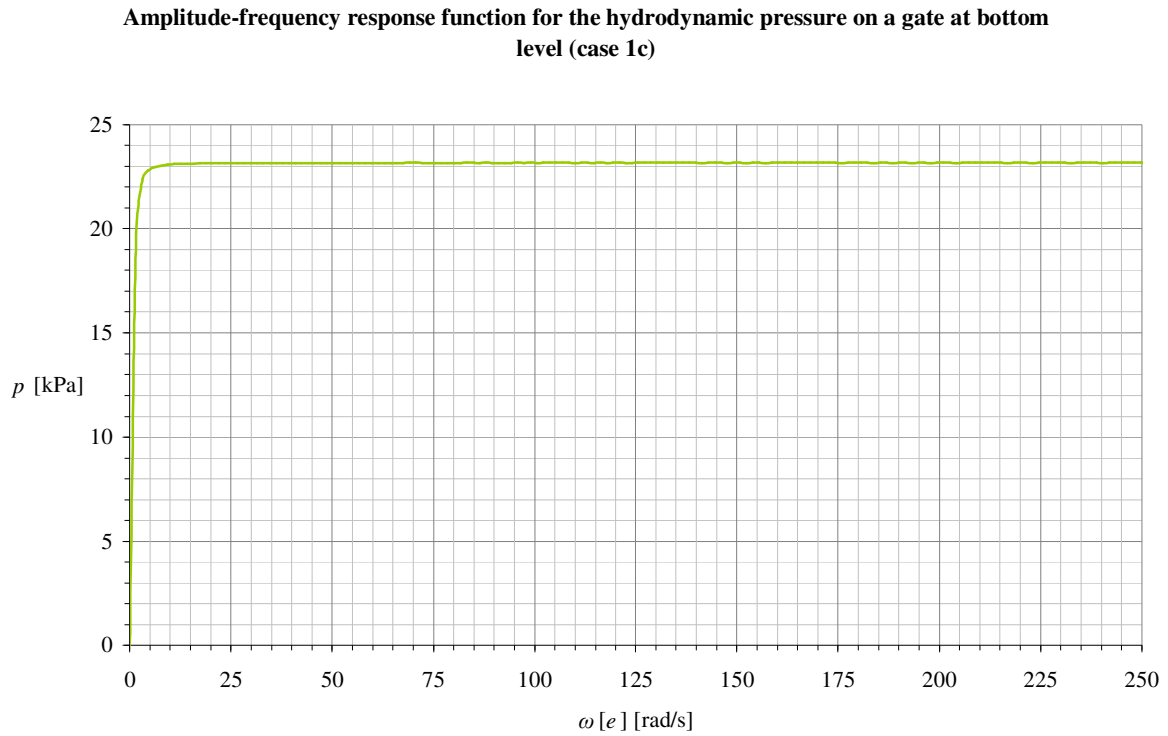
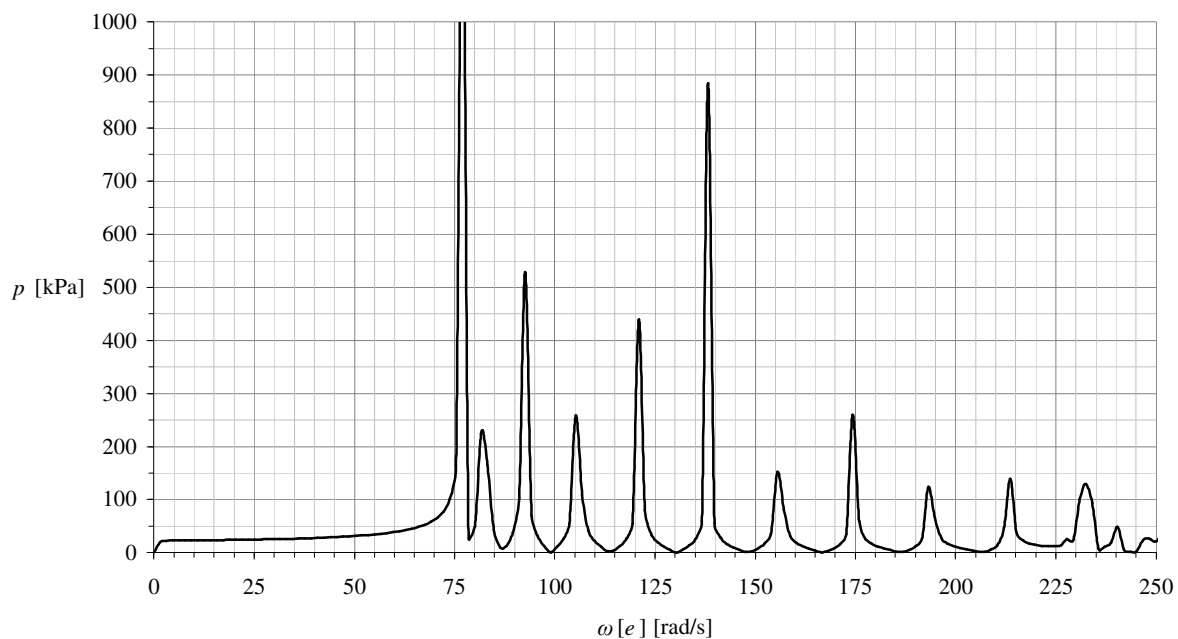


**Figure 8.7c Hydrodynamic pressures for case 1c (bottom and top level of gate)**

Amplitude-frequency response function for the hydrodynamic pressure on a gate at bottom level (case 1d)



Amplitude-frequency response function for the hydrodynamic pressure on a gate at top level (case 1d)

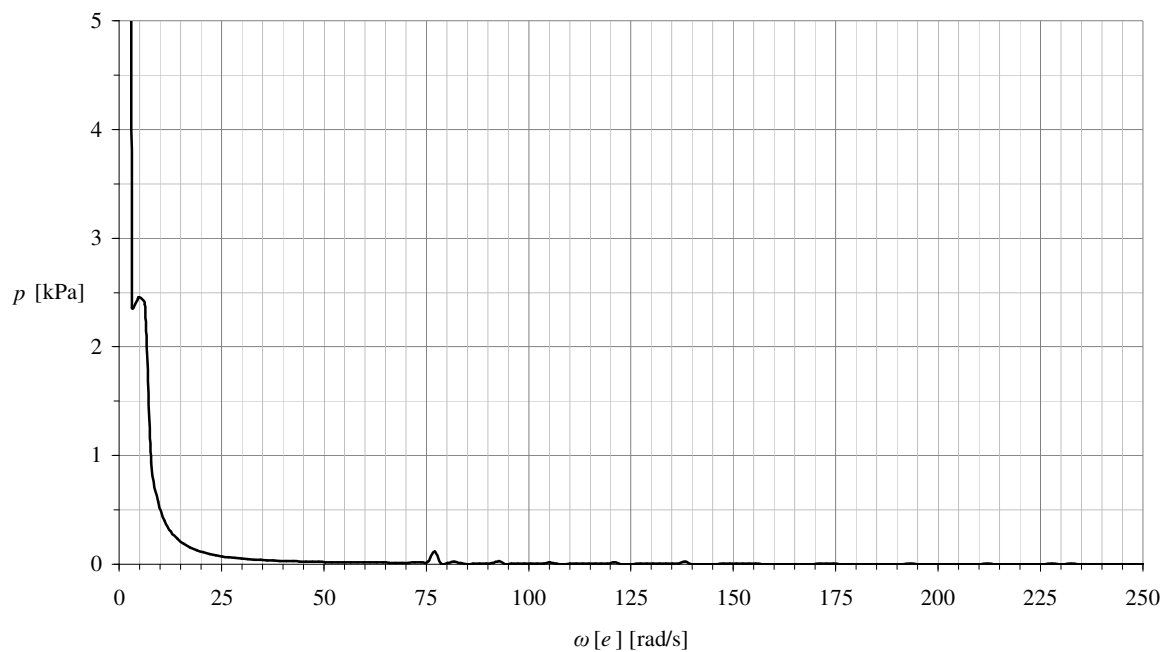
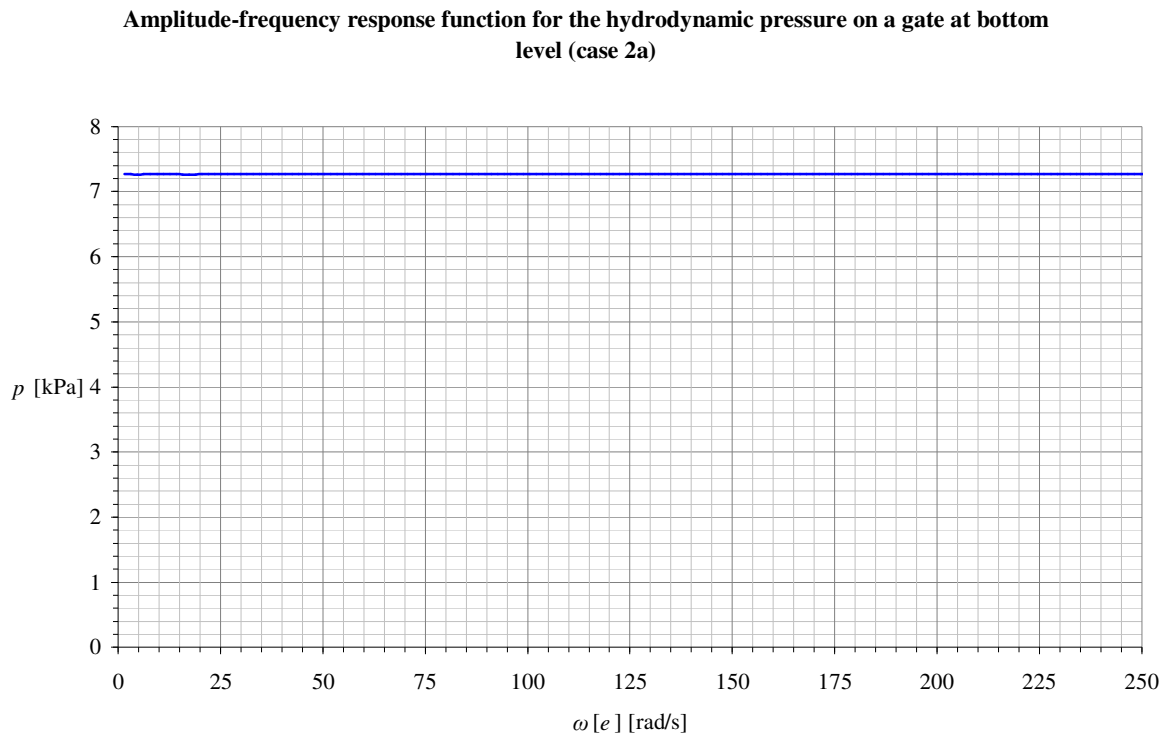


Figure 8.7d Hydrodynamic pressures for case 1d (bottom and top level of gate)

### 8.4.3. Hydrodynamic pressure at bottom of gate (situation shorter intermediate chamber)

Again, there is great resemblance between the cases with and without surface waves. Cases 2a and 2c show a frequency-independent result. Cases 2b and 2d, show an increase of pressure for increasing excitation frequencies.



**Figure 8.8a Hydrodynamic pressures for case 2a**

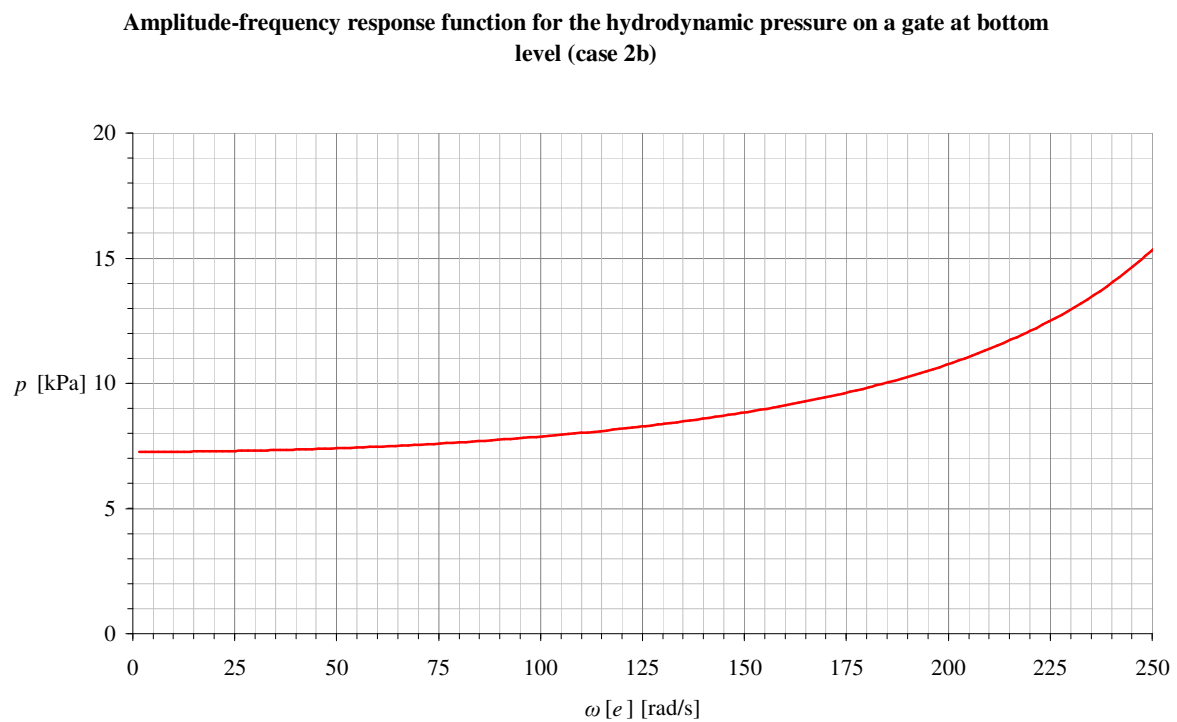


**Figure 8.8b Hydrodynamic pressures for case 2b**

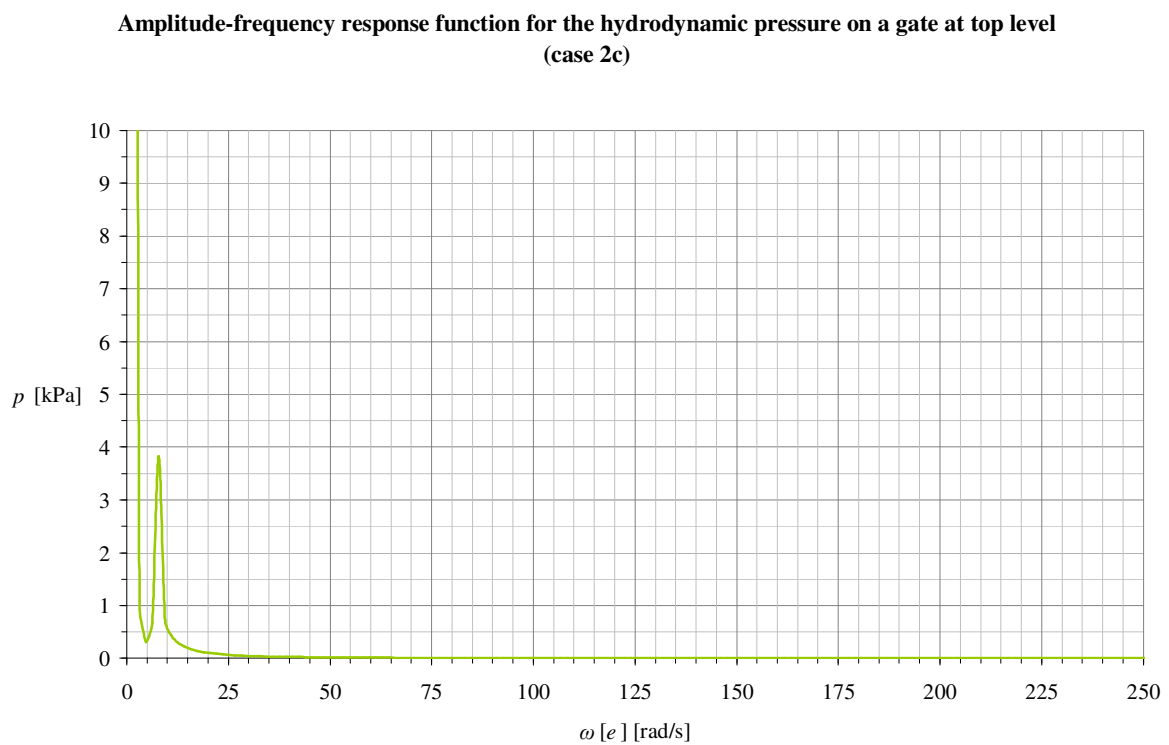
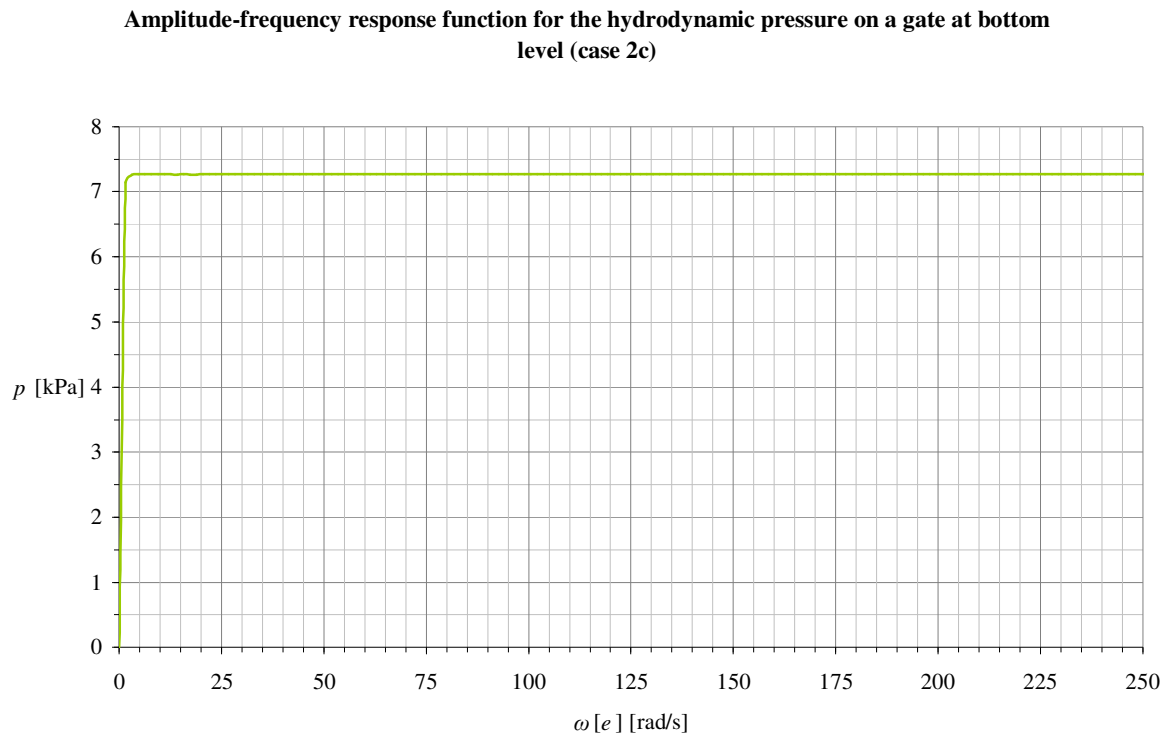


**Figure 8.8c Hydrodynamic pressures for case 2c (bottom and top level of gate)**

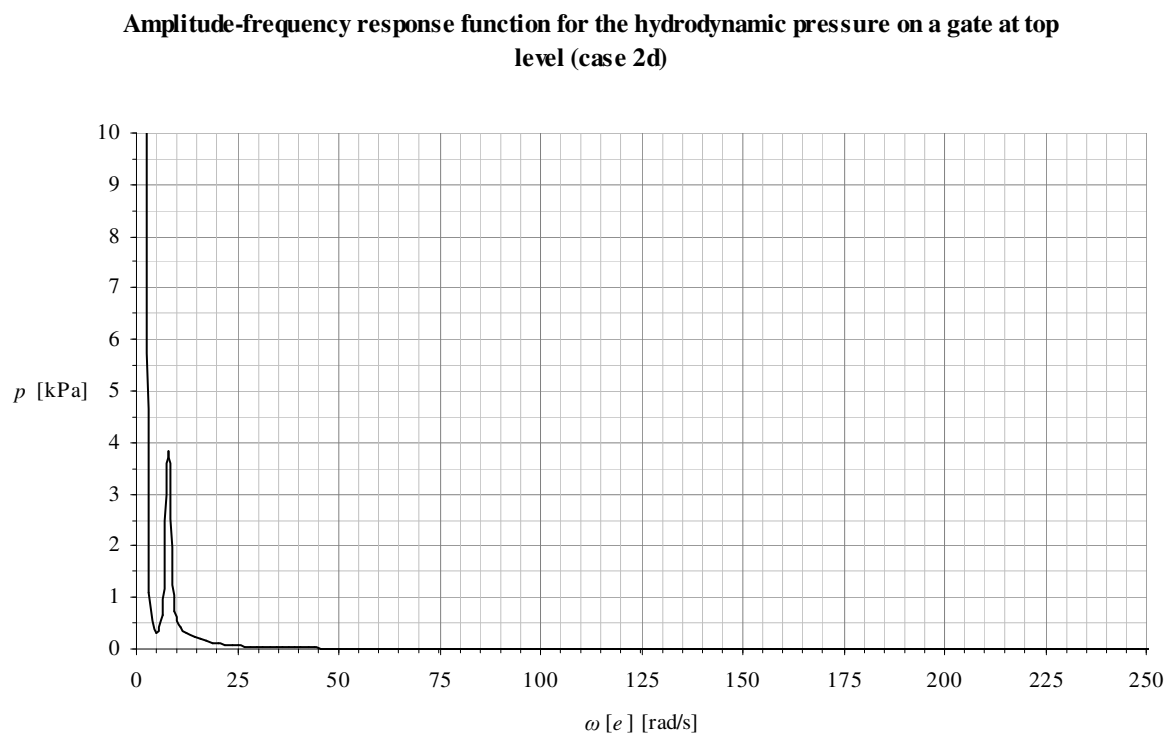
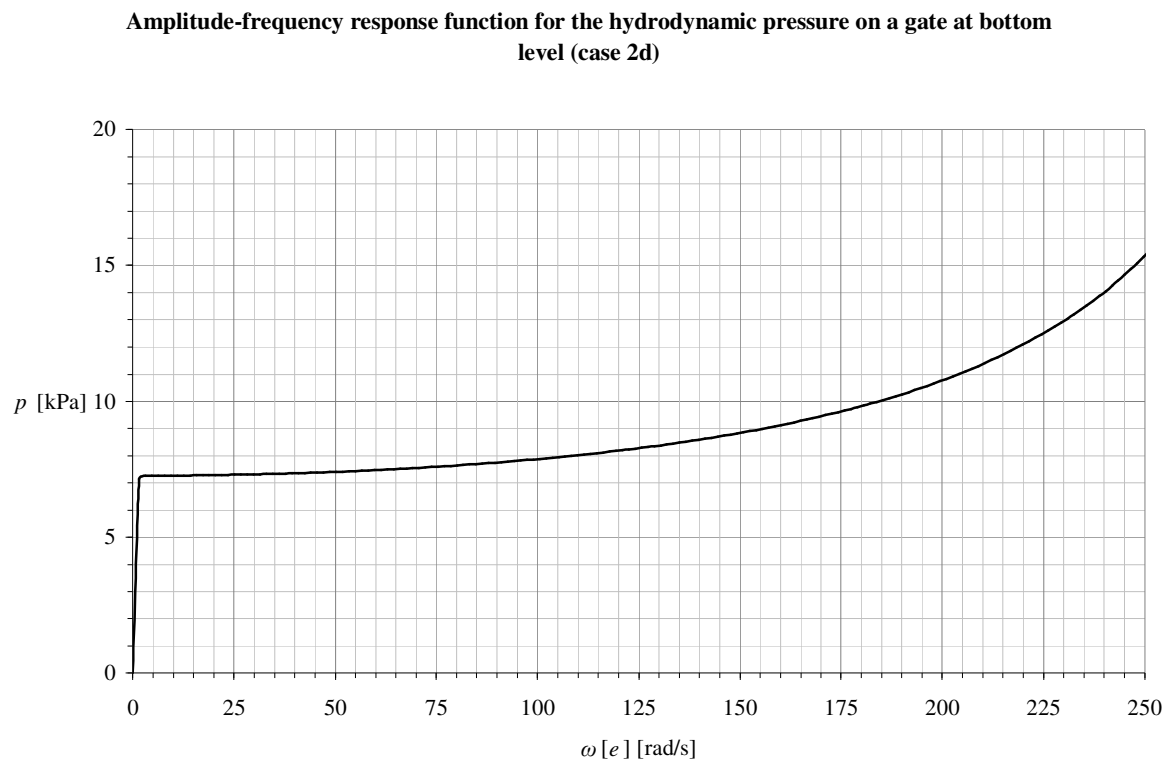


**Figure 8.8d Hydrodynamic pressures for case 2d (bottom and top level of gate)**

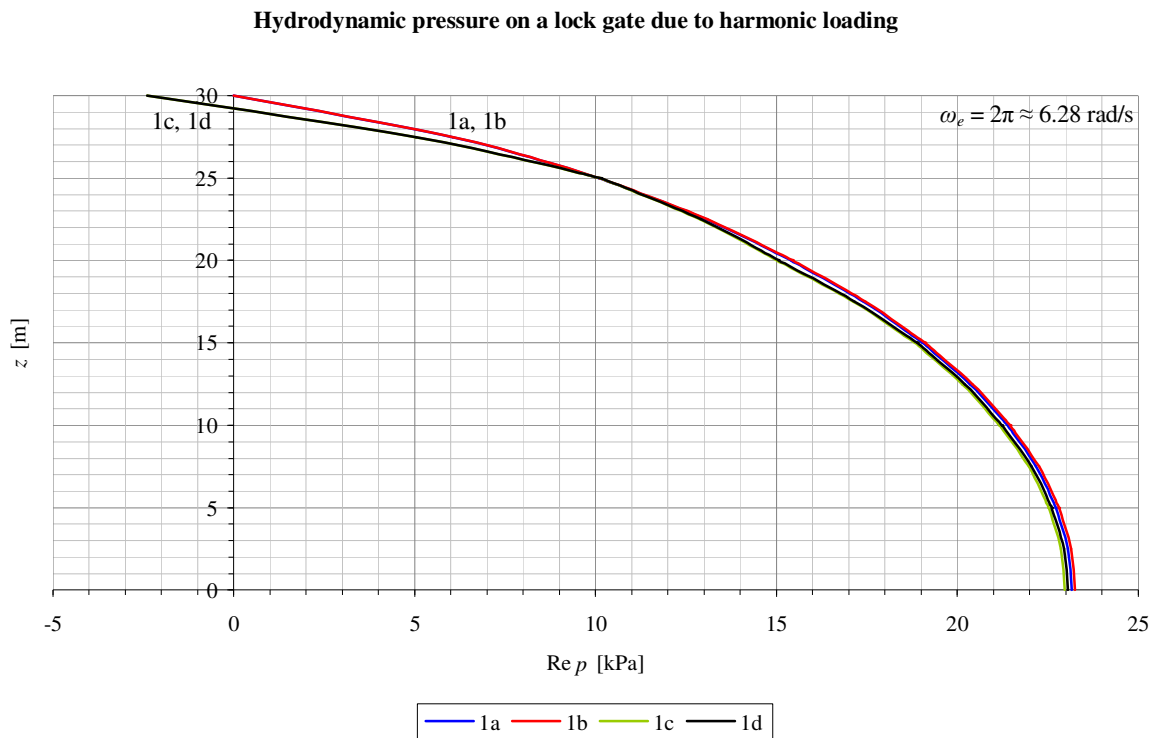
#### **8.4.4. Hydrodynamic pressure along the face of the gate (situation long lock chamber)**

For the selected frequencies in table 8.1 the hydrodynamic pressure distribution has been visualized. The frequencies are close to or in-between the eigenfrequencies related to compressibility from equation (8.2). The

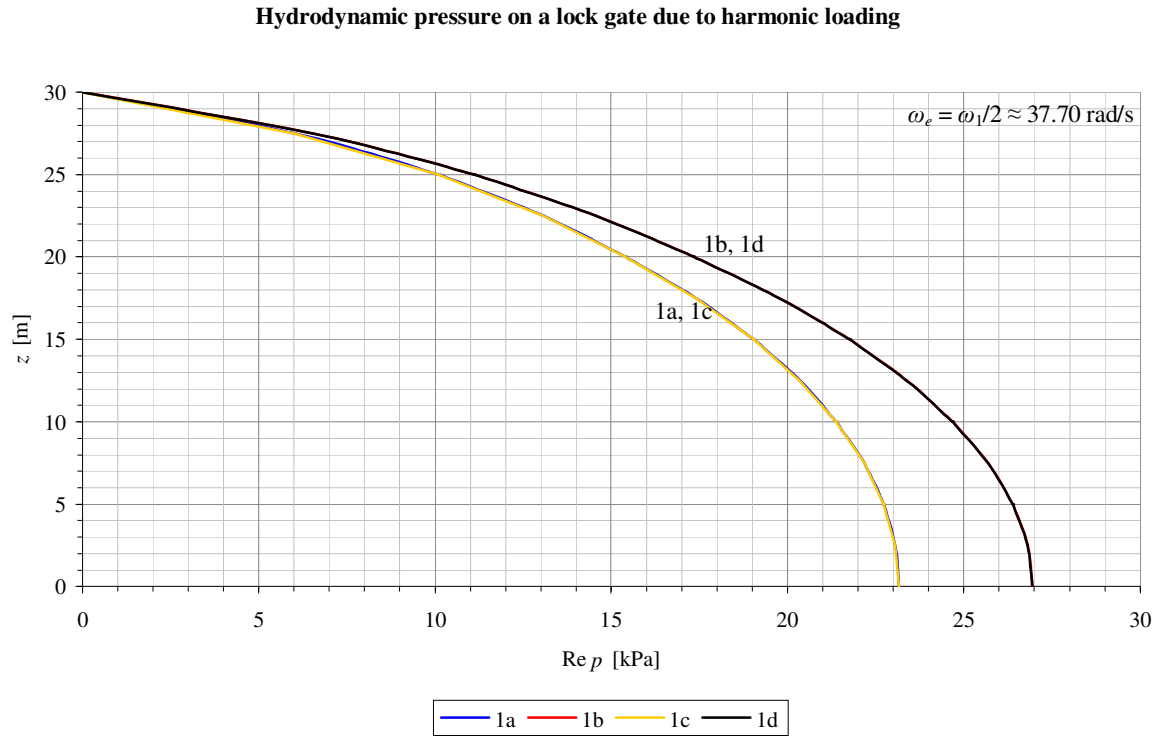
first two, at 1 and 6 Hz are also used in the 2D analytical model. The shape of the pressure distributions differs from the earlier obtained result from the 2D analytical model. While the results at 1 and 6 Hz are comparable, the parabolic shape of the distribution changes for higher frequencies in the case of compressible water. This clearly shows that the parabolic pressure distribution is not valid for frequencies above the fundamental eigenfrequency for compressible water.

Figure	Excitation frequency $\omega_e$ [rad/s]	Excitation frequency $f_e$ [Hz]
Figure 8.9	$2\pi \approx 6.28$	1.00
Figure 8.10	$\omega_1/2 \approx 37.70$	6.00
Figure 8.11	$< \omega_1 \approx 75.40$	12.00
Figure 8.12	$> \omega_1 \approx 76.97$	12.25
Figure 8.13	$(\omega_1 + \omega_2)/2 \approx 152.37$	24.25
Figure 8.14	$< \omega_2 \approx 227.77$	36.25
Figure 8.15	$> \omega_2 \approx 229.34$	36.50

**Table 8.1** Selected excitation frequencies with corresponding figures (situation long lock chamber)



**Figure 8.9** Hydrodynamic pressure distribution at  $\omega_e = 2\pi$  rad/s (1.00 Hz)



**Figure 8.10 Hydrodynamic pressure distribution at  $\omega_e = \omega_1/2 \approx 37.70 \text{ rad/s}$  (6.00 Hz)**

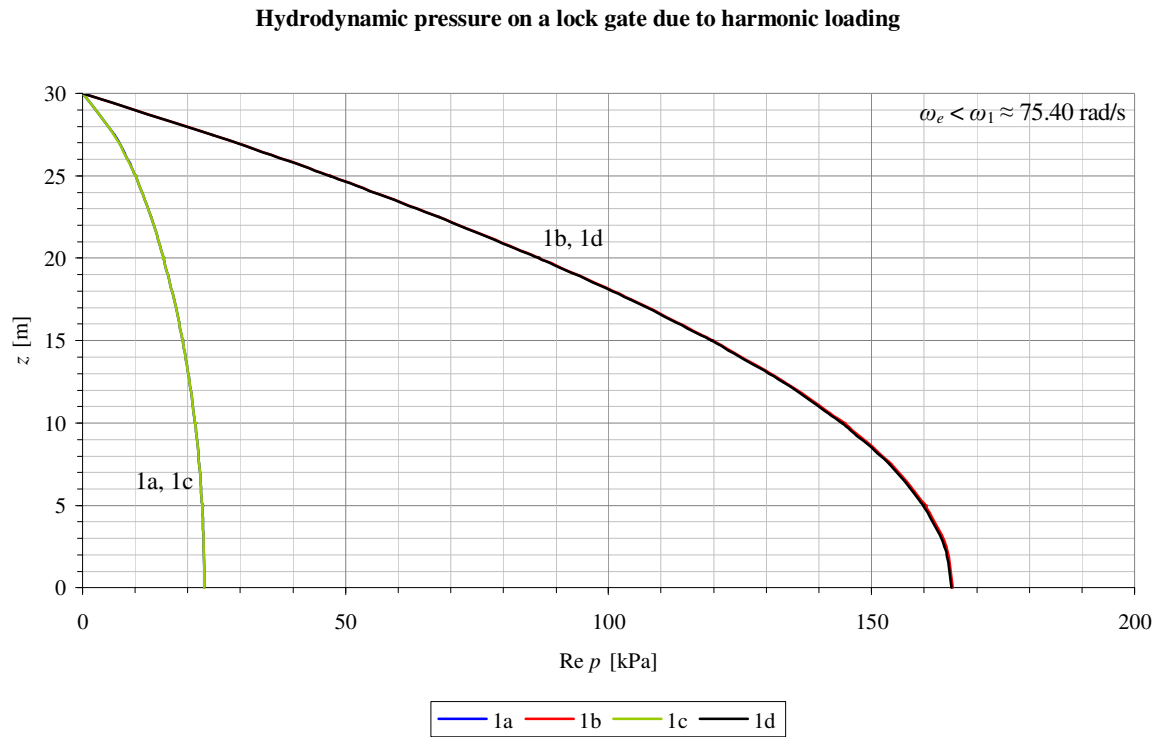


**Figure 8.11 Hydrodynamic pressure distribution at  $\omega_e < \omega_1 \approx 75.40 \text{ rad/s}$  (12.00 Hz)**

Hydrodynamic pressure on a lock gate due to harmonic loading

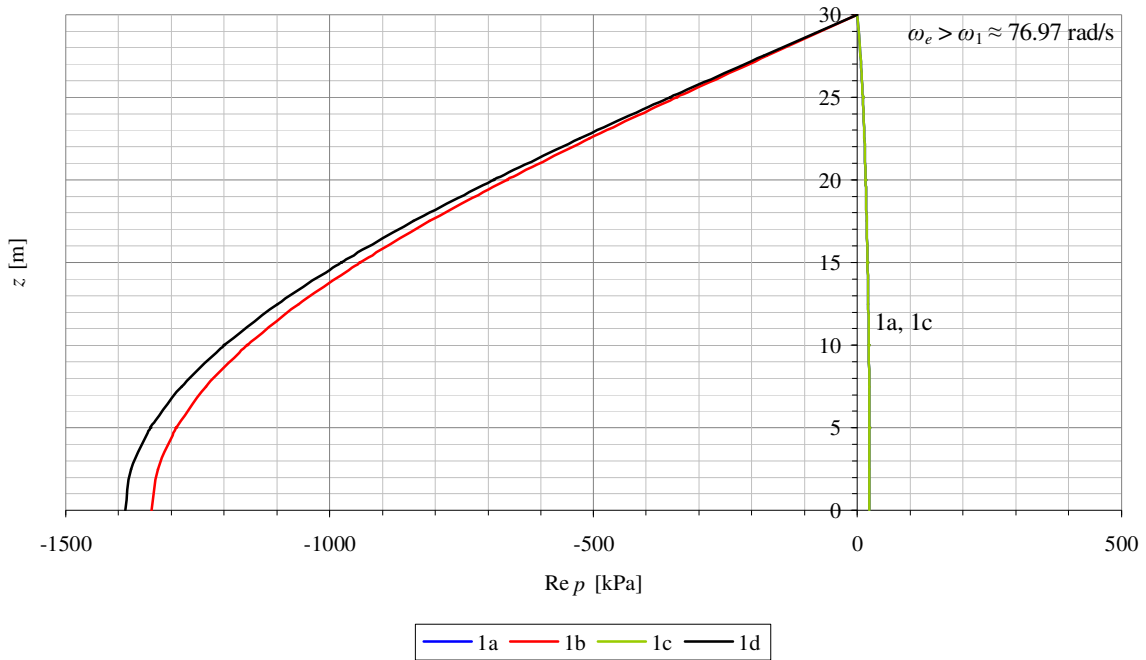


Figure 8.12 Hydrodynamic pressure distribution at  $\omega_e > \omega_1 \approx 76.97 \text{ rad/s}$  (12.25 Hz)

Hydrodynamic pressure on a lock gate due to harmonic loading

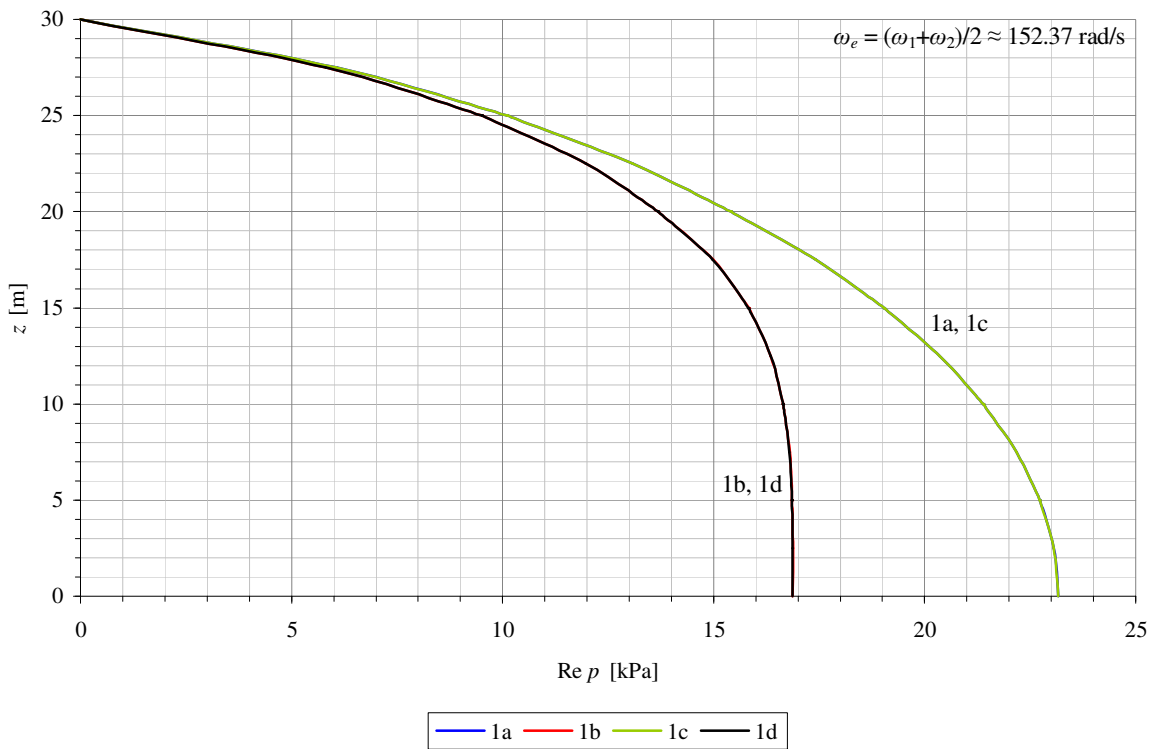


Figure 8.13 Hydrodynamic pressure distribution at  $\omega_e = (\omega_1 + \omega_2)/2 \approx 152.37 \text{ rad/s}$  (24.25 Hz)

Hydrodynamic pressure on a lock gate due to harmonic loading

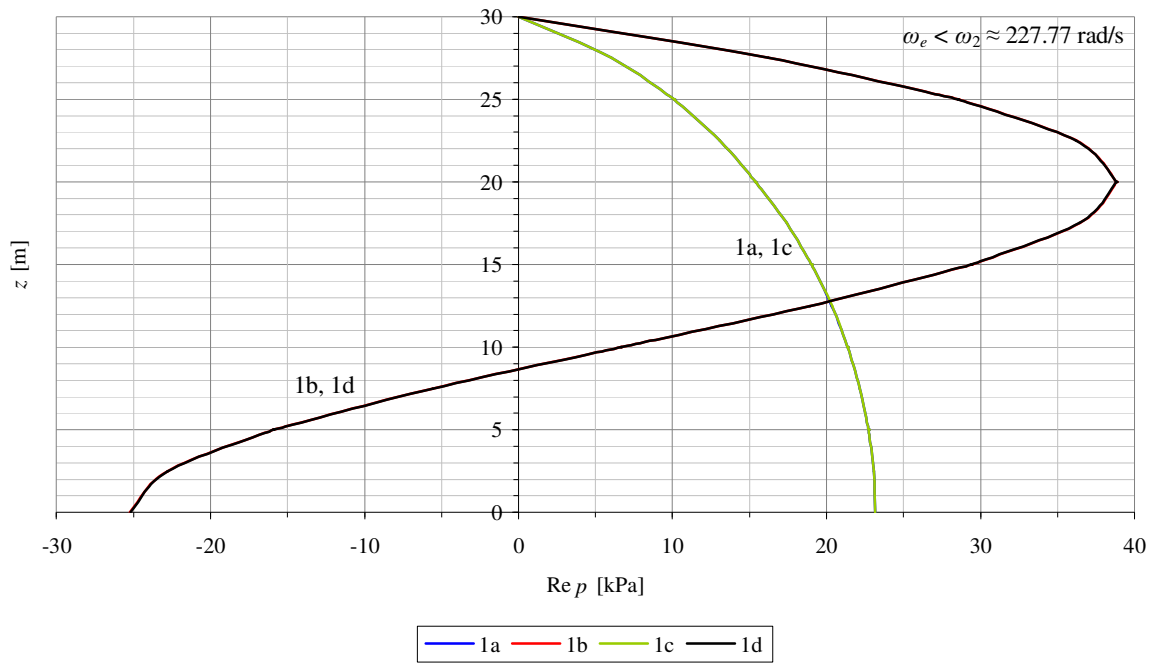


Figure 8.14 Hydrodynamic pressure distribution at  $\omega_e < \omega_2 \approx 227.77 \text{ rad/s}$  (36.25 Hz)

Hydrodynamic pressure on a lock gate due to harmonic loading

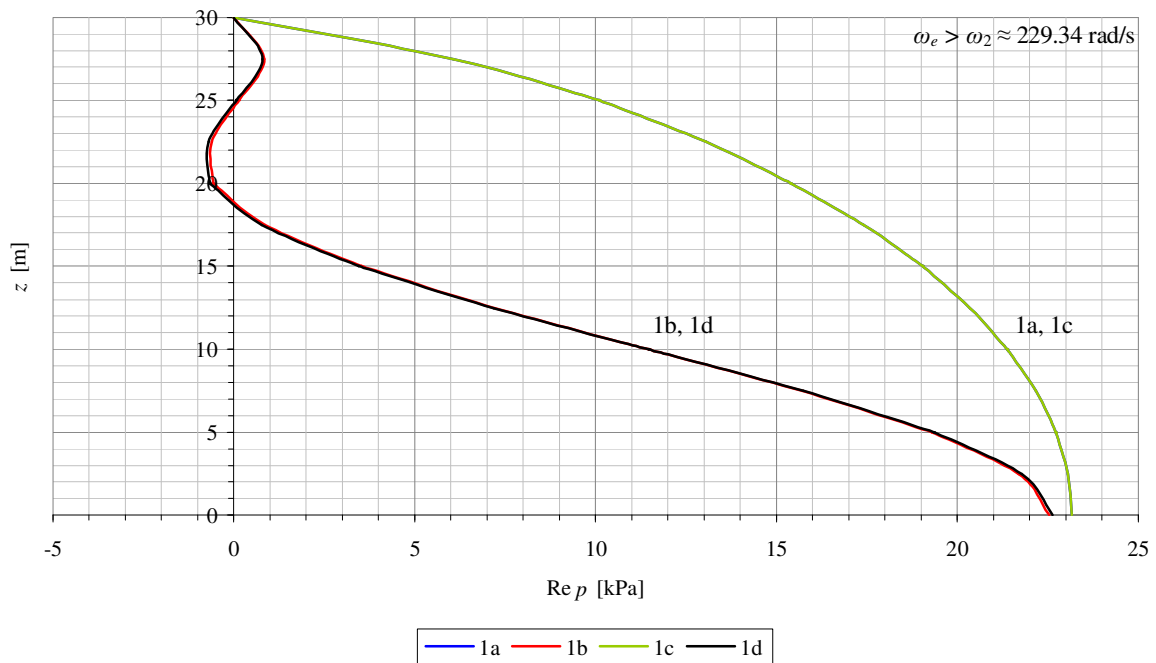


Figure 8.15 Hydrodynamic pressure distribution at  $\omega_e > \omega_2 \approx 229.34 \text{ rad/s}$  (36.50 Hz)

#### 8.4.5. Hydrodynamic pressure along the face of the gate (situation shorter intermediate chamber)

Unlike with the large chamber, the higher mode shapes are not visible for the 14 m chamber. In fact, the shape of the hydrodynamic pressure distribution is more or less constant. Corresponding figures to selected excitation frequencies can be found in table 8.2.

Figure	Excitation frequency $\omega_e$ [rad/s]	Excitation frequency $f_e$ [Hz]
Figure 8.16	$2\pi$	1.00
Figure 8.17	$\omega_1/2 \approx 37.70$	6.00
Figure 8.18	$< \omega_1 \approx 75.40$	12.00
Figure 8.19	$> \omega_1 \approx 76.97$	12.25
Figure 8.20	$(\omega_1+\omega_2)/2 \approx 152.37$	24.25
Figure 8.21	$< \omega_2 \approx 227.77$	36.25
Figure 8.22	$> \omega_2 \approx 229.34$	36.50

Table 8.2 Selected excitation frequencies with corresponding figures (situation long lock chamber)

Hydrodynamic pressure on a lock gate due to harmonic loading

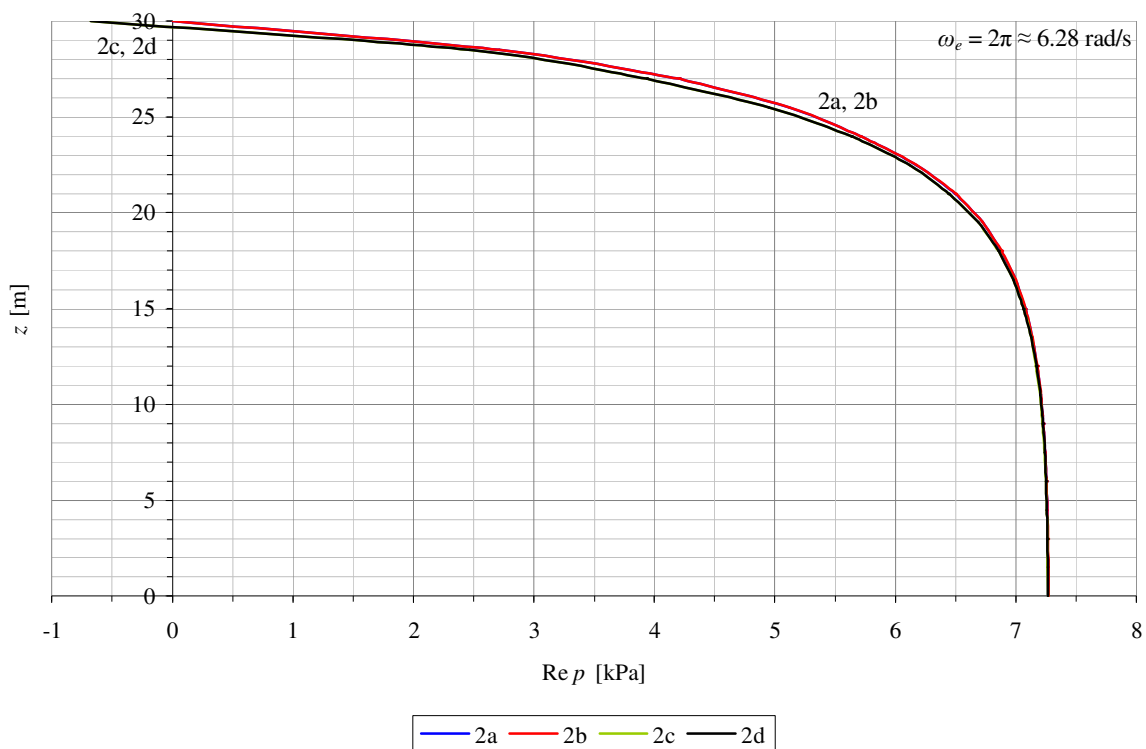


Figure 8.16 Hydrodynamic pressure distribution at  $\omega_e = 2\pi \approx 6.28$  rad/s (1.00 Hz)

Hydrodynamic pressure on a lock gate due to harmonic loading

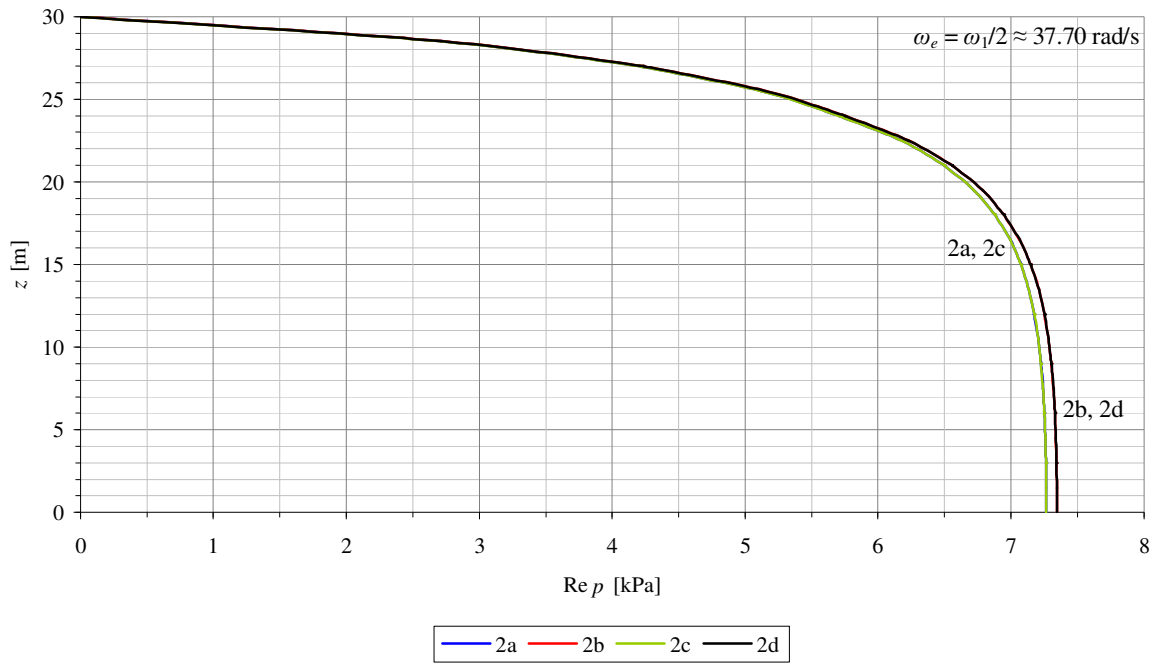


Figure 8.17 Hydrodynamic pressure distribution at  $\omega_e = \omega_1/2 \approx 37.70 \text{ rad/s}$  (6.00 Hz)

Hydrodynamic pressure on a lock gate due to harmonic loading

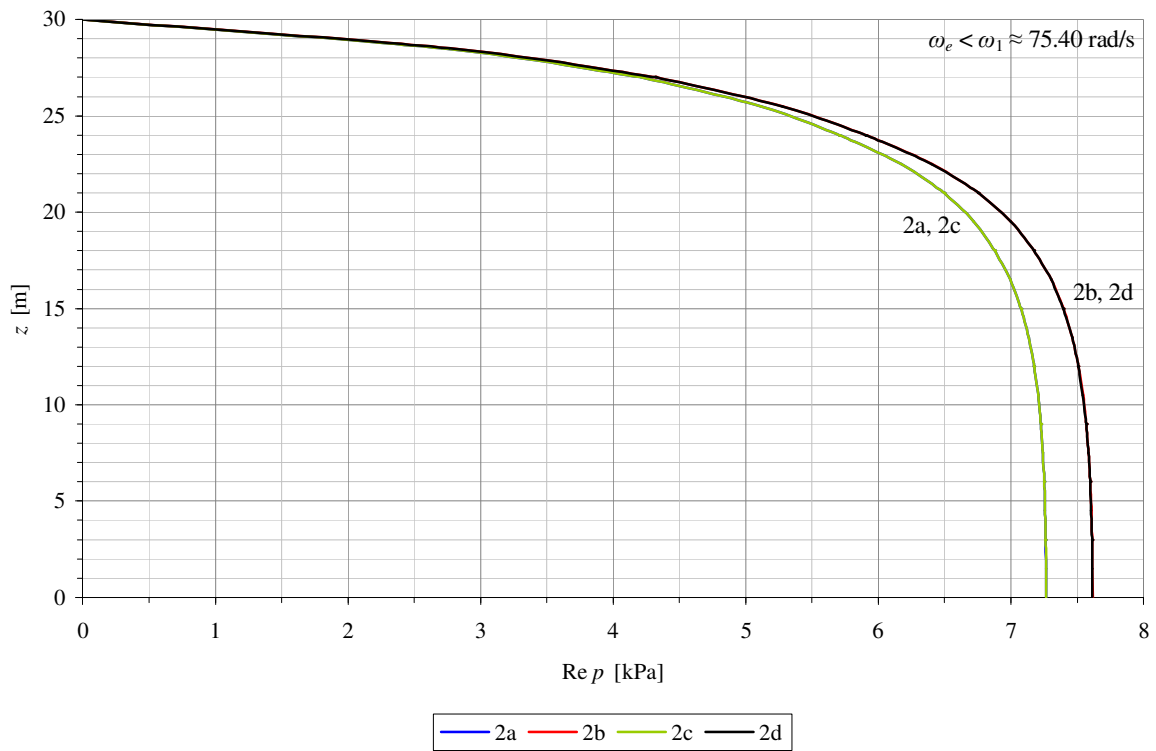
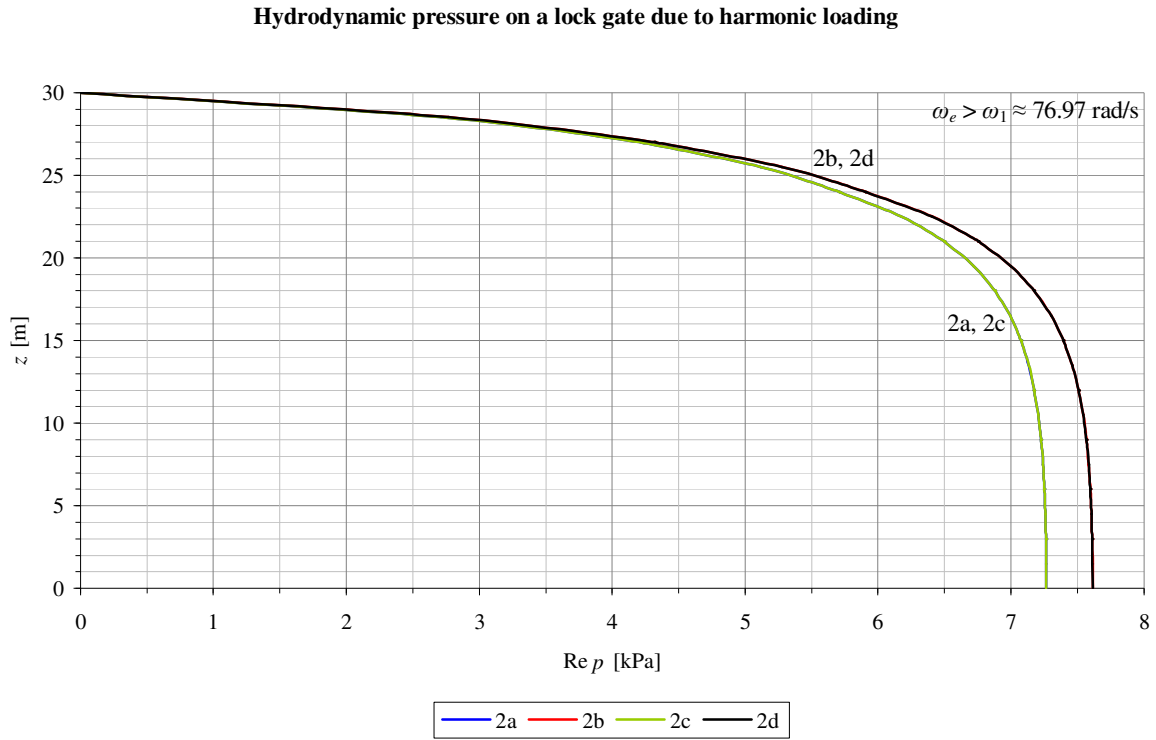
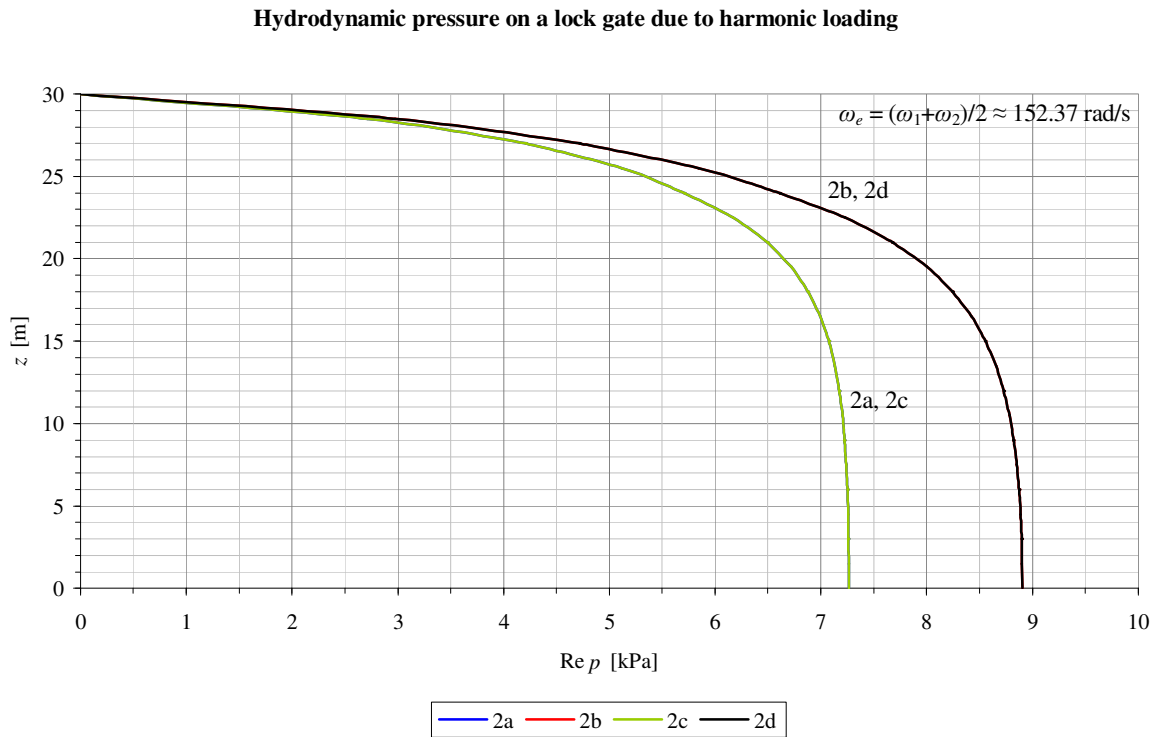


Figure 8.18 Hydrodynamic pressure distribution at  $\omega_e < \omega_1 \approx 75.40 \text{ rad/s}$  (12.00 Hz)



**Figure 8.19** Hydrodynamic pressure distribution at  $\omega_e > \omega_1 \approx 76.97 \text{ rad/s}$  (12.25 Hz)



**Figure 8.20** Hydrodynamic pressure distribution at  $\omega_e = (\omega_1 + \omega_2)/2 \approx 152.37 \text{ rad/s}$  (24.25 Hz)

Hydrodynamic pressure on a lock gate due to harmonic loading

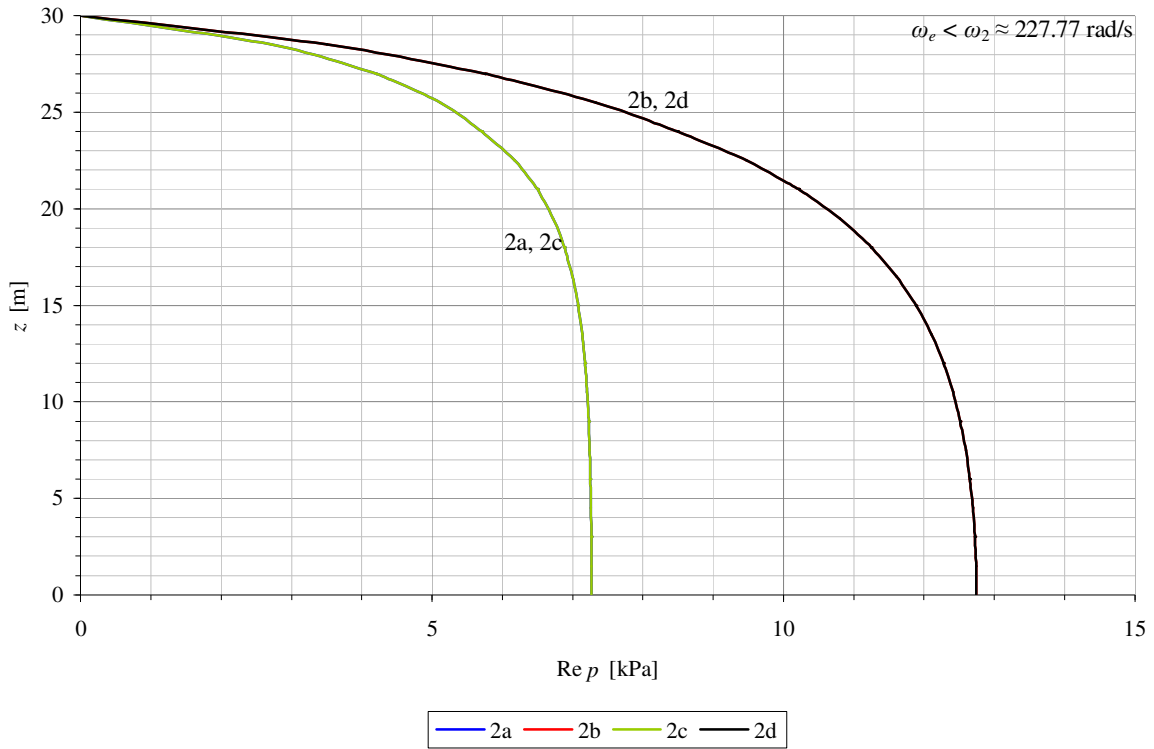


Figure 8.21 Hydrodynamic pressure distribution at  $\omega_e < \omega_2 \approx 227.77 \text{ rad/s}$  (36.25 Hz)

Hydrodynamic pressure on a lock gate due to harmonic loading

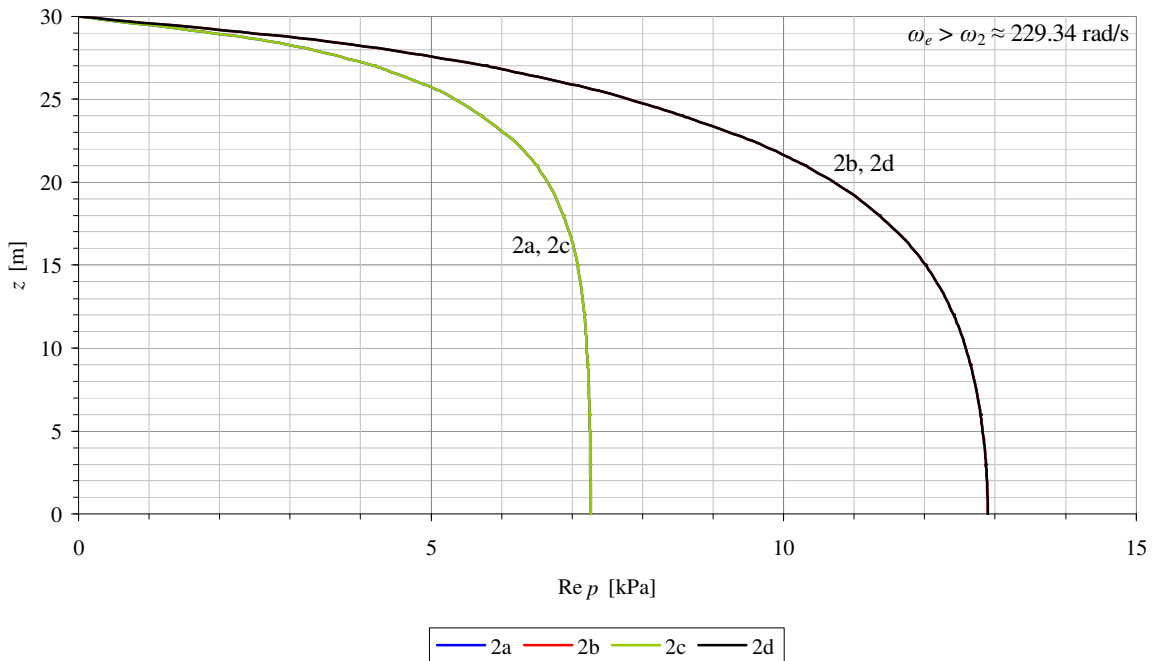
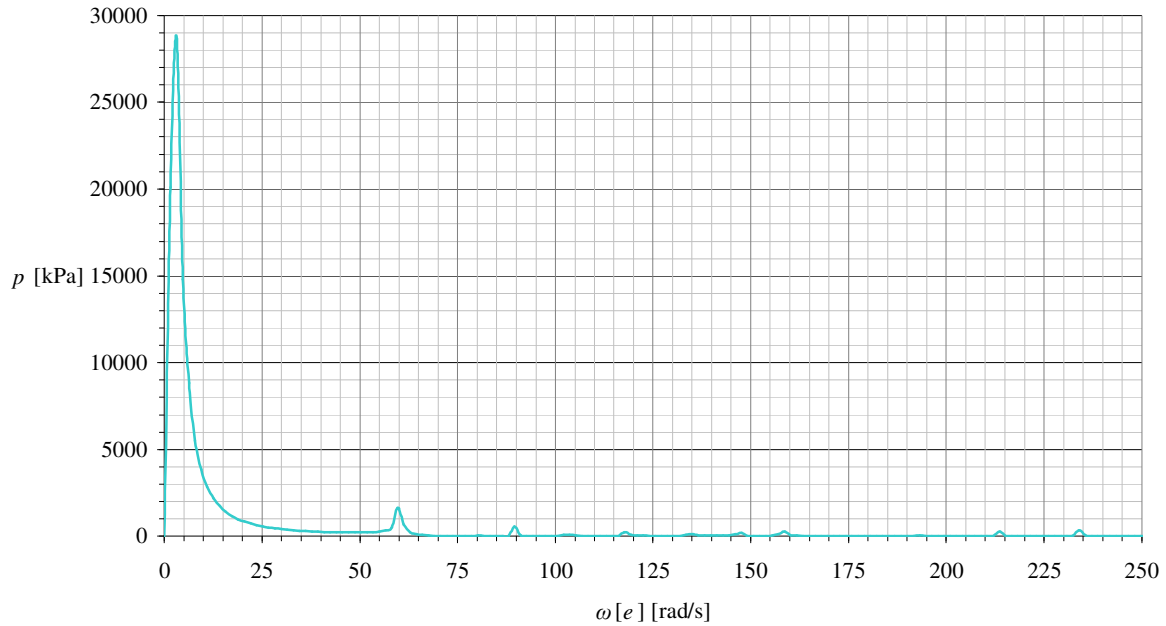


Figure 8.22 Hydrodynamic pressure distribution at  $\omega_e > \omega_2 \approx 229.34 \text{ rad/s}$  (36.50 Hz)

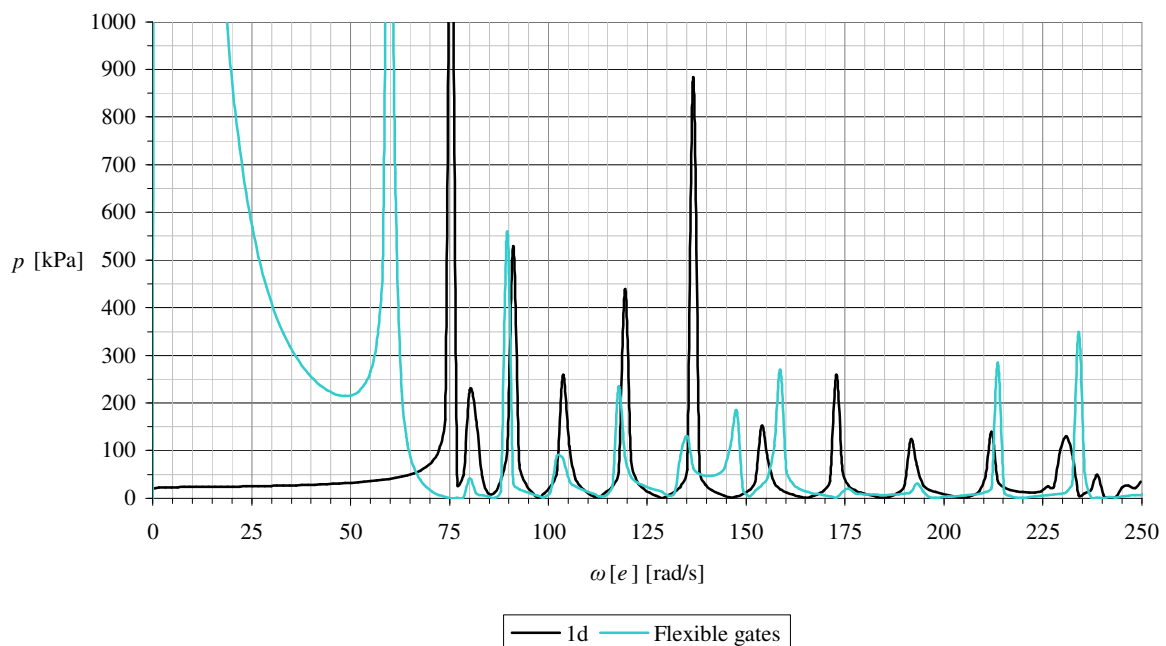
#### 8.4.6. Effect of the stiffness of the gates

The analytical and previous FEM results are based upon the assumption that the gates are rigid. With the removal of the tyings and added supports, the behavior of the gates will not be rigid anymore: the acceleration along the height of a gate will not be constant. This leads to different amplitudes and eigenfrequencies due to the bending stiffness of the gates. Results in the frequency domain for the bottom and top nodes can be found in figures 8.23 and 8.24; in which the results of case 1d and 2d are added as a reference. The pressure distributions on a gate are visualized in figure 8.25 and are computed for the same selected frequencies as before. Please note that the following results are based on a single case. The results are however significantly different.

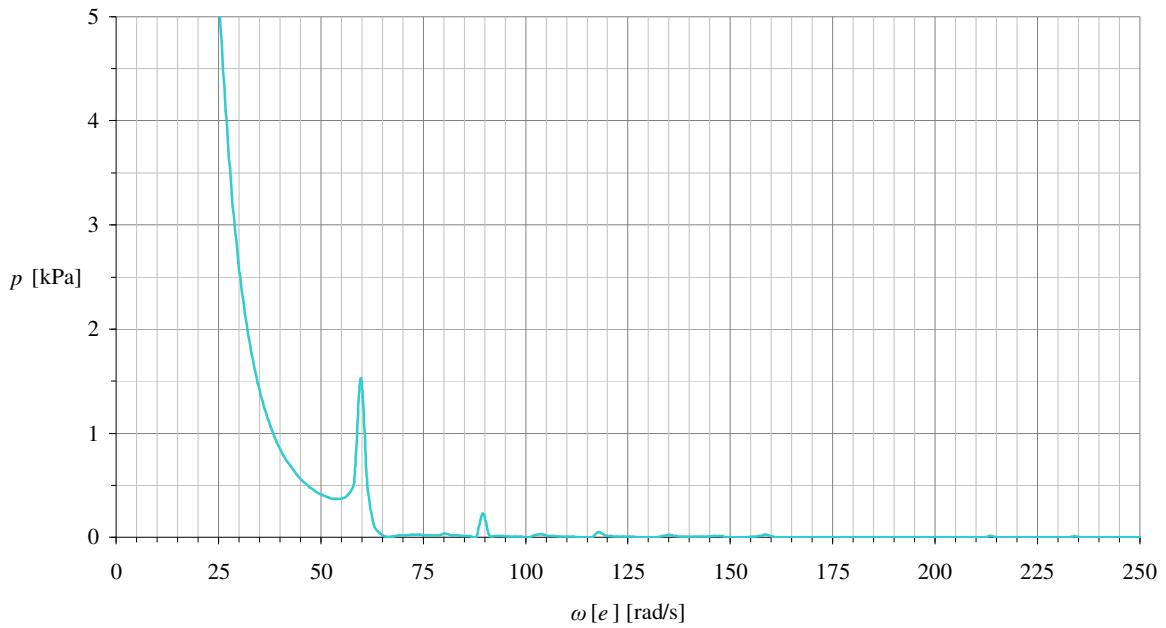
**Amplitude-frequency response function for the hydrodynamic pressure on a gate at bottom level (case flexible gates, long lock chamber)**



**Amplitude-frequency response function for the hydrodynamic pressure on a gate at bottom level (case flexible gates, long lock chamber)**

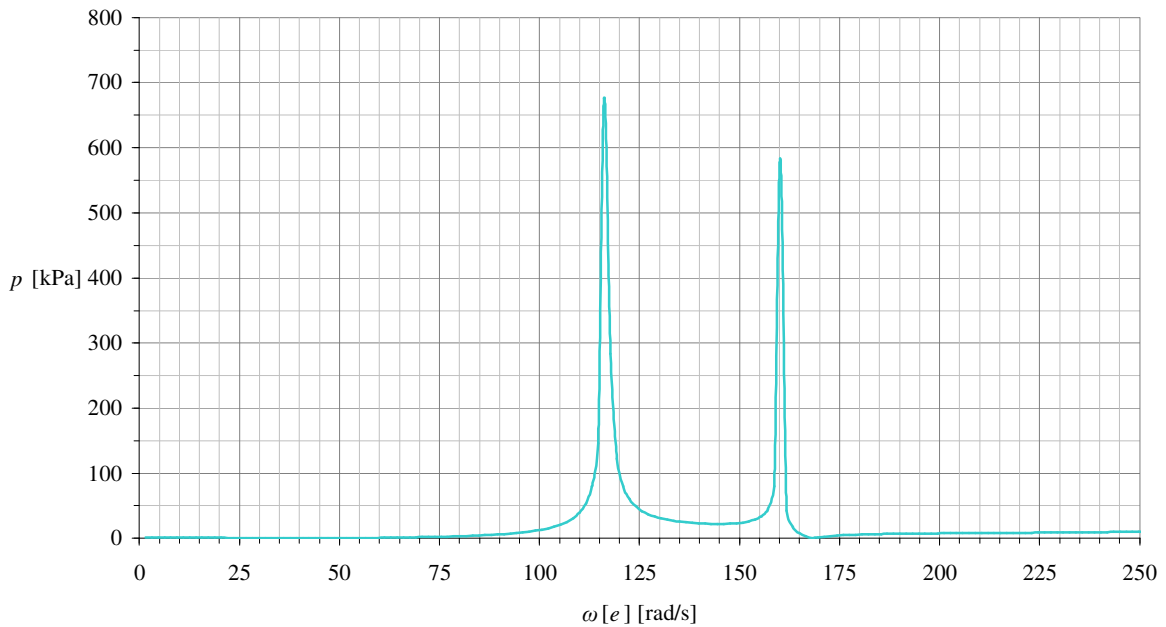


**Amplitude-frequency response function for the hydrodynamic pressure on a gate at top level  
(case flexible gates, long lock chamber)**



**Figure 8.23 Hydrodynamic pressures (case flexible gates, long lock chamber): bottom of gate (top), comparison with case 1d (center) and top of gate (bottom)**

**Amplitude-frequency response function for the hydrodynamic pressure on a gate at bottom level (case flexible gates, shorter intermediate chamber)**



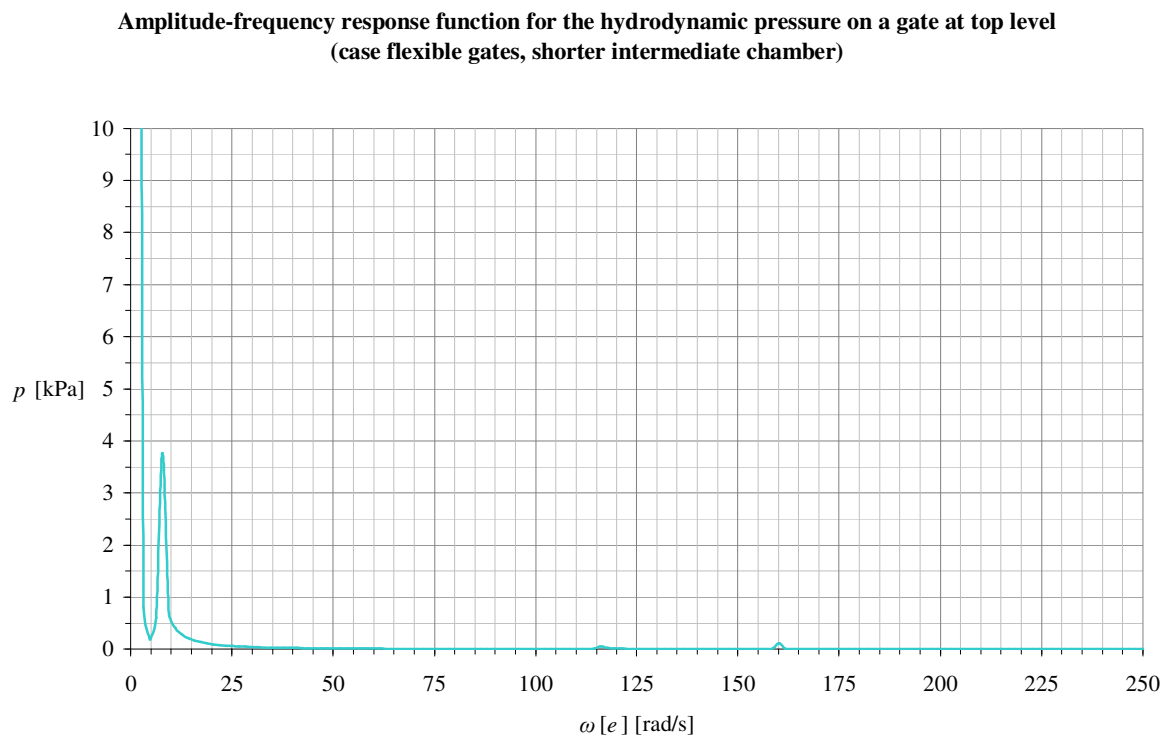
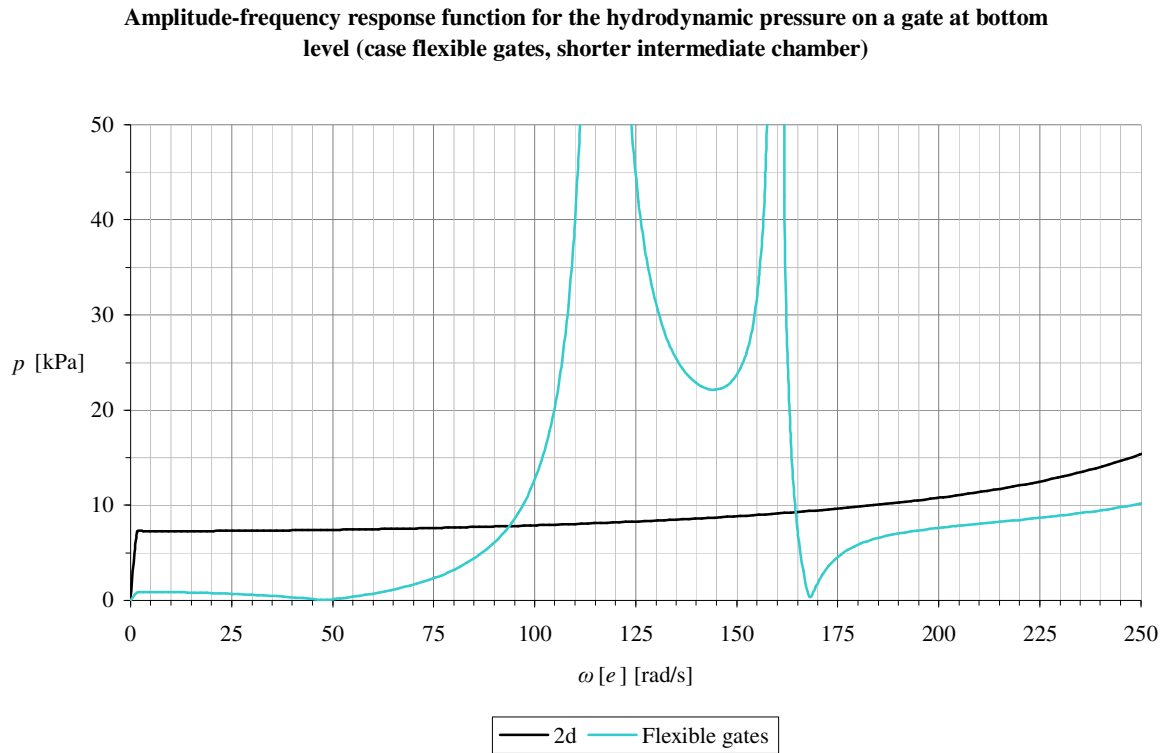
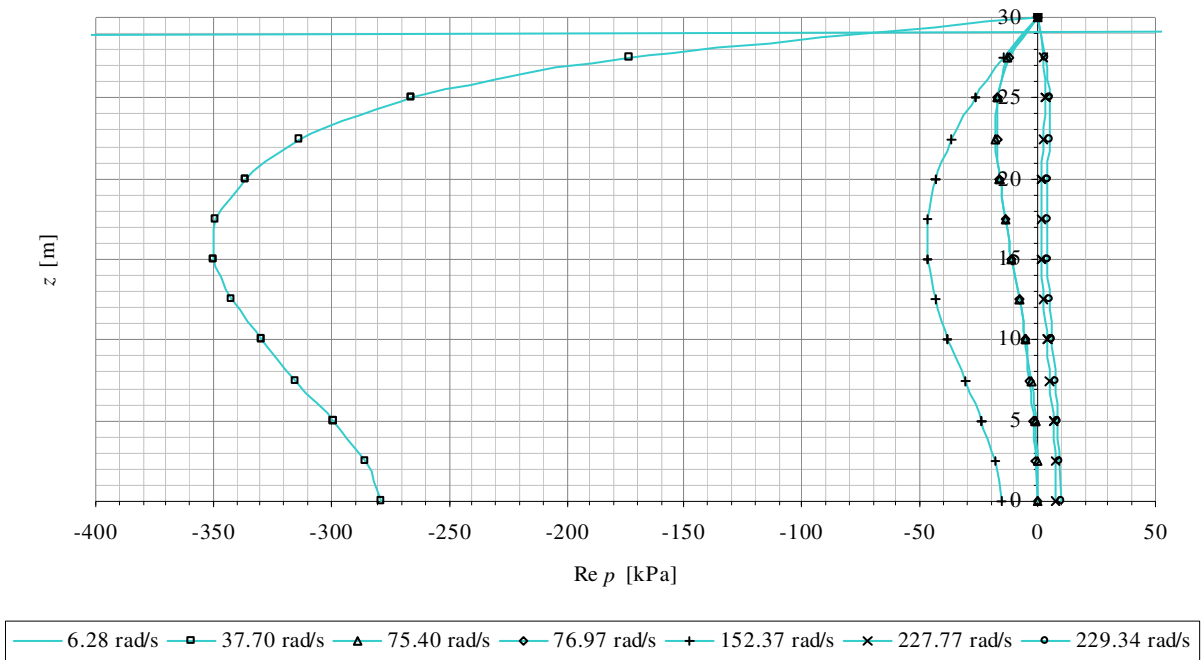


**Figure 8.24** Hydrodynamic pressures (case flexible gates, shorter intermediate chamber): bottom of gate (top), comparison with case 2d (center) and top of gate (bottom)

Hydrodynamic pressure on a flexible lock gate due to harmonic loading



Hydrodynamic pressure on a flexible lock gate due to harmonic loading

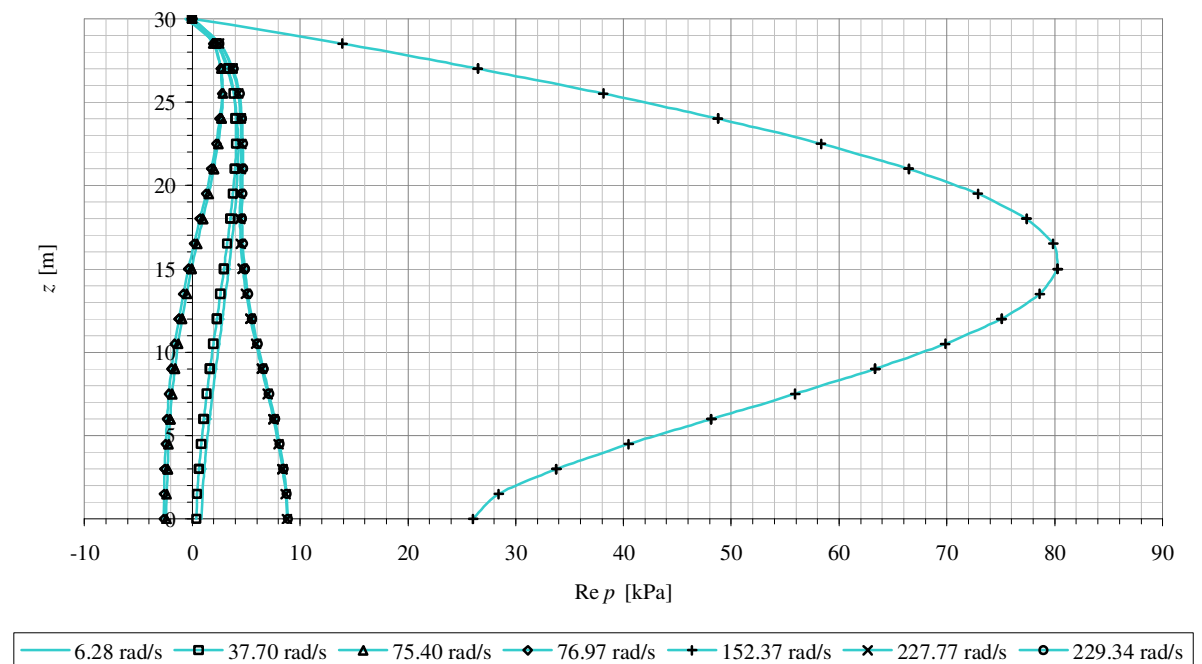


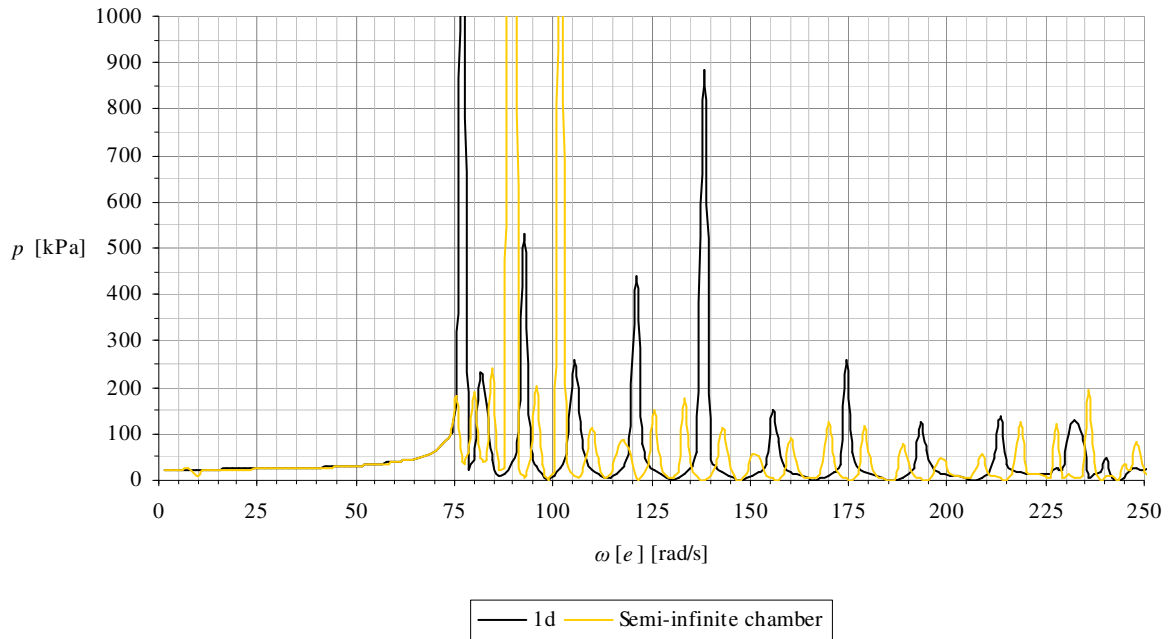
Figure 8.25 Hydrodynamic pressure distribution in case of flexible gates: situation long lock chamber (top) and situation shorter intermediate chamber (bottom)

8.4.7. Semi-infinite chamber

Previous models are all based on an enclosed chamber, with gates excited due to earthquake. The length of the lock chamber has an effect on the amplitude of the hydrodynamic pressure and the number of eigenfrequencies. An infinite length of the chamber is achieved by a radiation boundary. The energy that radiates from the source

(the gate) is absorbed by this boundary and no energy from infinity enters in the domain. Applied to figure 8.3 it means that (pressure) waves only move from left to right. Because of this frequency-dependent damping, the solution now also has an imaginary part. In the previous cases only a real part to the solution was present: the imaginary part was equal to zero for all cases at all frequencies. The imaginary part is however minor compared to the real part of the solution, but the mode shapes are identical. For low frequencies, results are the same as for an enclosed chamber. The eigenfrequencies at higher frequencies have the same pattern, but different values as with previous results. Refer to figures 8.26 and 8.27 for results; again, for the bottom nodes the result of case 1d is added as a reference.

**Amplitude-frequency response function for the hydrodynamic pressure on a gate at bottom level (case semi-infinite chamber)**



**Amplitude-frequency response function for the hydrodynamic pressure on a gate at top level (case semi-infinite chamber)**

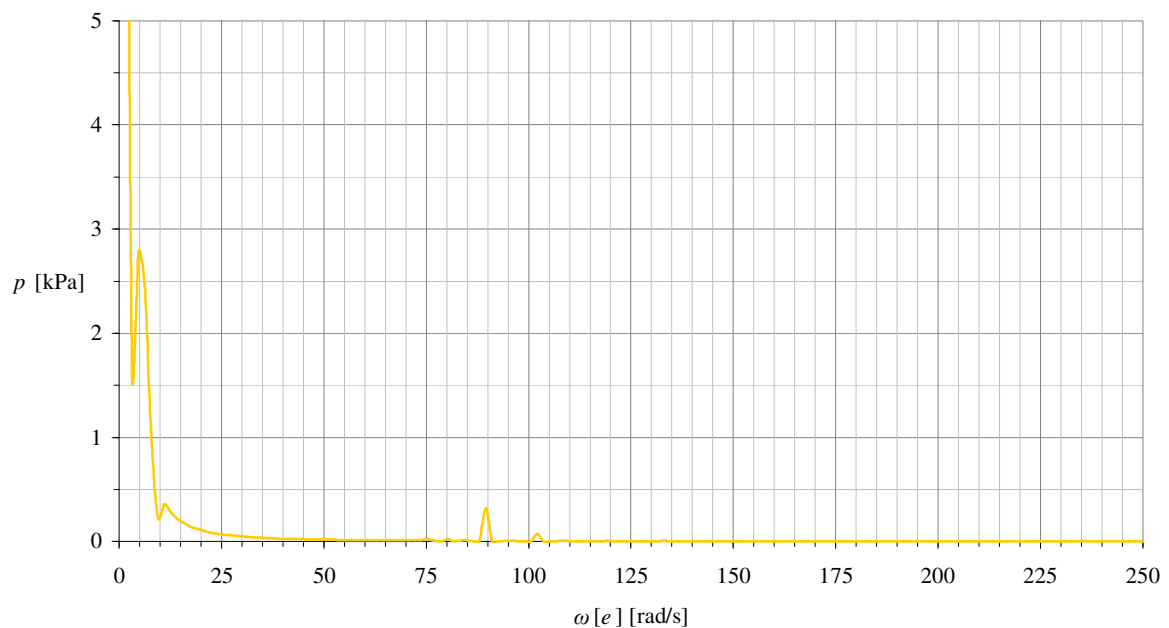


**Figure 8.26 Hydrodynamic pressures (case semi-infinite chamber): bottom of gate including comparison with case 1d (top) and top of gate (bottom)**

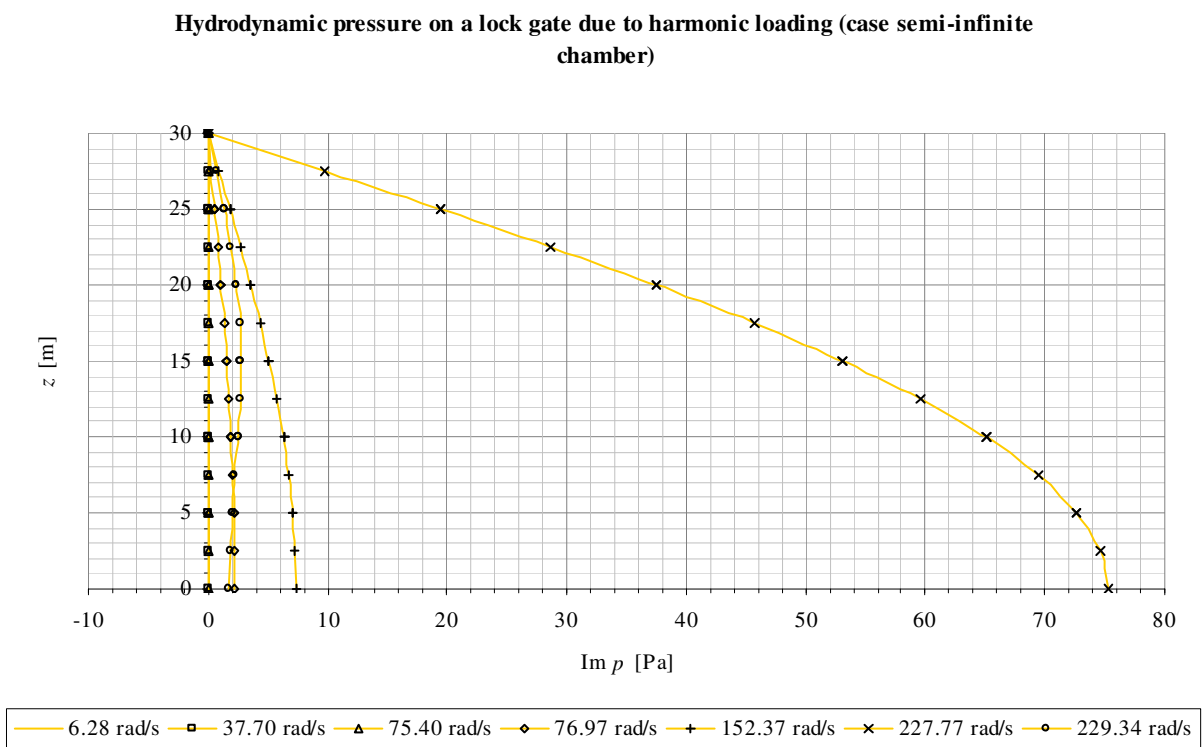
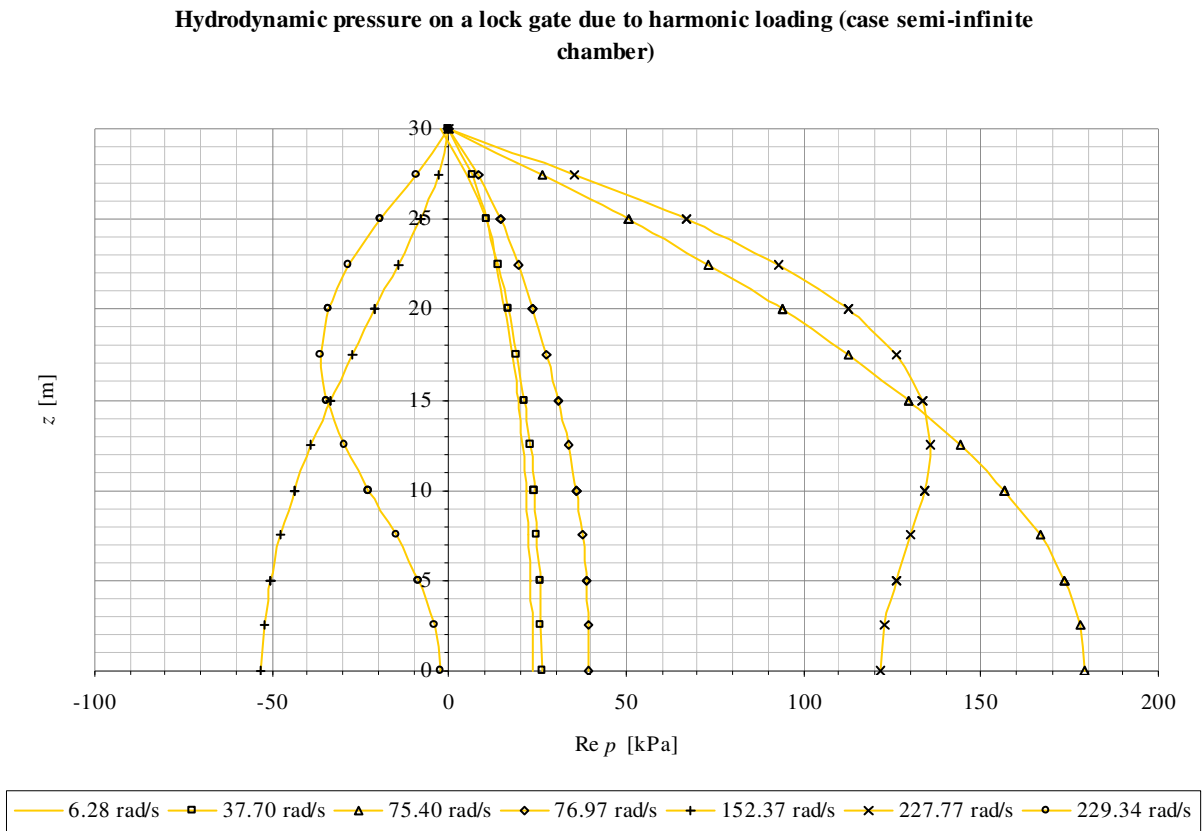


**Figure 8.27 Hydrodynamic pressure distribution in case of semi-infinite chamber: real (top) and imaginary parts (bottom)**

## 8.5. Conclusions 2D model for fluid-structure interaction

### 8.5.1. Solution

The DIANA model is based on the 2D analytical model. In order to ensure the gates are rigid, like in the analytical model, tyings are applied on the gates. For the calculation of hydrodynamic pressures the gates must have a differential acceleration with respect to the earthquake. This is achieved by adding a spring behind the gate, transforming it into an SDOF mass-spring system. Then, to eliminate the effect of the spring, the calculated pressures are scaled back to a gate acceleration of  $1 \text{ m/s}^2$ . This is possible due to the linear relation between the hydrodynamic pressure and the acceleration of the gate. Because of this setup a modal analysis is no longer possible, a direct frequency response approach is used. This means that the pressures are calculated for each frequency step. With this approach a phase shift between the two gates is not possible; the gates will therefore have the same acceleration. The approach is otherwise the same as with the 2D analytical model: two chamber dimensions are considered, with or without surface waves. The analytical model is based upon the assumption of incompressible water; with DIANA both compressible and incompressible water is investigated. As a result a larger frequency domain is treated.

### 8.5.2. Comparison of results with the 2D analytical model

Although there is a lot of similarity between the results of the 2D analytical model and the 2D FEM model, there is one essential difference: the DIANA models fails to identify the sloshing effects that are present in the analytical models. An exact reason why this is the case, is not found. The governing equation and the boundary conditions are the same in both approaches. Therefore, something in the FEM discretization or modeling of the problem does not implement the sloshing behavior correctly. The most likely is the used procedure to model and calculate the problem. The fluid-structure elements are based on a static interaction matrix  $\mathbf{R}^{13}$ , which relates unit displacements with pressures. It is therefore possible that the effect of the free surface boundary and thus sloshing is not taken into account in the interaction matrix, which dominates the computation. Another reason could be the used direct frequency approach with the rigid gates and tyings. As stated before, the exact reason is not known, but it clearly shows the possible different outcome of analytical and finite element results.

Apart from the above, the results obtained from the 2D analytical model (without phase shift) and the 2D FEM model have for the most part good resemblance in terms of amplitude; therefore the same conclusions can be made as with the analytical model in paragraph 7.10. There are however some differences:

- The pressure at the top of gate shows a different pattern at low frequencies as with the analytical model; besides the sloshing, this is most likely a result from the step size used. A smaller step size could give a higher accuracy. The effect of the pressure distribution on a gate is however the same, that is very limited;
- The DIANA model shows only real pressure for the regular models, the imaginary part is equal to zero. The analytical model did show both a real and imaginary part. This is a result of real matrices. In case of a radiation boundary there is a imaginary part because of the frequency-related damping;

Overall it can be concluded that the results from the 2D analytical and the DIANA model do well match in terms of amplitude, but the FEM approach does not identify the sloshing behavior. In reality these sloshing effects are however limited, but should be taken into consideration when a FEM calculation does not show any signs of sloshing.

### 8.5.3. Compressibility effects

Besides the impulsive and convective parts of the hydrodynamic pressure there is a third contribution from the compressibility of the fluid. As predicted in the evaluation of the analytical model; for lock structures, compressibility starts to play a role for relatively high frequencies. The results from cases 1b and 1d clearly shows this: besides the eigenfrequencies shown in the amplitude-frequencies response functions, the pressure distribution along the face of the gates shows interesting differences. The parabolic, or more precise the quarter sine-shape of the pressure distribution changes into higher modes shapes. This results in both a positive and negative pressure on the gate. Apart from the eigenfrequencies, the amplitudes are generally not higher than for low frequencies. For cases 2b and 2d, the eigenfrequencies related to a compressible fluid cannot be identified; either as a result of the used step size or because of the small length over depth ratio.

### 8.5.4. Special models

With the FEM model two additional cases are investigated that are more suited for a numerical than an analytical approach: flexible gates and a semi-infinite environment using a radiation boundary.

---

<sup>13</sup> Details can be found on pages 518–520 of the DIANA user's manual in appendix C.2

If the gates have a certain bending stiffness, instead of being rigid, the acceleration along the face will not be constant anymore. This influences the hydrodynamic pressure distribution on a gate. The eigenfrequencies of the system are no longer only a function of the water (mass of the system), but now also of the gate (stiffness of the system). The amplitude-frequency response functions show therefore a completely different frequency behavior, which does return in the pressure distribution on the gates. Although only one case is considered, with estimated parameters and supports, the behavior is different in such a way that the assumption of rigid gates might not be valid anymore.

For the case with a semi-infinite lock chamber this was achieved by means of a radiation boundary. Although the boundary was placed far way from the gate, no result comparable to Westergaard's or Chopra's solution was obtained. These solutions show only the depth-related eigenfrequencies due to the compressibility of the fluid; while with the finite-element model a result similar to a finite chamber length was achieved. The presence of the radiation boundary leads now to an imaginary part of the solution. The use of a semi-infinite environment did not produce a useful answer to the application to navigation locks.



## 9. Conclusions and recommendations

---

### 9.1. Conclusions

For the evaluation of hydrodynamic pressures on the gates and walls of large lock structures, two analytical (1D and 2D) and one 2D finite-element model are made. These models are based on linear theory. Three main aspects that contribute to hydrodynamic pressure are treated in detail:

- Lock dimensions and water levels;
- The effect of surface waves on the hydrodynamic pressure distribution;
- The stiffness of the structure.

In terms of dimensions, one of the main differences between lock chambers and large dams is the length of the chamber or reservoir. The length of the chamber affects the hydrodynamic pressures in two ways: it limits the impulsive (added mass) pressures but causes additional convective pressures due to sloshing. In general, the effect of the chamber length on the magnitude of the hydrodynamic pressure is however limited. Only in the case of a length over water depth ratio of 4 or smaller, there is a reduction of the pressure. For length over depth ratio higher than 4, results are identical. This means only the water close to the gate or wall reacts and that for large length the two boundaries can be treated individually. This is in agreement with the concept of added mass, which assumes a body of water moving with a wall. A phase difference between two boundaries has therefore almost no effect. Note that this can change for higher excitation frequencies.

The second way the chamber length influences the hydrodynamic pressure is a result of sloshing, which cannot occur in a semi-infinite environment. Although for the large lock chambers many sloshing frequencies can be found, in reality it takes too long for surface waves to cross the chamber to start the sloshing phenomenon. By that time the earthquake is already over. In case of a very small length also little to no sloshing effects are to be expected. If linear surface waves are neglected in the evaluation, the sloshing phenomenon cannot be identified. Given the fact that neglecting surface waves greatly simplifies the analysis and has almost no outcome on the solution; it can be concluded that this assumption of neglecting surface waves is also valid for navigation locks. This conclusion is based on the results obtained by the two analytical models. In the finite element results, no sloshing frequencies could be identified.

Another difference in dimensions between navigation locks and large, high-head dams is the water depth. If compressibility of water is taken into account, the impounded water has eigenfrequencies for hydrodynamic pressure. These eigenfrequencies are inversely proportional to the water depth, meaning that the fundamental eigenfrequency is lower for larger water depth. The water depth inside a navigation lock is directly related to the draught of the design vessel and is therefore much smaller than in the case of a high-head dam. For the maximum water depth of the Post-Panamax locks, around 30 m, the fundamental eigenfrequency related to compressibility is larger than the frequencies at which the most energy of an earthquake is distributed. For excitation frequencies below this fundamental eigenfrequency, the amplitude of hydrodynamic pressure is almost independent of the excitation frequency. Also, the assumption of incompressible water gives in this situation similar results. Therefore, the limited water depth in navigation locks means that in practice the hydrodynamic pressure is constant for the considered frequencies and the assumption of incompressible water is valid. The pressure distribution along the face of a gate/wall remains parabolic in this frequency range. For higher excitation frequencies, above the fundamental eigenfrequency related to compressibility, the pressure distribution is no longer parabolic, but sinusoidal and the assumptions are not valid anymore.

The above conclusions are based on the assumption of rigid gates and/or walls. With the aid of the 2D finite element model rigid gates were replaced with gates with a certain bending stiffness. The bending stiffness of the used gates and the position of the supports are estimated, but the result in amplitude is significantly different. The maximum pressure along the face is no longer at the bottom of the gate, but higher up. Although this applies to a single case, it shows that the assumption of rigid gates/walls has to be applied with care.

### 9.2. Recommendations

Based on the findings of this thesis the following recommendations can be made:

- The performed analyses are performed in a 2D environment, with direction of earthquake loading perpendicular to a lock gate. Other source-to-site directions and the effects of the side walls are not incorporated. The reduced amount of water that can react in both cases should lead to a reduction of the hydrodynamic pressure compared to the case in a 2D environment. This is shown by effect of the length of the chamber. The presence of a ship inside the lock chamber during an earthquake might also reduce the hydrodynamic pressure on the structure as the amount of water inside the chamber is less due to the displacement of the vessel. With a 3D analysis these effects can be investigated.

- Surface waves and effects like sloshing have little to no influence on the total pressure distribution. Therefore the assumption that the pressure at the water surface is equal to zero is also valid for navigation locks and recommended for practical design.
- The stiffness of the structure is not incorporated in the solution of the 2D analytical model or the Westergaard and Housner solution. An adaption of the 2D finite element model showed that the stiffness and support system of a lock gate do change the loading on the lock gate. Therefore it is recommended that a preliminary analysis is made to investigate if a closed or (semi-)opened gate, or the chamber itself can be treated as rigid. If not, the stiffness of the structure should be incorporated in the evaluation, as it can result in a significant in- or decrease of the hydrodynamic loading.
- Not only the horizontal component of an earthquake, but also the vertical component causes hydrodynamic pressures on walls. This aspect is not treated in this thesis, but would be an interesting element to include in future studies. The vertical component is in general smaller than the horizontal component.
- Analyses made in this thesis are done in the frequency domain; a time domain analysis is not performed but gives more insight in the hydrodynamic pressures during the event of an earthquake.
- The existing analytical methods by Westergaard or Housner give adequate accuracy and can be used in early design stages. The loads can be evaluated by means of pressure or the concept of added mass. An estimate for the accuracy can be obtained by comparing a spectrum with the fundamental eigenfrequency for the maximum design water level. For later design stages the use of advanced methods should be used to determine the hydrodynamic pressures and consequently the response of the structure. As stated before, the analytical Westergaard and Housner approaches do not incorporate the frequency-dependent motion of the structure, but assume a rigid behavior. A finite element analysis using fluid-structure interaction can incorporate these effects and will therefore give in general a more accurate result. That this is not always the case followed from the finite element model used in this thesis, which failed to identify possible sloshing frequencies.

## References

---

- BATTJES, J.A. (2002a) Fluid Mechanics. *Lecture notes CT2100, Faculty of Civil Engineering and Geosciences, Delft University of Technology, Delft*, pp. 47–65 (in Dutch)
- BATTJES, J.A. (2002b) Open Channel Flow. *Lecture notes CT3310, Faculty of Civil Engineering and Geosciences, Delft University of Technology, Delft*, pp. 7–24, 43–44, 50 (in Dutch)
- BRAHTZ, J.H.A. AND HEILBRON, C.H. (1933) Discussion on "Water Pressures on Dams During Earthquakes" by H.M. Westergaard. *Transactions, American Society of Civil Engineers (ASCE), Vol. 98, Paper No. 1835, New York City, NY*, pp. 452–454
- CHOPRA, A.K. (1966) Hydrodynamic Pressures on Dams During Earthquakes. *Report No. 66-2, Department of Civil Engineering, University of California, Berkeley, CA*, pp. 1–14
- HOLTHUIJSEN, L.H. (2007) Waves in Oceanic and Coastal Waters. *Cambridge University Press, Cambridge*, pp. 109–128, 342–345
- HOUSNER, G.W. (1954) Earthquake Pressures on Fluid Containers. *Eight Technical Report under Office of Naval Research, California Institute of Technology, Pasadena, CA*, pp. 1–13
- KRAMER, S.L. (1996) Geotechnical Earthquake Engineering. *Prentice Hall, Upper Saddle River, NJ*, pp. 536, 571
- KWON, T.H. (2005) Introduction to Finite Element Method. *Department of Mechanical Engineering, Pohang University of Science & Technology, Pohang*, pp. 5–6
- LIVAOGLU, R. (2008) Investigation of seismic behavior of fluid-rectangular tank-soil/foundation systems in frequency domain. *Journal, Soil Dynamics and Earthquake Engineering, Vol. 28*, pp. 132–134
- MOLENAAR, W.F., VAN BAARS, S., KUIJPER, H.K.T ET AL. (2008) Manual Hydraulic Structures – Loads, Materials and Temporary Structures. *Lecture notes CT3330, Faculty of Civil Engineering and Geosciences, Delft University of Technology, Delft*, pp. 1-48, 1-66–1-69
- NOZU, A., ICHII, K. AND SUGANO, T (2004) Seismic Design of Port Structures. *Journal of Japan Association for Earthquake Engineering, Vol. 4, No. 3 (Special Issue)*, pp. 197–198
- PANAMA CANAL AUTHORITY (2006) Proposal for the Expansion of the Panama Canal – Third Set of Locks Project, pp. 3–12, 41–49
- PAYER, H.G. (2005) Adequacy of Selected Lock Size Parameters for Expanded Panama Canal – Post-Panamax Lock Size Review Study. pp. 21–22
- TNO DIANA (2008) User's Manual – Analysis Procedures. *Release 9.3, TNO DIANA BV, Delft*, Edited by J. Manie and W.P. Kikstra, pp. 516–524
- U.S. ARMY CORPS OF ENGINEERS (2006) Coastal Engineering Manual – Part VI. *Publication Number EM 1110-2-1100, Proponent CECW-EW, Publication Date 1 June 2006, Washington, D.C.*, pp. VI-5-132–VI-5-136
- U.S. ARMY CORPS OF ENGINEERS (2003) Engineering and Design – Response Spectra and Seismic Analysis for Concrete Hydraulic Structures. *Publication Number EM 1110-2-6050, Proponent CECW-ET, Publication Date 30 June 1999, Washington, D.C.*, pp. 1-6, 2-13–2-21
- U.S. ARMY CORPS OF ENGINEERS (2003) Engineering and Design – Time-History Dynamic Analysis of Concrete Hydraulic Structures. *Publication Number EM 1110-2-6051, Proponent CECW-EW, Publication Date 22 December 2003, Washington, D.C.*, pp. 1-3–1-12, 2-25–2-37
- U.S. ARMY CORPS OF ENGINEERS (2007) Engineering and Design – Earthquake Design and Evaluation of Concrete Hydraulic Structures. *Publication Number EM 1110-2-6053, Proponent CECW-CE, Publication Date 1 May 2007, Washington, D.C.*, pp. 7-2, 4-1–4-5
- U.S. GEOLOGICAL SURVEY (1998) Map of Quaternary Faults and Folds of Panama and Its Offshore Regions. *Open File Report OFR 98-779*
- WESTERGAARD, H.M. (1933) Water Pressures on Dams During Earthquakes. *Transactions, American Society of Civil Engineers (ASCE), Vol. 98, Paper No. 1835, New York City, NY*, pp. 418–433



## Appendix A: Geological map of the Isthmus of Panama

---

### **A.1 Explanation**

This map [U.S. GEOLOGICAL SURVEY, 1998] shows detailed information of Panama's geological situation. The main map shows the location of fault lines, while the right hand side shows information over tectonic plate movement, and historic earthquakes. In the Canal Zone (Map A) the two major sources of earthquakes are the Rio Gatún fault (PA-13b) and the Pedro Miguel-Limón fault (part of PA-14). The North Panama Deformed Panama Belt is another source for earthquake. This major subduction zone is located a little over 100 km north of the Atlantic locks.





## Appendix B: Derivations and detailed calculations

### B.1 The Westergaard and Chopra solutions in detail

Chopra's solution [CHOPRA, 1966] is in the frequency domain in shown in equation (B.1):

$$p(x, z, t) = \frac{4\rho a}{\pi} \sum_{n=1}^{\infty} \frac{(-1)^{n-1}}{(2n-1) \sqrt{\alpha_n^2 - \frac{\omega_e^2}{c_p^2}}} e^{-x \sqrt{\alpha_n^2 - \frac{\omega_e^2}{c_p^2}}} \cos(\alpha_n z) e^{i\omega_e t} \quad (\text{B.1})$$

with:

$$\alpha_n = \frac{(2n-1)\pi}{2d} \quad (\text{B.2})$$

This solution is derived from the 2D wave equation (7.1) with the boundary conditions used by Westergaard (mentioned in paragraph 7.1). An identical procedure for finding Westergaard's and Chopra's solution, including derivations, is performed in chapter 7 and therefore not repeated here.

Taking the real part of equation (B.1) at  $x = 0$  results in:

$$p(0, z, t) = \frac{4\rho a}{\pi} \left\{ \sin(\omega_e t) \sum_{n=1}^{n_s-1} \frac{(-1)^{n-1} \cos(\alpha_n z)}{(2n-1) \sqrt{\frac{\omega_e^2}{c_p^2} - \alpha_n^2}} + \cos(\omega_e t) \sum_{n=n_s}^{\infty} \frac{(-1)^{n-1} \cos(\alpha_n z)}{(2n-1) \sqrt{\alpha_n^2 - \frac{\omega_e^2}{c_p^2}}} \right\} \quad (\text{B.3})$$

where  $n_s$  is a minimum value of  $n$  such that:

$$\alpha_n^2 > \frac{\omega_e^2}{c_p^2} \quad (\text{B.4})$$

Rewriting Westergaard's solution in equation (4.4), using the same notation, results in:

$$p(0, z, t) = \frac{4\rho a}{\pi} \cos(\omega_e t) \sum_{n=1}^{\infty} \frac{(-1)^{n-1} \cos(\alpha_n z)}{(2n-1) \sqrt{\alpha_n^2 - \frac{\omega_e^2}{c_p^2}}} \quad (\text{B.5})$$

Both results are equal in the case of:

$$\alpha_1^2 > \frac{\omega_e^2}{c_p^2} \quad \text{or} \quad \omega_1 < \frac{\pi c_p}{2d} \quad \text{or} \quad T_1 > \frac{4d}{c_p} \quad (\text{B.6})$$

The result of the Chopra formula in the frequency domain is shown in figure B.1. The theoretical eigenfrequencies are clearly visible, note that Chopra's solution concerns a semi-infinite environment.

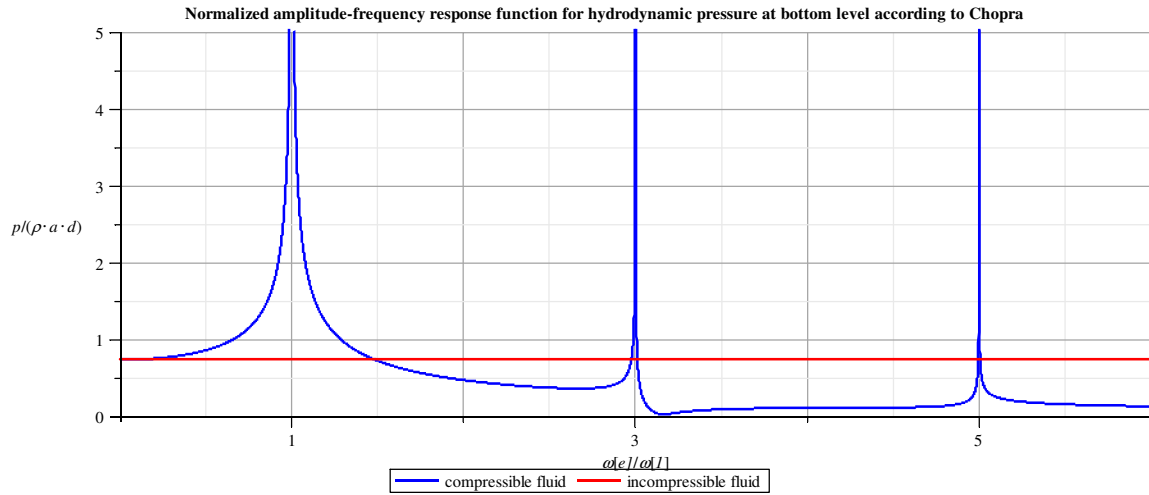


Figure B.1 Hydrodynamic pressures according to Chopra

## B.2 Solving Housner's SDOF model

In equation (6.11) the equation of motion for a SDOF mass-spring system is derived. Applied to the convective force in figure 5.2 yields:

$$M_1 \ddot{u}_1 + K_1 u_1 = -M_1 a_{\max} \sin(\omega_e t) \quad (\text{B.7})$$

As the loading is sinusoidal, the steady-state solution is sought in the form of:

$$u_1 = \hat{U}_1 \sin(\omega_e t) \quad (\text{B.8})$$

in which  $\hat{U}_1$  is a constant. Substitution of the particular solution (B.8) into the equation of motion (B.7) results in:

$$(-\omega_e M_1 + K_1) \hat{U}_1 = -M_1 a_{\max} \Rightarrow \hat{U}_1 = \frac{-M_1}{(-\omega_e M_1 + K_1)} a_{\max} \quad (\text{B.9})$$

Equation (B.9) can be rewritten into:

$$\hat{U}_1 = \frac{-a_{\max}}{\omega_e^2} \left( \frac{1}{1 - \frac{\omega_e^2}{\omega_1^2}} \right) \quad (\text{B.10})$$

This results in a displacement and acceleration of:

$$u_1(t) = \frac{-a_{\max}}{\omega_e^2} \left( \frac{1}{1 - \frac{\omega_e^2}{\omega_1^2}} \right) \sin(\omega_e t) \quad (\text{B.11})$$

$$\ddot{u}_1(t) = a_{\max} \left( \frac{1}{1 - \frac{\omega_e^2}{\omega_1^2}} \right) \sin(\omega_e t)$$

The reaction force on the walls, the force in the spring, follows now from:

$$F_1(t) = F_{spring}(t) = K_1 u_1(t) = -M_1 a_{\max} \left( \frac{1}{1 - \frac{\omega_e^2}{\omega_1^2}} \right) \sin(\omega_e t) \quad (\text{B.12})$$

The amplitude-frequency response function is equal to:

$$\left| \frac{F_1}{M_1 a_{\max}} \right| = \left| \frac{1}{1 - \frac{\omega_e^2}{\omega_1^2}} \right| \quad (\text{B.13})$$

### B.3 Derivation of the 1D shallow water equations

#### B.3.1 Introduction

Surface waves inside the lock chambers are modeled with the 1D wave equation, which can be derived from the 1D shallow water equations. The 1D wave equation is treated in appendix B.4. The shallow water equation is a combination of the 1D continuity and momentum balance equations. These two equations describe the equilibrium of water particles in motion.

#### B.3.2 Continuity equation

Let's consider a small control area with a width of  $\Delta x$  shown in figure B.2 in a short period of time  $\Delta t$ . There is an inflow  $q_1$  and an outflow  $q_2$ . The water depth and the flow are both functions of time and space. The net flow into the considered control area is equal to:

$$(q_1 - q_2) \Delta t = -\Delta q \Delta t \quad (\text{B.14})$$

This means that if this is positive, there is more inflow than outflow and the volume in the balance area increases:

$$\Delta V = (h_2 - h_1) \Delta x = \Delta h \Delta x \quad (\text{B.15})$$

Now, setting equation (B.14) equal to equation (B.15) leads to:

$$-\Delta q \Delta t = \Delta h \Delta x \quad (\text{B.16})$$

Dividing by  $\Delta x$  and  $\Delta t$  yields in the limit for  $\Delta x \rightarrow 0$  and  $\Delta t \rightarrow 0$ :

$$\frac{\partial h}{\partial t} + \frac{\partial q}{\partial x} = 0 \quad (\text{B.17})$$

The specific discharge  $q$  can be rewritten into term of depth  $h$  and velocity  $v$  by means of the following relation:

$$q = hv \quad (\text{B.18})$$

Substituting equation (B.18) into equation (B.17) leads to the mass-balance or continuity equation expressed in terms of water level and velocity:

$$\frac{\partial h}{\partial t} + \frac{\partial (hv)}{\partial x} = 0 \quad (\text{B.19})$$

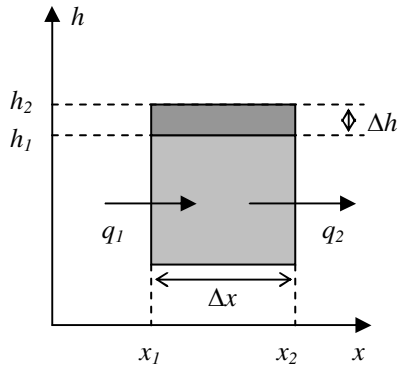


Figure B.2 Control area for derivation of the continuity equation

### B.3.3 Momentum balance equation

Consider an infinitely small fluid particle in motion with dimension  $\Delta V$ . Its mass  $\Delta m$  and momentum  $\Delta I$  are given by equation (B.20):

$$\begin{aligned}\Delta m &= \rho \Delta V \\ \Delta I &= (\Delta m) \vec{v} = (\rho \vec{v}) \Delta V\end{aligned}\quad (\text{B.20})$$

The fluid particle is assumed to be incompressible and with a density that is constant in time. This leads to:

$$\frac{D}{Dt} (\Delta m) \vec{v} = \rho \frac{D\vec{v}}{Dt} \Delta V \quad (\text{B.21})$$

Again consider the fluid particle, now with dimensions  $\Delta x$ ,  $\Delta y$ ,  $\Delta z$  and edges parallel to the axes of the coordinate system. There is a pressure against the two planes in  $x$ -direction, shear stresses are assumed to be non-existent. Refer to figure B.3 for details.

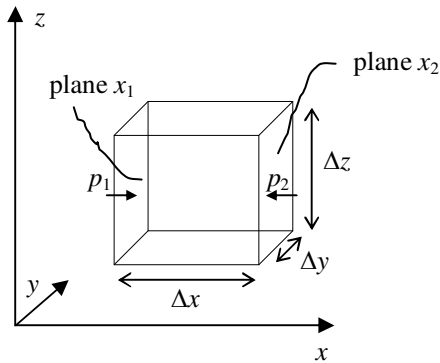


Figure B.3 Control volume for derivation of the momentum balance equation

On the plane  $x_1$  works an average compressive pressure  $p_1$  and on plane  $x_2$  an average compressive pressure  $p_2$ . If a unit vector is introduced, the resultant force on the fluid particle is equal to:

$$\vec{F}_{p,x} = (p_1 - p_2) \Delta y \Delta z \cdot \vec{e}_x \quad (\text{B.22})$$

For a small  $\Delta x$ , equation (B.22) can be rewritten into:

$$\vec{F}_{p,x} = \left( -\frac{\partial p}{\partial x} \Delta x \right) \Delta y \Delta z \cdot \vec{e}_x = -\frac{\partial p}{\partial x} \Delta V \quad (\text{B.23})$$

From equation (B.23) it follows that the force in  $x$ -direction is dependent on the  $x$ -component of the gradient of  $p$ . A similar result can be obtained for the other two directions. This leads to:

$$\vec{F}_{p,x} = -\left( \frac{\partial p}{\partial x} \vec{e}_x + \frac{\partial p}{\partial y} \vec{e}_y + \frac{\partial p}{\partial z} \vec{e}_z \right) \Delta V = (-\nabla p) \Delta V \quad (\text{B.24})$$

The gravity force on the particle follows from equation (B.20) and is equal to:

$$\vec{F}_g = \rho \vec{g} \Delta V \quad (\text{B.25})$$

The total force on the fluid particle is therefore equal to:

$$\vec{F}_{tot} = (-\nabla p + \rho \vec{g}) \Delta V \quad (\text{B.26})$$

With  $g$  as a constant, the gravity vector can be written as:

$$\vec{g} = -\nabla gz \quad (\text{B.27})$$

in which  $z$  is the vertical coordinate. Combining equations (B.26) and (B.27) leads to:

$$\vec{F}_{tot} = -\nabla (p + \rho gz) \Delta V \quad (\text{B.28})$$

Newton 2<sup>nd</sup> law for the fluid particle in motion can be rewritten as:

$$\frac{D}{Dt} m \vec{v} = \vec{F}_{tot} \quad (\text{B.29})$$

Substituting of equations (B.21) and (B.28) into (B.29) yields:

$$\rho \frac{D\vec{v}}{Dt} = -\nabla (p + \rho gz) \quad (\text{B.30})$$

Equation (B.30) is called Euler's equation and can be rewritten as:

$$\rho \frac{D\vec{v}}{Dt} = -\rho g \nabla h \quad (\text{B.31})$$

in which  $h$  is the height of the piezometric surface defined as:

$$h = z + \frac{p}{\rho g} \quad (\text{B.32})$$

If only the  $x$ -direction is considered, equation (B.31) reduces to:

$$\frac{Dv_x}{Dt} = -g \frac{\partial h}{\partial x} \quad (\text{B.33})$$

Because a moving fluid particle is considered, the total acceleration consists out of the local accelerations and the advective accelerations. Elaborating the left-hand side of equation (B.33) leads to:

$$\frac{Dv_x}{Dt} = \frac{\partial v_x}{\partial t} + v_x \frac{\partial v_x}{\partial x} + v_y \frac{\partial v_x}{\partial y} + v_z \frac{\partial v_x}{\partial z} \quad (\text{B.34})$$

As only one dimension is considered, equation (B.34) reduces to:

$$\frac{Dv_x}{Dt} = \frac{\partial v_x}{\partial t} + v_x \frac{\partial v_x}{\partial x} \quad (\text{B.35})$$

in which the first term on the right-hand side represents the local acceleration and the second term the advective acceleration of the fluid particle in motion. Combining equation equations (B.33) and (B.35) gives:

$$\frac{\partial v}{\partial t} + v \frac{\partial v}{\partial x} + g \frac{\partial h}{\partial x} = 0 \quad (\text{B.36})$$

in which the index  $x$  in the velocity terms has been omitted, because only one dimension is considered. Equation (B.36) is called the momentum balance or dynamic equation. This equation is derived from the equation of motion of the fluid particle. The momentum balance equation can also be derived directly. Again, a control area is considered. The momentum storage in the  $x$ -direction inside the area per unit width is equal to:

$$\begin{aligned}
\Delta I_{storage} &= \Delta(mv_x) = \rho v_x \Delta x \Delta z + \frac{\partial \rho v_x \Delta x \Delta z}{\partial t} \Delta t - \rho v_x \Delta x \Delta z \\
&= \frac{\partial \rho v_x}{\partial t} \Delta x \Delta z \Delta t = \rho \frac{\partial q_x}{\partial t} \Delta x \Delta t
\end{aligned} \tag{B.37}$$

in which a constant density is assumed and again equation (B.18) is used to write the equation in terms of specific discharge. Refer to figure B.4 for details.

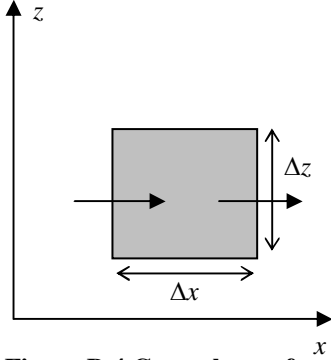


**Figure B.4 Control area for derivation of the momentum balance equation**

The net import of momentum in the  $x$ -direction follows from:

$$\begin{aligned}
\Delta I_{import} &= \rho v_x^2 \Delta z \Delta t - \rho \left( v_x^2 + \frac{\partial v_x^2}{\partial x} \Delta x \right) \Delta z \Delta t \\
&= -\rho \frac{\partial q_x v_x}{\partial x} \Delta x \Delta t
\end{aligned} \tag{B.38}$$

Dividing equations (B.37) and (B.38) by  $\Delta x \Delta t$  and  $\rho$  and combining them gives:

$$\frac{\partial q_x}{\partial t} + \frac{\partial q_x v_x}{\partial x} = \frac{F_{tot}}{\rho} \tag{B.39}$$

Or, with equation (B.18):

$$\frac{\partial h v}{\partial t} + \frac{\partial h v^2}{\partial x} = \frac{F_{tot}}{\rho} \tag{B.40}$$

where the index  $x$  has been omitted again. The right-hand side of equation (B.40) is equal to the gravity force from equation (B.33) per unit width:

$$\frac{F_{tot}}{\rho} = -gh \frac{\partial h}{\partial x} \tag{B.41}$$

Therefore, equation (B.40) can be rewritten as:

$$\frac{\partial h v}{\partial t} + \frac{\partial h v^2}{\partial x} + gh \frac{\partial h}{\partial x} = 0 \tag{B.42}$$

which is again the momentum balance equation from (B.36), but now in terms of  $h v$ . Equation (B.42) is apart from a factor  $\rho$ , equal to the momentum balance per unit width. The system of the continuity and momentum balance equations are called the shallow water or the St. Venant equations. The system of equations (B.19) and (B.42) is repeated in equation (B.43):

$$\begin{aligned}
\frac{\partial h}{\partial t} + \frac{\partial (h v)}{\partial x} &= 0 \\
\frac{\partial (h v)}{\partial t} + \frac{\partial (h v^2)}{\partial x} + gh \frac{\partial h}{\partial x} &= 0
\end{aligned} \tag{B.43}$$

## B.4 Derivation of the 1D wave equation

In order to solve 1D shallow water equations analytically, they are rewritten as into a linear single 2<sup>nd</sup> order differential equation. To achieve this, the continuity equation is differentiated to time and the momentum balance equation to space. Equation (B.43) now becomes:

$$\begin{aligned} \frac{\partial^2 h}{\partial t^2} + \frac{\partial^2 (hv)}{\partial x \partial t} &= 0 \\ \frac{\partial^2 (hv)}{\partial x \partial t} + \frac{\partial^2 (hv^2)}{\partial x^2} + gh \frac{\partial^2 h}{\partial x^2} &= 0 \end{aligned} \quad (\text{B.44})$$

Combining these two equations leads to:

$$-\frac{\partial^2 h}{\partial t^2} + \frac{\partial^2 (hv^2)}{\partial x^2} + gh \frac{\partial^2 h}{\partial x^2} = 0 \quad (\text{B.45})$$

To obtain a linear equation, the quadratic term is neglected which gives:

$$\frac{\partial^2 h}{\partial t^2} - c_w^2 \frac{\partial^2 h}{\partial x^2} = 0 \quad (\text{B.46})$$

in which the wave speed  $c_w$  is defined as:

$$c_w = \sqrt{gh} \quad (\text{B.47})$$

From equation (B.47) it can be seen the waves are non-dispersive: the velocity is independent of the wave frequency and is only a function of the water depth. This is a characteristic of shallow water waves. Equation (B.46) is called the elementary or acoustic wave equation and is valid for small displacements only.

## B.5 Solving the 1D model under wave loading

### B.5.1 Fluid boundaries

Applying equation (6.28) to the six fluid boundaries gives the boundary and interface conditions:

$$\begin{aligned}
\left. \frac{\partial \eta_1(x,t)}{\partial x} \right|_{x=x_0} &= -\frac{1}{g} \ddot{u}_e(x_0, t) \\
&\Rightarrow \left\{ -A_1 \omega_e \sin\left(\frac{\omega_e x_0}{c_{w,1}}\right) + B_1 \omega_e \sin\left(\frac{\omega_e x_0}{c_{w,1}}\right) \right\} e^{i\omega_e t} = -\frac{ae^{-i\frac{\omega_e x_0}{c_R}}}{g} e^{i\omega_e t} \\
\left. \frac{\partial \eta_1(x,t)}{\partial x} \right|_{x=x_1} &= -\frac{1}{g} \ddot{u}_{A,rel}(x_1, t) \\
&\Rightarrow \left\{ -A_1 \omega_e \sin\left(\frac{\omega_e x_1}{c_{w,1}}\right) + B_1 \omega_e \sin\left(\frac{\omega_e x_1}{c_{w,1}}\right) \right\} e^{i\omega_e t} = -\frac{\omega_e^2 \hat{U}_A}{g} e^{i\omega_e t} \\
\left. \frac{\partial \eta_2(x,t)}{\partial x} \right|_{x=x_1} &= -\frac{1}{g} \ddot{u}_{A,rel}(x_1, t) \\
&\Rightarrow \left\{ -A_2 \omega_e \sin\left(\frac{\omega_e x_1}{c_{w,2}}\right) + B_2 \omega_e \sin\left(\frac{\omega_e x_1}{c_{w,2}}\right) \right\} e^{i\omega_e t} = -\frac{\omega_e^2 \hat{U}_A}{g} e^{i\omega_e t} \\
\left. \frac{\partial \eta_2(x,t)}{\partial x} \right|_{x=x_2} &= -\frac{1}{g} \ddot{u}_{B,rel}(x_2, t) \\
&\Rightarrow \left\{ -A_2 \omega_e \sin\left(\frac{\omega_e x_2}{c_{w,2}}\right) + B_2 \omega_e \sin\left(\frac{\omega_e x_2}{c_{w,2}}\right) \right\} e^{i\omega_e t} = -\frac{\omega_e^2 \hat{U}_B}{g} e^{i\omega_e t} \\
\left. \frac{\partial \eta_3(x,t)}{\partial x} \right|_{x=x_2} &= -\frac{1}{g} \ddot{u}_{B,rel}(x_2, t) \\
&\Rightarrow \left\{ -A_3 \omega_e \sin\left(\frac{\omega_e x_2}{c_{w,3}}\right) + B_3 \omega_e \sin\left(\frac{\omega_e x_2}{c_{w,3}}\right) \right\} e^{i\omega_e t} = -\frac{\omega_e^2 \hat{U}_B}{g} e^{i\omega_e t} \\
\left. \frac{\partial \eta_3(x,t)}{\partial x} \right|_{x=x_3} &= -\frac{1}{g} \ddot{u}_e(x_3, t) \\
&\Rightarrow \left\{ -A_3 \omega_e \sin\left(\frac{\omega_e x_3}{c_{w,3}}\right) + B_3 \omega_e \sin\left(\frac{\omega_e x_3}{c_{w,3}}\right) \right\} e^{i\omega_e t} = -\frac{ae^{-i\frac{\omega_e x_3}{c_R}}}{g} e^{i\omega_e t}
\end{aligned} \tag{B.48}$$

With these 6 equations the unknowns  $A_1$  to  $A_3$  and  $B_1$  to  $B_3$  can be solved.

### B.5.2 Gates A & B

All constant have been solved except  $U_A$  and  $U_B$ , they need to be solved from the equations of motion of the gates. They can be found by substitution of the solutions to the wave equation (equation (6.22)), and the steady-state solution in equation (6.23) into equation (6.18). This leaves two unknowns and two equations from which the total solution can be obtained.

## B.6 Derivation of the 2D wave equation

Again, consider the control area of figure B.3. Combing equations (B.21) and (B.23) gives:

$$\frac{\partial v_x}{\partial t} = -\frac{1}{\rho} \frac{\partial p}{\partial x} \quad (\text{B.49})$$

in which  $p = p(x, z, t)$  is the total hydrodynamic pressure. A similar result can be obtained for the  $z$ -direction:

$$\frac{\partial v_z}{\partial t} = -\frac{1}{\rho} \frac{\partial p}{\partial z} \quad (\text{B.50})$$

For the volume balance the compressibility of water is now taken into account. An increase of volume will cause a pressure drop. Hooke's law for volumetric strain reads (compressive pressure is taken positive):

$$\sigma = -p = K \varepsilon \quad (\text{B.51})$$

in which:

$$\begin{array}{lll} \sigma & = & \text{stress} & [\text{Pa}] \\ \varepsilon & = & \text{volumetric strain of a fluid particle} & [-] \end{array}$$

The volumetric strain of a fluid particle in terms of velocity yields:

$$\varepsilon = \int \left( \frac{\partial v_x}{\partial x} + \frac{\partial v_z}{\partial z} \right) dt \quad (\text{B.52})$$

Combining equation (B.51) with (B.52) and differentiating with respect to time yields:

$$-\frac{\partial p}{\partial t} = K \left( \frac{\partial v_x}{\partial x} + \frac{\partial v_z}{\partial z} \right) \quad (\text{B.53})$$

Differentiating the momentum balance equations (B.49) and (B.50) to  $x$  respectively  $z$  gives:

$$\begin{aligned} \frac{\partial^2 v_x}{\partial x \partial t} &= -\frac{1}{\rho} \frac{\partial^2 p}{\partial x^2} \\ \frac{\partial^2 v_z}{\partial z \partial t} &= -\frac{1}{\rho} \frac{\partial^2 p}{\partial z^2} \end{aligned} \quad (\text{B.54})$$

Differentiating the volume balance equation (B.53) to  $t$  gives:

$$-\frac{\partial^2 p}{\partial t^2} = K \left( \frac{\partial^2 v_x}{\partial x \partial t} + \frac{\partial^2 v_z}{\partial z \partial t} \right) \quad (\text{B.55})$$

Substituting equation (B.54) into equation (B.55) results in:

$$\frac{\partial^2 p}{\partial t^2} = \frac{K}{\rho} \left( \frac{\partial^2 p}{\partial x^2} + \frac{\partial^2 p}{\partial z^2} \right) \quad (\text{B.56})$$

With equation (4.8) this results can be rewritten as:

$$\frac{\partial^2 p}{\partial x^2} + \frac{\partial^2 p}{\partial z^2} = \frac{1}{c_p^2} \frac{\partial^2 p}{\partial t^2} \quad (\text{B.57})$$

which is the two-dimensional wave equation for compressible fluids. This result is valid for small displacements, irrotational motion and neglected viscous effects.

## B.7 Solving the 2D model for hydrodynamic pressure

### B.7.1 Homogenous solution

In order to find the eigenfrequencies of the system, in the case of incompressible fluid, a homogenous solution is to be found. To do so, the forcing terms in the boundary conditions in equation (7.9) are removed. This leads to the following boundary conditions that need to be applied to the governing equation:

$$\begin{aligned}
\left. \frac{\partial p}{\partial x} \right|_{x=0} &= 0 \\
\left. \frac{\partial p}{\partial x} \right|_{x=L} &= 0 \\
\left. \frac{\partial p}{\partial z} \right|_{z=0} &= 0 \\
\left. \frac{\partial p}{\partial z} \right|_{z=d} &= -\frac{1}{g} \left. \frac{\partial^2 p}{\partial t^2} \right|_{z=d}
\end{aligned} \tag{B.58}$$

To find the homogenous solution to (7.3) the method of separation of variable is applied:

$$p(x, z, t) = \hat{P}_x(x, \omega_e) \cdot \hat{P}_z(z, \omega_e) \cdot e^{i\omega_e t} \tag{B.59}$$

Substitution of equation (B.59) into the Laplace equation (7.3) results in:

$$\frac{1}{\hat{P}_x} \frac{\partial^2 \hat{P}_x}{\partial x^2} = -\frac{1}{\hat{P}_z} \frac{\partial^2 \hat{P}_z}{\partial z^2} = -k^2 \tag{B.60}$$

in which  $k^2$  is the separation variable. Solving the two differential equation leads to:

$$\begin{aligned}
\frac{\partial^2 \hat{P}_x}{\partial x^2} + k^2 \hat{P}_x &= 0 \Rightarrow \hat{P}_x = A \sin(kx) + B \cos(kx) \\
\frac{\partial^2 \hat{P}_z}{\partial z^2} - k^2 \hat{P}_z &= 0 \Rightarrow \hat{P}_z = C \sinh(kz) + D \cosh(kz)
\end{aligned} \tag{B.61}$$

Substitution the result of equation (B.61) into the 1<sup>st</sup> boundary condition of equation (B.59) results in:

$$\left. \frac{\partial p}{\partial x} \right|_{x=0} = 0 = \hat{P}_z (Ak \cos(\alpha \cdot 0) - Bk \sin(\alpha \cdot 0)) \Rightarrow A = 0 \tag{B.62}$$

The 2<sup>nd</sup> boundary condition results in:

$$\left. \frac{\partial p}{\partial x} \right|_{x=L} = 0 = -\hat{P}_z (Bk \sin(kL)) \stackrel{B \neq 0}{\Rightarrow} \sin(kL) = 0 \Rightarrow k_n = \frac{n\pi}{L} \tag{B.63}$$

Similarly the 3<sup>rd</sup> boundary condition leads to:

$$\left. \frac{\partial p}{\partial z} \right|_{z=0} = 0 = \hat{P}_x (Ck \cosh(\alpha \cdot 0) + Dk \sinh(\alpha \cdot 0)) \Rightarrow C = 0 \tag{B.64}$$

And the last boundary condition leads to:

$$\left. \frac{\partial p}{\partial z} \right|_{z=d} = -\frac{1}{g} \left. \frac{\partial^2 p}{\partial t^2} \right|_{z=d} = \hat{P}_x (Dk \sinh(kd)) = \frac{\omega_e^2}{g} \hat{P}_x (D \cosh(kd)) \tag{B.65}$$

From (B.65) follows the expression of the eigenfrequencies of the system:

$$\omega_e^2 = kg \tanh(kd) \Rightarrow \omega_n^2 = \frac{n\pi}{L} g \tanh\left(\frac{n\pi}{L} d\right) \tag{B.66}$$

### B.7.2 Steady-state solution

The governing equation (7.3) and the boundary conditions in equation (7.9) are repeated here for the reader's convenience:

Governing equation:

$$\frac{\partial^2 p}{\partial x^2} + \frac{\partial^2 p}{\partial z^2} = 0 \quad (\text{B.67})$$

Boundary conditions:

$$\begin{aligned} \left. \frac{\partial p}{\partial x} \right|_{x=0} &= -\rho \ddot{u}_A \\ \left. \frac{\partial p}{\partial x} \right|_{x=L} &= -\rho \ddot{u}_B \\ \left. \frac{\partial p}{\partial z} \right|_{z=0} &= 0 \\ \left. \frac{\partial p}{\partial z} \right|_{z=d} &= -\frac{1}{g} \frac{\partial^2 p}{\partial t^2} \Big|_{z=d} \end{aligned} \quad (\text{B.68})$$

In order to have the same homogenous boundary as with the homogenous solution the following steady-state solution is proposed:

$$p(x, z, t) = \hat{P} e^{i\omega t} \quad (\text{B.69})$$

with:

$$\hat{P} = \tilde{P} + c_1 x + c_2 x^2 - c_2 z^2 \quad (\text{B.70})$$

Substitution into the governing equation (7.3) or (B.67) results in:

$$\frac{\partial^2 \tilde{P}}{\partial x^2} + \frac{\partial^2 \tilde{P}}{\partial z^2} + 2c_2 - 2c_2 = 0 \quad (\text{B.71})$$

which is again the Laplace equation. Incorporating (B.70) into the first boundary condition of equation (B.68) results in:

$$\left. \frac{\partial \hat{P}}{\partial x} \right|_{x=0} = -\rho a = \left. \frac{\partial \tilde{P}}{\partial x} \right|_{x=0} + c_1 + c_2 \cdot 0 \Rightarrow c_1 = -\rho a$$

Similarly for the second boundary condition in equation (B.68):

$$\left. \frac{\partial \hat{P}}{\partial x} \right|_{x=L} = -\rho a e^{-i\varphi} = \left. \frac{\partial \tilde{P}}{\partial x} \right|_{x=L} + c_1 + c_2 L \Rightarrow c_2 = \frac{\rho a}{2L} (1 - e^{-i\varphi})$$

The third boundary condition now becomes:

$$\left. \frac{\partial \hat{P}}{\partial z} \right|_{z=0} = 0 = \left. \frac{\partial \tilde{P}}{\partial z} \right|_{z=0} - 2c_2 \cdot 0$$

And the last boundary condition now reads:

$$\begin{aligned} \left[ \frac{\partial \hat{P}}{\partial z} - \frac{\omega_e^2}{g} \hat{P} \right]_{z=d} &= 0 = \left. \frac{\partial \tilde{P}}{\partial z} \right|_{z=d} - 2c_2 d - \frac{\omega_e^2}{g} (\tilde{P}(x, d) + c_1 x + c_2 x^2 - c_2 d^2) \Rightarrow \\ \left[ \frac{\partial \tilde{P}}{\partial z} - \frac{\omega_e^2}{g} \tilde{P} \right]_{z=d} &= 2c_2 d + \frac{\omega_e^2}{g} (c_1 x + c_2 (x^2 - d^2)) \end{aligned} \quad (\text{B.72})$$

Now, the boundary condition in terms of  $\tilde{P}$  are:

$$\begin{aligned}
\left. \frac{\partial \tilde{P}}{\partial x} \right|_{x=0} &= 0 \\
\left. \frac{\partial \tilde{P}}{\partial x} \right|_{x=L} &= 0 \\
\left. \frac{\partial \tilde{P}}{\partial z} \right|_{z=0} &= 0 \\
\left[ \frac{\partial \tilde{P}}{\partial z} - \frac{\omega_e^2}{g} \tilde{P} \right]_{z=d} &= 2c_2 d + \frac{\omega_e^2}{g} (c_1 x + c_2 (x^2 - d^2))
\end{aligned} \tag{B.73}$$

The first three boundary conditions now have a homogenous shape, which means that the same solution from the homogenous solution can be applied. From equations (B.62)–(B.64) follows:

$$\tilde{P} = \sum_{n=0}^{\infty} B_n \cos\left(\frac{n\pi}{L} x\right) \cosh\left(\frac{n\pi}{L} z\right) \tag{B.74}$$

The remaining constant  $B_n$  will have to be found by means of last boundary condition in (B.73) and the orthogonality property of normal modes. This procedure last is followed to get rid of the summation sign in front of the constants  $B_n$ . The orthogonality property of (co)sine functions states that integration of a multiplication of (co)sines is always equal to zero, unless the arguments are identical. In the latter case the function will have to form of  $\sin^2$  or  $\cos^2$  which has a range of 0 to 1. Any other (co)sine function has a range from  $-1$  to  $1$ ; therefore integration over one period results into zero. See also equation (B.75):

for all  $m, n = 1, 2, \dots, \infty$ :

$$\begin{aligned}
\int_0^L \cos\left(\frac{m\pi x}{L}\right) \cos\left(\frac{n\pi x}{L}\right) dx &= \begin{cases} \frac{L}{2} & \text{for } m = n \\ 0 & \text{for } m \neq n \end{cases} \\
\int_0^L \cos\left(\frac{m\pi x}{L}\right) \sin\left(\frac{n\pi x}{L}\right) dx &= 0 \quad \text{for all } m, n \\
\int_0^L \sin\left(\frac{m\pi x}{L}\right) \sin\left(\frac{n\pi x}{L}\right) dx &= \begin{cases} \frac{L}{2} & \text{for } m = n \\ 0 & \text{for } m \neq n \end{cases}
\end{aligned} \tag{B.75}$$

Substitution of (B.74) into the last boundary condition in (B.73) leads to:

$$\begin{aligned}
\left[ \frac{\partial \tilde{P}}{\partial z} - \frac{\omega_e^2}{g} \tilde{P} \right]_{z=d} &= \sum_{n=0}^{\infty} B_n \cos\left(\frac{n\pi}{L} x\right) \left\{ \frac{n\pi}{L} \sinh\left(\frac{n\pi}{L} d\right) - \frac{\omega_e^2}{g} \cosh\left(\frac{n\pi}{L} d\right) \right\} \\
&= 2c_2 d + \frac{\omega_e^2}{g} (c_1 x + c_2 (x^2 - d^2))
\end{aligned} \tag{B.76}$$

Multiplying both sides of equation (B.76) with  $\cos(k_m z)$  and integrating over the chamber length now results in:

$$\begin{aligned}
\sum_{n=0}^{\infty} B_n \left\{ \frac{n\pi}{L} \sinh\left(\frac{n\pi}{L} d\right) - \frac{\omega_e^2}{g} \cosh\left(\frac{n\pi}{L} d\right) \right\} \int_0^L \cos\left(\frac{m\pi}{L} x\right) \cos\left(\frac{n\pi}{L} x\right) dx \\
= \int_0^L \left\{ 2c_2 d + (c_1 x + c_2 (x^2 - d^2)) \right\} \cos\left(\frac{m\pi}{L} x\right) dx
\end{aligned} \tag{B.77}$$

Elaboration of the above equation results in the following expression for  $B_n$ :

$$B_n = \begin{cases} -\frac{1}{2}c_1L - c_2 \left( \frac{2gd}{\omega_e^2} + \frac{L^2}{3} - d^2 \right), & n = 0 \\ \frac{2L}{n^2\pi^2} \frac{c_1(1+(-1)^{n-1}) - 2c_2L(-1)^n}{\cosh(k_n d) - k_n \sinh(k_n d) \frac{g}{\omega_e^2}}, & n = 1, 2, \dots, \infty \end{cases} \quad (\text{B.78})$$

This leads to the following result:

$$p(x, z, t) = \left\{ \sum_{n=0}^{\infty} B_n \cos(k_n x) \cosh(k_n z) + c_1 x + c_2 (x^2 - z^2) \right\} e^{i\omega_e t}$$

$$B_0 = -\frac{1}{2}c_1L - c_2 \left( \frac{2gd}{\omega_e^2} + \frac{L^2}{3} - d^2 \right)$$

$$B_n = \frac{2L}{n^2\pi^2} \frac{c_1(1+(-1)^{n-1}) - 2c_2L(-1)^n}{\cosh(k_n d) - k_n \sinh(k_n d) \frac{g}{\omega_e^2}}, \quad n = 1, 2, \dots, \infty$$

$$k_n = \frac{n\pi}{L} \quad (\text{B.79})$$

$$c_1 = -\rho a$$

$$c_2 = \frac{\rho a}{2L} (1 - e^{-i\varphi})$$

$$\varphi = \frac{\omega_e L}{c_R}$$

In the case of no surface waves, the last boundary condition of equation (B.73) would become:

$$\tilde{P}(x, d) = -c_1 x - c_2 (x^2 - d^2) \quad (\text{B.80})$$

Again, multiplying both sides of equation (B.80) with  $\cos(k_n z)$  and integrating over the chamber length now results in:

$$\sum_{n=0}^{\infty} B_n \cosh\left(\frac{n\pi}{L}d\right) \int_0^L \cos\left(\frac{m\pi}{L}x\right) \cos\left(\frac{n\pi}{L}x\right) dx$$

$$= \int_0^L \left\{ -c_1 x - c_2 (x^2 - d^2) \right\} \cos\left(\frac{m\pi}{L}x\right) dx \quad (\text{B.81})$$

Elaboration of the above equation results in the following expression for  $B_n$  in the case of no surface waves:

$$B_n = \begin{cases} -\frac{1}{2}c_1L - c_2 \left( \frac{L^2}{3} - d^2 \right), & n = 0 \\ \frac{2L}{n^2\pi^2} \frac{c_1(1+(-1)^{n-1}) - 2c_2L(-1)^n}{\cosh(k_n d)}, & n = 1, 2, \dots, \infty \end{cases} \quad (\text{B.82})$$

The other expressions in equation (B.79) remain the same.



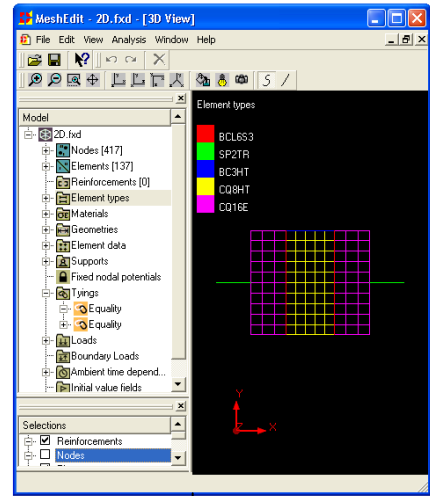
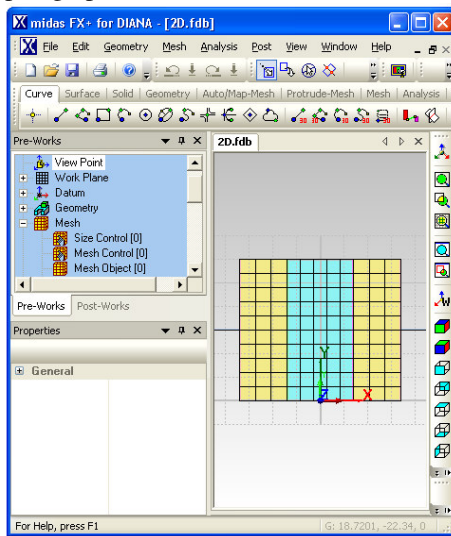
# Appendix C: The Finite Element program DIANA

## C.1 Workflow in DIANA

The general process of finite element analysis is explained in the following workflow where three major steps can be distinguished:

1. Preprocessing: in this step the model problem is defined by geometry, materials, loading and other input data;
2. Analysis: this step involves the actual calculation;
3. Postprocessing is the final step for examining the results.

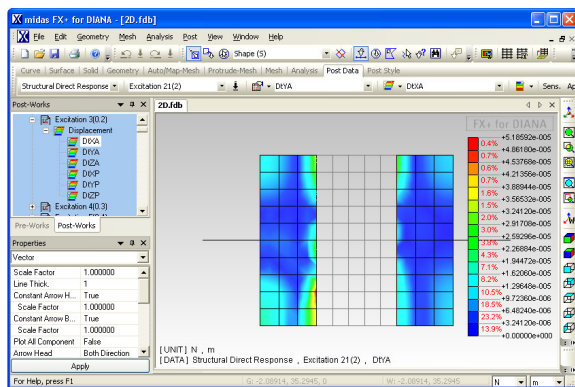
The example shown in the workflow is "model 2d", as discussed in paragraph 8.1.



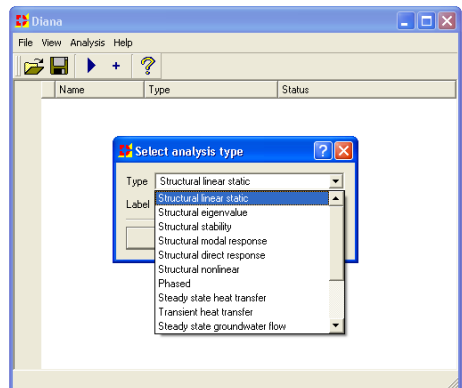
**Preprocessing: Mesh Editor**  
In the Mesh Editor the mesh can be checked or finalized by adding extra (material) data before commencing the analysis.



**Preprocessing: FX+ for DIANA**  
FX+ is one of the pre/postprocessors for DIANA. It translates the model of the lock gates into input data for the analysis in DIANA.



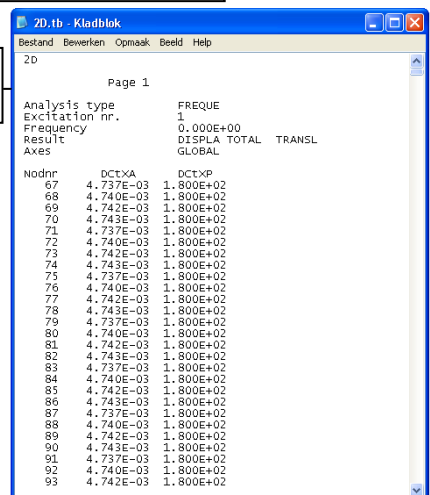
**Postprocessing: FX+ for DIANA**  
The results are imported back into FX+ for further actions.



**Analysis: DIANA**  
Performing calculations



**Postprocessing: tabulated output**  
Alternative for using a postprocessor



## C.2 DIANA brochure and background theory FSI

The following pages contain an outtake of the user's manual [TNO DIANA, 2008] background theory about the fluid-structure interaction procedure. Also a copy of a DIANA brochure<sup>14</sup> has been added with an overview of the program.

<sup>14</sup> Available from <http://tmodiana.com/DIANA>



## 32.5 Fluid–Structure Interaction Analysis

This section presents a brief overview of the background theory of the analysis of coupled fluid and structural systems, the so-called fluid–structure interaction analysis.<sup>9</sup> Effects of large scale flow in the fluid are excluded. Attention is paid to the discretization method, the numerical solution techniques and simplifications.

Figure 32.2 shows a general fluid–structure interaction geometry. The solid

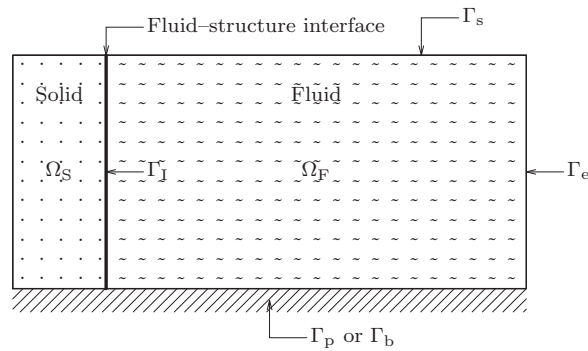


Figure 32.2: Fluid–structure interaction

extends throughout the region  $\Omega_S$ , and  $\Omega_F$  contains the fluid. Surface  $\Gamma_I$  defines the fluid–structure interface. The boundary of the fluid  $\Gamma_B$  may be separated in a fixed or prescribed part  $\Gamma_p$ , a part representing the bottom  $\Gamma_b$ , a part representing the free surface  $\Gamma_s$  and a part representing the infinite extent  $\Gamma_e$ .

### 32.5.1 Solid

In the solid, the discretization in the familiar form is given below and will be assumed throughout:

$$\mathbf{M}_S \ddot{\mathbf{u}} + \mathbf{C}_S \dot{\mathbf{u}} + \mathbf{K}_S \mathbf{u} + \mathbf{f}_I = \mathbf{f}_S^{\text{ex}}(t) \quad (32.53)$$

where  $\mathbf{M}_S$ ,  $\mathbf{C}_S$  and  $\mathbf{K}_S$  are mass, damping and stiffness matrices respectively and  $\mathbf{u}$  is a set of unknowns describing the displacements of the structure. The vector  $\mathbf{f}_I$  stands for forces due to the interface interaction with the fluid and  $\mathbf{f}_S^{\text{ex}}$  represents the external force contributions.

### 32.5.2 Fluid

The fluid is characterized by a single pressure (or potential) variable  $p$  and the coupling with the structure is achieved by consideration of interface forces and

<sup>9</sup>For a more detailed description of the underlying theory see for instance Zienkiewicz & Bettles [61, 7] and Olson & Bathe [47].

a standard finite element idealization. Assuming the state of the fluid is linear, the governing equation is the wave or acoustic equation

$$\nabla^2 p = \frac{1}{c^2} \ddot{p} \quad (32.54)$$

where  $p$  is the pressure (compression positive) and  $c$  the wave speed, given by

$$c^2 = \frac{\beta}{\rho} \quad (32.55)$$

where  $\beta$  is the bulk modulus and  $\rho$  the density. Appropriate boundary conditions of the following form can be imposed.

### 32.5.2.1 Solid Boundary

The conditions applying to the surface  $\Gamma_I$  being the interface between the fluid and structure, can be written as

$$\frac{\partial p}{\partial n} = -\rho_F \mathbf{n}_F^T \ddot{\mathbf{u}}_F \quad \text{and} \quad \boldsymbol{\sigma} \mathbf{n}_S = p_F \mathbf{n}_F \quad \text{on} \quad \Gamma_I \quad (32.56)$$

where  $\mathbf{n}_F$  and  $\mathbf{n}_S$  are respectively the outward normal to the fluid domain and the outward normal to the structural domain. The coupling between the fluid domain and the structural domain is realized by continuity between the normal displacements with the condition  $\ddot{\mathbf{u}}_F = \ddot{\mathbf{u}}_S$  and is obtained by combining this condition with (32.56)

$$\frac{\partial p}{\partial n} = -\rho_F \mathbf{n}_F^T \ddot{\mathbf{u}}_S \quad (32.57)$$

### 32.5.2.2 Prescribed Conditions

$$p = \bar{p} \quad \text{on} \quad \Gamma_p \quad (32.58)$$

where  $\bar{p}$  is a prescribed pressure often to be zero along part of the boundary  $\Gamma_p$ .

### 32.5.2.3 Free Surface

$$p = \rho_F g u_z \quad \text{on} \quad \Gamma_s \quad (32.59)$$

where  $g$  is the gravity acceleration and  $z$  is directed normal to the free surface. Noting that

$$\ddot{u}_z = -\frac{1}{\rho_F} \frac{\partial p}{\partial z} \quad (32.60)$$

Equation (32.59) can be written as

$$\frac{\partial p}{\partial z} = -\frac{1}{g} \ddot{p} \quad \text{on} \quad \Gamma_s \quad (32.61)$$

which is the linearized free surface condition for first order waves.

#### 32.5.2.4 Radiation for Boundary of Infinite Extent

If a boundary of infinite extent has been placed sufficiently far away, it may be assumed that only plane waves exist. In the existence of only outgoing waves, incoming waves are supposed to be absent, giving a solution of the form

$$p = f'(x - ct) \quad (32.62)$$

where a positive  $x$  is the outward direction. The radiation boundary condition is now obtained by eliminating  $f'$  and is given by

$$\frac{\partial p}{\partial x} = -\frac{1}{c_s} \dot{p} \quad \text{on } \Gamma_e \quad (32.63)$$

This condition is denoted as the Sommerfeld radiation condition and in general, will be applied in a plane normal to the direction of the wave speed. Due to the fact  $c_s$  can correspond to several possible wave velocities, this relation of (32.63) at the radiation boundary should be applied then using a frequency ( $\omega$ ) dependent velocity defined by

$$c_s = \frac{g}{\omega} \tanh \frac{\omega h}{c_s} \quad (32.64)$$

where  $h$  is the fluid depth.

#### 32.5.2.5 Bottom

The conditions applying to the surface  $\Gamma_b$  being the bottom of the fluid reservoir, can be written as

$$\frac{\partial p}{\partial n} = -\frac{1 - \alpha_B}{c(1 + \alpha_B)} \dot{p} \quad \text{on } \Gamma_b \quad (32.65)$$

where  $c$  is the wave speed given by (32.55) and  $\alpha_B$  is the wave reflection coefficient of the bottom. The wave reflection coefficient  $\alpha_B$  is the ratio of the amplitude of the reflected hydrodynamic pressure wave to the amplitude of a propagating pressure wave incident on the reservoir bottom. The wave reflection coefficient  $\alpha_B$  may range within the limiting values of  $-1$  and  $1$ . For rigid reservoir bottom materials  $\alpha_B = 1$  and for very soft reservoir bottom materials  $\alpha_B = -1$ .<sup>10</sup>

### 32.5.3 Discretized Coupled Equations

A standard finite element discretization has used approximating  $p$  in terms of nodal values  $\mathbf{p}$

$$p \approx \mathbf{N}_F \mathbf{p}^e \quad (32.66)$$

<sup>10</sup>For a more detailed description see for instance Fenves & Chopra [17] and Küçükarslan et al. [35].

and the discretization gives a system of equations in a form

$$\mathbf{M}_F \ddot{\mathbf{p}} + \mathbf{C}_F \dot{\mathbf{p}} + \mathbf{K}_F \mathbf{p} + \mathbf{r}_I = 0 \quad (32.67)$$

where  $\mathbf{M}_F$ ,  $\mathbf{C}_F$ ,  $\mathbf{K}_F$  and  $\mathbf{r}_I$  are defined in terms of the following element matrices:

$$[M_{ij}]_F^e = \frac{1}{g} \int_{\Gamma_s^e} N_i N_j \, d\Gamma + \frac{1}{c^2} \int_{\Omega_F} N_i N_j \, d\Omega \quad (32.68)$$

with  $\Gamma_s$  the free surface

$$[C_{ij}]_F^e = \frac{1}{c_s} \int_{\Gamma_e} N_i N_j \, d\Gamma \quad \text{with } \Gamma_e \text{ the radiation boundary} \quad (32.69)$$

$$[K_{ij}]_F^e = \int_{\Omega_F} \nabla N_i N_j \, d\Omega \quad \text{with } \Omega_F \text{ the fluid domain} \quad (32.70)$$

$$[r_i]_I^e = \int_{\Gamma_I} N_i \rho_F n_k \dot{u}_k \, d\Gamma \quad \text{with } \Gamma_I \text{ the fluid–structure interface} \quad (32.71)$$

The contribution  $\mathbf{f}_I$  from (32.53) can be written as

$$[f_{ik}]_I^e = - \int_{\Gamma_I} N_i^u n_k p \, d\Gamma \quad (32.72)$$

or

$$\mathbf{f}_I^e = -\mathbf{R}^{eT} \mathbf{p}^e \quad (32.73)$$

and likewise the contribution  $\mathbf{r}_I$  from (32.67) as

$$[r_i]_I^e = \int_{\Gamma_I} N_i^p \rho_F n_k \ddot{u}_k \, d\Gamma \quad (32.74)$$

or

$$\mathbf{r}_I^e = \rho_F \mathbf{R}^e \ddot{\mathbf{u}}^e \quad (32.75)$$

After assembling contributions from each type of element (i.e., solid, fluid–structure interface, fluid, boundary fluid elements), the following coupled system of equations is obtained

$$\begin{bmatrix} \mathbf{M}_S & \mathbf{O}^T \\ \rho_F \mathbf{R} & \mathbf{M}_F \end{bmatrix} \begin{Bmatrix} \ddot{\mathbf{u}} \\ \ddot{\mathbf{p}} \end{Bmatrix} + \begin{bmatrix} \mathbf{C}_S & \mathbf{O}^T \\ \mathbf{O} & \mathbf{C}_F \end{bmatrix} \begin{Bmatrix} \dot{\mathbf{u}} \\ \dot{\mathbf{p}} \end{Bmatrix} + \begin{bmatrix} \mathbf{K}_S & -\mathbf{R}^T \\ \mathbf{O} & \mathbf{K}_F \end{bmatrix} \begin{Bmatrix} \mathbf{u} \\ \mathbf{p} \end{Bmatrix} = \begin{Bmatrix} \mathbf{f}_S(t) \\ \mathbf{0} \end{Bmatrix} \quad (32.76)$$

### 32.5.4 Solution of Coupled System

The technique to be used for solving the system of equations (32.76) strongly depends on the form of the forcing function  $\mathbf{f}_S(t)$ .

### 32.5.4.1 Frequency Domain Analysis

If the forcing function of (32.76) has been expressed in, or can be transformed to a periodic form as

$$\mathbf{f}_S(t) = \hat{\mathbf{f}}_S e^{i\omega t} \quad (32.77)$$

then for linear problems the steady-state solution will exist in the same form, thus

$$\mathbf{u}(t) = \hat{\mathbf{u}} e^{i\omega t} \quad \text{and} \quad \mathbf{p}(t) = \hat{\mathbf{p}} e^{i\omega t} \quad (32.78)$$

Now a complex expression of the solution is obtained and can be written in the matrix form

$$\begin{bmatrix} -\omega^2 \mathbf{M}_S + \mathbf{K}_S + i\omega \mathbf{C}_S & -\mathbf{R}^T \\ -\omega^2 \rho_F \mathbf{R} & -\omega^2 \mathbf{M}_F + \mathbf{K}_F + i\omega \mathbf{C}_F \end{bmatrix} \begin{Bmatrix} \hat{\mathbf{u}} \\ \hat{\mathbf{p}} \end{Bmatrix} = \begin{Bmatrix} \hat{\mathbf{f}}_S \\ \mathbf{0} \end{Bmatrix} \quad (32.79)$$

from which the complex values of the amplitudes  $\hat{\mathbf{u}}$  and  $\hat{\mathbf{p}}$  can be found. A single set of complex equations for  $\hat{\mathbf{u}}$  is obtained by eliminating the pressure values  $\hat{\mathbf{p}}$  directly. The second subsystem of equations implied in (32.79) can be written

$$\hat{\mathbf{p}} = [-\omega^2 \mathbf{M}_F + \mathbf{K}_F + i\omega \mathbf{C}_F]^{-1} \omega^2 \rho_F \mathbf{R} \hat{\mathbf{u}} \quad (32.80)$$

or with  $\mathbf{H}_F(\omega) = [-\omega^2 \mathbf{M}_F + \mathbf{K}_F + i\omega \mathbf{C}_F]^{-1}$  as frequency response function

$$\hat{\mathbf{p}} = \omega^2 \rho_F \mathbf{H}_F(\omega) \mathbf{R} \hat{\mathbf{u}} \quad (32.81)$$

On substitution for  $\hat{\mathbf{p}}$  the result from above into the first subsystem of equations implied in (32.79) an additional fluid matrix  $\hat{\mathbf{K}}_I$  is obtained and is given as

$$\hat{\mathbf{K}}_I = -\omega^2 \rho_F \mathbf{R}^T \mathbf{H}_F(\omega) \mathbf{R} \quad (32.82)$$

In the above the matrix  $\hat{\mathbf{K}}_I$  is a complex quantity and can be written in a form

$$\mathbf{K}_I = -\omega^2 \rho_F \Re(\mathbf{R}^T \mathbf{H}_F(\omega) \mathbf{R}) + i\omega \rho_F \Im(\mathbf{R}^T \mathbf{H}_F(\omega) \mathbf{R}) \quad (32.83)$$

or

$$\mathbf{K}_I = -\omega^2 \tilde{\mathbf{M}}_F + i\omega \tilde{\mathbf{C}}_F \quad (32.84)$$

where  $\tilde{\mathbf{M}}_F$  and  $\tilde{\mathbf{C}}_F$  are denoted as the *added mass* matrix and the *added damping* matrix respectively. The structural matrix now takes the form

$$\left[ -\omega^2 (\mathbf{M}_S + \tilde{\mathbf{M}}_F) + \mathbf{K}_S + i\omega (\mathbf{C}_S + \tilde{\mathbf{C}}_F) \right] \hat{\mathbf{u}} = \hat{\mathbf{f}}_S \quad (32.85)$$

which can be solved with a direct solution procedure [§ 32.2.2 p. 509].

### 32.5.5 Simplification for Fixed Fluid Boundaries

If no surface waves are admitted and the effect of radiation waves at the infinite boundary is ignored, i.e.,

$$p = 0 \quad \text{respectively on } \Gamma_s \text{ and } \Gamma_e \quad (32.86)$$

and compression effects are neglected, i.e.,  $c = 0$  on  $\Omega_F$ , then the matrices  $\mathbf{M}_F$  and  $\mathbf{C}_F$  of (32.67) as well as the second of (32.76) become zero. The pressure vector  $\mathbf{p}$  can now be obtained directly in terms of  $\ddot{\mathbf{u}}$  as

$$\mathbf{p} = -\mathbf{K}_F^{-1} \rho_F \ddot{\mathbf{u}} \quad (32.87)$$

On substitution into the first of (32.76) the structural matrix now becomes of the general form

$$\left( \mathbf{M}_S + \tilde{\mathbf{M}}_F \right) \ddot{\mathbf{u}} + \mathbf{C}_S \dot{\mathbf{u}} + \mathbf{K}_S \mathbf{u} = \mathbf{f}_S(t) \quad (32.88)$$

where the added mass is simply given as

$$\tilde{\mathbf{M}}_F = \rho_F \mathbf{R}^T \mathbf{K}_F^{-1} \mathbf{R} \quad (32.89)$$

#### 32.5.5.1 Frequency Domain Analysis

If the structural damping is absent or not strongly, the solution in the frequency domain can be obtained by the mode superposition technique [§ 32.2.1 p. 508]. Now the solution  $\mathbf{u}$  will be obtained by superposition of the response in each mode:

$$\mathbf{u}(t) = \sum_{i=1}^{\dots} \phi_i \alpha_i(t) \quad (32.90)$$

where  $\phi_i$  is the  $i$ -th eigenvector and  $\alpha_i$  is the  $i$ -th generalized modal displacement. Therefore, it requires first the solution of a sufficient number of eigenvalues and corresponding eigenvectors of the problem in (32.88) with damping neglected

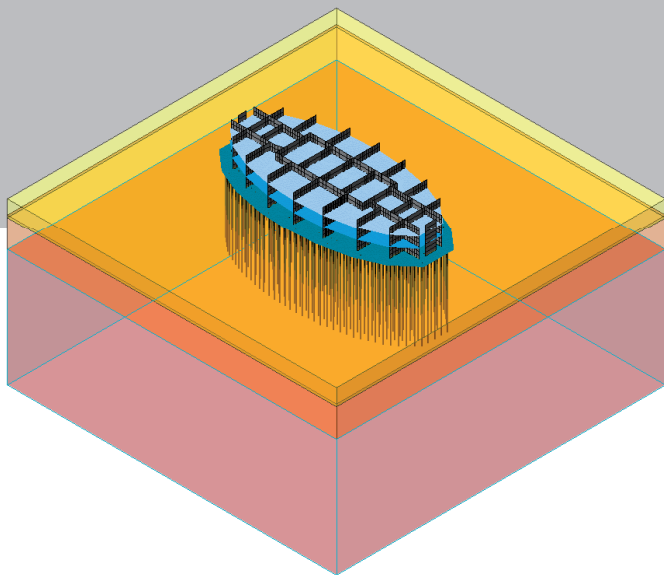
$$\left( \mathbf{M}_S + \tilde{\mathbf{M}}_F \right) \ddot{\mathbf{u}} + \mathbf{K}_S \mathbf{u} = 0 \quad (32.91)$$

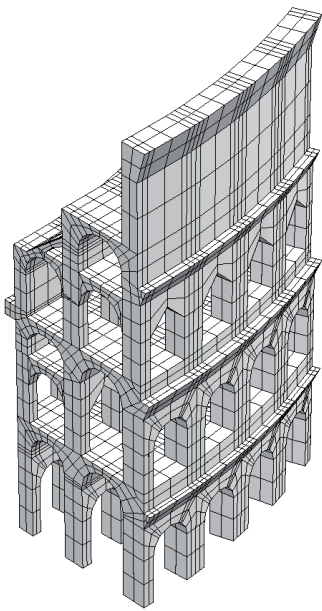
Next, the set of equations (32.88) are transformed to global coordinates and a decoupled set of equations is obtained provided that the damping matrix  $\mathbf{C}_S$  is proportional [§ 32.1.2.3 p. 507].

#### 32.5.5.2 Time Domain Analysis

In case of an arbitrary transient loading, the response of the simplified problem in (32.88) can now be obtained by a direct time integration method [§ 32.4 p. 512]. After the *added mass* matrix  $\tilde{\mathbf{M}}_F$ , given by (32.89), has been determined via the solution of (32.87), the transient analysis can be carried out in the usual way by Module NONLIN [Ch. 12 p. 199].

# DIANA FINITE ELEMENT ANALYSIS





## DIANA

DIANA (Displacement ANALyzer) is a multi-purpose finite element program, with especial strength in the field of civil engineering.

DIANA development started in 1972 at the TNO Building and Construction Research Institute in The Netherlands. In 2003 TNO DIANA BV was

established from the Computational Mechanics Department of TNO.

TNO DIANA BV continues to develop, market and support DIANA and undertakes customization, consultancy and client training activities on behalf of customers worldwide.

## Product functionality

### Fields of application

- Structural Engineering
- Geotechnical Engineering
- Oil & Gas Engineering

### Material models

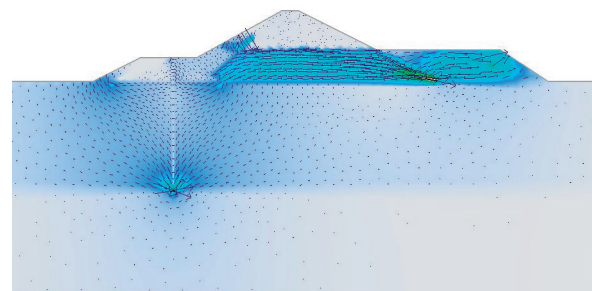
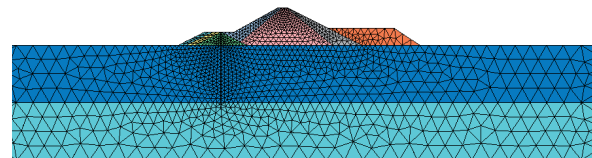
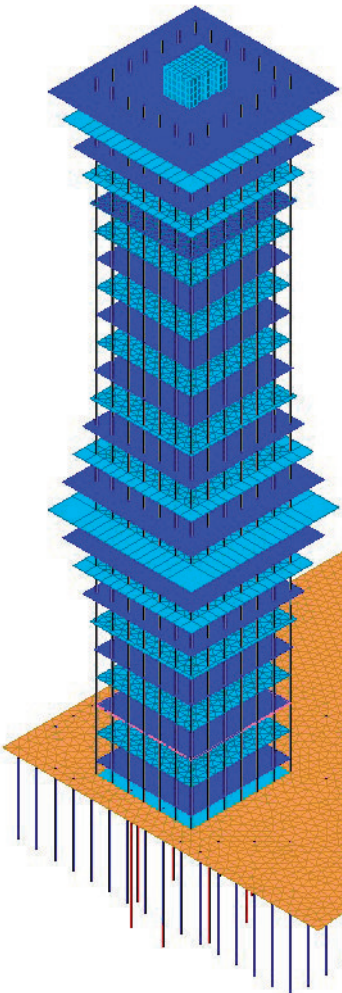
- Linear, non linear and modified elasticity
- Hyperelasticity
- Isotropic and orthotropic plasticity
- Viscoplasticity
- Smeared crack models
- Total strain fixed and rotating crack models
- Viscoelasticity
- Young hardening concrete models
- Creep and shrinkage
- Maekawa concrete model
- Soil specials
- Liquefaction models
- Model Code models for concrete and steel
- User-Supplied models
- Special models for interface elements
- Ambient and time dependent mechanical, heat transfer and groundwater flow properties

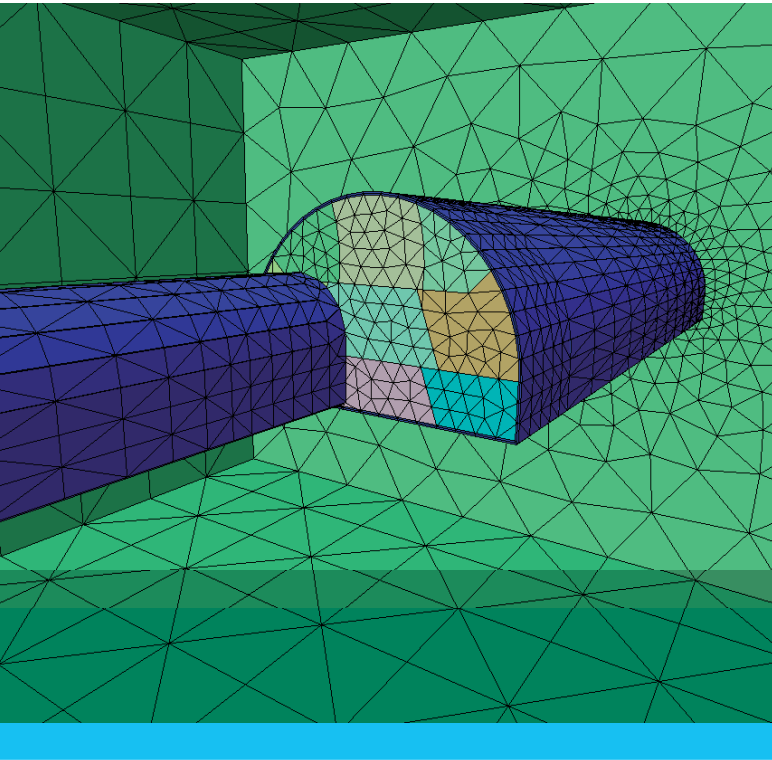
### Analysis types

- Linear static
- Fatigue failure
- Linear transient
- Frequency response
- Spectral response
- Physical and geometrical non linear
- Transient non linear
- Eigenvalue
- Buckling and post buckling
- Steady state and transient heat flow
- Detailed and regional groundwater flow
- Steady state and transient groundwater flow
- Coupled flow-stress
- Phased structural and potential flow
- Fluid-structure interaction
- Soil-structure-fluid interaction
- Parameter estimation
- Lattice

### Element types

- Truss
- Timoshenko, Bernoulli, and Mindlin Beam
- Plane stress and plane strain
- Complete/general plane strain
- Axisymmetric
- Plate bending
- Flat shell
- Curved shell
- Layered shell
- Solid
- Composed
- Interface
- Contact
- Discrete spring/dashpot
- Base spring
- Bounding
- Point mass/damping
- Embedded reinforcements
- Flow





## Why DIANA?

Standard finite element packages can solve only a limited range of conventional engineering problems. Non-conventional engineering problems require advanced modelling and analysis functionality. Examples are: analysis of big structures such as dams; complex non-linear material behaviour; stresses induced from extreme loading conditions such as fire, earthquake, explosions, etc; complex models where the structure interacts with soil/fluid.

DIANA, with its extensive library of material models and analysis capabilities, offers the solution for all types of analysis in the field of civil engineering, where standard packages fail.

The open structure of DIANA allows the user to fully control all analysis phases. User defined material models can also be defined.

As a result of the continuous collaboration with the most prominent universities and research institutions worldwide, DIANA provides the most up-to-date and high standard solution in the analysis of reinforced concrete structures, of soil, and of soil-structure-fluid interaction.

Behind DIANA is a team of expert engineers who provide technical support and offer customized assistance to companies in preparing the model for the analysis, or analyzing the model and interpreting the analysis results.

### Preprocessing

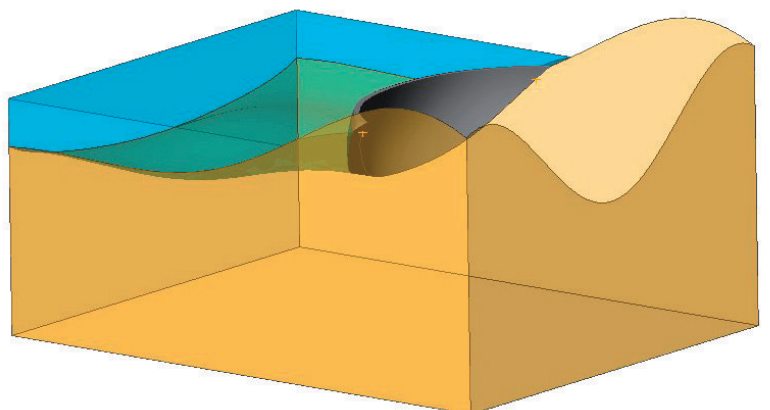
- CAD like geometry modelling functionality
- Advanced selection methods
- Advanced geometry modelling
- Boolean operation for solid modelling
- Geometry check and repair tools
- Practical mouse snapping
- Auto-, map- and protrude-mesh methods
- Mesh manipulation and check functionality
- Loads and boundary conditions applicable both on geometry or mesh
- Function based definition of loads and boundary conditions
- MS-Excel compatible tables

### Postprocessing

- Contour and vector plots
- Iso-surface, slice, clipping and partition plot
- Diagram and vector plot
- Results extraction to MS-Excel compatible table
- Screen-shots in different picture formats
- Animation

### Solution Procedures

- Automatic solution method
- Out-of-core direct solution method
- Iterative solution method
- Automatic substructuring
- Eigenvalue analysis
- Newton-Raphson, Quasi-Newton, Linear and Constant Stiffness iterative procedures
- Load and displacement control incremental procedures
- Arc length control incremental procedure
- Adaptive load and time increments
- Automatic incremental loading





[WWW.TNODIANA.COM](http://WWW.TNODIANA.COM)

TNO DIANA BV

Schoemakerstraat 97

2628 VK Delft

The Netherlands

T +31 15 276 3250

F +31 15 276 3019

